Propriétés électroniques à l'équilibre et hors équilibre des systèmes de type multicouche magnétique : la spintronique de dispositifs a base de jonctions tunnel

Coriolan Tiusan, Coriolan Tiusan

Faculté des Sciences
U.F.R. Sciences et Techniques de la Matière et des Procédés
Groupe de Formation Doctorale Energie Mécanique Matériaux

Habilitation à Diriger des Recherches

en Physique et Chimie de la Matière et des Matériaux

Propriétés électroniques á l'équilibre et hors équilibre des systèmes de type multicouche magnétique : la spintronique de dispositifs à base de jonctions tunnel

Coriolan-Viorel TIUSAN

Université Henri Poincaré Nancy I

Rapporteurs:

Agnes BARTHELEMY
Jacques TEILLET
Evgeny TSYMBAL

Membres du jury:

Bernard DIENY
Ron JANSEN
Daniel MALTERRE
Alain SCHUHL

Laboratoire des Physique des Matériaux
Faculté des Sciences, F-54500 Vandoeuvre lès Nancy
- soutenue le 22 Novembre 2006 -

Equilibrium and out-of-equilibrium electronic properties in magnetic thin film multilayer systems: spintronics of magnetic tunnelling devices

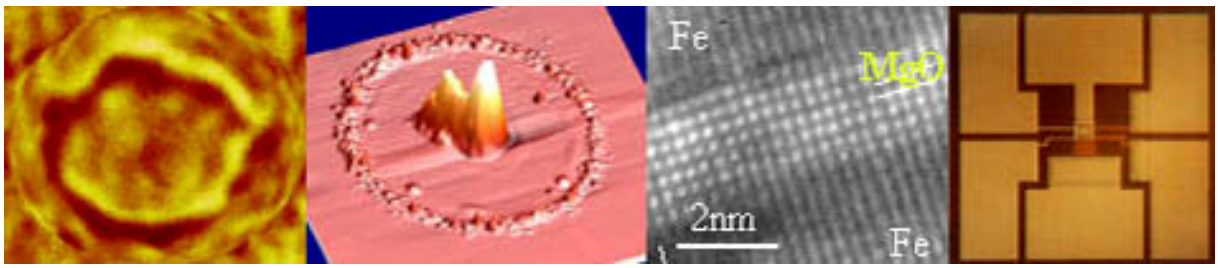

The only object of theoretical Physics is to calculate results that can be compared with experiment. It is quite unnecessary that any satisfying description of the whole course of the phenomenon must be given.

P. Dirac

Contents

Foreword

This report summarizes the scientific activities which I performed during the last ten years. It also presents the perspectives and the projects I would like to develop. The report is structured in several parts.

The first part of my report presents the scientific activities which I have already performed. Their content is integrated within the framework of the spin-electronics and focuses primarily on the study of magnetism and the spin-polarized transport in magnetic tunnel junctions systems. This work led me to elaborate magnetic tunnel junction systems and to study the correlation between their magnetic properties and the spin polarized transport at macroscopic and microscopic scales. The results obtained in epitaxial MTJs, showed that a physics beyond the free electrons model controls the electronic transport in the crystalline systems. The demonstration of the direct correlation between the electronic and chemical structure of the interface metal/oxide and the spin polarized tunnel transport, leads to important application perspectives for the engineering of interesting magnetoelectric characteristics of spintronic devices. Studies concerning the effects of the electronic coherence in structures with multiple tunnel barriers and those concerning the possibility to control the magnetic properties by spin polarized currents open the way toward new interesting spin application physics. The complexity of the transport mechanisms in epitaxial systems generated an important personal investment on the ab-initio techniques for the electronic structure analysis and the creation of modeling tools to describe the magnetic and the transport properties. Moreover, from the experimental point of view, the large spectrum of techniques which I used regroups the Sputtering and the Molecular Beam Epitaxy with regard to the elaboration of the samples, the optical lithography/ion etching techniques for patterning the micrometric size objects as well as other various characterization techniques. I mention here the in-situ Electron Diffraction (RHEED), the Auger spectroscopy and the ex-situ Atomic and Magnetic Force Microscopy and various other magnetometric and magneto-electric measure techniques for magneto-transport characterization.

A second part of the report summarizes some recent results obtained on complex or hybrid tunnel systems.

Another part of the report summarizes my research projects and objectives for the years to come. They consist in continuing the studies of magnetism and spin polarized transport in complex heterostructures of reduced dimensionality with a very particular accent on the development of a theoretical axis directed toward the modeling of electronic transport by ab-initio techniques.

The appendices of the manuscript contain further information, not detailed in the main text and some new results issued from scientific collaborations.

In the additional report joined to the present manuscript I present (in French) my Curriculum Vitae, the Scientific Production, a summary of all the teaching, collective responsibilities, participation in contracts and research management activities.

Avant propos

Le contenu de ce rapport vise à résumer l'ensemble des activités de recherche que j'ai menées durant ces dernières 10 années ainsi que les perspectives et les projets pour les années à venir. Le dossier se scinde en plusieurs parties.

La première partie de mon rapport expose mes travaux scientifiques effectués. Leur contenu s'intègre dans le cadre de l'électronique de spin et repose essentiellement sur l'étude du magnétisme et du transport polarisé en spin dans des systèmes de jonctions tunnel magnétiques. Ce travail m'a amené à élaborer des systèmes type jonctions tunnel magnétiques et à étudier la corrélation entre leurs propriétés magnétiques et leurs propriétés de transport polarisé en spin à des échelles macroscopiques et microscopiques. Les travaux sur les JTMs épitaxiées ont démontré qu'une physique au-delà du modèle des électrons libres gouverne le transport électronique dans les systèmes cristallins. La mise en évidence directe de la corrélation entre la structure électronique et chimique de l'interface métal oxyde et le transport tunnel polarisé en spin montre un fort potentiel pour le contrôle des caractéristiques magnéto-électriques de dispositifs spintroniques. Les études actuelles sur les effets de cohérence électronique dans des structures épitaxiées à multiples barrières tunnel et le contrôle de propriétés magnétiques par des courants de spin hors-équilibre ouvrent la voie vers une nouvelle physique et de nouvelles applications. D'une part, la complexité des mécanismes de transport dans les systèmes épitaxiés a généré un important investissement personnel dans les techniques de calcul de structure électronique ab-initio ainsi que dans la création des outils de modélisation des propriétés magnétiques et de transport tunnel. D'autre part, du point de vue expérimental, l'ensemble des techniques que j'ai utilisé regroupe l'épitaxie par jets moléculaires et la pulvérisation cathodique en ce qui concerne l'élaboration des échantillons, ainsi que des méthodes de caractérisation in situ (diffraction d'électrons RHEED, spectroscopie Auger) ou ex-situ (AFM pour la structure, MFM pour le micro magnétisme, VSM et effet Kerr pour le magnétisme macroscopique, et des diverses techniques de mesure électriques sous champ pour le magnéto-transport).

Une deuxime partie du rapport résume des résultats récents obtenus sur des systèmes tunnel complexes.

Une autre partie du rapport résume mes objectifs et projets de recherche pour les années à venir. Ils consistent à poursuivre les études de magnétisme et transport polarisé en spin dans des hétéro-structures complexes de faible dimensionalité avec un accent tout particulier vers le développement d'un axe théorique orienté vers la modélisation du transport électronique par des techniques type ab-initio.

Dans un rapport annexe , je présente mon Curriculum Vitae, ma production scientifique, et un résumé des activités que j'ai effectuées dans l'enseignement, l'administration de la recherche, la participation à des contrats et des responsabilités collectives.

Part I

Theoretical background of quantum tunneling in Magnetic Tunnel Junctions

Chapter 1

Tunneling transport

The manipulation of the electron spin and charge in magnetic multilayer structures represents the kernel of the spintronics. Once the large tunnel magnetoresistance effects (TMR) at room temperature [1] was demonstrated, one of the most interesting objects of the spintronics became the Magnetic Tunnel Junction (MTJ). The MTJ is constituted by two ferromagnetic layers separated by a thin insulating barrier. The electronic transport occurs by quantum tunneling effect, which is spin dependent. The relative orientation of the magnetization in the MTJ ferromagnetic layers is selectively controlled by magnetic fields, in architectures employing materials with significantly different magnetic properties (i.e. hard/soft architectures).
This chapter addresses the theoretical framework of the spin dependent tunneling in polycrystalline and in single crystal systems. It does not represent an exhaustive detailed overview on the quantum tunneling phenomena. Its main goal is to introduce to the reader the main concepts necessary for the understanding of the experimental results subsequently presented in the next chapters.

1.1 Polycrystalline MTJ

In polycrystalline systems the crystallographic axes have a random distribution. Therefore, their properties are isotropic: i.e. the electronic transport is independent on the direction of propagation. The physics of transport in these systems is well described within the free electrons model. The electrons of spin σ see a constant potential in the ferromagnetic materials and are described by an effective mass m_σ. In the most simple approach the tunnel barrier is rectangular (Figure 1.1) if the work functions of the two ferromagnetic materials are identical or trapezoidal if they are different. The transport is described using a two conductivity channel model, each channel being associated to one spin. Due to the exchange splitting, described in terms of a molecular field h, the potential seen by the up and down spins in the ferromagnets is different. In the ferromagnetic electrodes of the MTJ the electrons are described by plane waves $\Psi_i^\sigma \propto exp(ik_i^\sigma r)$, where $\sigma = \pm 1$ denotes the up ($\uparrow$) and down ($\downarrow$) spins and the $k_i^\sigma = \sqrt{\frac{2m_\sigma}{\hbar^2}(E + h\sigma)}$ is the spin dependent wave vector for an electron having the energy E and an effective mass m_σ in the ferromagnetic electrodes $i = 1, 2$.
In the barrier, the wave function of the electrons is evanescent $\Psi_\sigma \propto exp(-\kappa^\sigma r)$, the wave vector being given by $\kappa^\sigma = \sqrt{\frac{2m_\sigma}{\hbar^2}(V_B - E)}$, where V_B represents the barrier height. Within the free

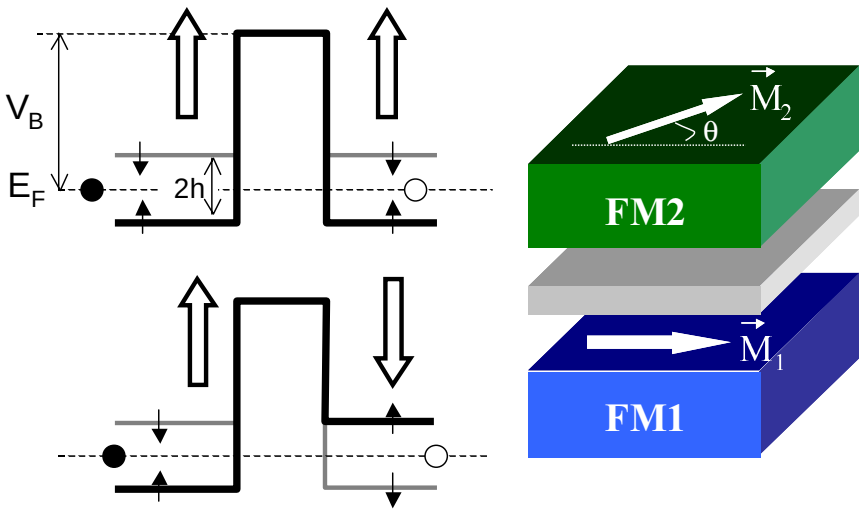

Figure 1.1: *Left panel*: Potential profile seen by up (thick line) and down spins (thin line) in a Magnetic Tunnel Junctions, in the parallel (top) and antiparallel configurations of magnetization. The exchange splitting in the ferromaagnets is $2h$. The rectangular barrier height is V_B, with E_F we denoted the energy of the electrons at the Fermi level. *Left panel*: Schematic representation of a magnetic tunnel junctions composed by two ferromagnetic layers FM1 and FM2 separated by a thin insulating barrier. The magnetization of the two FM layer can be adjusted independently, here we illustrate a configuration where the angle between $\vec{M}_1$ and $\vec{M}_2$ is θ.

electron model, for large barrier thickness limit, the attenuation of the wave function will be $T_\sigma \propto exp(-2\kappa^\sigma d)$ where d represents the rectangular barrier thickness. One can calculate the spin dependent transmission and the charge and spin currents for a given relative orientation θ of magnetization in the two ferromagnetic electrodes [2] of the junction. In the limit of thick barrier one find that the conductivity is a linear function of the cosine angle θ between the magnetic moments of the films:

$$G(\theta) = G_0(1 + P_1^{eff} P_2^{eff} cos(\theta))$$

where

$$G_0 = \frac{\kappa}{\hbar d}\left[\frac{e\kappa(\kappa^2 + k_1^{\uparrow}k_1^{\downarrow})(k_1^{\uparrow} + k_1^{\downarrow})}{\pi(\kappa^2 + k_1^{\uparrow 2})(\kappa^2 + k_1^{\downarrow 2})}\right]\left[\frac{e\kappa(\kappa^2 + k_2^{\uparrow}k_2^{\downarrow})(k_2^{\uparrow} + k_2^{\downarrow})}{\pi(\kappa^2 + k_2^{\uparrow 2)})(\kappa^2 + k_2^{\downarrow 2})}\right] exp(-2\kappa d)$$

This describes a typical spin valve effect, the tunnel magnetoresistance being defined as the relative variation of the tunnel conductivity between parallel and antiparallel orientation of magnetizations (one can consider an equivalent definition in terms of P and AP resistance).

$$TMR = (G_P - G_{AP})/G_{AP} = (R_{AP} - R_P)/R_P$$

Here P_i^{eff} is the effective polarization of the tunneling electrons given by:

$$P_i^{eff} = P_i \frac{\kappa^2 - k_i^{\uparrow}\, k_i^{\downarrow}}{\kappa^2 + k_i^{\uparrow}k_i^{\downarrow}}$$

where P_i represents the ferromagnetic electrode polarization ($i = 1, 2$) related to the spin dependent density of states $n_{i\sigma}$ given by:

$$P_i = \frac{n_i^{\uparrow} - n_i^{\downarrow}}{n_i^{\uparrow} + n_i^{\downarrow}}$$

The ferromagnetic electrode polarization can be measured by different techniques among which we mention here the superconducting tunneling experiments [3].
The effective polarization takes into account both the polarization of the ferromagnetic electrodes and the probability of transmission of a given state through the barrier. It represents therefore not an intrinsic property of the ferromagnets but describes the couple ferromagnet/tunnel barrier.
A model that it was widely used to describe the tunnel magnetoresistance (based on the free electron model) is the model of Jullière [4]. This model is extremely intuitive and relates the TMR effect to the polarization. In the standard Jullière model, the considered polarization is the polarization of the ferromagnetic electrodes (defined in terms of density of states for up and down spins). Based on the Fermi Golden Rule, and a two channel model associated to each spin, the main assumption is that the tunneling probability is only a product between the density of states in the electrodes on each side of the barrier, the transmission probability being neglected. Within this simplified approach, the TMR will be given by:

$$TMR = \frac{(n_1^{\uparrow} n_2^{\uparrow} + n_1^{\downarrow} n_2^{\downarrow}) - (n_1^{\uparrow} n_2^{\downarrow} + n_1^{\downarrow} n_2^{\uparrow})}{(n_1^{\uparrow} n_2^{\downarrow} + n_1^{\downarrow} n_2^{\uparrow})} = \frac{2P_1P_2}{(1 - P_1P_2)}$$

For the free electrons (parabolic bands) one can write: $P_i = (k_i^{\uparrow} - k_i^{\downarrow})/(k_i^{\uparrow} + k_i^{\downarrow})$.
Different tunneling experiments have illustrated that the polarization of the ferromagnetic electrode is not suitable to describe correctly the spin filtering effects in a MTJ. If one takes into account the transmission probability by tunneling, one has to replace the ferromagnetic polarization by the effective polarization. This will lead to a generalized Jullière model where the TMR will be described in terms of effective polarization.
Even more generally, one can derive [5] a Jullière-like formula for conductance by replacing the concept of electrode polarization by an averaged interfacial transmission polarization defined by:

$$P = \frac{< T^{\uparrow} > - < T^{\downarrow} >}{< T^{\uparrow} > + < T^{\downarrow} >}$$

where the average spin dependent transmission polarization is defined as:

$$< T^{\sigma} >= \sum_{k_{\parallel}, i} < T^{\sigma}(k_{\parallel}, i; 0, j) >$$

the $T^{\sigma}(k_{\parallel}, i; 0, j)$ represents the diffuse transmission probability for an electron to scatter at left interface from $(k_{\parallel}, i)$ on the left to $(0, j)$, where $(0, j)$ is the slowest decaying state in the barrier. In this case the conductance is given by the Landauer formula:

$$G = \frac{e^2}{h} \sum_{k_{\parallel}, j; k'_{\parallel}, i} T(k_{\parallel}, j; k'_{\parallel}, i)$$

where the transmission probability can be factorized as:

$$T(k_{\parallel}, i; k'_{\parallel}, l) = T_L(k_{\parallel}, i; 0, j) T_R(0, j; k'_{\parallel}, l) exp(-2\kappa(0, j)d)$$

This expression is simplified if the system has a translational symmetry ($k_{\parallel}$ is conserved ($k_{\parallel} = k'_{\parallel}$)). The condition of application of the Jullière model are: (i) the tunneling barier has to be thick in order to have very small wave functions overlap and (ii) the averaged interfacial transmission polarization must been determined for the considered electrode-barrier couple. This formalism may describe satisfactory the tunneling across amorphous 'thick' barriers.
Within the free electron model some other interesting features may be calculated. Indeed, from the calculation of the spin currents one can obtain the exchange coupling effects [2].
In the equilibrium case when the tunnel junction is not biased ($V = 0$), the coupling is derived from the torque produced by rotation of the magnetization from one ferromagnetic layer relative to another (see the appendix E). This is described in terms of a spin-flip current probability calculated from the stationary wave functions of the free-electron Schrödinger equation. The conservative exchange coupling strength has the form:

$$J = \frac{(U - E_F)}{8\pi^2 d^2} \frac{8\kappa^3(\kappa^2 - k_{\uparrow}k_{\downarrow})(k_{\uparrow} - k_{\downarrow})^2(k_{\uparrow} + k_{\downarrow})}{(\kappa^2 + k_{\uparrow}^2)^2(\kappa^2 + k_{\downarrow}^2)^2} e^{-2\kappa d}$$

The sign of the coupling is given by the term $(\kappa^2 - k^{\uparrow}k^{\downarrow})$. Then, it can be ferromagnetic ($J > 0$) or antiferromagnetic ($J < 0$).
In the presence of the voltage ($V \neq 0$), two interesting effects are also predicted within the free electrons calculation framework of Slonczewski [2]. They involve an irreversible exchange term in the coupled dynamics of the ferromagnets. For one sign of the voltage, the effect describes a relaxation of Landau-Lifshitz type. For the opposite sign of voltage, it describes a pumping action which can determine spontaneous growth of magnetic oscillations. This out-of-equilibrium effects are widely exploited nowadays for applications concerning either the magnetization dynamics/reversal by spin-torque or the study and the realization of high frequency oscillators based on spin transfer.
The free electrons formalism has been successfully used for decades to describe the magneto-transport properties in polycrystalline MTJ [6] (typically involving amorphous aluminum oxide barriers). By fitting the experimental transport characteristics with analytical free electrons models one can extract parameters such as the barrier width and height for a given experimental system.

1.2 Single crystal MTJ

The physics of transport becomes more complex in single crystal systems. Here, the space is anisotropic, the electronic properties (i.e. the transport properties) being dependent of the crystallographic direction. The potential seen by an electron has the periodicity of the crystal. Consequently, the electrons are described by Bloch wave functions

$$\Psi_{nk_i^{\sigma}}(r) = u_{nk_i^{\sigma}}(r) exp(ik_i^{\sigma} r)$$

which are plane waves modulated by a function u_{nk} having the crystal periodicity. This implicates that the wave function will present in-plane oscillations perpendicular to the propagation direction (z), the quantity

$$k_{\parallel}^{\sigma} = \frac{\left\langle \Psi \left| \frac{\partial^2}{\partial x^2} + \frac{\partial^2}{\partial y^2} \right| \Psi \right\rangle}{\langle \Psi | \Psi \rangle}$$

being nonzero.

Within the ferromagnetic electrodes the wave vector is given by:

$$k_i^{\sigma} = \sqrt{\frac{2m_{\sigma}}{\hbar^2}(E + h\sigma) - k_{\parallel}^{\sigma 2}}$$

and in the insulator

$$\kappa^{\sigma} = \sqrt{\frac{2m_{\sigma}}{\hbar^2}(V_B - E) + k_{\parallel}^{\sigma 2}}$$

with an attenuation probability $T \sim exp(-2\kappa^{\sigma} d)$. One can immediately see that the oscillations of the wave function parallel to the interface enhance the decay rate perpendicular to the interface (the $k_{\parallel} \neq 0$ enhances the κ). The role of the symmetry is to determine the number of nodes of the wave function in the plane of the interface. States that are primarily s like have therefore the smaller attenuation rate. The p-like states with more nodes are more attenuated and the d-like states typically even more. Following this intuitive simplified picture, one can try to regroup the atomic orbitals with respect to symmetry criteria (Figure 1.2). Within a given symmetry state, we have the same in plane modulation. Therefore we can identify the Δ_1 symmetry regrouping (s, p_z and d_z^2) orbitals, the Δ_5 regrouping (p_x, p_y, d_{xz}, d_{yz}), Δ_2 regrouping $d_{x^2-y^2}$ and Δ_2' regrouping d_{xy}. Then we can argue that the attenuation rate of different symmetries will be different: $\kappa_{\Delta_1} < \kappa_{\Delta_5} < \kappa_{\Delta_{2,2'}}$. This simple and intuitive explanation for the symmetry dependent attenuation rate is mainly valid for vacuum barriers where in the term $\frac{2m_{\sigma}}{\hbar^2}(V_B - E)$ the barrier heigth V_B is the same for all the symmetries. It describes correctly the attenuation in MgO barriers. However, in other oxides (i.e. SrTiO3) the attenuation rate of the Δ_5 state can be lower than the one corresponding to the Δ_1. Therefore, the analysis of the complex band structure of the oxide has to be considered [7, 8, 9] in order to determine the corresponding attenuation rate for each symmetry. In the case of the MgO barrier, the simple explanation works because from the complex band structure one gets that the barrier height $V_B^{\Delta_1} < V_B^{\Delta_5} < V_B^{\Delta_2}$ which is not the case for example for the SrTiO3.

This simple model is highly intuitive but is insufficient to describe some important phenomena that are predicted to occur in realistic systems. In order to describe correctly the physics of tunneling in single crystal systems, one has to involve ab-initio calculations. Most frequently, these calculations are performed using the LKKR technique [11, 10]. The main results of these calculations are resumed here below.

In agreement with the intuitive explanation based on lateral variation of the wave function, the large TMR ratios in single-crystal tunnel junctions are determined by the different tunneling mechanisms and symmetry-related decay rates of the Bloch waves for the majority and the minority spin channels. Roughly, an emitter single-crystalline ferromagnetic (FM) electrode, filters in terms of symmetry the electrons, subsequently injected across the insulating (I) barrier. The filtering effect can be easily understood from Figure 1.3 where we illustrate the bulk band

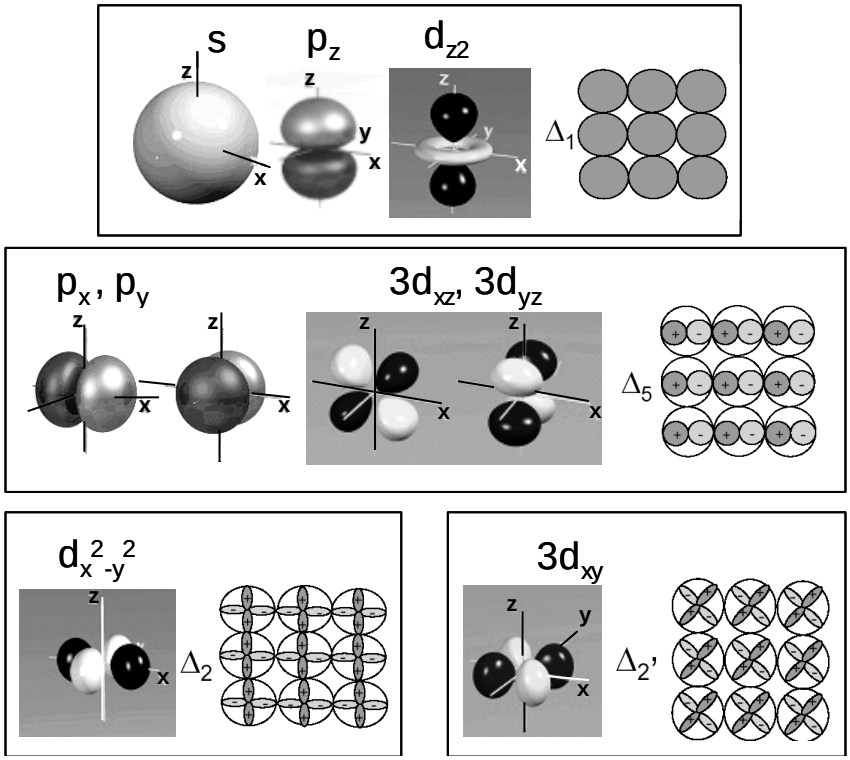

Figure 1.2: The atomic-like orbital regrouped by the symmetry properties. One can distinguish the orbital component of each of the symmetries Δ_1, Δ_5, Δ_2, $\Delta_{2'}$. These symmetries are particularly important for the electron propagation along a direction perpendicular to the Fe(001) surface.

structure of bcc Fe, along the high symmetry $\Gamma - H$ direction, for the majority and minority spins. The direction $\Delta = \Gamma - H$ corresponds to electrons with $k_{\|} = 0$, which propagate along the (100) direction in the crystal. At the Fermi level for the majority electrons, we have the following states: a Δ_1 (*spd*-like character state), a Δ_5 (*pd*) and a Δ_2' (*d*). Due to the exchange splitting, at E_F, there is no Δ_1 state for the minority spin. Therefore, one can immediately see that the Fe behaves as a half-metal in terms of the Δ_1 symmetry and that this is only valid for the (100) (Δ) direction. The tunnel transport probes: (i) the differences in spin injection (extraction) efficiency (directly related to the interfacial FM/I matching/coupling), and (ii) the differences in decay rates when tunneling across the barrier. The epitaxial growth of the MgO on Fe, via a rotation by 45° of the MgO lattice with respect to the Fe one, provides the symmetry conservation across the junction stack. The ab-initio calculations [10, 12] confirmed that the Δ_1 state has the smallest decay rate across the MgO, followed by the Δ_5 then the $\Delta_{2,(2')}$.

Consequently, for large MgO thickness in the asymptotic regime and in the parallel (P) configuration, the tunneling is found to be governed by the Δ_1 state. The conductance in the antiparallel (AP) configuration is very low,being only related to the $\Delta_{5,(2')}$ state propagation with a larger decay rate. In the AP configuration, an injected Δ_1 state cannot find equivalent symmetry in the opposite electrode with reversed magnetization. The spin asymmetry is predicted to increase above 1000%. On the contrary, when the thickness of the insulating layer

decreases, the contribution of the double degenerate *pd* character state Δ_5 and even $\Delta_{2,(2')}$ becomes significant, the conductivity in the AP state increases and therefore the TMR ratio decreases.

The above simplified picture for tunneling summarizes the main results [10, 12] of the theoretical predictions considering only the simplified situation where we analyze the electrons having $k_{\|} = 0$. This is essentially valid for large insulating thickness (asymptotic regime). The situation gets more complex at low MgO thickness, where the contribution of $k_{\|} \neq 0$ electrons becomes significant. Moreover, in the thin MgO barrier thickness regime, the tunnel transmission gets strongly affected by resonant effects at the interfaces [13, 10, 12, 14].

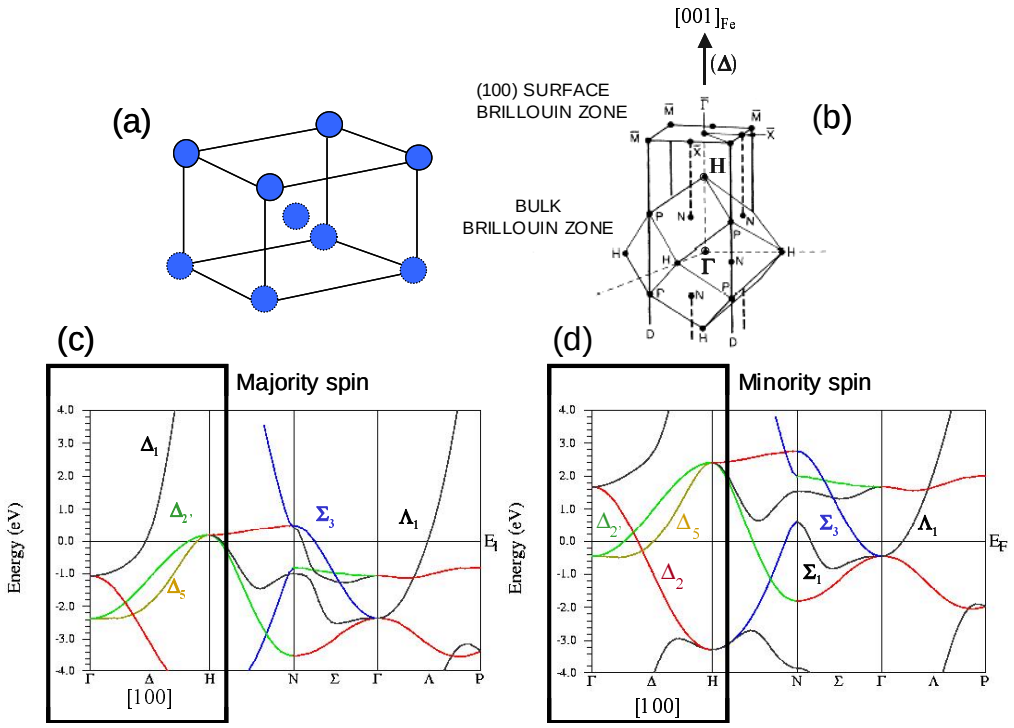

Figure 1.3: (a) Real space and (b) reciprocal space (right) representation of the bcc Fe lattice. For the reciprocal space (Brillouin zone) one can distinguish the high symmetry points and also the specific$(\Gamma - H)$ direction denoted by Δ. This direction correspond to the propagation of electrons perpendicular to the (100) plane in the real space. The (100) surface Brillouin zone is also represented, one can distinguished the specific direction $\bar{\Gamma} - \bar{X}$ where the $k_{\|}$ is 0 in $\bar{\Gamma}$. (c) Bulk band structure diagram for the majority spin of bcc Fe (d) Bulk band structure diagram for the minority spin of bcc Fe. We highlighted the $\Gamma - H$ direction which is important for the propagating electrons perpendicular to (100) surface of Fe ($k_{\|} = 0$). The states along this direction are labeled by Δ, the different indexes corresponding to different symmetries of the wave function (see the figure 1.3 for the orbital composition of each symmetry). One can see that at the Fermi level one can find spin dependent states: i.e. there is no Δ_1 state for the minority spin. This half metallic behavior of Fe with respect to a given symmetry is only valid along the Δ direction. The other directions illustrated in the band structure diagrams are (Σ) corresponding to (110) direction and Λ corresponding to the (111) in the real space.

Indeed, for the Fe(001)/MgO interface, an interfacial minority state is found above the Fermi

Energy. This is represented in the sketched diagram of the minority surface band structure of Fe(001) shown in Figure 1.4 (left panel). The surface state crosses E_F for a specific value $k_{\|} \neq 0$. Its contribution to the conduction becomes significant when it lies within a bulk band (gray areas in the diagram), situation when the surface state becomes an interfacial resonance state (IRS). Such interfacial resonances, from both sides of the barrier, may couple to each other leading to a resonant tunneling mechanism [13] which manifests itself as spikes in the conductance distribution in particular $k_{\|}$ points in the two-dimensional Brillouin zone. The width of these spikes is determined by the strength of the coupling in the barrier, which decreases exponentially with the barrier thickness. Consequently, the conductance from an interfacial resonance state is particularly important for extremely thin barriers. Here, the contribution of the resonant assisted tunneling is major even in the equilibrium regime, and determines the antiferromagnetic coupling interactions observed in our Fe/MgO/Fe system [16]. Alternatively, the contribution to the tunneling of an interfacial state may be activated, by biasing the junction at finite bias voltage, even at large MgO thickness regime. This can strongly affect the amplitude of the TMR effects.

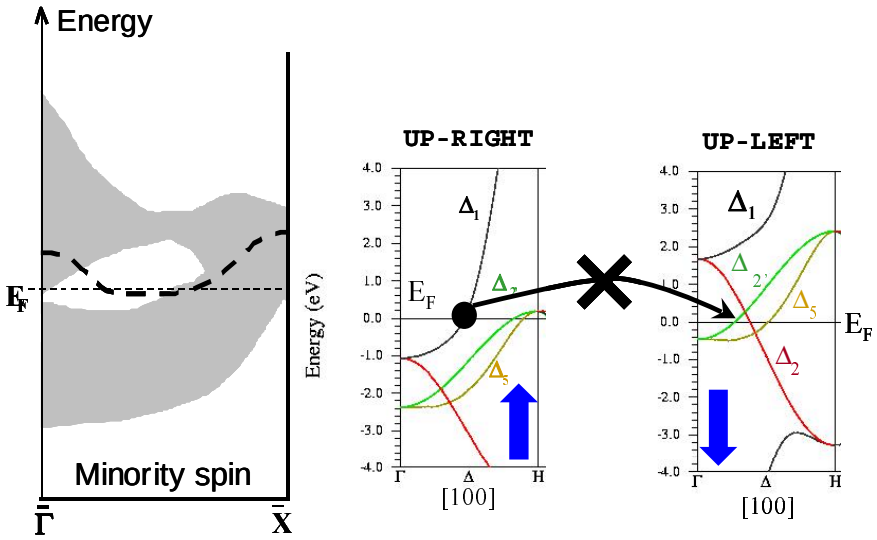

Figure 1.4: *Left*: Schematic band structure diagram for the minority spin along the $\bar{\Gamma} - \bar{X}$ direction of the (100)Fe surface Brillouin zone. Along this direction $k_{\|}$ varies ($k_{\|} = 0$ in $\bar{\Gamma}$). The gray area correspond to the bulk bands. The thick dashed line depicts the dispersion of the minority surface state of Fe. When this state crosses a bulk band it becomes interfacial resonance. *Right*: Bulk band structure representation corresponding to $k_{\|} = 0$ for the majority spin channel propagation from one electrode of the MTJ to the other one when the electrodes are in the antiparallel configuration of their magnetizations. One can see that an injected Δ_1 state from one side cannot find an equivalent symmetry state on the other side, its propagation being then forbidden. However, if one takes into account the interfacial resonance of Fe which is d_{z^2} like and belongs to the Δ_1 symmetry, an injected Δ_1 could propagate via an interfacial resonance of the opposite electrode in the antiparallel configuration.

Indeed, the large filtering effect in the Fe/MgO MTJ is related to the half metallic properties of Fe(001) with respect to the Δ_1 symmetry which can propagate only in the parallel configuration

and should be blocked in the antiparralel one. If one consider only the bulk contribution to the tunneling, in the AP state an injected Δ_1 state should not find equivalent state on the opposite electrode with opposite orientation of magnetization (see the diagrams from right panel of Figure 1.4). If now, one takes into account the interface electronic structure, one can see that the surface state of Fe(001) belongs to the Δ_1 symmetry (it has d_{z^2} orbital character). This state may activate a resonant conduction channel in the AP configuration. This will drastically reduce the conductivity contrast between the P and AP state and therefore the TMR. Moreover, the AP conductivity associated to the interfacial resonance may become in some specific situations larger than the conductivity in the parallel state. Then the TMR ratio will get negative, as wed will show experimentally in the paragraph dedicated to transport properties of MTJs. An important point worths to be mentioned here. The bulk and the interface polarization sign of Fe(001) are opposite. Whereas the bulk electronic structure provides a high positive polarization (100% with respect to Δ_1 state), the interface provides a 100% negative polarization, related to the minority spin surface state.

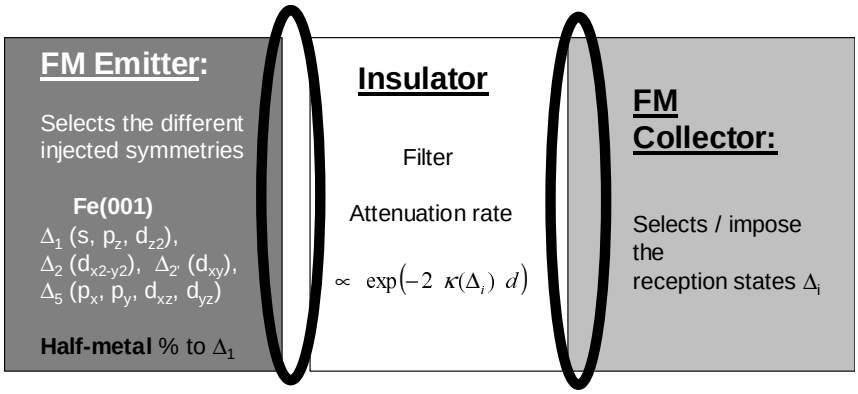

Figure 1.5: Simplified model of a single crystal magnetic tunnel junction. The model assumes independent propagating channels, each channel being associated to a given spin and a given symmetry of the wave function. As illustrated in figure 1.3, the ferromagnetic emitter selects the different wave function symmetries which will be injected across the barrier. The collector impose the received states. A given state will be accepted or not if an equivalent symmetry exists available in the collector. The single crystal barrier provides a special filtering effect: the attenuation rate of the wave function depends on its symmetry. The three subsystems are coupled by the interfaces where the wave function are matched. The role of the interfaces will be therefore major for the electron propagation.

Then, the coupling of the interface to the bulk which determines its contribution to the tunneling will have an extremely important impact on the amplitude of the positive TMR effets expected. Theoretically, one should neglect the contribution to the direct tunneling of interfacial resonances expected to be strongly attenuated in the asypthotic regime. However, in real systems, diffusion mechanisms may enhance the coupling of the interface to the bulk. Then, the very low conductivity regime of the AP configuration can be extremely sensitive to each new channel which may be activated for conduction. Recent theoretical results obtained by the team of Tsymbal [15] show that the surface state of the Fe can be quenched if one intercalate an Ag thin overlayer between the Fe and the MgO, without affecting the positive polarisation of the

Δ_1 state.

Based on the results of the ab-initio calculation, we can suggest a simplified model for the tunnel transport in an epitaxial MTJ. The following basic hypotheses are assumed. The main one concerns the conservation of symmetry across the stack and the conservation of $k_{\parallel}$. The transport occurs in a multichannel scheme, each channel being associated to a given spin and symmetry of wave function. In a perfect system we suppose that the spin and the symmetry are conserved during the transport across the MTJ stack. However, in a real system one can imagine spin-flip events or equivalent symmetry-flip events (or symmetry remixing). If the spin-flip events are related to electron-magnon interactions, the symmetry flip can be induced by diffusion events on local potential with a specific spatial symmetry. Therefore, the structural quality of the MTJ stack which will insure the conservation of symmetry will have a strong impact on the amplitude of the filtering effects.

Scattering events can also change the k (elastic) and/or the energy of the propagating wave function which may complicate the transport modeling. Following the Figure 1.5, one can distinguish the role of the MTJ electrodes and barrier. The ferromagnetic emitter selects the different injected symmetries, the insulating barrier provides a symmetry dependent attenuation rate and the ferromagnetic collector selects/impose the reception states. However, the coherent transport implicates the wave function matching at the interface. One can immediately understand that the interfaces will have a strong impact on the tunnel characteristics. Therefore, one can engineer the spin filtering features and the magneto-transport characteristics by controlling the interfacial electronic and chemical structure.

1.3 Résumé de chapitre en français

Introduction dans la thèorie du transport tunnel polarisé en spin dans les jonctions tunnel magnétiques

Jusqu'à présent, les structures utilisant l'effet tunnel polarisé en spin étaient constituées dans leur grande majorité d'électrodes magnétiques poly-cristallines séparées par une barrière isolante amorphe. Dans ces structures parfaitement isotropes le transport électronique est décrit de manière satisfaisante par un modèle de type électrons libres.
En revanche, les systèmes mono-cristallines sont anisotropes. Une description correcte et précise des mécanismes de transport tunnel dans de tels systèmes est extrêmement complexe. En effet, dans l'état actuel des modélisations théoriques, seule la connaissance des positions atomiques, notamment dans la barrière tunnel, permet de modéliser les phénomènes électroniques dans la multicouche. L'étude des phénomènes de transport dans les systèmes épitaxiés met en avant l'impact de la symétrie cristalline des métaux ferromagnétiques ou de la barrière. Ces résultats nous invitent à ne plus considérer que le caractère orbital des électrons mais aussi leur comportement dans l'environnement cristallin qu'ils perçoivent : les mécanismes de transport sont alors différents suivant la symétrie électronique.
Ces systèmes introduisent également une idée nouvelle : la polarisation en terme de symétrie électronique, notion intimement liée à la structure de bande et au magnétisme du cristal métallique. Ce concept novateur est à l'origine des fortes valeurs de magnétorésistance tunnel, prédites dans de nombreux systèmes épitaxiés (supérieures à plusieurs milliers de pour-cent pour le MgO). De plus, les mécanismes de transport tunnel propres à ces systèmes montrent une augmentation de la magnétorésistance avec l'augmentation de l'épaisseur de MgO (résultat contraire à ce qui est observé dans le cas d'isolants amorphes au-delà de 1.5nm).
La forte magnéto-résistance tunnel était alors expliquée d'une part par la symétrie imposée par les électrodes ferromagnétiques et d'autre part par l'atténuation dans la barrière tunnel, atténuation qui dépend de la symétrie de la fonction d'onde. Dans les systèmes épitaxiés, les électrons sont classés en fonction des propriétés de symétrie des orbitales auxquelles ils appartiennent par rapport au groupe d'espace du cristal. Dans le cas du Fe(100), le niveau de Fermi est peuplé d'états de Bloch Δ_1,Δ_5, Δ_2, pour le spin majoritaire et Δ_5,Δ_2, $\Delta_{2'}$ pour le spin minoritaire. L'analyse de la structure en bandes complexes donne le taux de décroissance dans la barrière tunnel associé à chacune de ces symétries électroniques : $\kappa_{\Delta_1} < \kappa_{\Delta_5} < \kappa_{\Delta_2} < \kappa_{\Delta_{2'}}$. Compte tenu des taux d'atténuation et le Fe(100) étant un demi-métal pour la symétrie Δ_1, le transport dans la configuration parallèle est dominé par le canal majoritaire Δ_1 alors que le canal Δ_5, gouverne la conductance antiparallèle. Or, comme $\kappa_{\Delta_1} < \kappa_{\Delta_5}$, la résistance dans l'état parallèle est beaucoup plus petite que la résistance dans l'état antiparallèle. Ainsi, s'il n'y a pas de mélange en symétrie dans la structure à cause de défauts, une magnéto-résistance supérieure à 1000% est théoriquement prédite.
Nous proposons un modèle multicanal pour décrire le transport électronique dans les jonctions mono-cristallines.

Part II

Magnetism and spin tunneling phenomena in polycrystalline Magnetic Tunnel Junctions

Chapter 2

Correlation between micromagnetism and tunnel magnetoresistance in poly-crystalline magnetic tunnel junctions using artificial antiferromagnetic systems

2.1 Introduction

The tunneling probability of electrons in magnetic tunnel junctions, and therefore the resistance of a tunnel junction, is controlled by the relative orientation of the magnetization in its ferromagnetic electrodes. In practice, this requires a pair of electrodes for which the orientation of each magnetization can be reversed independently. Commonly, a magnetically hard-soft system is used for this purpose. While the methods used to obtain the soft layer are quite the same, they differ significantly for the hard layer. Growth induced uniaxial anisotropy or exchange biasing a ferromagnetic layer using an antiferromagnetic layer have been extensively used to fix the magnetization of the hard layer [17]. However, uniaxial anisotropies are difficult to control in polycrystalline systems and the rigidity of exchange biased films shows in general a rapid decrease when increasing temperature. We report here an alternative way to harden a magnetic film by using an artificial antiferromagnetic sub-system (AAF) made of two ferromagnetic layers with different magnetic moments, antiferromagnetically coupled by an exchange interaction through a non magnetic spacer. The main advantages of such hard sub-systems are the large thermal stability (above 250°C) and the high coercive field of the net magnetization achieved by varying the thickness of the two magnetic layers, these two features being of essential importance for potential sensor applications. A large number of combination of metals gives rise to the appearance of an oscillatory antiferromagnetic coupling [18, 19, 20, 21, 22, 23, 24], but only a few are suitable for such applications. The antiferromagnetic coupling strength must be as large as possible in order to duplicate the domain structure of one layer in the other. We demonstrate in this chapter that this is the key factor to pin the largest magnetic moment against rotation

and in this way to increase the magnetic rigidity. Since the highest coupling strength has been measured in Co/Ru/Co [21] and Co/Rh/Co sandwiches [25, 26], our experimental choice has turned toward the use of Ru as a spacer.

This chapter is devoted to the examination of the field dependent micromagnetic behavior of Ru based AAF and the analysis of the consequences on the transport properties in magnetic tunnel junctions which use this AAF as a magnetic hard layer. Magnetic force microscopy studies have shown that the magnetization reversal in AAF systems occurs through the formation of Néel type 360° domain walls. The stability of these walls is demonstrated to be different in the two magnetic layers of the AAF. These aspects have major effects in magnetic tunnel junction devices, due to the extreme sensitivity of spin tunneling to spatial variations in local magnetic order. A systematic analysis of the magnetic properties of the constituent layers (the single layers) reveals that the behaviors of the two AAF magnetic layers, during the magnetization process, are substantially different. Besides the different shapes of the magneto resistance(MR) curves as a function of the stacking sequence of the constituent layers, the overall shape of the MR loop can be explained within our model. A microscopic study of the domain structure of the AAF sub-system by Magnetic Force Microscopy (MFM) gives insights on the magnetization processes responsible for the magnetization reversal. Evidence is given that reversal occurs through irreversible antiphase domain structure [24], which gives rise to Néel type 360° domain walls after rotation of the magnetization in each domain. We demonstrate that these generated walls persist after the reversal has occurred up to higher field values in the thin layer than in the thick layer. The source of wall pinning relates to the fluctuation of the exchange coupling between the two ferromagnetic layers.

The tunnel magnetoresistance of the samples, in the range of 20-30% at room temperature, makes the tunnel junctions highly sensitive to magnetic fluctuations. A sharp switching of the soft magnetic layer upon field reversal prevents a domain structure from occurring in the soft magnetic layer, in the field window used for our micromagnetic studies. The tunnel device can thus be used as a sensitive probe for measuring small magnetic fluctuations associated with micromagnetic defects, domains and walls in the AAF system. These fluctuations modulate the resistance of the tunnel junction and are fully reflected in the shape and the amplitude of the TMR signal. The correlation between macroscopic transport measurements and the microscopic distribution of magnetization shows that the presence of a domain structure leads to the appearance of different resistance channels and therefore has a direct consequence on the TMR signal.

2.2 Multilayer film preparation and experiments

2.2.1 Growth and study of the buffer layer

Since quantum tunneling between metal electrodes through an insulating barrier is known to be strongly dependent on the morphology of the metal/insulator interfaces, much effort has been devoted to optimize the flatness of these interfaces. To ascertain the quality of the interfaces, we have optimized the growth of a complex buffer layer which leads to AAF sub-system with characteristics close to those achieved in high quality Molecular Beam Epitaxy (MBE) grown

samples [21, 27].
The entire growth of the multilayer film was done *in situ*, in a high vacuum Alliance Concept sputtering system having a base pressure of 2×10^{-8} mbar. The Figure 2.1(a) shows a typical layer sequence with the stack of a Cr/Fe/Cu buffer layer on Si(111), a Ru based AAF sub-system (Co/Ru/Co or Co/Ru/CoFe), an Al_2O_3 tunnel barrier, a CoFe/Fe detection bilayer and a Cu/Cr capping bilayer.
Reproducible characteristics of the magnetic active layers have been achieved by first growing a Cr(1.6nm)/Fe(6nm)/Cu(30nm) buffer layer on a previously sputter-etched 3 inch diameter Si(111) wafer. The topographic and magnetic properties of the magnetic active part of each sample have been optimized as a function of Cu and Fe thickness. As a preliminary, changes in the topography of the surface of the buffer and topmost AAF Co or CoFe layer were studied as a function of the Fe and Cu layer thickness, using *ex situ* atomic force microscopy (AFM). The buffer roughness was found to decrease with increasing Fe thickness and decreasing Cu thickness. The addition of a Cr seed layer, necessary to obtain a higher coercivity of the AAF magnetic layers, reinforces this trend. The best compromise was obtained by setting the thicknesses of the Cr, Cu and Fe to 1.6nm, 6nm and 30nm respectively. The 30nm Cu layer ensured a small resistance of the bottom current lead of the junctions (buffer layer) as compared to the resistance of the barrier in the final sensor devices[1] [28], as well as a magnetic decoupling of the Fe seed layer and AAF structure. A thickness of 6nm of Fe was sufficient to achieve a suitable buffer smoothness, while introducing a parasitic magnetic signal sufficiently small so as not to hinder the interpretation of the magnetization curves recorded on the complete junction stacks.
By using such Cr/Fe/Cu buffer layers, a reasonable surface roughness of the hard subsystem topmost layer was achieved (peak to peak and RMS values of 8 Å and 1.8Å respectively), irrespective of the Ru and Co or CoFe layer thickness. Notice that a significant increase of the surface roughness was eventually observed after the formation of the Al oxide layer on top of the AAF sub-system. The peak to peak and RMS roughness then reached 13Å and 3Å respectively.

2.2.2 Growth and study of the tunnel barrier and the magnetic soft layer

The Al oxide barrier was formed using the oxidation technique first developed by Greiner [29]. This technique allows the oxidation process to be carried out within a standard commercial sputtering plant without the need of accessing a separate chamber having a glow discharge plasma source. An Al layer is first deposited on top of the AAF sub-system. The substrate table then serves as a cathode for generating a **rf** Ar/O_2 plasma. A competition thus occurs at the Al surface between sputter etching by Ar ions and oxidation by oxygen ions, which leads to a self-limited oxidation process. In this study, the **rf** power density was set to 0.05 W/cm^2, the partial pressure of both Ar and O_2 gases to $9 \cdot 10^{-3}$ mbar and the oxidation time was optimized by X-ray Photoelectron Spectroscopy (XPS) experiments to obtain fully oxidized Al barriers for a given thickness of the as deposited Al (details can be found in ref. [30]). The optimization of the oxidation time is an extremely important step, in order to avoid over and under oxidation of the barrier, both known to result in detrimental effects on the MTJ's magneto-transport

[1] A spurious geometrical enhancement of the TMR effect is likely to occur if the resistance of the barrier is too small as compared to that of the current leads

properties [31].
A magnetically soft system was sputtered on top of the Al oxide tunnel barrier. The so-called detection bilayer (DL) used in our MTJ, consisting of $Co_{50}Fe_{50}$ (1nm)/Fe(6nm) bilayers have a coercive field smaller than 20 Oe, driven mainly by the 6nm thick Fe layer. The CoFe layer increases the electron polarization in the magnetic layer adjacent to the oxide barrier. In agreement with the Jullière model [4], an enhancement of the TMR signal is expected by the use of a CoFe mixture because of the larger spin polarisation of CoFe compared to Co (larger average magnetic moment of Co in CoFe).
The multilayer stack shown in Figure 2.1(a) is illustrated by a cross section Transmission Electron Microscopy (TEM) image in Figure 2.1(b). It gives an insight on the MTJ multilayer sequence, with a zoom on the Al oxide tunnel barrier. The TEM image indicates that the small roughness observed *ex situ* by AFM is conserved after depositing the rest of the stack. Furthermore, it shows that the roughness of the layers is correlated (corrugation of interfaces) as illustrated by the TEM image (Figure 2.1(b)). Roughness induced large fluctuations in the thickness of the different layers are therefore avoided, leading to high quality tunnel barrier without pinholes which would act as hot conduction points.

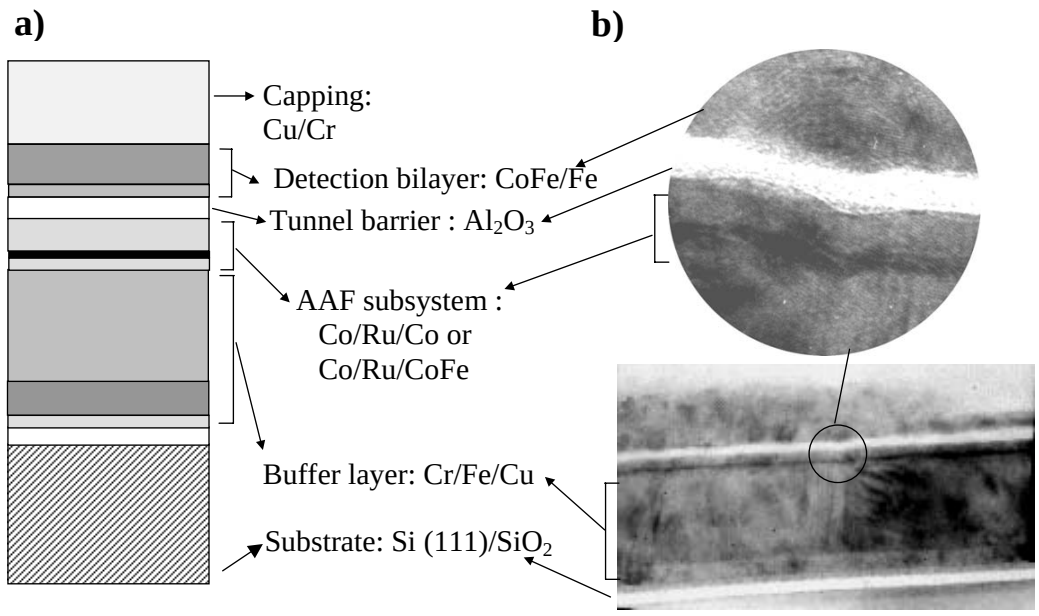

Figure 2.1: (a) Magnetic tunnel junction (MTJ) stack design: Si(111)/[Cr(1.6nm)/Fe(6nm)/Cu(30nm)]/ [Co(1.8nm)/Ru(0.8nm)/Co(3nm) or CoFe(3nm)]/ Al_2O_3(1.5nm)/CoFe(1nm)/Fe(6nm)/Cu(10nm)/Cr(5nm). (b) Transmission Electron Microscopy (TEM) cross section image of the MTJ stack

In order to perform tunnel transport measurements, the as-deposited 3 inches wafers, containing the stack described above, were patterned in four UV lithography-etching steps into large arrays of junctions with square shaped tunnel barrier of nominal surface areas S = 10x10, 20x20 and 50x50 μm^2. Detailed information of the wafer processing are described elsewhere [32]. The

junctions were measured at room temperature [30] using a conventional 4-point technique with a dc voltage source.
The magnetic properties of the as-deposited multilayer films were studied at both macroscopic and microscopic scales. The macroscopic magnetization curves were measured using an Alternating Gradient Field Magnetometer (AGFM) at room temperature. At a microscopic scale, the domain structure has been observed using a Magnetic Force Microscope (MFM) in zero and finite in plane applied fields up to | H | = 600 Oe. The MFM setup consists of a *Nanoscope Dimension 3100* equipped with a magnetic CoCr coated Si tip, magnetized along the tip axis. The scans have been performed at about 30 nm above the surface in the tapping-lift (interleave) mode developed by Digital Instrumental. This mode allows us to disentangle the long-range magnetic and the short-range topographic information during the same image acquisition. Since the detected signal (frequency shift of the vibrating cantilever) is proportional to the second derivative of the local field, this technique provides a good signal to noise ratio.

2.3 Macroscopic Magnetic Properties

The use of the artificial antiferromagnetic structures as hard sub-systems in a tunnel junction device requires the understanding of its magnetic response when submitted to an external applied field. The AAF consists of an asymmetric trilayer stack composed of two Co or Co and CoFe layers of different thicknesses, both layers being antiferromagnetically coupled by exchange interaction through a nonmagnetic spacer layer. The top layer is thicker and has therefore a larger moment m_1, than the bottom layer with moment m_2. In this work, Ru has been used as a spacer layer mainly due to its high coupling strength [27]. The magnetic layers consist of either pure cobalt layers (Co/Ru/Co) or Co and CoFe (Co/Ru/CoFe) which allows us to investigate a large range of gain in rigidity, as will be shown in the next sections. The antiferromagnetic (AF) coupling of both systems shows similar coupling strength as well as an oscillatory behavior as a function of Ru thickness (t_{Ru}), with maxima at t_{Ru} = 3Å and t $=_{Ru}$ 8Å, signature of interface quality comparable to MBE grown samples [21, 20, 27, 33]. In this study, a Ru layer thickness of 0.8nm has been used to increase the thermal stability of the AAF and avoid the presence of a biquadratic coupling that exists for Ru thicknesses in the range of 4-6 Å[27].

2.3.1 Macroscopic magnetic properties of an artificial antiferromagnetic system

The room temperature magnetization of a typical AAF system: Buffer / Co(1.8nm) / Ru(0.8nm) / Co(3nm) / Al_2O_3(2nm) is shown in Figure 2.2(a). The insets describe the relative orientation of the magnetic moments at different fields along decreasing field branch from the positive saturation field ($+H_s$) to the negative saturation field ($-H_s$). The topmost arrow gives the net magnetic moment orientation of the thick Co layer, m_1, the middle arrow the thin Co layer m_2, and the bottom arrow the Fe layer included in the buffer layer m_{Fe}. Decreasing the field from $+H_s$ saturation, a first hysteresis appears in the flank region in a field range varying from 4-2kOe (Figure 2.2(a)). This hysteresis is attributed to the development of a domain structure during the reversal of the thin AAF layer [24] with the smallest magnetic moment (m_2).

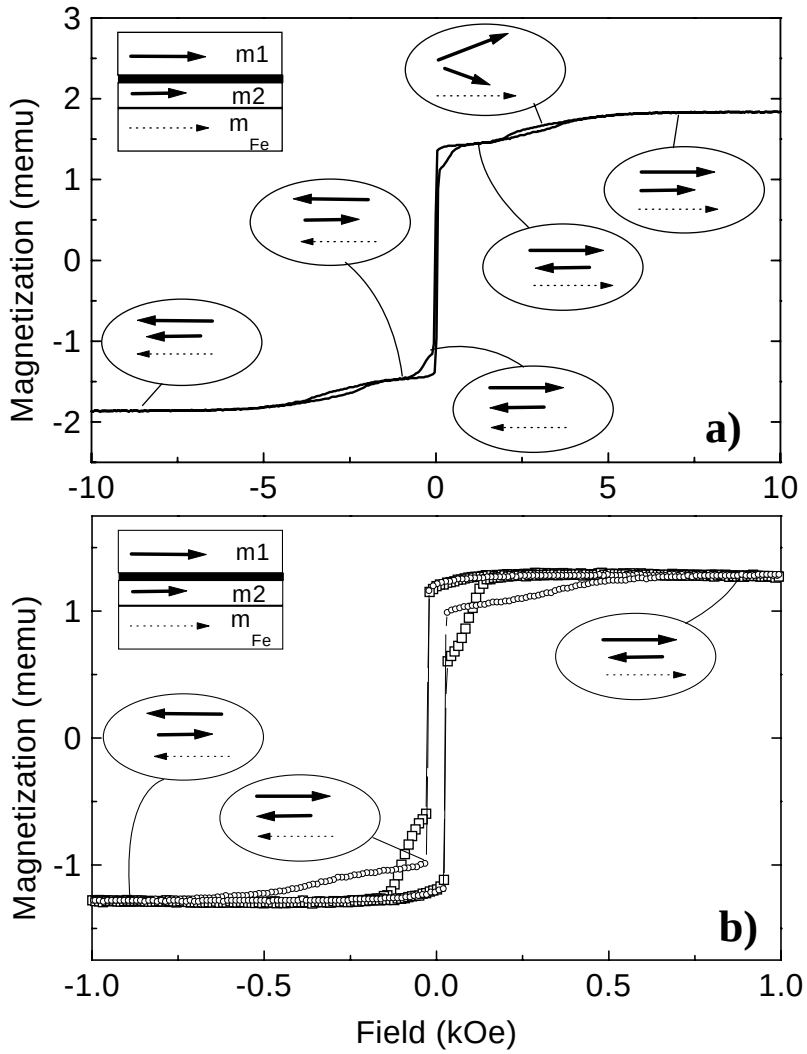

Figure 2.2: (a) Magnetization curve of a typical AAF subsystem: buffer / Co(1.8nm) / Ru(0.8nm) / Co(3nm) / Al_2O_3. (b) Zoom on AAF magnetization curve ($\pm$ 1kOe) ($-\circ-$) and comparison with the magnetization curve of a single cobalt layer made on the same conditions (open square).

The net magnetic moment remains oriented along the positive applied field. Consequently, the magnetic moment of the thick AAF layer (m_1) remains oriented along the positive field while the magnetic moment of the thin AAF layer (m_2) reverses to be oriented opposite to the field. Furthermore, since the magnetic layers are polycrystalline, the local sense of rotation of the magnetic moments inside a layer can be influenced by thermal activation, small inhomogeneities of local exchange interactions or local anisotropy. Therefore, regions spaced far enough to overcome the exchange interactions will rotate clockwise or counterclockwise, leading to the appearance of magnetic domains when decreasing the applied field. By further decreasing the applied field, the domain structure in the thin magnetic layer, and therefore this hysteresis, disappears and the *M-H* curve shows a plateau for which the net magnetization remains constant. $H_p = 1.5$ kOe measures the width of the plateau in positive field (Figure 2.2). On the plateau,

the magnetizations of both magnetic layers are strongly antiferromagnetically coupled and each layer is uniformly magnetized. The width of the plateau is given by the following expression [34] (a detailed analysis containing an analytical model for an artificial antiferromagnetic systems may be found in the appendix of this manuscript):

$$H_p = (m_1 - m_2)/(m_1 + m_2)H_s \tag{2.1}$$

This width defines the operational field-window of the tunnel device using the AAF sub-system. Therefore, we focus our investigation on minor loops for applied fields $-H_p \leq H \leq +H_p$. In negative applied magnetic field, the Fe layer switches first abruptly at 20 Oe followed by the continuous reversal of the net magnetization of the AAF. This reversal is completed when the net moment $(m_1 - m_2)$ is oriented along the negative field direction, giving rise to a plateau in the negative side of the curve. On this plateau, the magnetic moments of both magnetic layers are again mutually firmly antiferromagnetically coupled. The gain in rigidity, induced by the AF coupling of the two magnetic layers of the AAF system is given [34] by the ratio Q (total magnetic moment at saturation over net magnetic moment at the plateau, i.e. $Q = (m_1+m_2)/(m_1-m_2)$). This theoretically predicted gain in rigidity is experimentally verified by comparing the coercive fields of the AAF ($\simeq$400 Oe) and the single cobalt layer($\simeq$100 Oe) (Figure 2.2(b)). The rigidity of a single magnetic layer stems from the frictional torque against rotation, originated from the microscopic (local) anisotropy of the randomly oriented crystallites that constitute the layers. The layers do not exhibit any pronounced macroscopic magnetic anisotropy in the plane of the films. As shown in Figure 2.2(b), the AAF amplifies [2] the magnetic rigidity of a single magnetic layer that enters in its structure by the factor Q (here $Q \simeq 3$). Consequently, the magnetic properties (i.e. coercivity) of the single magnetic layer strongly determine the rigidity of the AAF. Therefore, the larger the coercivity of the single layer, the better the magnetic response of the AAF for the use as a hard layer. The next paragraph describes the best conditions used to achieve a large coercivity for the single magnetic layers of the AAF.

2.3.2 Magnetic macroscopic properties of a single Co and CoFe magnetic layers

The macroscopic *M-H* loops of a buffer/Co(3nm) single layer covered by 3nm of Ru were studied. As a buffer layer, we have used the optimized Cr(1.6nm)/Fe(6nm)/Cu(30nm). The switching of the Fe buffer corresponds to the steep change of M at low fields (20 Oe) and is not further discussed (Figure 2.3). The corresponding hysteresis loop shows a gradual reversal of the Co

[2] The *M-H* curves (Fig. 2b corresponding to the Co/Ru/Co and Fig. 3b corresponding to the case of Co/Ru/CoFe artificial ferrimagnets) allow to estimate the experimental values Q_{exp} by comparing the AFi coercivity with the coercivity of the single Co or CoFe layers.The experimental gains in rigidity (Q_{exp}=3 in the Co/Ru/Co AFi and Q_{exp}=2 in the Co/Ru/CoFe) are smaller than the theoretical predictions (Q=4), computed from the previous definition relation between Q and the magnetic moments of each AFF layer (m_1 and m_2). One reason is an unequal intermixing degree for the Co and CoFe at the Co/Ru and CoFe/Ru interfaces. Co will loose magnetic moment at the interface with Ru and Al oxide while the $Co_{50}Fe_{50}$ is preserving its 'as deposited magnetic moment' due to a low intermixing degree at the interfaces. Consequently the experimental values for m_1 and m_2 in each of the two AFi systems are not equal with the theoretical estimations by taking into account the sputtered thicknesses

layer, with a coercive field of about 100 Oe, in contrast to a steep switching and a larger coercivity for a Co layer grown on the same buffer but covered with Cu, for which the coercive field is about 250 Oe (Figure 2.3(a)). It appears that by capping with Ru, the softening of the Co layer was caused by the interfacial mixing between Co and Ru. Several explanations converge towards the idea that at the interface, Ru is strongly intermixed with Co in comparison with a very low intermixing degree in the case of Co/Cu [35] . Due to the granular structure of Co, Ru can diffuse between the grains at the interface and decrease the magnetic thickness and the exchange coupling between the grains. The chemical affinity of these elements tends to mix the interface, independently of the deposition technique. The intermixed region is over 3 ML at each interface [27].

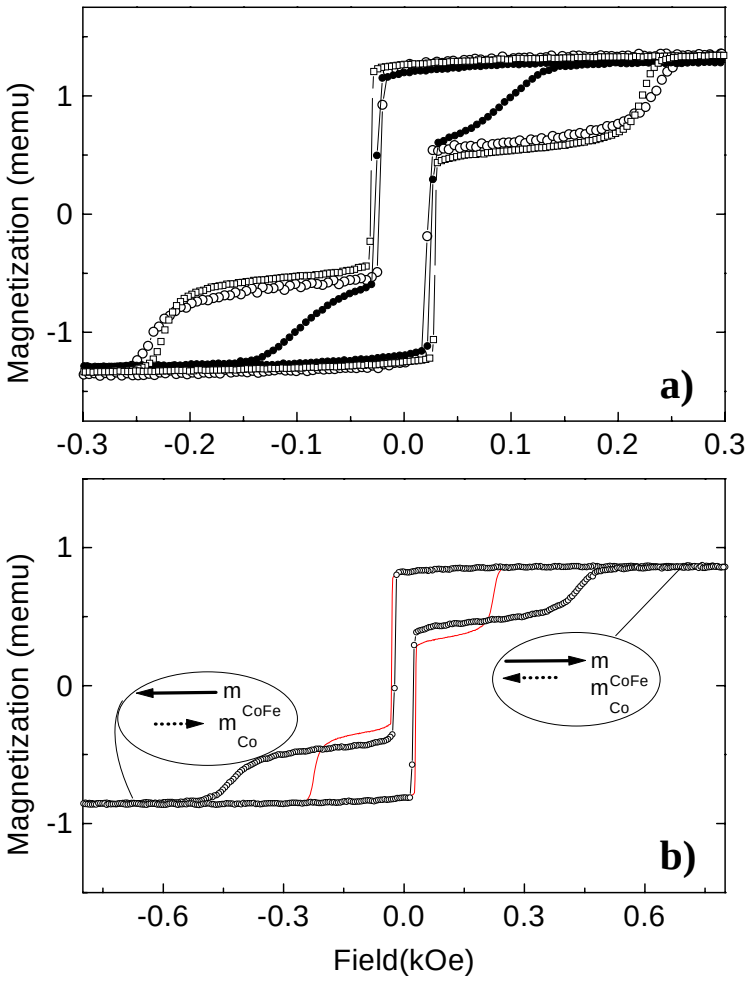

Figure 2.3: (a) Magnetization curve of single Co(3nm) layer sputtered on Si(111) / Cr(1.6nm) / Fe(6nm) / Cu(30nm) buffer layer capped with Ru (− • −) and Cu (− ∘ −). The $Co_{50}Fe_{50}$ (3nm) capped with Ru, sputtered on the same buffer layer, has similar properties (open square) with the cobalt single layer capped with Cu. (b) Magnetization curve for Co(2nm) / Ru(0.8nm) / $Co_{50}Fe_{50}$ (3nm) AAF in a field range of ± 1kOe (− ∘ −) by comparison with the single $Co_{50}Fe_{50}$ (3nm) layer performed on the same conditions (− − −). The experimental enhancement of rigidity gives a factor (Q_{exp}=2).

To overcome the magnetic consequences of intermixing in the case of Co and Ru, we have added Fe in the Co layer since Fe and Co show a large chemical affinity being totally miscible. Due to a higher chemical affinity between Co and Fe than between Co and Ru, the mixing of the $Co_{50}Fe_{50}$ /Ru interface has been strongly reduced. An experimental proof is given in Figure 2.3(a) where the magnetization curves of the $Co_{50}Fe_{50}$ sample capped with Ru seem to be identical to those of the Co capped with Cu. Indeed, the coercive field is high (more than 220 Oe), 2 to 3 times higher than in Co/Ru layers grown on the same buffer layer and the magnetization reversal is much sharper. Moreover, a systematic study of magnetization versus thickness of a pure CoFe film capped with Ru has shown that only half of a monolayer is magnetically dead at the interface while more than 2 atomic layers are magnetically dead for pure Co capped with Ru.
The advantage of building Co/Ru/$Co_{50}Fe_{50}$ AAF instead of Co/Ru/Co is related to the larger coercivity of $Co_{50}Fe_{50}$ compared to the coercivity of a single Co layer capped with Ru. In this way a large rigidity of the AAF can be achieved by a smaller amplification factor Q. Indeed, as shown in Figure 2.1(b), the rigidity of Co/Ru/CoFe with Q_{exp}=2 is similar to the one observed for the Co/Ru/Co system with Q_{exp}=3. This has strong effects in the domain structure developed during the magnetization reversal, as we will be shown in the next paragraph.

2.3.3 Transport properties of MTJ using the artificial antiferromagnetic system as hard magnetic layer

We have investigated in detail the two following magnetic tunnel junctions, for which the only difference is the topmost AAF magnetic layer: S_1: [*hard subsystem* Co/Ru/Co] / Al_2O_3 / [*soft bilayer* CoFe/Fe] and S_2: [*hard subsystem* Co/Ru/CoFe] / Al_2O_3 / [*soft bilayer* CoFe/Fe]. The *M-H* and corresponding *TMR* loops for S_1 and S_2 (shown in Figure 2.4(a,b)) measured in the operational field window of the tunnel device, demonstrate the influence of the magnetic behavior of the hard subsystem on the shape of the *TMR* signal.
In the positive part of the plateau (Figure 2.4(a) corresponding to Co/Ru/Co/Al_2O_3/CoFe/Fe tunnel junction), the detection bilayer and the topmost (thick) layer of the AAF are aligned along the field direction. Consequently, a parallel configuration of magnetization for the layers adjacent to the barrier induces a high probability of tunneling and so a small resistance of the MTJ. By reversing the applied magnetic field, the detection bilayer reverses its magnetization inducing an antiparallel configuration responsible for a high resistance of MTJ. This antiparallel state is preserved as long as the net magnetic moment of the AAF, $(m_1 - m_2)$, remains rigid and oriented along the positive field direction. As soon as the reversal of the net moment $(m_1 - m_2)$ is completed, the magnetization of the topmost layer of the AAF becomes again parallel with the detection bilayer giving rise to a small resistance of the MTJ device. The shape and the amplitude of the TMR signal are modified by using the Co/Ru/$Co_{50}Fe_{50}$ AAF as a magnetic hard layer in the MTJ device, as shown in Figure 2.4(b). One of the significant advantages of using $Co_{50}Fe_{50}$ at the interface with the tunnel barrier is that the amplitude of the TMR signal is enhanced from 22% to 30%, due to the higher spin polarization at the $Co_{50}Fe_{50}$ /oxide interface. Particularly important is that the antiparallel state does not give a flat plateau in the TMR curve as shown in Figure 2.4(a). This confirms that the AAF system is not a fully magnetically homogeneous and rigid block but consists of domains which start to develop in negative field.

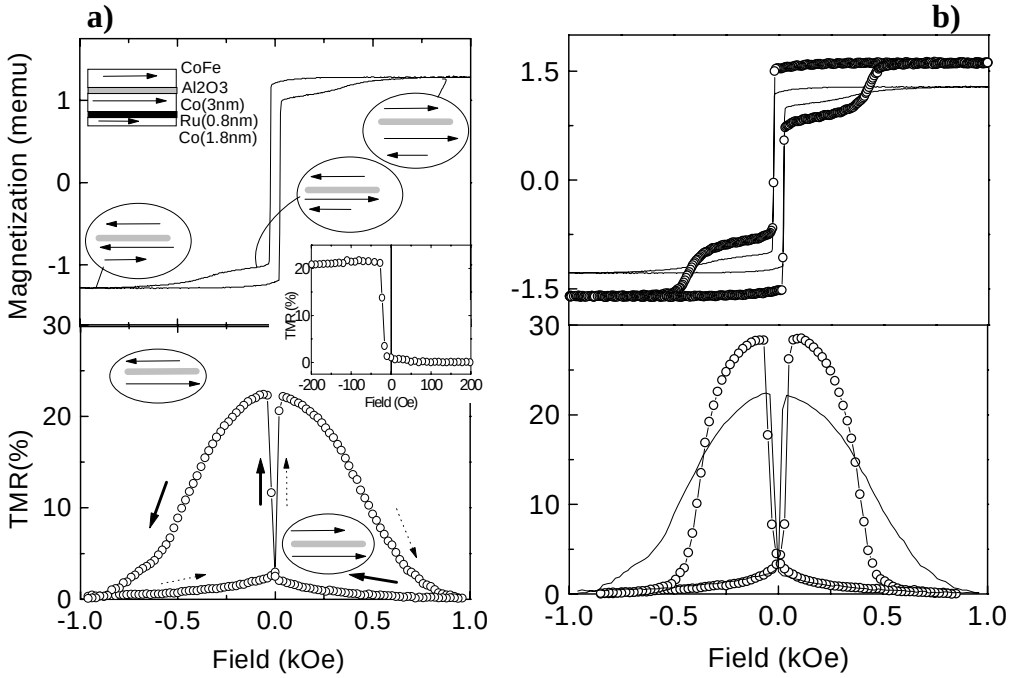

Figure 2.4: (a) Magnetization curve of a typical Co / Ru / Co / Al_2O_3 / CoFe / Fe stack ($- - -$) in a field range of $\pm$ 1kOe, correlated with the TMR curve ($- \circ -$). (Inset) Minor TMR loop for the detection layer in a field range where the AAF acts as a rigid block. (b) Influence of the AAF magnetic properties on the *TMR* signal shape and amplitude. The MH and corresponding *TMR* curves for the MTJ having $Co_{50}Fe_{50}$ as the top layer of the AAF interfaced with the tunnel barrier ($- \circ -$) differ in shape and amplitude from the corresponding case when the top layer of the AAF system is Co ($- - -$).

The difference in shape of the *TMR* curves for the Co/Ru/$Co_{50}Fe_{50}$ AAF stems from differences in the reversal characteristics of this hard subsystems in comparison with Co/Ru/Co.
The reversal process as well as the signal height is controlled by the field dependent micromagnetic structure of the two coupled magnetic layers. Understanding this requires a detailed analysis of local MFM features together with correlation of the *MR* curves, which is the purpose of the next section.

2.4 Microscopic Magnetic Properties

Models for magnetization reversal rely on the well known ripple domain configuration in thin magnetic films [36, 37, 38, 39, 40, 41]. The Co and CoFe alloy layers are polycrystalline and are made of small magnetic grains coupled by exchange interactions. On a macroscopic scale, the layers are magnetically isotropic due to a random orientation of the easy magnetic axis of each grain. However, on a microscopic scale an effective local anisotropy can be defined as well as an effective correlation, which length scale is characterized by the exchange correlation length l_{ex}. This correlation length is very sensitive to spatial variations of the anisotropy, to the magnetic moment and coupling strength between grains and to thermal fluctuations. Therefore a spatial fluctuation of l_{ex} is expected over the layer surface. The coupling strength depends on the

thickness of the magnetic film [41]. Micromagnetic calculations show that for small thicknesses and weakly-coupled grains, the reversal of the layer magnetization proceeds by rotation of the individual grain magnetic moments. A characteristic ripple structure starts to appear when either the thickness or the coupling between the grains is increased [41].

2.4.1 Magnetic microscopic properties of a single layer

The magnetization reversal for a $Co_{50}Fe_{50}$(3nm) single layer covered with Ru is illustrated in the Figure 2.5 using a magnetization curve and a set of corresponding MFM images obtained at specific applied fields. By reducing the external field from positive saturation to zero, dark and bright contrasts corresponding to magnetic charge accumulations begin to form, consistent with randomly distributed small fluctuations of the magnetization orientation relative to the field axis direction. This domain structure is created by independent rotation of magnetization from site to site as we proceed from saturation towards zero applied field. When the field is reversed, the moments inside uniformly magnetized regions weakly coupled with the neighboring regions will rotate first, in agreement with the increase of contrast in the MFM image (Figure 2.5(b)). Then, increasing the negative field, the magnetization inside the tightly coupled regions will start to rotate. When regions with different sense of rotation of their local magnetization meet, correlated Néel walls start to establish as shown from the fine correlated structures which appear on Figure 2.5(c). As the negative field further increases, the neighboring moments are dragged in the field direction by exchange interactions. Consequently, correlated 360° Néel walls are formed, increasing their effective wall length. Appendix A shows that the MFM signal is consistent with the stray fields for a 360° wall. These walls are clearly evidenced by the presence of correlated channels on the MFM images (Figure 2.5(d,e)). The walls remain pinned at fields higher than fields for which the reversal of the magnetization in domains is almost completed. This is shown in Figure 2.5(e), where isolated stable 360° walls are still present despite the absence of charge accumulation within the regions separated by the walls, (absence of contrast) indicating that in domains the magnetization is fully aligned along the direction of the field. This unstable situation (the center of the wall has its magnetization oriented oppositely to the field) is overcome at fields of 300 Oe, large enough to allow the wall to escape from the pinning centers (Figure 2.5(f)). The distribution of de-pinning fields is consistent with the gradual disappearance of the 360° walls observed in the MFM images.

These reversal features are sketched in Figure 2.6. The figure shows a model for the evolution of the magnetic moment distribution in uniformly magnetized regions, as a function of a negative applied field H. The clockwise rotation of the bottom left moment, m_{bl}, and counterclockwise rotation of the bottom right moment, m_{br}, give rise to a region where the torque is compensated and therefore the magnetic moment of this center region, m_{bc}, remains along the positive saturating field direction (Figure 2.6(a)). With the increase of the negative applied field, the rotation of m_{br} and m_{bl} proceeds and leads to the appearance of two 180° winding Néel type walls (Figure 2.6(b)). Since the lateral extension of m_{bc} (shaded region in the figures) does not exceed the size of the 180° walls, the magnetization rotates continuously from the m_{bc} to the m_{bl} direction. Therefore, the region separating m_{bc} from m_{bl} can be described as a single 360° winding Néel type wall which center is ascribed to m_{bc}. As the negative field increases, the

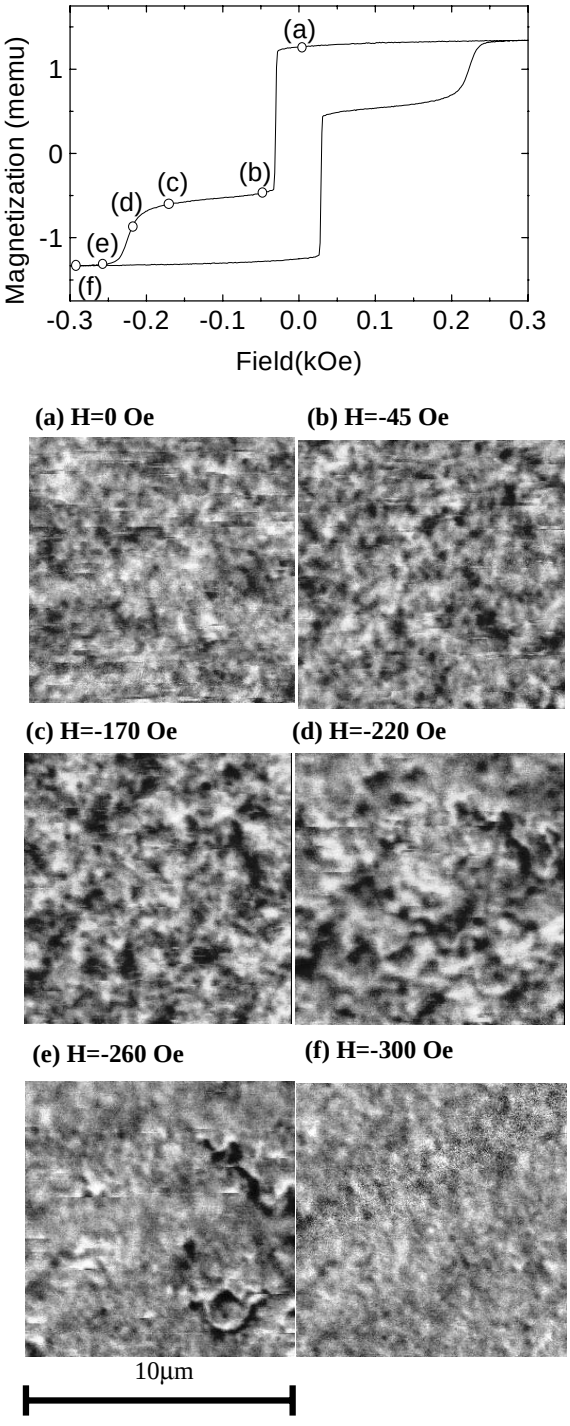

Figure 2.5: Successive set of MFM images for buffer/$Co_{50}Fe_{50}$ (3nm) magnetization reversal at some significant magnetic field values, indicated on the attached *M-H* curve: (a) 0 Oe, (b) -45Oe, (c) -170 Oe, (d) -220 Oe, (e) -260 Oe, (f) -300 Oe. During the reversal connected Néel walls appear. Black arrows point isolated stable 360° walls.

neighbor moments will be dragged in the field direction by exchange interactions. Consequently, correlated 360° Néel walls will form increasing the effective wall length as sketched in Figure 2.6(c,d). After the reversal is completed, for fields larger than the local pinning fields, walls or segments of walls disappear (Figure 2.6(f)).

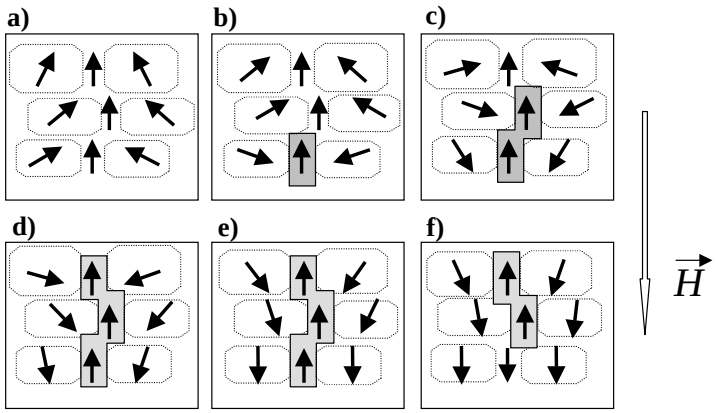

Figure 2.6: Sketch showing how connected Néel walls are formed during reversal in negative magnetic field. In an AAF system, each magnetic moment has its antiferromagnetic image mirrored in the other magnetic layer, due to the strong AF coupling.

2.4.2 Magnetic microscopic properties of the artificial antiferromagnetic system

As shown in the previous section, the competition between the local anisotropies and the exchange interactions govern the development of the domain structure in single magnetic films. In the AAF system, the AF coupling between the two magnetic layers adds an *additional* contribution to the nucleation and stability of the domain structure. Indeed, roughness induced variations in the Ru spacer thickness produce inhomogeneities in the AF coupling distribution that hinder a rotation in unison of the layer's magnetization and act as nucleation and wall pinning centers). Consequently, the density of walls increases in comparison with a single layer and their stability under a reversed applied field is enhanced by the AF coupling. These assumptions are supported by the field dependent microscopic magnetic analysis in two AAFs with different net moment, Co(1.8nm)/Ru(0.8nm)/Co(3nm) and Co(2nm)/Ru(0.8nm)/$Co_{50}Fe_{50}$(3nm). Figure 2.7 compares the MFM images of these two systems, measured at characteristic field values. Results allow to analyze the field dependent magnetic properties of an artificial antiferromagnetic system when decreasing its net magnetic moment.

Similarly to the single magnetic layers, when decreasing the field from saturation, uniformly magnetized regions appear, whose effective magnetic moments are aligned within an angle bisected by the direction of the positive saturation field. The MFM contrast of the remanent state (not shown) is then similar to the one observed in a single CoFe layer (Figure 2.5(a)). When reversing the field the moments inside the areas presenting the smallest coupling (direct lateral exchange coupling and indirect AF interlayer coupling) will rotate first. The sense of rotation of

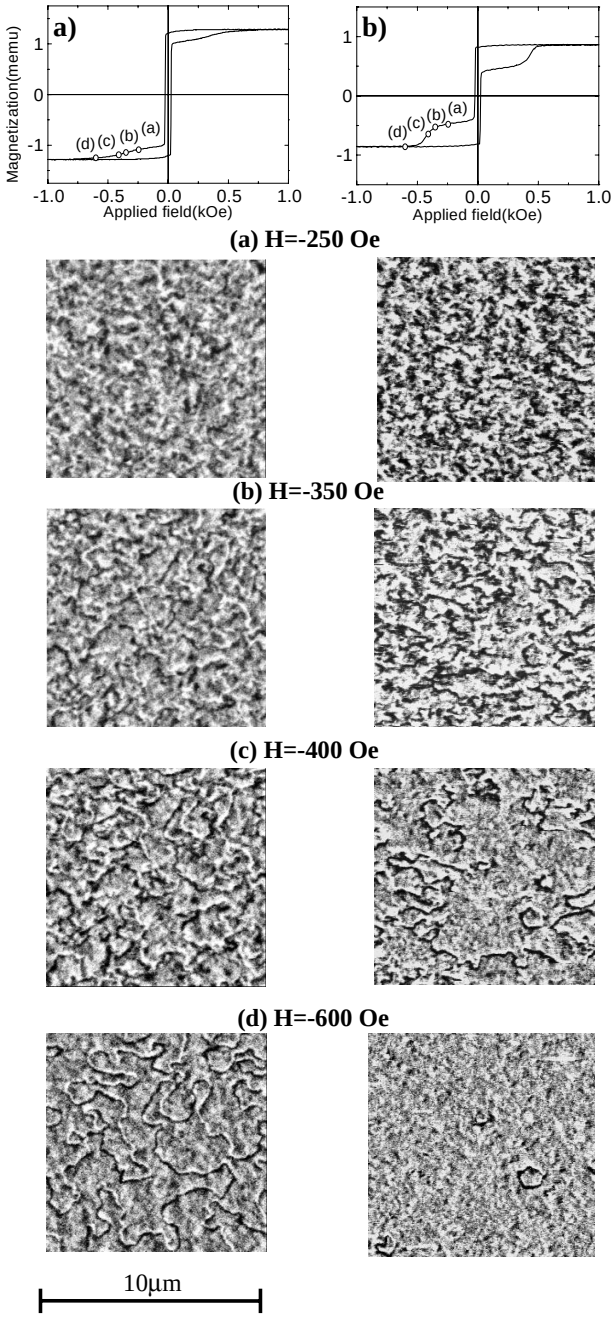

Figure 2.7: MFM images on Co/Ru/Co (a) and Co/Ru/CoFe (b), showing the appearance of long connected Néel walls during the reversal of the net magnetic moment and their stability in negative magnetic field. The main difference between Co/Ru/Co and Co/Ru/CoFe consists in a lower Q value in the CoFe case, which plays an important role in the stability of the walls. Successive set of MFM images for both Co and CoFe AAF at significant fields are shown: (a) -250 Oe, (b) -350 Oe, (c) -400 Oe, (d) -600 Oe together with the corresponding MH curves. Black arrows point isolated stable 360° walls.

the moments is determined by the local effective anisotropy. Increasing the negative field causes the magnetization inside the areas with stronger coupling to start to rotate. Large domains separated by 360° Néel type walls appear at the end of reversal ($M/M_{plateau}$=-0.90) when most of the regions have reversed their magnetization.

The reversal mechanism of the AAF net magnetic moment differs from that of a single layer by the presence of the interlayer coupling that enhances local frictions against rotation. The development of the 360° walls is more pronounced in the AAF coupled systems than in the single films (Figure 2.7(b) and Figure 2.5(c)). Fluctuations in the antiferromagnetic coupling strength and the AF duplication of the domain structure from one layer to the other, increase the density of 360° walls. Due to the strong interlayer coupling, the features are mirrored in both AAF magnetic layers with antiparallel Néel walls. This has a strong impact on the stability of the walls. While the thick layer develops walls with centers opposite to the field direction (similar to the single layers case), in the thin layer the mirrored walls have their centers along the field direction, that makes them energetically very stable (see Appendix B). At a critical field, the wall in the thick film disappears by collapse (the center of the wall, oriented opposite to the field, shrinks). The expansion of the center part of the wall in the thin layer is prevented by the strong AF coupling with the thick layer which is oriented along the field direction. The stable walls located in the thin layer, pin the walls in the thick layer due to the exchange coupling, up to fields at which the Zeeman energy overcomes the exchange.

This is consistent with the micromagnetic observations of annihilation of walls in the thick layer. Indeed, as shown in Figure 2.7(c,d), the 360° walls subsist up to large fields, located in the AF plateau, for which the magnetization in wall adjacent domains is completely reversed. The field needed to annihilate the 360° Néel walls in the thick layer is inversely proportional to the Q factor [34](which determines the relative difference between the magnetization of the two layers) because of the larger rigidity of the magnetizations when Q decreases. The MFM observations (Figure 2.7(c,d)) show that the stability of the 360° walls is increased when the net moment of the AAF gets smaller. The larger density of remaining domain walls when measured at the same field in the case of Co/Ru/Co compared to the Co/Ru/CoFe (smaller net magnetic moment in Co/Ru/Co than in the Co/Ru/CoFe) is a good indication that the total restoring torque induces a pressure on the domain wall that is proportional to the net moment [34].

To summarize, we have shown that the reversal of the artificial antiferromagnetic system in the plateau occurs through the formation of 360° walls. After the reversal occurs, these walls becomes unstable in the thick layer and the field at which they collapse is inversely proportional to the Q factor. In contrast, in the thin layer, the walls remain very stable in the operational field window, and start to collapse at fields close to the end of the plateau. The field evolution of the domain structure governs the transport properties of the tunnel device. To test our interpretations, we have performed MR experiments in several configurations including swapping both layers, results which are reported in the next section.

2.5 Magneto-transport properties of tunnel junctions using AAF: impact of the domain structure in the shape and the amplitude of TMR signal

The artificial antiferromagnetic system acts as a rigid block only for applied fields usually below 250 Oe, less than the operating field window (Figure 2.4(a), inset concerning a minor TMR loop). Outside this field window, the magnetization of the AAF is locally disturbed and therefore no clear extended plateau could be observed in the resistance versus applied field MR curve. The shape of the MR curves is therefore strongly dependent on the microscopic magnetic characteristics of the AAF. How the local structure perturbs the MR signal, is sketched in Figure 2.8. The two following parameters are at the origin of the proposed scenario. First, the tunneling current decreases exponentially with distance through the barrier. Therefore, the preferential conduction channels are the shortest paths for electrons to travel across the insulator. Because of that, the most important factor determining the magnitude of the tunnelling current is the relative local orientation of the ferromagnetic moments directly across the barrier. Secondly, the TMR signal depends only on the magnetic configuration of the magnetic layers located directly at the interface with the tunnel barrier. A direct consequence of these two features is that the domains and domain walls give rise to conduction channels with different resistances determined by the lateral fluctuations of the angle between the magnetic moments of the magnetic layer in contact with the tunnel barrier. When the detection bilayer has a single domain configuration after switching, the TMR signal is only sensitive to the magnetic structure of the topmost layer of the AAF. Much effort has been put on optimizing the magnetic properties of the DL which consist of $Co_{50}Fe_{50}$(1nm)/Fe(6nm) bilayers. The magnetization curve of the detection bilayer shows a square loop, with a coercive field smaller than 20 Oe and the magnetization reversal takes place in a field range less than 2 Oe [30]. Therefore, for applied fields above 30 Oe, the reversal of the detection bilayer is completed and it can be considered as being in single domain state. Consequently, only the magnetic state of the topmost layer of the AAF will influence the MR signal. As shown in Figure 2.4(a,b) correlated with Figure 2.7, the domain structure of the top layer of the AAF and especially the 360° Néel type walls, having the magnetization in their center opposite to the magnetization of the domains will strongly influence the amplitude and the shape of the TMR signal. While the detection bilayer forms a single domain state, oriented along the direction of the field, domains separated by 360° Néel type walls are created in the AAF during its reversal in negative applied field. The walls in the topmost AAF layer, in contact with the tunnel barrier, give rise to high resistance channels in the tunneling process because of their antiparallel alignment of magnetization with the detection bilayer. In contrast, the magnetic domains give rise to low resistance channels (Figure 2.8(c,d)) because of the parallel alignment of the local magnetization with the detection bilayer (see panel Figure 2.8(c)). The resistance of a certain spin conduction channel, determined by a region located in the top layer of the AAF where the magnetization makes an angle θ relative to the detection layer magnetization's orientation, can be estimated:

$$r = \frac{1}{2}(r_P + r_{AP}) + \frac{1}{2}(r_P - r_{AP})\cos(\theta) \tag{2.2}$$

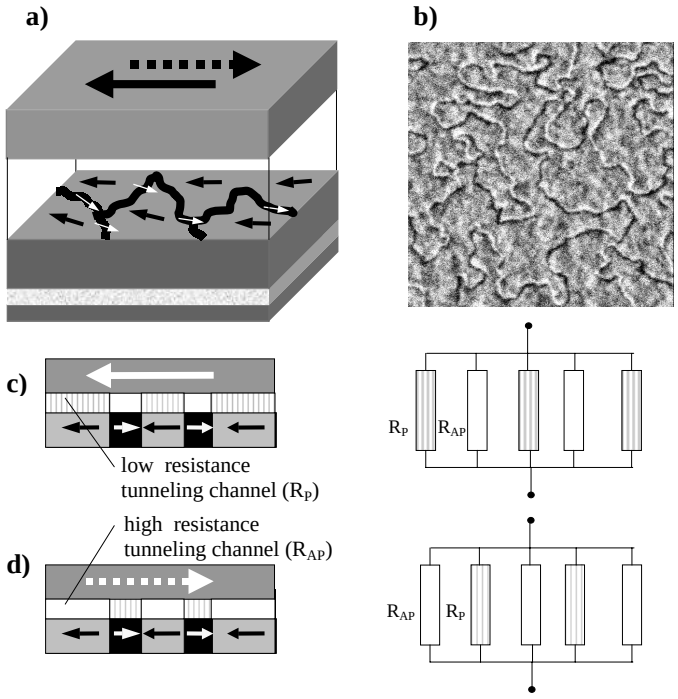

Figure 2.8: (a) The influence of the 360° walls on the resistance of the MTJ sensor. (b) MFM image associated with the model displayed (a) showing the 360° walls which appear in the top layer of the AAF during the reversal of its net magnetic moment. (c,d) The MTJ junction is modeled by a network of in cascade resistances determined by the different resistance conduction channels corresponding to walls and respectively domains as a function of the relative orientation of magnetization in detection bilayer and the top layer of the AAF system.

where r_P and r_{AP} are resistances of the same spin conduction channel in a parallel ($\theta = 0$) and antiparallel ($\theta = \pi$) configuration, respectively. Because of the existence of several spin channels, the resistance of the tunnel junction can be described by a set of parallel high and small resistances, corresponding to either a domain or a domain wall oriented respectively parallel or antiparallel to the detection bilayer. Most importantly, the situation will be totally opposite when reversing the detection bilayer from an initial magnetic state in which 360° walls are still present in the topmost layer of the AAF. In such conditions, the domains constitute conduction channels with high resistance having their magnetization oriented antiparallel with the magnetization of the detection bilayer, while the walls constitute low resistance channels (Figure 2.8(c,d)). Acting like *shortcuts*, the presence of walls will not allow the resistance of the junction to reach its maximum value.

By using the model of in-cascade-resistances network, calculations concerning the variation of the MTJ resistance induced by 360° walls give a value of about $\Delta R/R$= 3.5% at $H = -600$ Oe. The density of walls was estimated from the corresponding MFM image (Figure 2.7(d)) and the one wall conduction channel resistance was computed by taking into account the 360° wall profile $\cos(\theta(x))$. The calculated $\Delta R/R$ is in reasonable agreement with the value extracted from the corresponding TMR curve shown in Figure 2.4(a,b) ($\Delta R/R = 5\%$). The difference can

be attributed to local fluctuations in the orientation of magnetization inside the domains. These fluctuations are fully reflected in the MFM contrast as a *magnetic roughness* inside a domain, that decreases gradually when increasing the magnetic field towards domain magnetization saturation (Figure 2.7(c,d)).
These predictions have been tested in several experimental configurations as described below.

2.5.1 Illustration of the domain structure effect on the TMR signal

Figures 2.9 and 2.10 summarize three different magnetic histories to illustrate the low and high resistance channels invoked by the presence of domain structure. Each figure shows the magnetization and the corresponding TMR curve, completed with a micromagnetic sketch drawn to show a view of the magnetic configuration in the tunnel junctions at some characteristic fields. In each panel, the direction of the detection bilayer (DL) and the external field are represented as well as the distribution of magnetization within the thick and the thin magnetic layers of the AAF, illustrated by the top and bottom lines of arrows respectively. The gray areas locate the center of the 360° Néel type wall in each of the layers.

Major loop, thick magnetic layer of AAF in contact with the tunnel barrier

Let us first consider the case where the topmost layer of the artificial antiferromagnetic system is the thick magnetic layer. For this purpose, the magnetization (Figure 2.9(a)) and the corresponding TMR (Figure 2.9(b)) curves have been measured on a Co(1.8nm) / Ru(0.8nm) / Co(3.0nm) / Al_2O_3 / CoFe(1nm) / Fe(6nm) magnetic tunnel junction. The thick layer is then in contact with the tunnel barrier and therefore its magnetic behavior governs the shape and amplitude of the TMR signal. Prior to the measurement, the sample was saturated in a positive applied field and therefore all magnetic layers are expected to be in a single domain state (state (a) of Figure 2.9(a,b,d)). In the AF plateau, the layers of the AAF are firmly antiferromagnetically coupled. The decrease of the positive applied field leads to the appearance of uniformly magnetized regions whose effective magnetic moments are aligned within an angle bisected by the direction of the positive saturation field (Figure 2.9(d)b). These domains are separated by regions where the torque on the magnetic moments is zero defining the location of the emerging 360° walls. This magnetic state, antiferomagnetically duplicated in the thin magnetic layer by the exchange coupling, is the source of the small increase of resistance on the (a-b) branch of the *M-R* curve in Figure 2.9(b). After the switching of the DL, corresponding to a sharp increase of resistance (Figure 2.9b(c) and Figure 2.9d(c)), the resistance decreases slowly. Indeed, the clockwise and counterclockwise rotation of the uniformly magnetized domains proceeds continuously and is mirrored in the thin magnetic layer (Figure 2.9d(d)). The 360° walls formed in the thick magnetic layer during its reversal are unstable. The magnetic moment at the center of the walls (Figure 2.9d(e)) are oriented opposite to the field direction and disappear after completion of the topmost layer reversal (Figure 2.9d(f)). However, the 360° walls formed in the thin magnetic layer during its reversal are very stable. Indeed, they have their center moments (Figure 2.9d(e)) oriented along the field direction. Applied fields higher than the H_{max} =1 kOe accessible in our experimental setup are just not strong enough to complete the saturation of the thin layer (the walls in the thin layer disappear just in the flank towards saturation). Since the

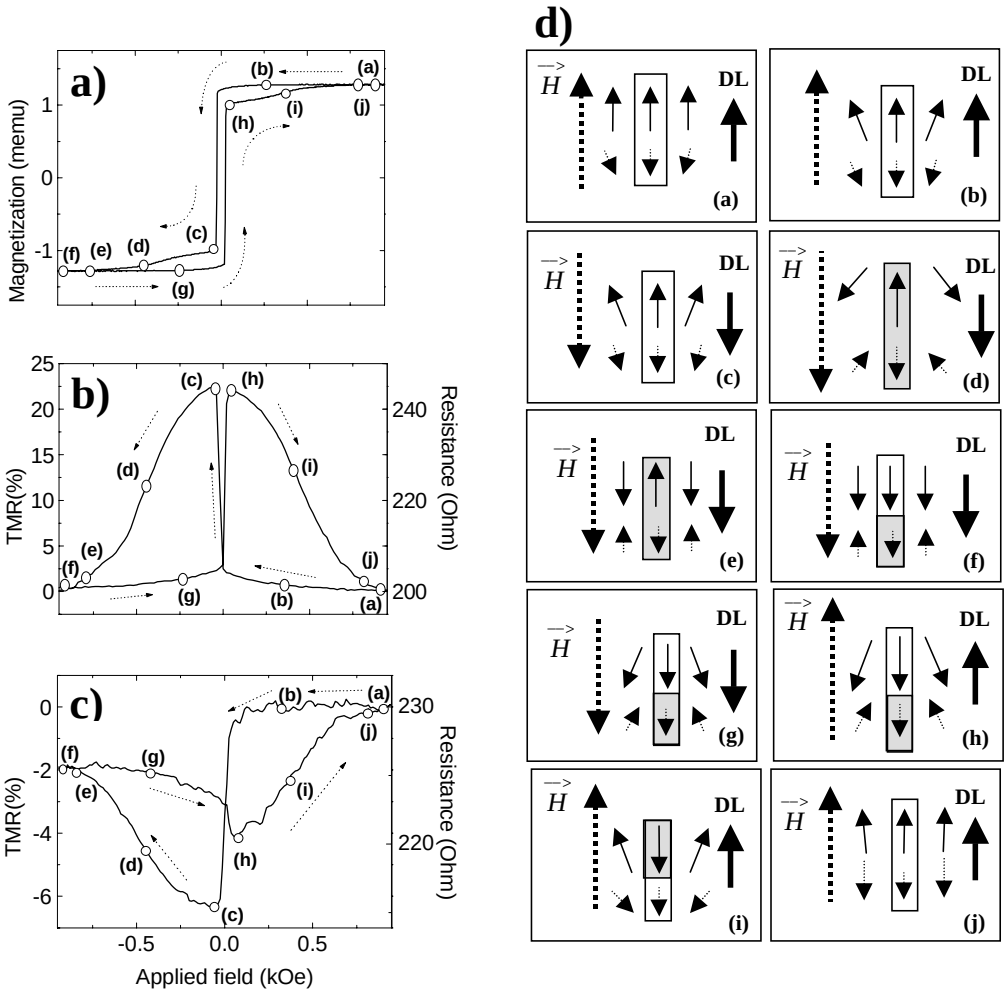

Figure 2.9: Influence of the 360° walls on the shape of the TMR curve for Co / Ru / Co / Al_2O_3 / CoFe MTJ. A sketch of the micromagnetic configurations for barrier adjacent magnetic layers (detection bilayer DL and the layers of the AAF stack) is presented on some significant fields in the TMR curves. (a) Magnetization curve for the Co(1.8nm) / Ru(0.8nm) / Co(3nm) / Al_2O_3 / CoFe(1nm)/Fe(6nm) MTJ stack. (a) The TMR curve for the Co(1.8nm) / Ru(0.8nm) / Co(3nm) / Al_2O_3 / CoFe(1nm) / Fe(6nm) stack. The topmost layer of the AAF stack is the thicker layer. The 360° walls formed in the thick layer, during reversal, are unstable and disappear by shrinking after completion of the reversal.(c) The TMR curves is displayed for the Co(3nm) / Ru(0.8nm) / Co(1.8nm) / Al_20_3 / CoFe(1nm) / Fe(6nm) MTJ. Here, the topmost layer of the AAF stack is the thinner layer. In the thin layer, the 360° walls are stable in an external field, having their center oriented along the field direction, they will disappear just after leaving the AF plateau, in the flank toward saturation. (d) Sketch of the micromagnetic configurations for barrier adjacent magnetic layers (detection layer DL and the layers of the AAF stack) at some significant fields in the MH and TMR curves.

thick magnetic layer is saturated in a negative applied field of $-H_{max} = -1$ kOe, its behavior on the ($-H_{max}$, H_{max}) branch of the MR curve is similar than the (H_{max}, $-H_{max}$) branch. So, the MR curve is symmetric.

The validity of this model is further supported by additional measurements performed on a magnetic tunnel junction for which the thin layer of the AAF is in contact with the tunnel barrier.

Major loop, AAF thin magnetic layer in contact with the tunnel barrier

The stability of the 360° walls in the thin magnetic layer at negative applied fields of $-H_{max} = -1$ kOe is exemplified by the transport properties of Co(3nm) / Ru(0.8nm) / Co(1.8nm) / Al_20_3 / CoFe(1nm) / Fe(6nm) MTJ (Figure 2.9(c)). While its *M-H* curve is identical to the reversed case (Figure 2.9(a)), the MR curve shows a large asymmetry in the signal (Figure 2.9(c)). Here, the topmost layer of the AAF stack is the thin layer and therefore its field dependent micromagnetic structure governs the shape and amplitude of the TMR signal.
Here again, prior to measurement, the sample was saturated in a positive applied field and therefore all magnetic layers are in a single domain state (State (a) of Figure 2.9(a,c,d)). In contrast to the previous case, the resistance of the MTJ is then maximum because of the antiparallel alignement between the magnetization of the DL and the thin magnetic layer. (Figure 2.9d(a)). Only small fluctuations in the orientation of the magnetization, duplicated in the thin magnetic layer by the exchange coupling, explain an almost constant resistance on the (a-b) branch of the MR curve (Figure 2.9(c)). After the reversal of the DL, a sharp decrease of resistance occurs because of the parallel alignment of both adjacent layers, (Figure 2.9c(c) and Figure 2.9d(c)). By further increasing the field, the resistance value increases slowly due to the clockwise-counterclockwise rotation of the uniformly magnetized domains in each magnetic layer of the AAF (Figure 2.9d(d)). The existence and stability of the 360° walls in the thin magnetic layer up to high negative fields is demonstrated on the TMR curves which never reach the high resistance state obtained in the positive saturated state (state (a)). As shown in Figure 2.9d(f) and Figure 2.8d, the walls act as low resistance channels, the direction of the center of the walls being oriented along the magnetization of the detection bilayer. By reducing the applied field, from $-H_{max} = -1$ kOe to zero, the rotation of the uniformly magnetized domains in each magnetic layer proceeds (Figure 2.9d(g)) and the resistance slowly decreases.
Here, the collection of parallel resistances is composed of high resistance channels (for which the magnetizations of the domains are nearly opposite to the magnetization of the DL) and by low resistance channels (for which the network of 360° domain walls have their center magnetization parallel to the magnetization of the DL) (Figure 2.8d). The resistance obtained at zero field depends clearly on the density of walls which remained at $-H_{max}$ (Figure 2.9d(g)). In Figure 2.9c(h) and d(h), the two networks of resistances are almost equivalent and therefore, the reversal of the DL gives rise to a small variation of the *TMR* signal. Then, the further increase of resistance is related to the rotation of the magnetization within the domains and the annihilation of the walls (Figure 2.9d(j)).

Minor loop, AAF thick magnetic layer in contact with the tunnel barrier

The process of magnetic reversal and the collapse of the unstable 360° Néel type walls in the thick magnetic layer is exemplified in Figure 2.10 using measurement of minor MR curves. We must keep in mind that in this sample the thick magnetic layer is again in contact with the

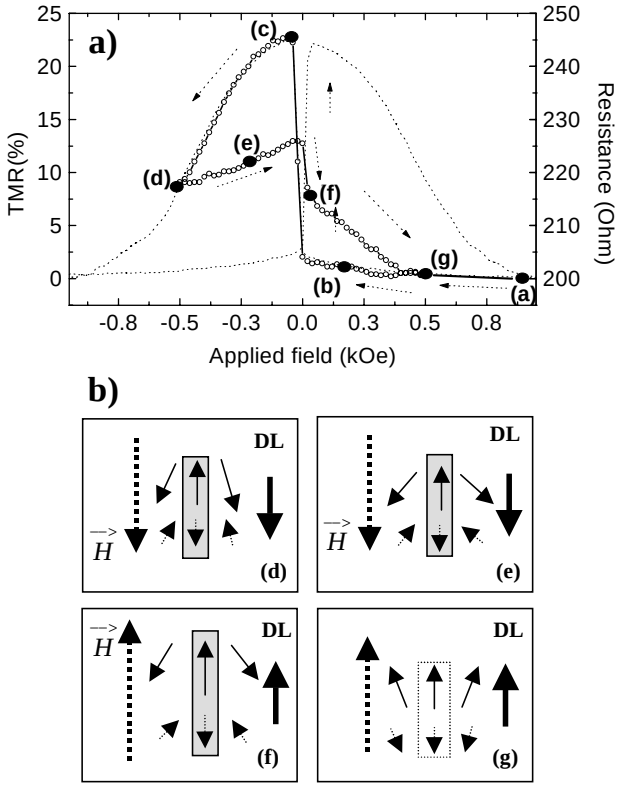

Figure 2.10: (a) Minor loop and corresponding TMR curves of the Co(1.8nm) / Ru(0.8nm) / Co(3nm) / Al_2O_3 / CoFe(1nm) / Fe(6nm) MTJ in a field range where the 360° walls are preserved in the thick layer (the reversal is not completed in negative field). The domain structure in the top layer of the AAF is clearly evidenced on the TMR signal, the walls act as high resistive channels due to their center opposite to the detection bilayer. (b) Micromagnetic sketch showing the magnetic configuration in the barrier adjacent magnetic layers (AAF and DL) at some significant values of the applied magnetic field.

tunnel barrier. The field decreasing branch of the MR curve in Figure 2.10(a) is the same as in Figure 2.9(b). Increasing the field in the negative direction gives a curve which is identical to Figure 2.9. However, the process is not reversible. Stopping before saturation, at point (d) and decreasing the negative field towards zero, then increasing the field in the positive direction, leads to a clear irreversible change in the TMR signal. This indicates clearly that the reversal of the thick layer in point (d) is not yet completed. A network of 360° walls and fluctuations of magnetization in domains (magnetic roughness) still exists (Figure 2.10b(d)) in the thick layer, too. In a decreasing negative field the resistance increases gradually due to a small relaxation of magnetization in the uniformed magnetized domains towards the direction of the positive saturating field (Figure 2.10d(e)). In this negative field branch, the 360° walls are stable. By reversing the field, the DL switches leading to a jump in the MR signal. At this characteristic field (panel 10b(f)), the center of the 360° walls is parallel to the detection bilayer while the domains are still nearly opposite to the direction of the DL. The amplitude and especially the

sign of the jump in the MR curve (State (f) of Figure 2.10) is of particular importance. Indeed, a steep drop of resistance in the MR curve indicates that the switch of the DL has activated a predominant low conductive channel, associated with the network of walls. Interestingly, the conduction channels associated with the domains are of much higher resistance but do not dominate the resistive process since the resistance of the sample decreases after the switch of the DL. This irreversible process confirms the validity of the model of resistances in cascade associated to magnetic domains and domain walls.

In this chapter, the existence of stable and unstable walls and their influence on the magnetoresistance of the tunnel sensor have been demonstrated. For overcoming the effects on the TMR signal of stable walls located in tunnel barrier adjacent magnetic layer, AAFs with a smaller Q (so a smaller gain in rigidity) have to be used in MTJ devices. However, a large coercivity for hard layers is needed because it provides a large magnetic rigidity. The alternative to obtain high rigidity is to build AAF with single magnetic layers having large coercivities. Consequently, a given rigidity of the AAF can be reached by amplification of a larger rigidity of a single layer by a smaller Q factor (larger net magnetic moment). Therefore, the stability of the walls will be decreased. Results on systems with different amplification factors Co/Ru/Co (Q=4) and Co/Ru/$Co_{50}Fe_{50}$ (Q=2) have shown that similar rigidities are reached by starting from a higher coercivity in the case of CoFe single layer. As shown in Figure 2.7, the stability of the walls is much more pronounced in the AAF with the higher Q and its consequence is relevant on the TMR curves. The field window in which the resistance remains constant is inversely proportional with the amplification factor, for constant coercivities (Figure 2.4(b)). This result is consistent with the increase of the density of reminiscent walls at large fields for larger Q factor as shown in Figure 2.7 (d), which compares the situations for Co/Ru/Co and Co/Ru/CoFe samples.

2.6 Conclusion

In a magnetic tunnel junction device, the spin dependent phenomena are strongly dependent on the magnetic state of the two magnetic metal/oxide interfaces. The resistance of the junction depends on the relative orientation of the two magnetic layers magnetizations. When the magnetic layers that are in contact with the barrier form a domain structure, the resistance of the junction is strongly influenced. The reversal of the AAF was investigated in detail, supported by local MFM imaging and TMR results. We have shown that a reduction in the TMR signal is correlated with the existence of 360° walls in the AAF top layer. This leads to tunneling channels with different resistances, determined by the relative local orientation of the magnetizations in the two magnetic layers separated by the tunnel barrier. The tunneling device, having the AAF subsystem in a multidomain configuration, has been modeled by a network of resistances in cascade. Each resistance corresponds to a section in the junction containing a magnetic domain or a magnetic domain wall with a given local orientation relative to the detection bilayer. One of the most significant results of our study was the demonstration of the tunnel device as a sensitive probe for measuring small magnetic fluctuations associated with micromagnetic defects, domains and walls. These fluctuations, which modulate the resistance of the tunnel junction are fully reflected in the shape and the amplitude of the TMR signal.

Detailed analysis of the field-dependent domain structure evolution in artificial antiferromagnetic systems analyzed by spin-polarized tunnel transport in magnetic tunnel junctions can be found in our papers [52, 53, 54]. A quantitative analysis of the domain structure using spin polarize tunneling as sensitive probe is summarized in the appendix of this report.
Other investigation axis which we focused on concern the enhancement of the thermal stability of magnetic tunnel junctions employing artificial antiferromagnetic systems [55]. We have fabricated magnetic tunnel junctions that use Co/Ru/Co and Co/Ru/$Co_{50}Fe_{50}$ artificial antiferromagnetic systems as hard magnetic electrodes and AlOx as tunnel barrier. The thermal behavior of the two AAF, incorporated in tunnel junctions, presents dramatic differences, the most remarkable being the much greater thermal stability of the Co/Ru/CoFe system, up to 400 °C.

2.7 Résumé de chapitre en français

Conséquences de la structure en domaines dans les électrodes magnétiques sur le transport tunnel dépendant du spin dans une jonction magnétique à effet tunnel

Ce chapitre présente l'étude des propriétés magnétiques et du transport polarisé en spin à des échelles macroscopiques et microscopiques dans les jonctions tunnel simples constituées par des couches poly-cristallines. L'objectif de mes travaux a convergé vers la mise en évidence de l'effet des inhomogénéités de l'aimantation sur le transport tunnel polarisé en spin et réciproquement sur l'utilisation du transport tunnel comme une sonde locale du micro-magnétisme. L'effet tunnel dépendant du spin dans une structure métal ferromagnétique / isolant / métal ferromagnétique, composant une jonction tunnel magnétique (JTM), est largement utilisé pour l'élaboration de nouveaux dispositifs micro-électroniques (mémoires non-volatiles, capteurs magnéto-résistifs, etc.). Dans une JTM, la transmission par effet tunnel des électrons polarisés par les électrodes magnétiques dépend de l'orientation relative des aimantations des électrodes et des caractéristiques de la barrière isolante. Le contrôle de l'orientation de l'aimantation d'une électrode par rapport à l'autre se fait dans une architecture appelée douce-dure, reposant sur l'association d'une couche magnétique dure et d'une couche magnétique douce comme électrodes magnétiques de la jonction tunnel.

La particularité de mon travail à été la réalisation et la caractérisation des propriétés magnétiques et de transport polarisé en spin dans des JTMs utilisant comme sous-système magnétique dur un antiferromagnétique artificiel (AAF). Un tel système est constitué de deux couches magnétiques (Co et/ou CoFe) d'épaisseurs différentes, ayant leurs aimantations arrangées antiparallèlement par un couplage de type RKKY à travers une couche non magnétique (Ru). Ce travail effectué en collaboration avec les laboratoires de recherches de SIEMENS, Erlangen, nous a amené à élaborer des jonctions tunnel magnétiques de taille micronique et à étudier la corrélation entre les propriétés magnétiques et leurs propriétés de transport polarisé en spin à des échelles macroscopiques et microscopiques. Il s'est avéré que, grâce à la sensibilité extrême du transport tunnel polarisé en spin par rapport aux fluctuations de l'aimantation aux interfaces métal ferromagnétique/isolant, les jonctions magnétorésistives sont des systèmes idéaux pour étudier sélectivement l'évolution de la structure en domaines des couches ferromagnétiques en contact avec la couche isolante avec le champ magnétique appliqué. En combinant l'analyse microscopique à l'aide de la Microscopie à Force Magnétique avec l'analyse macroscopique des caractéristiques électriques magnétoresistives des jonctions tunnel, j'ai pu corréler l'évolution de la structure en domaines dans les électrodes d'une jonction tunnel avec sa variation de résistance en fonction du champ magnétique appliqué. Plus précisement, j'ai démontré sans ambiguité que le renversement magnétique des couches se faisait avec la création et l'annihilation (ou la persistance) des parois de domaines à 360 degrés, dont la densité en fonction du champ magnétique a été estimée par des mesures électriques en utilisant un modèle analytique que j'ai developpé.

Chapter 3

Magnetic roughness induced magnetostatic interactions in magnetic tunnel junctions

3.1 Introduction

The increasing implication of magnetic tunnel junctions (MTJs) for spin electronic devices requires the understanding and the control of the magnetic properties of their ferromagnetic (FM) electrodes. Beyond aspects concerning the interfacial magnetism of ferromagnetic metal/insulator interfaces in MTJs, an important parameter is the coupling between the two electrodes of the MTJ. These interactions between the magnetically hard (reference) and the soft (detection) layer of the MTJ are of particular importance as they influence the reversal characteristics of the FM layers, and thus, the magnetoresistive response of the tunnel device.
This chapter is dedicated to a specific class of magnetic interaction which appear in samples involving polycrystalline magnetic films. We have shown that in these samples, beyond the orange peel coupling, an important class of interaction is related to the dispersion fields associated to magnetic inhomogeneities. These magnetization fluctuations were described in terms of magnetic roughness arising from the local anisotropy fluctuations. Therefore, using roughness data extracted from atomic/ magnetic force microscopy analysis, the amplitude and the variation with distance of the magnetostatic interactions were selectively quantified.

3.2 Long range 'Orange peel' magnetostatic interactions in multilayer systems

Several mechanisms can be implicated in the magnetic coupling between two FM films separated by a thin insulating layer. However, when assuming a continuous and pinhole-free insulating layer, the direct FM coupling associated to discontinuity of the insulator can be excluded. Moreover, when the voltage dependent coupling induced by the tunneling of spin polarized electrons [2] is negligible, the most important class of interactions are magnetostatic. In this last category, two main contributions have been identified. The first one is the antiferromagnetic

coupling related to the lateral closure of the stray fields between the magnetic layers of the MTJ. It becomes significant when reducing the lateral size of the MTJ FM electrodes and increasing their aspect ratio. The second contribution is related to stray fields induced by magnetic charge accumulations in the junction's ferromagnetic layers and are usually associated to the roughness of the interfaces, referred as the orange peel effect [56, 57]. However in polycrystalline magnetic materials, the local anisotropy fluctuations act as an additional source of charge accumulations created by magnetization fluctuations described here in terms of magnetic roughness. This, may be responsible for coupling effects similar to the orange peel coupling. As we show in this chapter, this effect has to be considered when discussing ferromagnetic coupling and furthermore, the range of these interactions can be significantly larger than the one of the orange peel.

3.2.1 Sample structure

The junctions, with lateral size superior to 10 μm to reduce the dipolar antiferromagnetic coupling intensity, are elaborated in a complex stack, as described in the previous chapter. Briefly, a Cr(1.6nm)/Fe(6nm)/Cu(30nm) buffer layer is grown on a Si(111) wafer. On the top of the buffer, a magnetically hard subsystem constituted by an antiferromagnetically coupled trilayer CoFe(1.8nm)/Ru(0.8nm)/CoFe(3nm) is stacked. This hard subsystem is separated by a 1-2nm thick Al oxide barrier from a CoFe(1nm)/Fe(6nm) magnetically soft subsystem or detection layer (DL) protected by a Cu(5nm)/Cr(3nm) bilayer.

3.2.2 Magnetic properties analysis at microscopic and macroscopic level

Analysis of cross-section transmission electron microscopy images as well as tunnel barrier mapping measurements [61] revealed a good quality and continuous insulating layer. Therefore the direct FM coupling is automatically excluded. However, magneto-transport measurements show a net ferromagnetic coupling as illustrated by Figure 3.1. Indeed, a sharp reversal corresponds to the DL switching from the antiparallel to parallel configuration with respect to the hard layer net moment. This reversal is completed at a field around 40 Oe. When the DL switches from the parallel to the antiparallel configuration, the reversal occurs in successive steps, sign of wall blocking phenomena, and is completed only at fields around 70 Oe leading to the appearance of a field bias offset. This set of measurements has been performed for bias voltage applied to the junction ranging from 5 to 100 mV. No variation of the coupling with dc bias was detected. Moreover, the intensity of the coupling strength was found to increase when decreasing the barrier thickness and when increasing the net magnetic moments of the junction's ferromagnetic subsystems. Therefore we conclude that the FM coupling present in our system is purely magnetostatic.

More insight in the magnetostatic coupling origin in our MTJs is given by the study of the magnetization reversal of the Fe layer in the buffer stack. This Fe layer is separated from the hard subsystem by a 30 nm thick Cu layer. Therefore, typical orange peel magnetostatic coupling with the hard subsystem should be insignificant and a direct RKKY coupling across this thick Cu layer is also excluded. However, a field offset of $\sim$5 Oe can be measured on the curve obtained with the hard subsystem in a remanent configuration (Figure 3.1(b) $-\bullet-$). This field offset disappears as soon as the hard subsystem is in a demagnetized state (Figure 3.1(b),

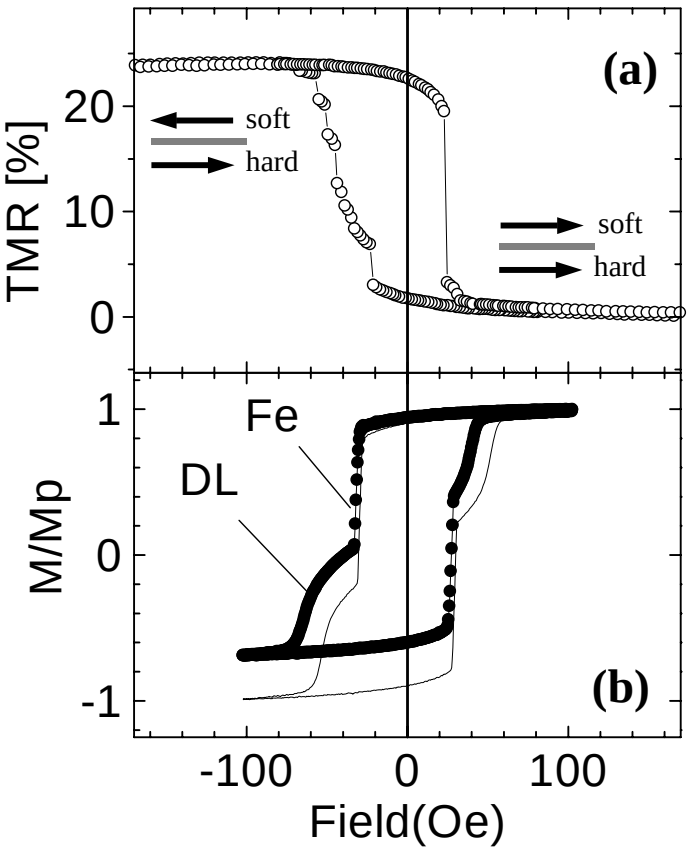

Figure 3.1: (a) Minor magnetoresistance loop measured on a CoFe/Ru/CoFe/AlOx/CoFe/Fe MTJ. Arrows illustrate magnetizations in the hard subsystem layers and in the DL; (b) Minor magnetization loop for a continuous film MTJ stack measured in two distinct situations: the hard layer is in a remanent (-•-) or a demagnetized (—) state.

continuous line). It appears then that one of the origins of the FM coupling in our MTJ stack is dependent on the microscopic magnetization state of the hard CoFe/Ru/CoFe subsystem. We attribute then the FM coupling in our MTJ stack to dispersion fields associated to magnetic inhomogeneities i.e. small angular fluctuations of magnetization in the hard magnetic system. These stray fields influence the local field experienced by a 'neighbor' magnetic layer, therefore having a direct impact on the layer magnetic reversal in an external field.

A model based on the concept of 'magnetic roughness' was developed in order to quantify these interactions and is illustrated in Figure 3.2. Figure 3.2(a) shows a magnetic force microscopy (MFM) measurement performed in the remanent state of the hard subsystem. The black (resp. white) contrasts correspond to repulsive (resp. attractive) interactions of the tip with the stray fields from the local charge accumulations derived from the small angular fluctuations of magnetization inside the poly-cristalline layer. The presence of dipoles is clearly confirmed in Figure 3.2b and in the remnant state, all the dipoles are oriented in the same direction leading to the appearance of a sequence of white/dark stripes (Figure 3.2a). We sketched this magnetization configuration in Figure 3.2c, the stray fields associated to all these dipoles add up and the re-

sultant field is oriented along the hard subsystem net moment. Since the length of the dipoles is less or equal to the length of the non horizontal arrows (equal to the exchange length, L_{ex}), the length of the dipoles and the distance between them are not equivalent along the applied field direction (horizontal lines). The stray fields associated to all these dipoles add up and the resultant field is not zero and oriented along the hard subsystem's net moment. It acts as a positive biasing field for the DL and Fe magnetization reversal, and is equivalent to a FM coupling observed in our junctions. We have validate our model by demagnetizing the hard subsystem. In this case, the magnetization of each dipole is randomly oriented resulting in a zero stray field and no FM coupling of the buffer Fe layer and the hard subsystem (Figure 3.1b, curve (—)).

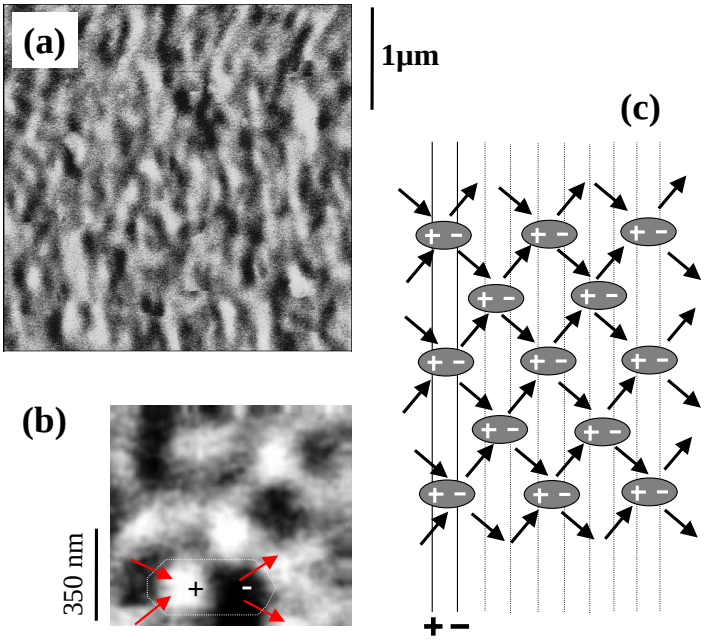

Figure 3.2: (a) MFM image of the remanent state of the MTJ hard subsystem. Alternating black and white stripes are directly associated to the magnetic dipoles, clearly illustrated in the inset of figure (b). (c) Sketch in two dimensions used for explaining the MFM contrast illustrated in (a). The periodic array of dipoles gives rise to parallel lines of successive positive and negative local charge accumulations, responsible of repulsive respectively attractive interactions with the MFM tip.

In conclusion, either topographic or remanent magnetic roughnesses generate equivalent periodic arrays of magnetic dipoles. The stray field associated to these dipoles can be selectively quantified using data extracted from AFM/MFM measurements. To estimate the coupling field H associated to each type of roughness, we used the equation derived previously for the orange peel coupling [56, 57]

$$H = \frac{\pi^2}{\sqrt{2}} \left(\frac{h^2}{\lambda t_F} \right) M_s \exp\left(-2\pi\sqrt{2} t_s/\lambda\right) \tag{3.1}$$

The significance of each term is illustrated in Figure 3.3: t_F and t_s represent the thickness of the soft respectively insulating spacer layer; λ_T, λ_M the period of the topographic respectively magnetic roughness; h the amplitude of roughness fluctuations. For the topographical roughness,

we used for h the peak to peak value measured in the cross section AFM measurement. In the case of the magnetic roughness, h was correlated with the thickness of the hard subsystem, where the magnetic fluctuations occur. M_s is the unit volume saturation magnetization for the hard subsystem magnetic material.

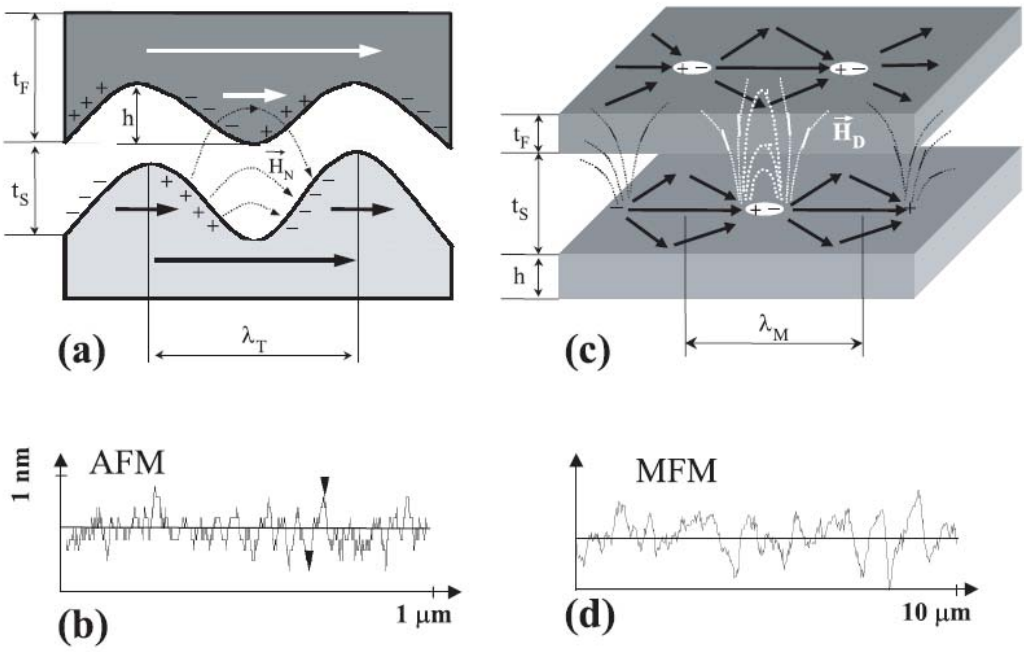

Figure 3.3: Model used to quantify the coupling field associated to a periodic arrangement of magnetic dipoles. The origin of these dipoles is either the topographic roughness (a) or the magnetic roughness (c). Characteristic lengths are depicted on these pictures and are extracted from cross sections taken on AFM (b) respectively MFM (d) pictures.

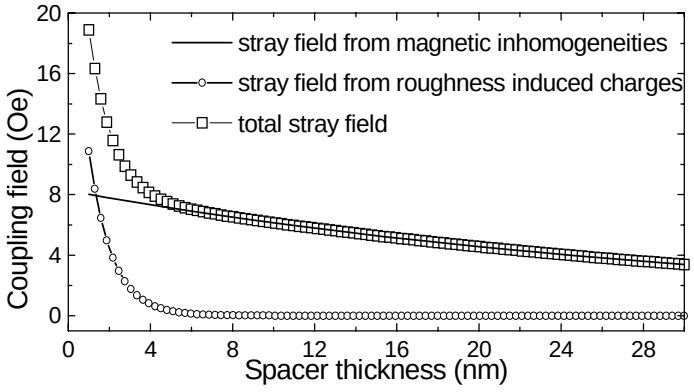

Figure 3.4: Calculated stray fields originating from topographic and magnetic roughnesses as a function of distance to the hard subsystem.

The cross section in the AFM (Figure 3.3b) and MFM (Figure 3.3d) images illustrate that

roughly $\lambda_M > 10\lambda_T$. Therefore, as calculated using the equation (1) and illustrated in Figure 3.4, the stray field originating from the roughness induced charges vanishes exponentially at short distance (4-6 nm) while the stray field associated to magnetic inhomogeneities has a much longer range. Indeed, this stray field remains significant at a distance of 30 nm ($\sim$ 4 Oe) and in good agreement with the offset measured for the Fe buffer layer ($\sim 5Oe$ from Figure 3.1b). Therefore, at long distance, the main magnetostatic interactions are related to the magnetic roughness associated stray fields while at short distance, the layers probe the contributions of both orange peel and magnetic roughness stray fields simultaneously. In the case of our MTJ, we estimate for the DL spaced of about 1nm from the hard subsystem, an average orange peel coupling of about 11 Oe while the magnetic roughness induced coupling was estimated to about 8 Oe. Therefore, the estimated resulting coupling field acting on the DL ($\sim$ 20 Oe) is in good agreement with the measured offset field in the magnetotransport curves (Figure 3.1).
In conclusion, the reduction of magnetostatic coupling interactions involved in MTJs covers two aspects. First, the coupling associated to topographical roughness is a short range coupling. It can be significantly reduced by decreasing the interfacial roughness or increasing the insulating barrier thickness. Up to now, it was the most common solution invoked to reduce the electrode ferromagnetic coupling. However in polycrystalline materials, often used as hard magnetic electrodes, the spatial distribution of local anisotropies creates magnetic roughness which gives also rise to a long range magnetostatic coupling. This coupling can be reduced using growth conditions of the magnetic layers which stabilize an uniaxial magnetic anisotropy. This innovative solution paves the way to further reduce the electrode coupling when interfacial roughness or insulating barrier thickness are pushed to their limits.

3.3 Compensation of magnetostatic interactions in magnetic tunnel junctions with artificial antiferromagnets

We illustrated above the magnetostatic interactions related to magnetic inhomogeneities. In this section we address the coupling between the magnetically hard and soft electrodes of tunnel junction devices employing artificial antiferromagnetic structures as hard subsystems. This coupling is found to depend drastically on the thickness and the stacking sequence of the ferromagnetic layers of the artificial antiferromagnet. In this section we examine how, by adjusting the thickness and the stacking sequence of the AAF layers one can influence the coupling originating from magnetostatic interactions between the AAF and the soft electrode [1].

3.3.1 Sample structure

The junction systems analyzed here are sputtered on Si(111) substrates. A buffer trilayer of Cr (1.6 nm)/Fe(6 nm)/Cu(30 nm) provides a good seed system for extremely smooth interfaces (0.5nm peak-to-peak after the barriers formation) and optimized magnetic properties of the junctions. We continue with the deposition of the $Co_{50}Fe_{50}$/Ru/$Co_{50}Fe_{50}$ AAF followed by

[1] This work has been performed in collaboration with T. Dimopoulos, currently working in Nano-System Technologies/ ARC-Seibersdorf Research GmbH (Vienna, Austria), during his PHD thesis work performed in IPCMS, Strasbourg (France) and Siemens Laboratory (Erlangen, Germany)

the formation of the Al oxide tunnel barrier by plasma oxidation of a metallic Al film. The thickness of the barrier after oxidation is 2nm. The soft subsystem consists of a CoFe(1 nm)/Fe(6 nm) bilayer, capped with Cu(5 nm)/ Cr(3 nm). The AAF structures employed in the tunnel devices are the following ones: AAF1: [CoFe (1 nm)/Ru(0.8 nm)/CoFe(2 nm) (Normal)]; AAF2: [CoFe (4 nm)/Ru(0.8 nm)/CoFe(2 nm) (Inverse)]; AAF3: [CoFe (2 nm)/Ru(0.8 nm)/CoFe(1 nm) (Inverse)]. The terms normal and inverse AAF relate to the stacking sequence of the artificial antiferromagnet. In the case of the normal (inverse) AAF, the thicker (thinner) layer is in contact with the barrier. All AAFs have the same Q value $Q = 3$. We remember that $Q = M_1t_1 + M_2t_)/(M_1t_1 - M_2t_2)$, where M_i and t_i $(i = 1, 2)1$ are, respectively, the saturation magnetization and thickness of the ferromagnetic of the AAF.

3.3.2 Magnetic analysis

The types of magnetostatic coupling existing in the present junctions are the orange peel ferromagnetic coupling due to the correlated FM metal interfaces adjacent to the barrier (Neel coupling) and the coupling due to magnetization fluctuations (MF) inside the magnetic layers constituting the junction. As a result, an additional offset field is acting on the soft electrodes magnetization, which is written as:

$$H_{tot} = H_N + H_{MF}$$

With the assumption of infinite thicknesses of the hard and soft electrodes and a sinusoidal, conformal interface roughness, the following equation applies for the offset field due to the orange peel coupling:

$$H = \frac{\pi^2}{\sqrt{2}} \left(\frac{h^2}{\lambda t_{SE}} \right) M_H \exp\left(-2\pi\sqrt{2}t_B/\lambda\right) \tag{3.2}$$

where where h and λ are, respectively, the amplitude and wavelength of the interfacial waviness, M_H is the saturation magnetization of the hard electrode, t_{SE} is the thickness of the soft electrode and t_B the thickness of the barrier. This equation assumes interaction only between the magnetic charges at the FM metal/barrier interfaces. In our case, the CoFe AAF layers employed, being very thin, we have to take the algebraic sum of the offse fields resulting from the magnetic charges distributed at the interfaces 25 of the AAF, as sketched in Figure 3.5 (for a normal AAF). The offset fields due to the second and third interfaces have signs opposite to those due to the first and fourth interfaces (Figure 3.5).

We calculated the net orange peel coupling for the three AAFs considered in this work, using as parameters: h =0.5nm (as extracted from AFM and TEM images), $\lambda = 10nm$ (extracted from TEM images), M_H =1910 emu/cm^3 (saturation magnetization for CoFe) and t_B= 2 nm. The corresponding offset fields are 6 Oe for AAF1, 6O e for AAF2 and 3 Oe for AAF3. However, note that the model used certainly overestimates the orange peel coupling as it assumes that the magnetization of the FM layers is rigid, uniform and parallel to the field axis, which is not the case for polycrystalline materials.

In Figure 3.6 we present rotating field and minor TMR curves corresponding, respectively, to the rotation and reversal of the soft layers magnetization. Prior to these measurements we have

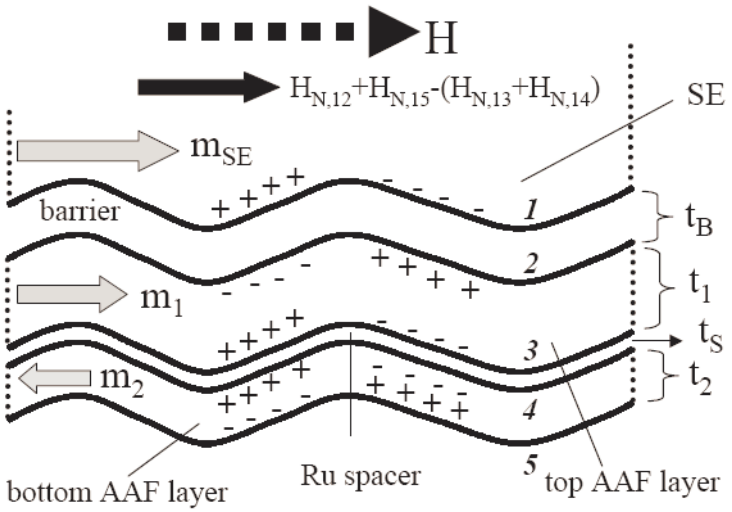

Figure 3.5: Schematic representation of the interfaces of the FM layers of the AAF (labeled 25) and of the soft electrode, having correlated roughness profiles. $H_{N,1_i}$ stands for the Neel offset field originating from the interaction of magnetic charges at the ith interface and at the interface between the soft electrode and the barrier (labelled 1).

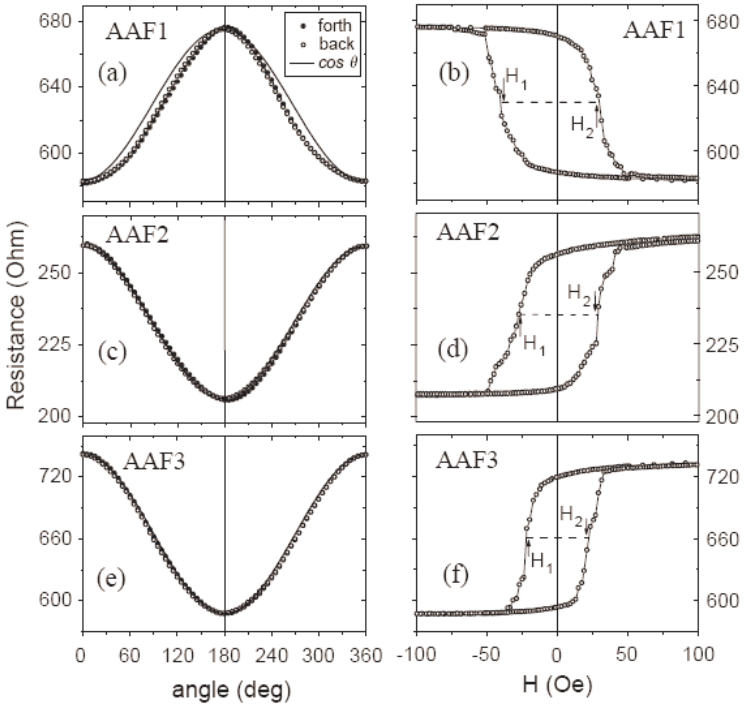

Figure 3.6: Rotating field (a,c,e) and minor TMR curves (b,d,f) for junctions employing the AAF1, AAF2, AAF3 structures.

saturated the junctions in 12 kOe and then decreased the field to 100 Oe. For the rotating field measurements the field (100 Oe) was successively rotated 360° clockwise and counterclockwise. As the applied field is only able to make the magnetization of the soft electrode rotate, the

junctions resistance should follow the cosine behavior:

$$R = (1/2)[R_{AP} + R_P] - (1/2)[R_{AP} - R_P]\, cos\theta$$

where R_P and R_{AP} are the junctions resistance for parallel and antiparallel alignments of the FM layers adjacent to the barrier and θ is the angle between the magnetization of the soft layer and the direction of the AAFs net moment. This equation is valid if there is no coupling between the soft and the hard layer. Figure 3.6(a) presents the rotating field curve in the case of the normal AAF (AAF1). The resistance variation deviates significantly from the cosine function. A flattening of the experimental $R(\theta)$ around its minima (parallel alignment) reveals that a net ferromagnetic coupling exists between the hard and the soft subsystems. From the corresponding TMR loop (Figure 3.6(b)), we extracted the offset field $H_{tot} = (H_1 - H_2)/2 \sim 5$ Oe. In contrast, we can see in Figure 3.6(c)(f) that there is almost no coupling in the case of the junctions employing the inverse AAF2 and AAF3, despite the fact that the orange peel coupling is calculated to be the same for AAF1 and AAF2.

We expect magnetostatic interactions between the hard and the soft layer of the junction, related to magnetic inhomogeneities (distribution of magnetic charges), as explain in the previous section. The soft electrode is subjected to the stray fields originating from these charges. Importantly, the stray fields arising from the AAF layer which is closer to the soft electrode always give rise to a FM coupling (adding to the orange peel coupling), while those arising from the other AAF layer always result in an AF coupling (counteracting the orange peel coupling), irrespective of the stacking sequence. Therefore, the total MF offset field acting on the soft electrode is given by:

$$H_{MF} \sim t_2/r_{23} - t_1/r_{13}$$

where where r_{23} and r_{13} represent the distances between the bottom (t_2) and top (t_1) layers of the AAF with respect to the the detection layer (t_3). This expression clearly shows that for junctions with normal AAF1 ($t_2 > t_1$, $r_{23} < r_{13}$) the net MF coupling is always ferromagnetic and thus adds systematically to the orange peel coupling. However, the last equation suggests that by placing that of the two AAF FM layers with the smaller thickness closer to the soft electrode ($t_2 < t_1$), i.e. by using an inverse AAF scheme, and by adjusting the thicknesses t_1 and t_2, one might be able to control both the intensity and the sign of the net MF coupling. In particular, choosing appropriate thicknesses we can generate an antiferromagnetic MF coupling that fully compensates the (ferromagnetic) orange peel coupling. This is what is more or less achieved in the junctions containing AAF2 and AAF3, which exhibit a zero overall coupling.

3.4 Résumé de chapitre en français

Interactions magnétiques liées aux fluctuations magnétiques dans les électrodes d'une JTM

Au-delà des aspects concernant l'évolution des caractéristiques micro-magnétiques des électrodes dans un champ magnétique extérieur, un paramètre important qui influence le transport tunnel polarisé en spin dans une JTM est l'interaction entre les deux électrodes magnétiques de la jonction séparées par la barrière d'oxyde. En fonction de l'intensité de ce couplage magnétique, les propriétés magnétiques des électrodes peuvent être fortement modifiées. En effet, le couplage entrane également des modifications des mécanismes impliqués dans le renversement de l'aimantation des électrodes ainsi que dans la réponse d'une JTM sous champ magnétique.
En utilisant la corrélation entre les caractéristiques magnétiques microscopiques déterminées à l'aide de la microscopie à force magnétique et les mesures de cycles mineurs d'aimantation et de magnétorésistance tunnel, nous avons effectué une analyse détaillée des interactions magnétiques qui existent entre les électrodes magnétiques des jonctions tunnel poly-cristallines. Cela nous a permis de mettre en évidence la présence d'un couplage net ferromagnétique. Suite à une analyse complète des mécanismes d'interaction magnétique entre deux systèmes ferromagnétiques séparés par une barrière tunnel, nous avons démontré l'origine magnétostatique des interactions observées. A l'origine de ce couplage se trouvent les inhomogénéités magnétiques (la fluctuation spatiale de l'aimantation dans le plan des couches, déterminée par la distribution de l'anisotropie dans un matériau poly-cristallin).
Ainsi, ce type de couplage est l'analogue du couplage de Néel dû aux inhomogénéités structurales (la rugosité des couches). La corrélation des rugosités d'interface de l'AAF et de la couche de détection avec la barrière d'oxyde détermine un couplage ferromagnétique de type peau d'orange. De même, les champs de fuite créés par les inhomogénéités magnétiques (parois, domaines) localisées dans une des couches magnétiques de l'empilement multicouche peuvent influencer le champ magnétique local vu dans une autre couche de l'empilement et par conséquent son renversement magnétique. Une idée centrale qui émerge de nos études concerne la possibilité de réduire les interactions magnétostatiques en utilisant des systèmes magnétiques présentant une anisotropie axiale bien définie. Pour profiter de tous les avantages offerts par un système AAF, une solution largement utilisée aujourd'hui dans les dispositifs électroniques repose sur l'utilisation d'un AAF ayant une anisotropie unidirectionnelle induite par le couplage d'échange avec un antiferromagnétique classique (PtMn, IrMn) et par le dépôt des couches magnétiques dans un champ magnétique externe ou bien l'utilisation de l'anisotropie magnétocristalline présente dans des échantillons élaborés par épitaxie à jet moléculaire. En utilisant dans un empilement JTM le système AAF, dont la configuration multicouche et le moment magnétique net peuvent être ajustés, les interactions magnétostatiques peuvent être fortement réduites.

Chapter 4

Quantum coherent transport in semiconductor free double barrier metal/insulator structures

4.1 Introduction

Magnetic tunnel junctions (MTJ) are promising candidates as storage elements in non-volatile magnetic random access memories (MRAM), where each magnetoresistive MTJ cell corresponds to one single bit of information [62]. The most typical MRAM technology adds an additional semiconductor switch in series with the memory cell to enhance the read/write contrast and to avoid 'cross-talk' in the memory array. Integrating CMOS transistors with sub-micron MJT, leads to systems whose packing density is limited not by the size of the active memory cell (MTJ) but by the semiconductor correlation length requested by the silicon technology. Indeed, the minimum cell size of in-plane transport SC devices is limited by quantum effects in the semiconductors occurring when the lateral size of the device reaches the order of magnitude of the associated scale lengths. Even if extremely small lateral size transistors (with nanometer range base length) are nowadays elaborated in laboratory, their optimal properties in terms of power consumption/dissipation are strongly altered at reduced size. To circumvent this size-related limit, one of the most interesting solution would be the use of a metal-insulator-metal switch integrated vertically within the tunnel memory such that the total cell size is now the size of the active memory.

In this chapter we present the experimental concept of a metal/oxide switch acting as a diode, integrated vertically in a magnetic tunnel junction[1]. We show that resonant effects and hot electron transport in this double barrier metal/insulator/metal (MIM) system are used for achieving a large asymmetry in the current-voltage characteristic at room temperature (diode-like effect) in a semiconductor free device. In such a double barrier system (see Figure 4.1(a)), the electrons are injected by tunneling from the bottom ferromagnetic electrode (FM_1) across the first tunnel

[1]This research topics constituted the topics of the PHD thesis of A. Iovan (2000-2003) developed in IPCMS Strasbourg (France) and Siemens Laboratory Erlangen (Germany). It integrates the European Project NANOMEM IST-1999-13471 concerning the realization of Semiconductor-free Nanoscale Non-Volatile Electronic and Memories Based On Magnetic Tunnel Junctions

barrier (I_1). When resonant effects take place in the middle metallic interlayer (M), sandwiched in between the two insulators, an energy selection of electrons occurs and modulates the electron current which is subsequently injected by tunneling across the second insulating barrier (I_2) and detected by th top ferromagnetic electrode (FM_2). Moreover, the energy selection gives rise to an asymmetry of the current depending on the orientation of the current vector or, in other words, of the sign of the applied voltage. Since the transport occurs in the CPP geometry (Current-Perpendicular-to Plane), this physical effect is not laterally sensitive unlike the semiconductor switch, making this concept suitable for vertical integration as a blocking element in new generations of nanoscale spin electronic devices.

4.2 Coherent tunneling in double barrier MTJ system

One of the first concepts reported in literature to obtain asymmetric current-voltage (I-V) characteristics using metal/oxide junctions exploited the asymmetric potential profile (trapezoidal barrier) of a single insulating barrier configuration. Such a profile arises from the difference in the work functions of the two metallic electrodes. Experimental results at room temperature [63] show that the current asymmetry in this case is small ($A = I^{\mathrm{f}}/I^{\mathrm{b}} << 1.3$, $I^{\mathrm{f(b)}}$ indicates forward(backward) current), making this concept unsuitable for potential applications as blocking diode.

A new concept is proposed here. It exploits in addition to the asymmetry of the potential profile the coherent electronic transport in double barrier MIM systems. Indeed, in the case of a double barrier system, by varying the two insulating layers one can get different barrier parameters (Figure 4.1(a)). Beyond an 'intrinsic' asymmetry of the I-V characteristics, related to the asymmetric potential profile of the two barrier configurations, the asymmetry can be 'enhanced' by two main features of electron tunneling in the MIM quantum well system: i) Coherent resonant tunneling and ii) Hot electron transport.

Few fundamental aspects may be detrimental to resonant tunneling at room temperature in experimental systems implicating MIM quantum wells: the effect of the fluctuations related to interfacial roughness combined with a larger Fermi wave vector in metals with respect to SC quantum wells and also a high density of scattering centers in metals. However, even when the resonance contributions are completely destroyed by fluctuations, a large asymmetry can be achieved by exploiting the hot electron transport, as qualitatively illustrated in Figure 4.1. Indeed, for forward (positive) applied voltage V_a, one can see that if the voltage drop V_1 in the first barrier gets superior to the second barrier height U_2, the electrons become hot for the second barrier. Therefore, they only undergo the first barrier in terms of tunneling (Figure 4.1(c)). The corresponding current is high. For a similar backward (negative) V_a, the electrons undergo both barriers (Figure 4.1(d)). Thus, a large asymmetry ratio A is theoretically expected. The asymmetry between V_1 and V_2 is related to the difference in barrier parameters ($U_1 \neq U_2, d_1 \neq d_2$) and to the scattering in the middle metallic layers [64]. Moreover, in case of resonant tunneling a much stronger current asymmetry ratio A is expected. This can be easily explained by the model illustrated in Figure 4.1 with one resonant energy level located in the quantum well. Indeed, when applying a forward voltage, the current is strongly enhanced when the energy of

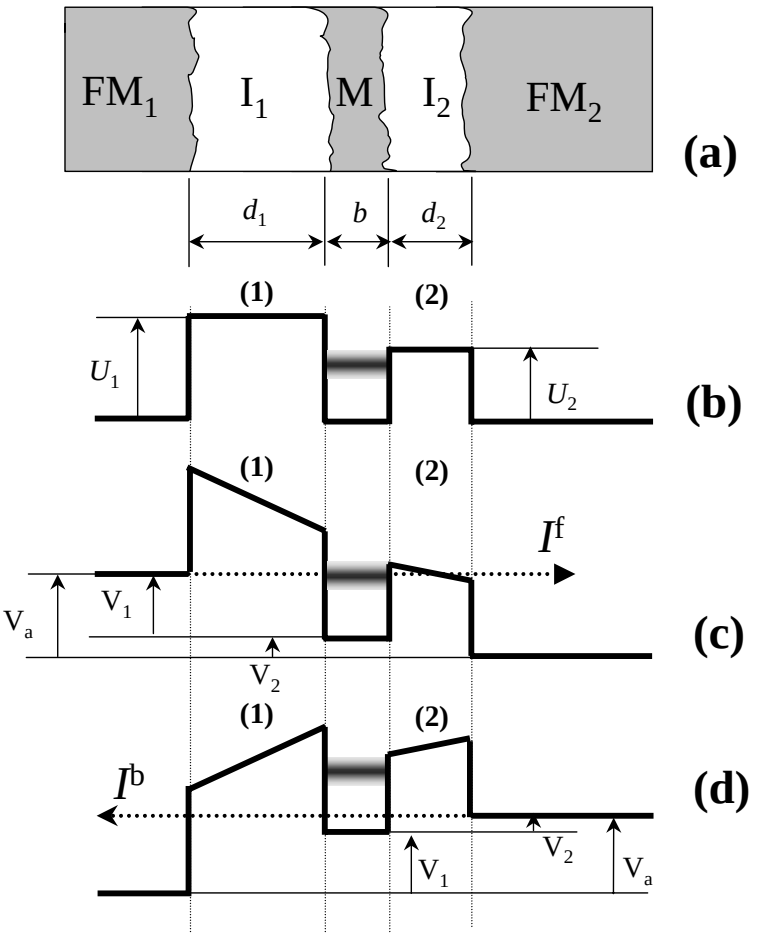

Figure 4.1: (a) Sketch of a double barrier tunnel structure and its corresponding potential profile without applied voltage (b), under positive and negative (c and d) applied voltage (V_a). A broad resonant level is depicted in the metallic interlayer. The parameters of the barriers are (1): height U_1, width d_1 (2): height U_2, width d_2 and b is the thickness of the metallic interlayer. The voltage drops in each barrier are denoted by V_1 and V_2.

the electron injected by tunneling across the first barrier reaches the resonance level. Therefore, a strong increase in the current is expected when the forward V_a is increased. This increase of the current follows exactly the distribution in energy of the resonance level in case of realistic systems, where the resonance level has a given width due to limited fluctuations and electron scattering in the interlayer. Thus, similarly to the case of SC quantum well structure [65], we expect a kink in the forward branch of the I-V curve, corresponding to the situation where the energy of the injected electron crosses the 'core' of the resonance level. The width of this kink is directly related to the width of the resonance level. On the other hand, for a backward voltage the energy of the injected electron moves away from the resonant level and no resonant tunneling occurs. Consequently, in this case the current is much lower than the one corresponding to resonant assisted current.

There are two important requirements for exploiting the concepts exposed above: (1) the two barriers have to be chosen properly in order to have the required asymmetry in the voltage drops V_1 and V_2 that would allow hot electrons to tunnel across the second barrier; (2) the level of

fluctuations has to be very small, in order to allow the resonant assisted tunneling [64].
These two criteria can be tested in a realistic experimental system if the thickness of the metallic interlayer sandwiched in between the two insulators becomes less than the characteristic lengths of the coherent transport. Increasing the thickness of the interlayer would increase the probability of the elastic (inelastic) scattering leading to loss of the coherence in the transport so that the current asymmetry vanishes [64].

4.3 Sample elaboration

Our samples have been elaborated by sputtering and patterned in micronic junctions (10x10 μm^2) by UV lithography [53, 60]. They are composed of two ferromagnetic electrodes of CoFe(3 nm) separated by AlOx(1.5 nm)/ Cu(1 nm)/AlOx(1 nm). As will be discussed later, the Cu metallic spacer layer is discontinuous and is formed by embedded spherical clusters with a very narrow distribution of size and inter grain spacing, as illustrated by the cross section TEM picture (Figure 4.2(a)). The cluster size was estimated to be about 3 nm with an average spacing of around 2 nm. Estimated barrier parameters are respectively $d_1 = 1.5$ nm, $U_1 = 2.3$ eV and $d_2 = 1$ nm, $U_2 = 0.8$ eV. For this structure, one can expect Coulomb blockade effects at low temperature [66].

4.4 Transport characteristics

Figure 4.3 shows strongly asymmetric I-V characteristics, measured on a 10×10 μm^2 junction. The bias-voltage variation of the current asymmetry ratio (Figure 4.3(a)) shows that it increases monotonously with V_a and reaches a maximum value (about 20 around 1 V) whose origin is a direct proof for the presence of the resonant state in the metallic quantum well. This maximum value corresponds to the maximum value for the forward current when the energy of the electrons injected across the barrier matches the resonance level (as illustrated in the model exposed in Figure 4.1(c)). The maximum corresponds to the kink measured around 1 V on the positive branch of the I-V curve. Extremely important for potential applications of the MIM double barrier diode is not only a high value for the asymmetry but also its variation with the external voltage. In our samples, a large asymmetry ratio is preserved for a wide voltage range of 1 V±0.5 V around the applied voltage corresponding to the maximum value of the current asymmetry (Figure 4.3(a)).
This system can be modeled as illustrated in Figure 4.2(b) where the conduction involves two tunneling channels: (1) a low resistive highly asymmetric coherent channel R^* associated to metallic clusters paths (Figure 4.2(c)); (2) a high resistive channel R associated to the thick insulator regions located between the clusters. In this model the resistance of the junction is governed by the low resistive one. Their very small lateral size (< 3 nm) insures very low fluctuations for the local transport in favor of resonant tunneling. Each cluster-associated channel can be modeled by a potential profile analogous to the one illustrated by Figure 4.1(a-d). The hot electron transport criteria is achieved for forward voltage when the voltage drop V_1 allows the injection of hot electrons across the second barrier with a small height.

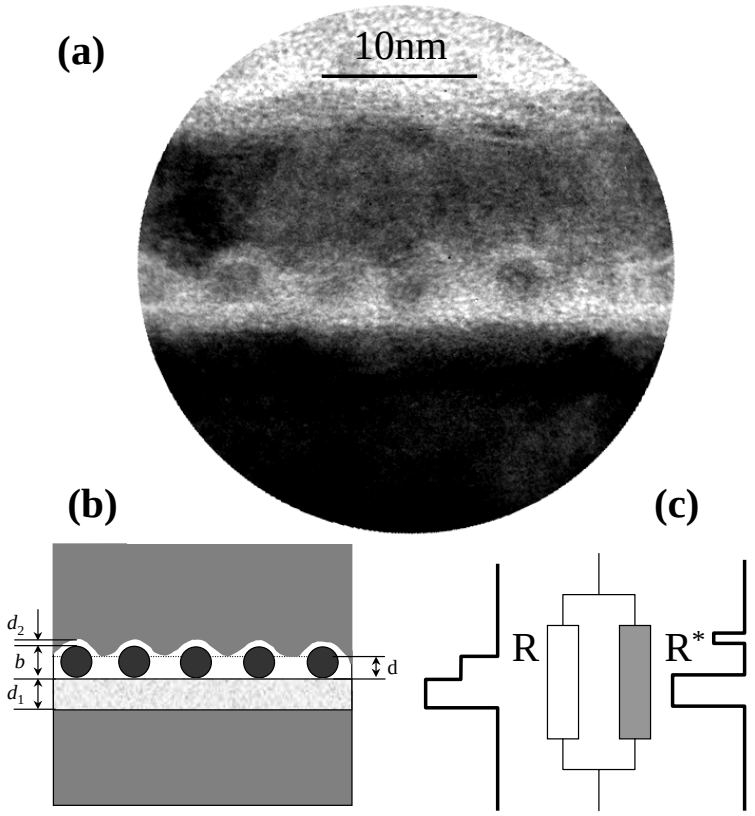

Figure 4.2: (a) Cross section transmission electron microscopy image; (b) the corresponding sketch-model for a double barrier system with discontinuous metallic interlayer. d_1, d_2 represents the thickness of the first and the second insulating barrier, respectively, b is the average cluster diameter, d indicates the thickness of the inter-grain insulator. (c) Two-conduction channels model versus the corresponding potential profile.

A crucial step during the sample elaboration was the optimization of the electron tunneling across the first barrier. The extreme fluctuation level has been reduced up to $RMS \sim 1$ Å for the top surface roughness and < 1 Å for the barrier thickness [61]. Such a low level of fluctuations is a key parameter for achieving resonant-assisted tunneling and insures a very homogeneous current distribution upon the whole junction area.

Remarkably, as illustrated on the inset of Figure 4.3(b), the experimental I-V characteristic matches perfectly to the theoretical expectation, calculated in the framework of a quantum mechanical model developed in ref. [64]. Theoretically, the shape of the I-V characteristics and its asymmetry is explained by the existence of quantum well states in the middle metallic layer which give rise to resonances in the current. Under applied voltage the positions of the resonant levels are shifted and for asymmetric structures this shift is different for the forward and backward bias voltage (Figure 4.1(c,d)). As a result, the I-V curve is highly asymmetric, demonstrating a diode-like behavior (inset of Figure 4.3(b)). Roughly, the shape of the I-V curve (in particular, the position and the shape of the kink) is related to the width of resonant levels which is defined by the amplitude of electron scattering in the middle metallic layer broadening the resonant peaks.

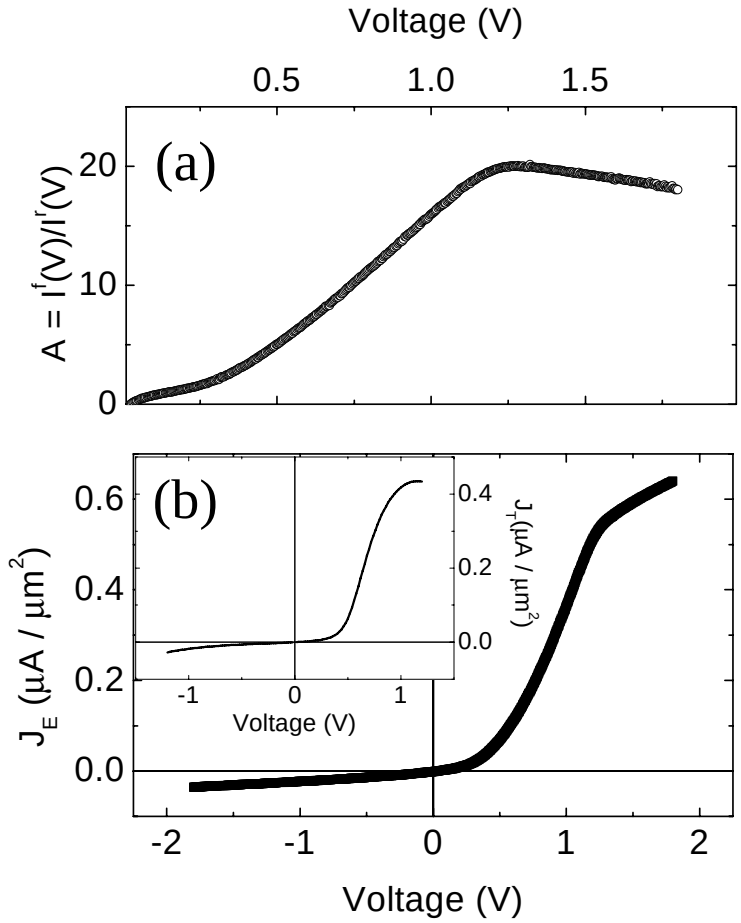

Figure 4.3: (a) Variation of the asymmetry ratio with the external voltage. (b) Experimental I(V) characteristics of double barrier system. Inset : theoretical curve, expected for coherent resonant tunneling.

4.5 Perspectives

For potential application of the MIM double barrier diodes few perspectives are considered.

1. Reducing the forward resistance of the diode by using alternative insulating materials and by varying their elaboration techniques.

2. Enhancing the asymmetry ratio and the position in voltage of the asymmetry maximum value (kink). This can be done by changing the interlayer material (i.e. Co, CoFe) or by varying the growth parameters (sputtering rate, pressure) and/or the thickness of the sputtered metallic layer in order to adjust the size of the clusters; Following the main concepts an results presented within this chapter, the asymmetry ratio has been enhanced to 200 by Iovan et al [67] in standard double barriers MTJs. More recently, another class of double tunnel barrier structures have been addressed by Iovan et al. They use a scanning tunneling microscope which provides a first vacuum barrier between the point and the sample. The samples are composed of metallic nanoparticles deposited onto an oxidized bottom electrode. Current rectification ratios of 100 up to 1000 for tunneling through such quantum objects have been then demonstrated at room temperature [68].

3. Using a ferromagnetic interlayer represents an interesting challenge, since crossing this layer the electrons remain polarized. Therefore, one can envisage a magnetically controlled diode [64] which represents itself a storage and blocking element suitable for data storage potential applications.

These aspects will be experimentally addressed in the very next future in systems employing epitaxial Fe/MgO/Fe magnetic tunnel junctions. The epitaxial growth will insure a better control of the thickness (reduce fluctuations). We plan to investigate different classes of systems grown by epitaxy. The first one is double barrier systems: Fe/MgO/FM/MgO/Fe with continuous FM intermediate layer and different thickness MgO barriers. In the second class of systems the intermediate metallic layer ferromagnetic (FM) or nonmagnetic (NM) will be discontinuous (either clusters or impurities). The third class will implicate a different second tunnel barrier (i.e. Al_2O_3) with either continuous or discontinuous intermediate layer. As illustrated in a next chapter, the realization of these hybrid systems requires the combination of two elaboration techniques: the Molecular Beam Epitaxy and the sputtering. As will be shown in a next chapter, intrinsically the Fe/MgO/Fe MTJs provide a giant tunnel magnetoresistive effect (up to almost 200%). Then, we expect to achieve simultaneously large TMR ratio and blocking effect within the same MTJ element. The high structural quality of these systems will provide a closer approach with respect to a model system. Then, one could investigate more accurately specific aspects of spin transport using transport spectroscopy techniques. In a double barrier system, the electrons polarized by the first ferromagnetic system FM_1 are injected by tunneling across the first thin tunnel barrier I_1. The spin polarized current is detected by FM_2 (or NM) and subsequently injected by tunneling across I_2 in FM_3. When the middle metallic layer is NM, the spin detection occurs in the third ferromagnetic layer FM_3. As a function of the bias voltage applied to the device and of the relative ratio between the I_1 and I_2 barrier heights, we can selectively investigate the spin injection/detection and the transport of normal, ballistic or hot electrons in the middle electrode and across the second tunnel barrier. Important spin polarized transport parameters such as spin diffusion length, relaxation length, spin precession/relaxation, etc, can be extracted from transport characteristics, investigated as a function of the thickness of the middle metallic layer FM_2 or NM. One of the most interesting configuration which insures an electric contact on the intermediate electrode, in a three terminal device will allow to control independently the voltage drop on the two barriers. This will provide an accurate energy control during the spectroscopic analysis.
Interesting aspects related to the coherent or sequential tunneling in the double barrier devices will be addressed using high frequency noise measurements in a temperature range from 0.4-300K). These studies will be developed within a research collaboration project with the team of Prof. F. Aliev from Madrid University (see the chapter dedicated to the research prospective projects).

4.6 Résumé de chapitre en français

Etude du transport tunnel cohérent/incohérent dans les systèmes composés de barrières tunnel multiples

En empilant deux à plusieurs jonctions tunnel les unes sur les autres on peut envisager la réalisation de dispositifs microélectroniques nouveaux et originaux basés sur le contrôle du transport électronique cohérent/ balistique dans une multicouche de type $FM_1/I_1/FM_2/I_2/FM_3$ avec (FM = matériau ferromagnétique, I = isolant). Les trois électrodes FM ont des champs coercitifs différents qui permet de stabiliser toutes les configurations relatives d'aimantation. L'utilisation de barriéres alternatives dotées de paramétres intrinséques différents (hauteur et/ou largeur de barriére, masse effective) au sein d'une même structure à barriéres multiples permet d'étudier les phénoménes de transport dépendant du spin avec un grand degré de liberté et de réaliser des diodes et de transistors magnétiques. Par rapport aux homologues classiques, les caractéristiques de transport d'un transistor ou d'une diode de spin peuvent être contrlées par un champ magnétique extérieur. Ceci est possible grâce aux effets magnétorésistifs des JTM qui peuvent atteindre quelques dizaines de pourcent. Cette étude expérimentale a suscité le développement d'une activité théorique dédiée à l'effet tunnel cohérent et/ou balistique dans des barriéres multiples. Suite à des modélisations théoriques, nous avons réalisé des systémes type jonctions tunnel à double barriére qui présentent une trés forte asymétrie de la caractéristique courant - tension (caractéristique de rectification). Ainsi, ces systémes présentent de bonnes propriétés type diode et cela dans une architecture sans semi-conducteur. Nous pouvons envisager des applications trés intéressantes tant du point de vue de la miniaturisation (forte potentialité d'intégration) que du fonctionnement à trés haute fréquence, régime où tout dispositif basé sur les semi-conducteurs subit de fortes limitations. Le fonctionnement de ces dispositifs repose sur le transport tunnel balistique/cohérent des électrons dans une double barriére tunnel. Lorsque les deux barriéres isolantes sont différentes, le profil de potentiel est asymétrique. Ceci engendre une asymétrie des propriétés de transport en fonction du signe de la tension de polarisation. Ainsi, pour une polarisation positive de la jonction à partir d'une tension critique les électrons ne 'voient' qu'une seule barriére tunnel, tandis qu'ils traversent la deuxiéme de maniére balistique. D'autre part, pour une polarisation négative ils devront traverser simultanément l'ensemble des deux barriéres. Comme le courant dépend de maniére exponentielle de l'épaisseur de l'isolant traversé, on attend alors une forte asymétrie entre le courant direct et inverse. Théoriquement, cette asymétrie pourra être encore fortement augmentée par l'effet des niveaux résonants localisés dans le puits de potentiel, lorsque le transport tunnel s'effectue de maniére cohérente. Expérimentalement, le régime de transport tunnel cohérent est atteint dans une configuration particuliére où la couche métallique intermédiaire est constituée d'une couche discontinue (ensemble de clusters de taille latérale nanométrique). Du point de vue théorique ce systéme est modélisé par un réseau d'éléments en paralléle, chaque élément étant déterminé par un des clusters métalliques granulaires. Dans une premiére génération de 'diodes', l'asymétrie du courant atteint un facteur supérieur à 20 pour une tension de polarisation de $1V$, alors que dans les toutes derniéres générations de diodes réalisées l'asymétrie dépasse le facteur 200. Basée sur ces résultats trés prometteurs, l'étape suivante de recherche vise la réalisation de diodes tun-

nel résonantes via l'épitaxie par jet moléculaire. Ainsi on envisage des systémes avec des puits quantiques constitués par des couches continues, dont la fluctuation d'épaisseur est fortement réduite par un contrle précis in-situ de la croissance bidimensionnelle. Ce projet se déroule au sein du Laboratoire de Physique des Matériaux de Nancy dans le cadre d'une thése de doctorat que je co-encadre actuellement.

Chapter 5

Atomic scale fluctuations in tunneling

This chapter addresses some fundamental aspects related to the statistics of the tunnel transport. The spatially resolved analysis of the tunneling current allows to investigate the atomic scale fluctuations of the insulating barrier in Metal/Oxide/Metal Magnetic Tunnel Junctions. The limitation of these fluctuations represents a key parameter to optimize the transport properties of a tunnel device.

The local transport properties of Al_2O_3 tunnel barriers have been investigated at a nanometric spatial scale with an unconventional near field microscope operating in a conductive mode[1]. Using the tunneling effect, which is extremely sensitive to fluctuations of the barrier parameters (less than 0.1 to 0.2 nm), a strong method is introduced to investigate and to improve the tunnel barrier quality. Thus, we studied [69] the interfacial phenomena related to the fabrication of thin Al oxide tunnel barriers and their thermal evolution (phenomena related to the plasma oxidation of thin metallic Al layers: how the barriers over oxidation influences the local transport characteristics of the oxide layers and the results are correlated with the magnetotransport properties of patterned microsized as-deposited and annealed junctions). Interestingly, the oxygen reservoir existing at the ferromagnetic metal, degenerating the tunnel device, can be used to improve the junctions magnetotransport properties by means of thermal annealing processing.

In a first order theoretical approach of the tunnel current statistical fluctuations, one can assume that these fluctuations are only related to thickness fluctuations of the barrier width (i.e. Gaussian distribution of thickness). These fluctuations are determined by the roughness of the top and bottom interfaces of the barrier with the ferromagnetic electrodes. In a realistic system one also has to consider fluctuations related to the barrier height. Moreover, in epitaxial MTJ devices, the statistics of tunneling becomes even more complex. A short paragraph related to these specific aspects concerning single crystal MTJ will be presented in a next chapter.

Here, in the following review paper, we summarize few interesting features of the tunnel transport statistics in polycrystalline MTJs.

[1]This technique has been developed in IPCMS Strasbourg by V. da Costa (1997) following the pioneering theoretical approach on rare events impact on tunneling developed by F. Bardou [112]. Nowadays, the standard Atomic Force Microscope are commonly equipped with this option. However, the research activities developed in IPCMS within this field represent important pioneering steps

VOLUME 85, NUMBER 4 PHYSICAL REVIEW LETTERS 24 JULY 2000

Tunneling Phenomena as a Probe to Investigate Atomic Scale Fluctuations in Metal/Oxide/Metal Magnetic Tunnel Junctions

V. Da Costa, C. Tiusan, T. Dimopoulos, and K. Ounadjela

Institut de Physique et Chimie des Matériaux de Strasbourg, CNRS (UMR 7504) and Université Louis Pasteur, 23 rue du Loess, 67037 Strasbourg Cedex, France

(Received 28 February 2000)

Local transport properties of Al_2O_3 tunnel barriers have been investigated at a nanometric spatial scale with an unconventional near field microscope. Using the tunneling effect, which is extremely sensitive to fluctuations of the barrier parameters (less than 1 to 2 Å), a unique method is introduced to investigate the tunnel barrier quality. This technique provides atomic scale information on the barrier characteristics which cannot be obtained by conventional surface analysis techniques since they are all subject to averaging over surface and depth.

PACS numbers: 85.70.–w, 73.40.Gk, 73.40.Rw

Systems combining metal/oxide interfaces and oxide surfaces constitute a diverse and fascinating class of materials. Their properties play crucial roles in an extremely wide range of physics. The characteristics of high-T_c superconductors, the passivation of metal surfaces against corrosion, the failure of dielectric materials because of an applied voltage, the spin polarized transport in tunnel junctions—all of these phenomena are dependent upon the properties of metal-oxide surfaces and/or the interfaces between metal oxides and other materials. Metal-insulator-metal (MIM) tunnel junctions are nonlinear electronic devices consisting of two metallic electrodes separated by a thin insulating barrier. When the electrodes are composed of ferromagnetic metals, they form magnetic tunnel junctions (MTJ). In a MTJ, the electrical tunnel transport across the insulating barrier is spin dependent and is controlled by the relative orientation of the magnetization in the two magnetic layers adjacent to the tunnel barrier [1]. This property of MIM junctions allow the development of a new generation of sensors for microelectronic devices and magnetic heads for data storage applications, such as magnetic random access memory (MRAM). A successful operation of these junctions requires a chemically homogeneous (free of impurities) insulating barrier as well as little fluctuations of the barrier thickness. Therefore it is important to characterize, spatially resolved, the tunnel barrier and relate it to the macroscopic tunnel magnetoresistance.

While conventional transmission electron microscopy (TEM) and x-ray photoelectron spectroscopy (XPS) studies provide global information on the atomic organization, surface-interface structure, and chemical composition, these techniques give incomplete information on the tunnel barrier quality at the atomic scale because they average over depth and surface. However, the physical relevant parameter in MIM junctions is the tunnel current which is determined by the tunnel barrier quality. More specifically, the tunneling current decreases exponentially with increasing barrier width and/or barrier height. Consequently the preferential conduction channels will be given by those with the highest tunnel current. It is therefore important to investigate the tunneling current spatially resolved.

Here, we demonstrate a unique technique to probe the local tunnel current at the nanoscopic scale using an unconventional direct space near field microscope (barrier impedance scanning microscope, BISM). This technique gives direct information on the correlation between the metal-oxide interfaces at the atomic level. The system studied here is based on Al_2O_3 insulating layers, used as a tunnel barrier in our micronic size tunnel junctions. Two samples, which are found to be identical at the atomic level when examined using standard surface techniques, show large differences both in their transport properties at the nanoscopic spatial scale (tunnel current distribution) and at the microscopic scale (magnetoresistance in micronic sized tunnel junction devices). This result shows the power of the BISM technique to control and optimize the tunnel barrier quality, before making micronic tunnel junction devices by lithography.

The method consists in measuring *in situ* the local tunnel current across the oxide layer with a modified atomic force microscope (AFM) operating with a conducting tip (Fig. 1, top). This technique allows us to map simultaneously the surface roughness and the current intensity transmitted through the oxide layer. In this way we probe directly the physical parameter needed for characterizing the tunnel barrier: the tunnel current. Since quantum tunneling between metal electrodes through an insulating barrier is strongly dependent on the morphology of the metal/insulator interfaces, much effort has been dedicated to optimizing the flatness of these interfaces. The quality of the interfaces in our magnetic tunnel junctions has been ascertained by using a complex buffer layer. It consists in a Cr(1.6 nm)/Fe(6 nm)/Cu(30 nm) trilayer, sputtered on a Si(111) substrate in a high vacuum sputtering system [2]. A magnetically hard subsystem is grown on top of the buffer layer consisting in an artificial ferrimagnet (AFi) Co(1.8 nm)/Ru(0.8 nm)/Co(3 nm) with coercive field of

 0031-9007/00/85(4)/876(4)$15.00

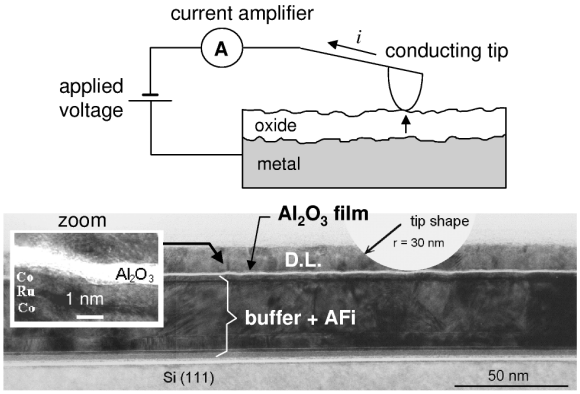

FIG. 1. Cross-section TEM image of a Si(111)/buffer/Co/Ru/Co/Al_2O_3/CoFe/Fe/capping layers. The size of the photo is 257 nm per 80 nm (lateral size comparable to the scan size of the images of Fig. 2). We have intentionally reported a wavy region (zoom at the left) which shows a clear correlation between the two metal/oxide interfaces. Illustration of the tip in contact with the tunnel barrier has been drawn to compare the tip/oxide/metal point contact vs the lateral microscopic size MTJ. On top of the figure is reported a schematic principle of our experimental setup. The conducting AFM tip probes directly the top of the Al oxide surface.

about 400 Oe [2–4]. By using such buffer layers, AFM observations have shown a low surface roughness detected on top of the Al oxide layer (maximum peak to peak and rms values of 7 and 1 Å, respectively). The Al oxide barrier was formed by rf Ar/O_2 plasma oxidation of a previously deposited Al layer on top of the AFi. The oxidation time was optimized with XPS experiments to obtain fully oxidized Al barriers for a given thickness of the as-deposited Al. The optimization of the oxidation time is an important step to avoid over and under oxidation of the barrier, both known to result in detrimental effects on the MTJ's magnetotransport properties [5].

To identify the importance of the correlation between adjacent interfaces, we have prepared two samples differing in the Ar/O_2 pressure during the oxidation procedure, keeping the relative percentage of Ar and O_2 constant: sample I with 5 mTorr and sample II with 50 mTorr Ar/O_2 pressure. For both samples TEM, XPS, and AFM investigations did not indicate any differences in the tunnel barrier quality. A MTJ multilayer stack, typical for both types of samples studied, is illustrated by the cross section TEM image shown in Fig. 1. The Al_2O_3 thin oxide film (white stripe in Fig. 1) has been coated with a magnetically soft bilayer. It consists in a $Co_{50}Fe_{50}$(1 nm)/Fe(6 nm) stack, and acts as a spin detection layer (DL) for electrons injected across the barrier from the hard AFi layer. This TEM image shows that the Al_2O_3 oxide film ($\simeq$11 Å thick) is uniform and continuous in a range of at least several hundreds of nm. No obvious microstructure has been distinguished in the Al_2O_3 layer which would indicate formation of dislocations and/or grain boundaries. Finally, the TEM pictures indicate that the top oxide surface follows the topography of the metal/oxide underlayer, as seen in the zoom of Fig. 1 at least at the resolution of the TEM microscope (TEM has low depth resolution). This means that even when the roughness of each interface is large (compared to the oxide thickness: peak to peak $\simeq$5 Å), the fluctuation in the barrier thickness is reduced to a few Å by the correlation of the roughness of the lower and top interfaces which may lead to small variation of the tunnel current. The TEM and XPS are techniques commonly used to characterize the structural and chemical quality of the tunnel barrier as a whole. Conventional AFM provides information only on the spatial distribution of the top surface roughness. However, as shown in the following, these techniques are unable to provide information on the spatial homogeneity of the tunnel barrier width and height.

This latter point has been addressed by performing local transport measurements at a nanoscopic scale. The local measurements were performed just after the growth of the Al oxide layer. The structure of the investigated sample is then as follows: Si(111)/buffer/AFi/Al_2O_3, the detection layer was not deposited, thus the oxide is on the top surface. The conducting AFM tip (Si_3N_4 coated with 30 nm thick TiN) *probes* directly the top of the Al oxide surface and is used as the second electrode of the tunnel junction. The topography was obtained by standard AFM measurements in *contact mode* and at constant force. A bias voltage (typically 1 V) was applied between the bottom metallic layer and the conducting tip, so as to generate a current flow from the sample to the probe (see sketch shown in Fig. 1). Other details on the technique can be found elsewhere [6–8].

Figures 2(c) and 2(d) show 200×200 nm^2 current maps recorded on samples I and II. The measured topography images [Fig. 2(a) and 2(b)] are similar for both films and reveal extremely smooth surfaces (rms $\simeq$ 1 Å). The image Fig. 2(c) represents the cartography of the tunnel current of a higher quality tunnel barrier corresponding to sample I: the Ar/O_2 pressure (5 m Torr) and the oxidation time are well optimized. Note the variation of the tunnel current which varies locally by no more than 2 orders of magnitude. The blue background identifies regions with tunnel current in the order of 100 pA, while the green spots are indicative of higher tunnel current zone (1–10 nA). The small amplitude of the measured current is due to the small contact area between the tip and the insulating barrier. The contact spot area is estimated to be about 100 Å^2. In order to illustrate this resolution the relative tip size (radius of 30 nm) with respect to the scanned area is drawn on top of the TEM image of the complete MTJ (Fig. 1).

Figure 2(d) shows the typical tunnel current map for sample II with a less optimized tunnel barrier. As

VOLUME 85, NUMBER 4 PHYSICAL REVIEW LETTERS 24 JULY 2000

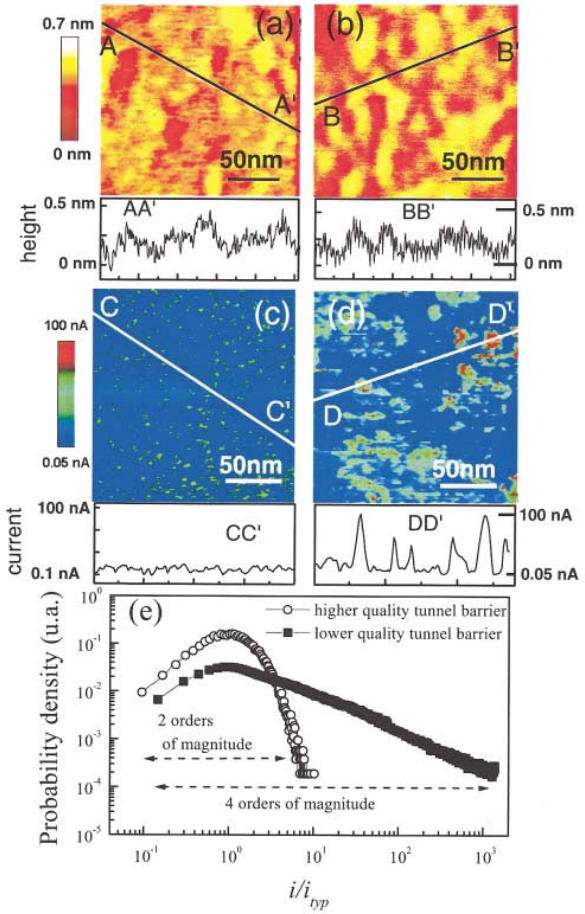

FIG. 2 (color). The 200 × 200 nm^2 size (a),(b) topographical and (c),(d) current images performed on an Al_2O_3. (a),(c) and (b),(d) images are simultaneously acquired. (a),(c) and (b),(d) are, respectively, measured on higher quality (sample I) and lower quality (sample II) insulating barriers. Also displayed are height and current profiles along lines shown in the image. (e) represents the current intensity distributions for the higher (− ∘ − sample I) and for the lower (−■− sample II) quality insulating barriers.

already mentioned, the oxidation procedure does not seem to affect the topography of the films when comparing the peak to peak and rms values of the oxide surface of both samples [see Figs. 2(a) and 2(b)]. However, the tunnel current cartography shows a drastic difference when compared to sample I with current inhomogeneity over 4 orders of magnitude. Note on the image, the red spots indicate current intensities up to 100 nA. Even in these hot spots, the current has still a tunneling character and not a shortcut current. This aspect is verified by measuring nonlinear I-V characteristics. From the current cartography, we have calculated the statistical distributions of local currents to quantify the quality of the insulating barrier. Previous works [9,10] have shown that a broad distribution of the current intensity with a long tail characterizes significant spatial variations of the oxide properties (thickness fluctuation of about 1 to 2 Å). On the other hand, a narrow current distribution indicates very small spatial variations (less than 0.1 Å) of the tunnel barrier parameters and is a signature of very high homogeneity in the physical parameters of the tunnel barrier. Figure 2(e) shows the distributions of local currents for both samples. For sample I the current distribution decreases quickly for the larger currents. It appears that the reduced current i/i_{typ} intensities (i_{typ} is the value for which the current distribution is maximum) vary from 0.1 to 10, so the tunnel current variations extend to *only* 2 orders of magnitude. This indicates that the buried metal-oxide interface is correlated with the top surface at the angstrom scale. For sample II the values of tunnel current variations extend over 4 decades ($i/i_{\mathrm{typ}} = 0.1$ to 1000). The current distribution curve is broad with a relatively slow decrease for larger current intensities.

Both fluctuations of the barrier height and width would coexist and have similar consequences on the statistical properties of quantum tunneling. For instance, considering only the fluctuation of the barrier width enables one to extract quantitative values for thickness fluctuation. As discussed in Refs. [9,10], a log-normal model of current distribution could be applied to estimate the oxide thickness fluctuation σ. Thus, we obtain for samples I and II, $\sigma = 0.3$ Å and $\sigma = 1.6$ Å, respectively; see note in [11] for details. This result suggests that the high partial pressure applied during the oxidation of the Al affects the correlation between the top and bottom interfaces of the oxide layer without deteriorating the smoothness of the top oxide surface. Note that the loss in correlation is small enough to be undetectable using cross section TEM experiments.

Whether such small fluctuation in barrier physical parameters can be detected using complementary investigations has been addressed by (i) measuring the tunnel magnetoresistance of micronic junctions as well as (ii) purposely creating breakdowns on the surface of the films.

To allow a comparison between both oxidation conditions for samples I and II, tunnel magnetoresistances (TMR) have been measured on microscopic tunnel junctions. The TMR is the only pertinent parameter to characterize the quality of the spin polarized tunnel current in a MTJ. The amplitude of the TMR signal reflects the atomic organization of the interfaces due to the local electronic structure, the tunneling mechanism, and the fluctuations in barrier parameters. For this purpose, complete stacks have been patterned by UV lithography into large arrays of square shaped junctions (10 × 10 μm^2). Several junctions with high quality tunnel barrier prepared in the same conditions as sample I, measured at room temperature using a conventional four-point technique with a dc voltage source, present large tunnel magnetoresistance which varies from 26% to 30%. However, junctions with less well optimized tunnel barrier (equivalent to sample II) present much lower TMR values varying from 11% to a maximum of 16%. These results show that averaging at the

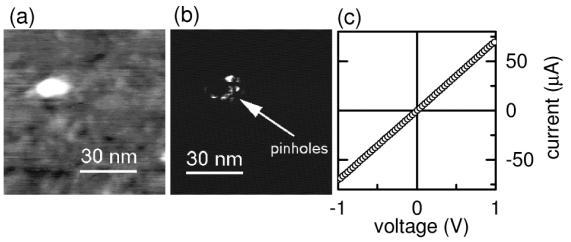

FIG. 3. Images of pinholes intentionally created by applying a large voltage. (a) Topography of the surface, (b) current image, and (c) the current-voltage characteristic measured with the tip localized on the pinhole.

microscopic scale the tunnel transport properties reflects implicitly the Al_2O_3 tunnel barrier quality measured with nanometer resolution.

Another type of investigation is to compare the stability of both types of surfaces to dielectric breakdowns. We have intentionally created the breakdowns on top of the oxide surface by applying high voltage between the tip and the sample using the same setup with the tip at rest. Interestingly, the pinhole defects at the origin of the breakdown are created for both oxide surfaces at similar bias voltage (in the range of 6 V, electric field $E = 5.5 \times 10^9$ V/m for a tunnel barrier of 11 Å) and it seems not to depend critically on the quality of the oxide layer. These defects are clearly evidenced in Fig. 3 which show localized current spots with very high current intensities, usually in the range of 50 μA for 1 V, 3 orders of magnitude higher than the highest detected tunnel current. Moreover, when the tip probes the pinhole, the current response is characterized by a linear I-V behavior indicating an electrical metal transport conduction; see Fig. 3(c). This experiment reveals two interesting features: (i) the breakdowns appear at a bias voltage around 6 V, 6 times higher than the electrical breakdowns observed in micronic junctions [12]. This difference can be explained because the micronic junction probes a large number of high current nanometric sites enhancing the probability to have those sites producing a lower voltage breakdown. Since the size of contact (tip-sample) in our experiment is in the range of 100 Å^2, this confirms that decreasing the size of the tunnel junction will enhance their stability to dielectric breakdowns vs bias voltage. (ii) More importantly, the breakdown appears in the same range of bias voltage for both oxide surfaces which indicates that despite the large contrast observed in the spatial distributions of tunnel currents between samples I and II, only very tiny spatial fluctuations of tunnel barrier thickness, more likely in the angstrom range, can account for these differences. This can be explained by the inversely proportional relationship between electric field for breakdown vs barrier width compared to the exponential dependence of the tunnel current with the barrier width, making the electrical field breakdowns less sensitive to spatial fluctuations of barrier physical parameters.

In summary, the quality of Al oxide layers, used as tunnel barriers in MTJ devices, has been investigated in terms of tunnel current homogeneity, by using a modified AFM/STM technique (STM: scanning tunneling microscopy). This technique provides a unique way to make an *electrical mapping* of the tunnel barriers before building micronic sized magnetic tunnel junctions. Thus, we are able to test locally the quality of the barrier, to examine the presence of possible *electrical defects* which would alter the magnetoresistive response of the MTJ device. More importantly, we have succeeded to detect fluctuations in the oxide barrier quality, from sample to sample, which were not accessible using any other surface techniques. These fluctuations are reflected in the TMR signal of the MTJ. Finally, the dielectric breakdown voltage does not seem to be strongly dependent on the quality of the oxide layer in contrast to the local tunnel current mapping.

The authors gratefully thank G. Würtz, G. Ehret, M. Hehn, F. Bardou, and U. Ebels. This work was supported by the EC Framework IV Materials Technology Programme (Contract No. BRPR-CT98-0657), the *Dynaspin* program, *TMR* network (Contract No. FMRX-CT97-0147), and *Nanomem* Programme (No. IST-1999-13741).

[1] J. S. Moodera, L. R. Kinder, T. M. Wong, and R. Meservey, Phys. Rev. Lett. **74**, 3273 (1995); T. Miyazaki and N. Tezuka, J. Magn. Magn. Mater. **139**, L231 (1995).
[2] C. Tiusan, M. Hehn, K. Ounadjela, Y. Henry, J. Hommet, C. Meny, H. A. M. van den Berg, L. Baer, and R. Kinder, J. Appl. Phys. **85**, 5276 (1999).
[3] H. A. M. van den Berg, W. Clemens, G. Gieres, G. Rupp, M. Vieth, J. Wecker, and S. Zoll, J. Magn. Magn. Mater. **165**, 524 (1997).
[4] C. Tiusan, T. Dimopoulos, K. Ounadjela, M. Hehn, H. A. M. van den Berg, V. da Costa, and Y. Henry, Phys. Rev. B **61**, 580 (2000).
[5] J. S. Moodera, E. F. Gallagher, K. Robinson, and J. Nowak, Appl. Phys. Lett. **70**, 3050 (1997).
[6] F. Houzé, R. Meyer, O. Schneegans, and L. Boyer, Appl. Phys. Lett. **69**, 1975 (1996).
[7] M. A. Lantz, S. J. O'Shea, and M. E. Welland, Rev. Sci. Instrum. **69**, 1757 (1998).
[8] V. Da Costa, F. Bardou, C. Beal, Y. Henry, J. P. Bucher, and K. Ounadjela, J. Appl. Phys. **83**, 6703 (1998).
[9] F. Bardou, Europhys. Lett. **39**, 239 (1997).
[10] V. Da Costa, Y. Henry, F. Bardou, M. Romeo, and K. Ounadjela, Eur. Phys. J. B **13**, 297 (2000).
[11] Experimental data were fitted with a log-nomal distribution which gives the parameters α' and β where α' is a scale factor and $\beta = \sigma/\lambda$ is a fluctuation parameter [9,10]. σ and λ indicate, respectively, the fluctuation of the barrier thickness and the attenuation length in the barrier. To calculate σ, we set $\lambda = 0.6$ Å which is a good value for Al_2O_3 tunnel barriers.
[12] W. Oepts, H. J. Verhagen, and W. J. M. de Jonge, Appl. Phys. Lett. **73**, 2363 (1998).

Chapter 6

Hybrid silicon spin diffusion transistor

Another aspect of my research activity concerns the electronic transport in hybrid structures which combine the tunnel junctions and the semiconductor materials (SC). The SC are very interesting for the spin electronics due to the high mobility of electrons, the very high spin diffusion length and their adjustable conduction mechanisms by doping, temperature etc.
The work within this topics has been carried out in direct collaboration with the group of Prof. J. Gregg (Clarendon Laboratory, Oxford). It has been developed within framework of the PHD thesis of C. Dennis. It relates to the realization of a new spin transistor with semiconductor base.
The operation of the first generation of transistors is based on the direct injection of spin polarized electrons through a Schottky barrier in a FM/SC/FM structure. The semiconductor is composed of doped silicon (n or p). These transistors were manufactured at the University of Southampton with regard to the semiconductor base and in IPCMS (Strasbourg) and the LPM (Nancy) with regard to the multi-layer structures which constitute the emitter and the collector[1].
The electrodes of the transistor, structured by optical lithography, present different aspect ratios in order to exploit the influence of the form anisotropy of their magnetic properties and thus to allow the control of the magnetoresistive response of the transistor. Promising results, show transistor type electronic characteristics, similar to the traditional bipolar transistors. These results are summarized in the following review paper.
A very interesting perspective of this topics concerns the spin injection in a semiconductor across an epitaxial Fe/MgO tunnel barrier. Indeed, this single crystal tunnel injector may provide particularly large spin polarization, as illustrated in a next chapter.

[1]Within this project, I was mainly implicated on the realization, the characterization and theoretical modeling of structural and magneto-transport properties of the multilayer stacks where the injection of spin has been addressed by tunneling across an insulating barrier.

Silicon spin diffusion transistor: materials, physics and device characteristics

C.L. Dennis, C.V. Tiusan, J.F. Gregg, G.J. Ensell and S.M. Thompson

Abstract: The realisation that everyday electronics has ignored the spin of the carrier in favour of its charge is the foundation of the field of spintronics. Starting with simple two-terminal devices based on giant magnetoresistance and tunnel magnetoresistance, the technology has advanced to consider three-terminal devices that aim to combine spin sensitivity with a high current gain and a large current output. These devices require both efficient spin injection and semiconductor fabrication. In the paper, a discussion is presented of the design, operation and characteristics of the only spin transistor that has yielded a current gain greater than one in combination with reasonable output currents.

1 Introduction

Everyday electronic devices manipulate carriers solely based on their charge, either positive or negative. Their operation ignores the fact that those carriers also have a spin, either spin up or spin down. Spintronics aims to remedy this deficiency by manipulating the spin as well as the charge of the carrier in nanoscale devices. Spintronics goes beyond the simple use of magnetic fields to alter the movement of charge, as in the Hall effect. Instead, spintronics determines and/or senses the spin orientation of the carriers by incorporating magnetic materials into conventional devices. Spins injected into a material are polarised either optically or by passing through a magnetic material, which polarises the carriers parallel (or antiparallel depending on the material) to the direction of magnetisation. The difference in behaviour of carriers of different spin types only becomes apparent when they travel through a magnetic material. For example, when spin-up electrons are injected into a magnetic material with the net magnetisation pointing in the same direction, these spins pass through relatively unscathed. However, spin-down electrons are heavily scattered. This leads to different conductivities (resistivities) for the different spin types. It is upon this principle that most of the suggested devices are based.

This field has expanded rapidly in recent years. It was only a few years from the discovery of giant magnetoresistance (GMR) [1] to the first commercial production of a GMR-based read head for a disk drive (by IBM in 1997). Recent research has focused on expanding the scope of spintronics from two-terminal to three-terminal devices. This has led to the development of a number of different three-terminal designs [2–9] (which will be briefly discussed in Section 2) that aim to exploit the spin-dependent scattering of charge carriers to yield a device with high current gain and high magnetic sensitivity. This paper will focus on the silicon-based spin diffusion transistor, the only spin transistor which yields a current gain greater than one. The discussion will begin with the fabrication, followed by the experimental results. It will conclude with a discussion of how the fabrication and materials affect the output characteristics.

2 General operating principles of spin transistors

2.1 Johnson transistor

The first spin transistor was the Johnson bipolar transistor [2], which added a third terminal connection to the nonmagnetic spacer layer in a CPP-GMR trilayer (see Fig. 1). Bipolar has double meaning: positive and negative charge carriers, up- and down-spin carriers, and output which is either a positive or negative current/voltage. This spin transistor device requires that the thickness of the layers be comparable to or smaller than the spin diffusion length of the material.

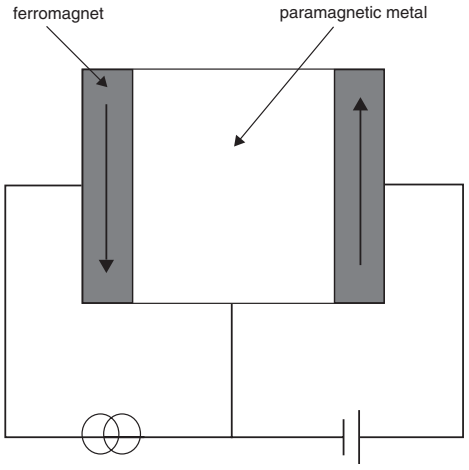

Fig. 1 *Schematic of the Johnson bipolar transistor*

IEE Proceedings online no. 20050008

doi:10.1049/ip-cds:20050008

Paper first received 10th January and in revised form 1st April 2005

C.L. Dennis and J.F. Gregg are with the Clarendon Laboratory, Parks Road, Oxford OX1 3PU, UK

C.V. Tiusan is with the Laboratoire de Physique des Materiaux, Faculté des Sciences, Université H. Poincaré, Nancy 1, Boulevard des Aiguillettes B.P. 239 54506 Vandoeuvre les Nancy, France

G.J. Ensell is with the Department of Electronics, University of Southampton, Southampton SO17 1BJ, UK

S.M. Thompson is with the Department of Physics, University of York, York, YO10 5DD, UK

E-mail: c.dennis1@physics.ox.ac.uk

As the electrical characteristics of this purely ohmic device are magnetically tunable, it can potentially be used as a field sensor or as nonvolatile magnetic random access memory. However, owing to its all-metal construction, its operation yields only small voltage output changes and no power or current gain (power gain may be possible in 5-terminal (as opposed to a 3-terminal) architecture). If such a device could generate a current gain, it could potentially be used to make logic devices [10].

2.2 Monsma transistor

The next step was to try and incorporate semiconductors with magnetism to further expand the field of spintronics by generating novel functionality. The Monsma transistor [3], produced at the University of Twente, was the first hybrid spintronic device (see Fig. 2). (The Mizushima MIFS transistor [4] is a second variant on this design, where one of the Schottky barriers is replaced by a tunnel barrier.) First fabricated in 1995, it sandwiched a CPP-GMR multilayer between two semiconductors (silicon). Schottky barriers form at the interfaces between the silicon and the metal structure and these absorb the bias voltages applied between pairs of terminals. The collector Schottky barrier is back-biased and the emitter Schottky is forward-biased. This injects (unpolarised) hot electrons from the semiconductor emitter into the metallic base high above its Fermi energy. If the hot electrons travel across the thickness of the base and retain enough energy to surmount the collector Schottky barrier, then they will exit through the collector; otherwise, they will exit via the base.

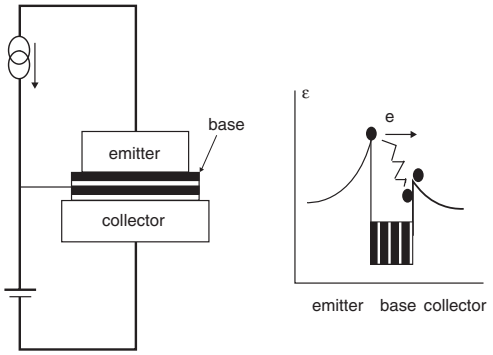

Fig. 2 *Schematic of the Monsma transistor (from [3])*

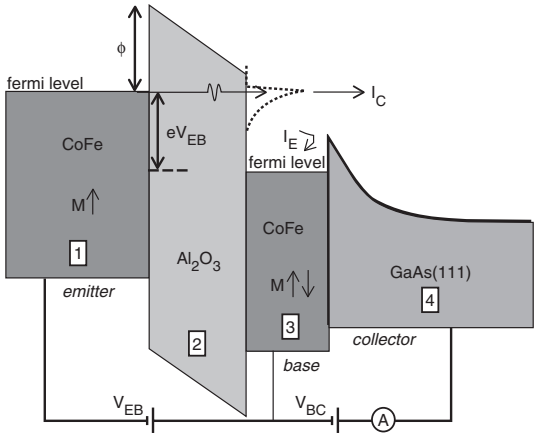

Fig. 3 *Schematic of the magnetic tunnel transistor (from [5])*

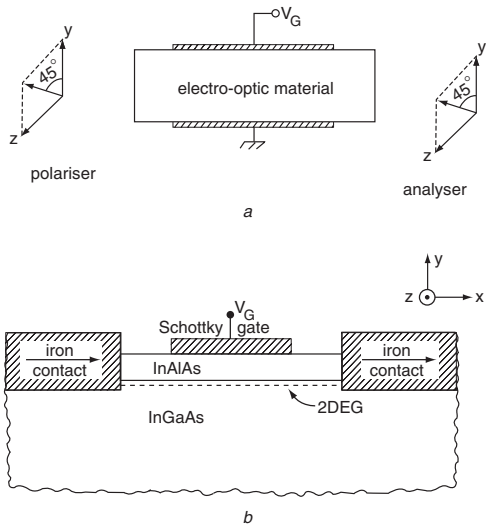

Fig. 4 *Schematic of the spin FET (from [7])*

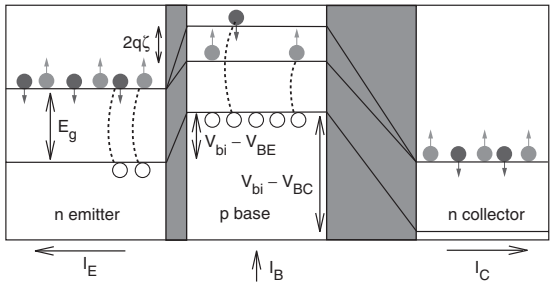

Fig. 5 *Schematic of the magnetic bipolar transistor (from [8])*

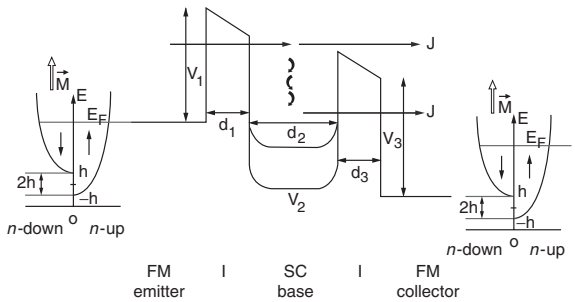

Fig. 6 *Band structure of the spin diffusion transistor*

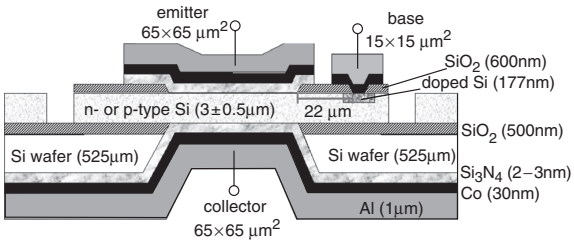

Fig. 7 *Structural schematic diagram of the fabricated spin diffusion transistor with silicon base*

The collector-emitter separation is 2.2 μm and the emitter-base separation is 22 μm. Note that the collector and emitter contacts are metal-insulator-semiconductor junctions and the base contact is ohmic (metal-semiconductor junction). All three contacts have a thin film of cobalt, but the base cobalt film is present simply for ease of fabrication

By varying the magnetic configuration of the base magnetic multilayer the operator can determine how much energy the hot electrons lose in their passage across the base. If the magnetic layers are antiferromagnetically aligned in the multilayer, then both spin types experience heavy scattering in one of the magnetic layer orientations, so the average energy of both spin types as a function of distance into the base follows an exponential decay curve. On the other hand, if the magnetic multilayer is in an applied field and its layers are all aligned, one spin type gets scattered heavily in every magnetic layer, whereas the other travels through the structure relatively unscathed. It may thus be seen that, for parallel magnetic alignment, spins with higher average energy impinge on the collector barrier and the collected current is correspondingly higher.

However, one limiting factor of this device is that it only used the semiconductor to control the distribution of applied potentials across the device; it is the metallic components that are spin selective. Despite this, the Monsma transistor represents a very important step in the evolution of spintronics. It has electrical characteristics that are magnetically tunable, plus a current gain and magnetic sensitivity that are sufficiently large so that, with help from some conventional electronics, it is a candidate for a practical working device. However, to release the full potential of hybrid spintronics, the devices need to exploit spin-dependent transport in the semiconductor itself.

2.3 Magnetic tunnel transistor (MTT)

The next generation of spin transistor devices modified the Monsma transistor by incorporating the knowledge gained from the theoretical analysis of spin injection. The Schottky barriers were replaced by tunnel barriers to form the magnetic tunnel transistor [5]. This device (shown in Fig. 3) is fabricated by depositing a magnetic tunnel junction on top of a GaAs substrate. The first ferromagnet acts as the emitter, the second ferromagnet as the base, and the semiconductor acts as the collector. The device works by injecting spin-polarised electrons across the tunnel barrier from the first ferromagnet into the second ferromagnet. The voltage applied between the emitter and collector is dropped across the tunnel barrier, thereby controlling the amount of current that reaches the base (the second ferromagnet). If the base is thin enough, then the current reaching the base will travel ballistically across the base and have enough energy to surmount the Schottky barrier between the second ferromagnetic metal and the semiconductor. (The ferromagnet/insulator/ferromagnet/insulator/metal (FIFIM) transistor by Ounadjela and Hehn [6] is a variant on this, where the Schottky barrier is replaced by another tunnel junction.) Any electrons that do not have enough energy will be swept out the base as a base current. The magnetic sensitivity again derives from the differential scattering of hot electrons of different spin types in the second magnetic layer. The sensitivity is dramatically 'amplified' by the exponential spin-energy decay; incidentally, this latter feature makes the magnetic trilayer structure on the left of the device a very effective spin polariser. However, it is again the metallic components that determine the magnetic sensitivity.

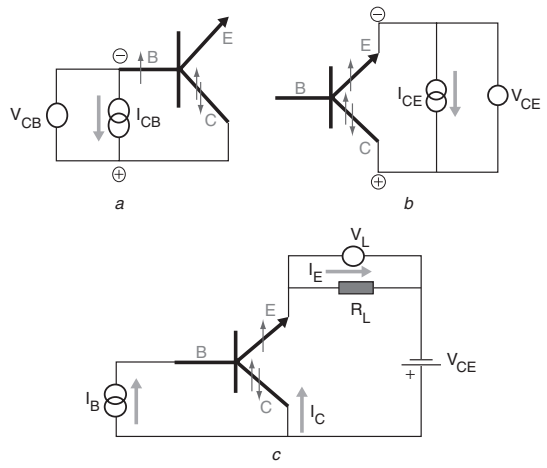

Fig. 8 *Measurement circuit for the collector to base circuit, the collector to emitter circuit, and common-collector configuration*
The collector, base and emitter are labelled C, B and E, respectively. The grey arrows indicate sign conventions for positive current. A black single arrow indicates that the magnetic layer on that contact is fixed, whereas the black double arrows indicate that the magnetisation of that contact is free. The + and − signs indicate the polarity of the applied voltage. Note that the sign conventions are the same regardless of whether the Si base is p-type or n-type
a Collector to base circuit
b Collector to emitter circuit
c Common-collector configuration

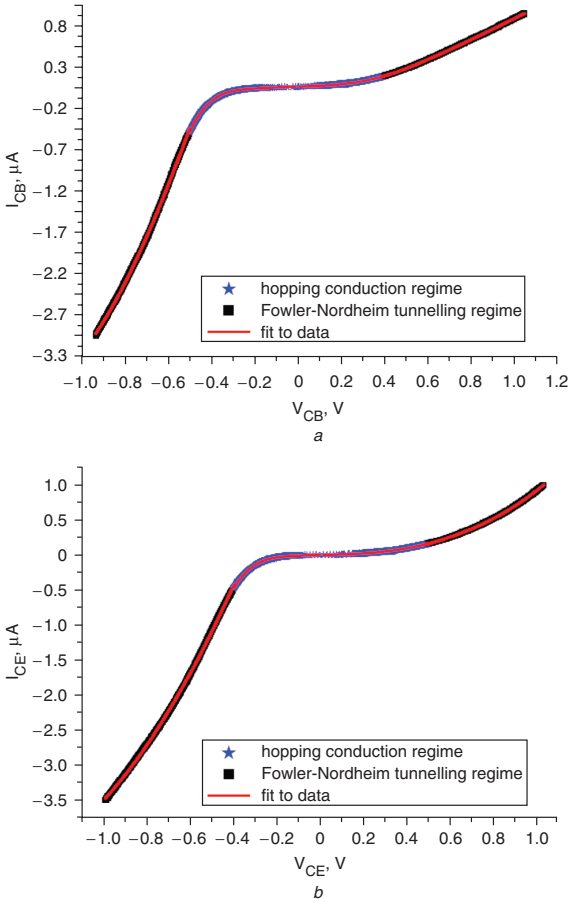

Fig. 9 *Two-terminal characteristics of the p-type transistor*
The dots indicate measured data points (where black dots indicate the region where Fowler–Nordheim tunnelling dominates and blue dots indicate the region where hopping conduction dominates) and the solid red lines are the fits, according to the regime the data is in
a V–I curve for p-type spin transistor (II-6): collector to base, four regimes and their fits
b V–I curve for p-type spin transistor (II-6): collector to emitter, four regimes and their fits

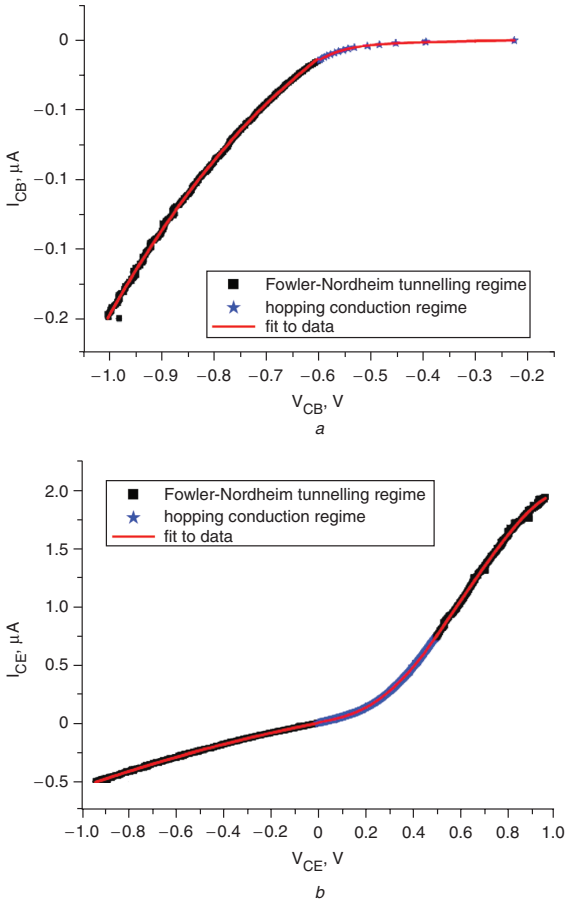

Fig. 10 *Two-terminal characteristics of the n-type transistor*
The black dots indicate measured data points (where black dots indicate the region where Fowler–Nordheim tunnelling dominates and blue dots indicate the region where hopping conduction dominates) and the solid red lines are the fits, according to the regime the data is in
a V–I curves for n-type spin transistor (II-8): collector to base, four regimes and their fits
b V–I curve for n-type spin transistor (II-8): collector to emitter, four regimes and their fits

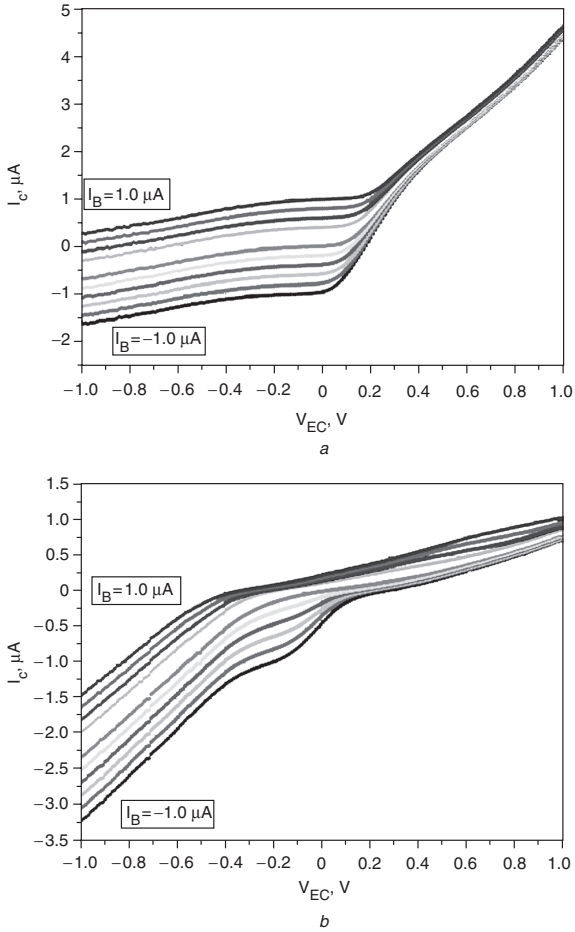

Fig. 11 *I_C–V_{EC} characteristics of spin diffusion transistors in common-collector configuration and zero applied field*
The load resistor $R_L = 9976\,\Omega$. The step size of I_B is 0.2 μA with the starting and ending currents as indicated in the boxes
a Common collector configuration of p-type Southampton spin transistor (II-6), H = 0 Oe, $R_L = 9.976\,k\Omega$
b Common collector configuration of n-type Southampton spin transistor (II-8), H = 0 Oe, $R_L = 9.976\,k\Omega$

2.4 Spin field-effect transistor (spin-FET)

A fourth transistor was developed in parallel with the previous devices: the experimental realisation of a spin-FET (see Fig. 4) based on the proposal by Datta and Das [7] in 1990. This transistor is a modification of a field-effect transistor (FET), where an applied electric field changes the width of the depletion region and, hence, its electrical resistance. In a spin FET, spin-polarised electrons are injected from a magnetic source into a semiconductor channel. During passage through the channel, these electrons undergo Rashba precession, the frequency of which depends on the gate voltage. Finally, the electrons are analysed by spin selective scattering in the magnetic drain. Hence, the actual electrical characteristics are dependent on, not only the magnetic orientation of the source and drain, but also on the gate voltage. Gardelis and co-workers [11] have made a step towards realising this device, but the gate functionality remains to be demonstrated. It may be noted that the characteristics of the spin FET differ from those of the device in the following subsection in that its g_m may be a periodic function of gate voltage and may change sign on application of a magnetic field.

2.5 Magnetic bipolar transistor (MBT)

This fifth variant, which is analogous to an ordinary bipolar junction transistor (BJT), has been explored theoretically in [8, 9]. Like the spin FET, the magnetic bipolar transistor (see Fig. 5) has not yet been realised experimentally, although a prototype has been fabricated [12]. Like the BJT, this device consists of two p–n (n–p) junctions connected in series and operates in a similar manner. The active (current amplification) region occurs under the same conditions for both devices: the emitter-base junction is forward-biased and the base-collector junction is reverse-biased. However, in the MBT, the emitter and collector are nonmagnetic, but the base is magnetic, creating spin-split conduction bands (see Fig. 5). It may also have a spin-polarised injector. As the conduction band in the base has a spin splitting $2q\zeta$, the electrons that flow from emitter to base are spin polarised. As such, the emitter efficiency is dependent on the number of electrons available to flow into the base. Hence, the current amplification $\beta = \Delta I_C/\Delta I_B$ can be controlled, not only by the spin polarisation in the base, but also by the nonequilibrium spin in the emitter. This additional dependence of β in an MBT is called [9] magnetoamplification.

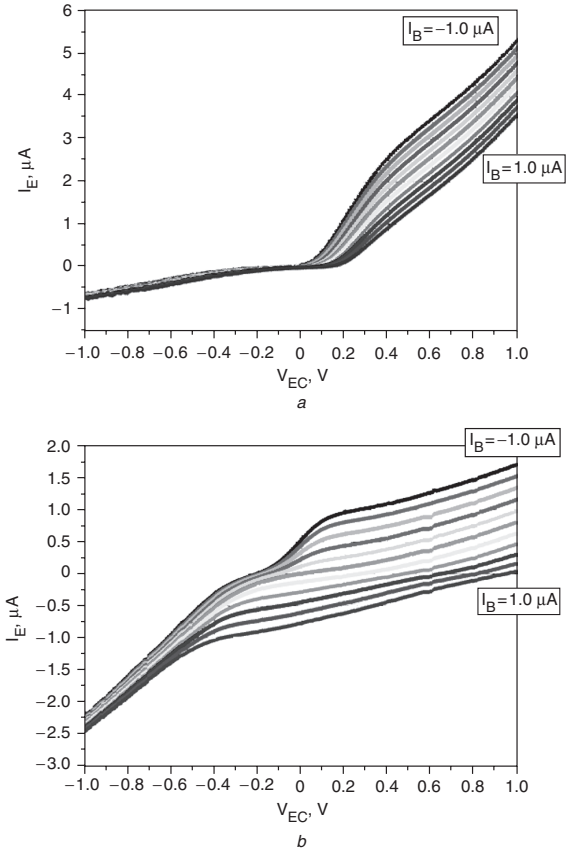

Fig. 12 *I_E–V_{EC} characteristics of spin diffusion transistors in common-collector configuration and zero applied field*
Load resistor $R_L = 9985\,\Omega$. The step size of I_B is 0.2 μA with the starting and ending currents as indicated in the boxes
a Common collector configuration of p-type Southamptom spin transistor (II-6), H = 0 Oe, $R_L = 9.985\,k\Omega$
b Common collector configuration of n-type Southamptom spin transistor (II-8), H = 0 Oe, $R_L = 9.985\,k\Omega$

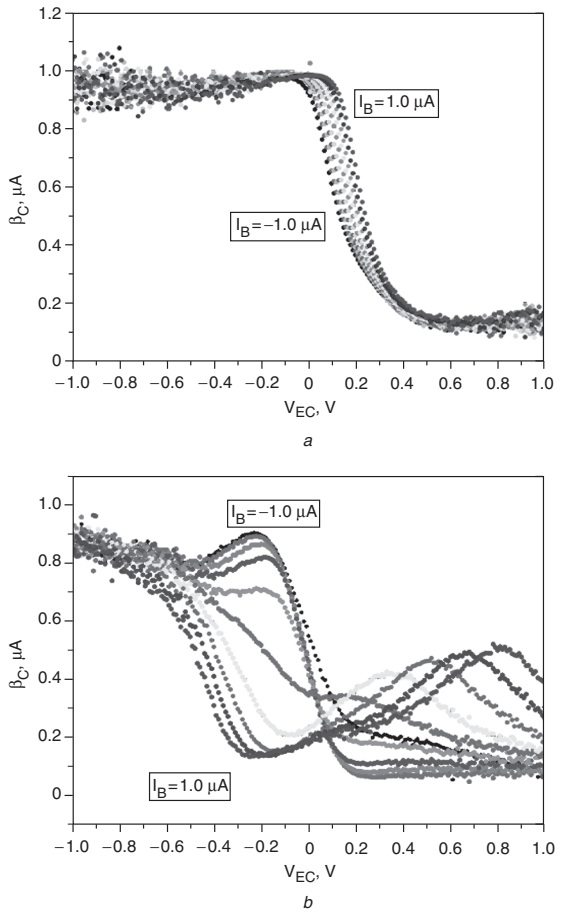

Fig. 13 *Calculated current gain at zero field as a function of emitter-collector voltage*
For p-type and n-type spin diffusion transistors in zero applied magnetic field. The step size of I_B is 0.2 μA with the starting and ending currents as indicated in the boxes. The current gain is determined by calculating the change in collector current for change in base current and was done between adjacent pairs of base currents (as shown in the legend) at all voltages
a Collector current gain of p-type Southampton spin transistor (II-6) in common collector configuration: H = 0 Oe; $R_L = 9.976\,k\Omega$
b Collector current gain of n-type Southampton spin transistor (II-6) in common collector configuration: H = 0 Oe; $R_L = 9.976\,k\Omega$

3 General operating principles of spin diffusion transistor

In the preceding Section, we summarised the state of the art in three-terminal spintronics. These devices comprised both all-metal and hybrid metal-semiconductor transistors. The fabricated devices all have a common feature, namely that the spin selectivity/spin transport is limited to the metallic components of the device. In this paper, we discuss a different design, which is distinguished by two main features. First, the semiconductor does more than simply control the distribution of applied voltages; the operation of the device depends on spin transport within the semiconductor itself. Secondly, it is the only spin transistor design capable of current gains equal to or in excess of unity (against other spin transistors which have a current gain of less than 10^{-3}). Reference [13] illustrates why this low current gain is the main sticking point for industrial applications, as well as some of their other limitations. In the remainder of the paper, we discuss the fabrication and characterisation of this new spin diffusion transistor.

The basic operation of this device is similar to a bipolar junction transistor (although it is most closely related to the classical tunnel transistor [14, 15]). This spin diffusion transistor injects a spin-polarised current from the emitter into the electric-field-screened base region. The current which diffuses across the base is driven primarily by a carrier concentration gradient, which forces the carriers injected by the emitter to wander towards the base along the top of an extended energy barrier, at the bottom of which lies the collector. This energy barrier is also spin-selective (according to the magnetic orientation of the collector) and determines if these polarised carriers are allowed to fall into the collector or not. Thus, we have a device with a respectable current gain from which power gain may be derived, but whose characteristics may be switched by manipulating the spin selectivity of the energy barrier via an externally applied magnetic field. In this particular device (see Fig. 6), tunnel barriers are used to provide the electric-field shielding of the semiconductor base. However, as outlined in [16], a wide variety of designs are possible in principle, including variants that use p–n junctions, Schottky barriers or spin tunnel junctions.

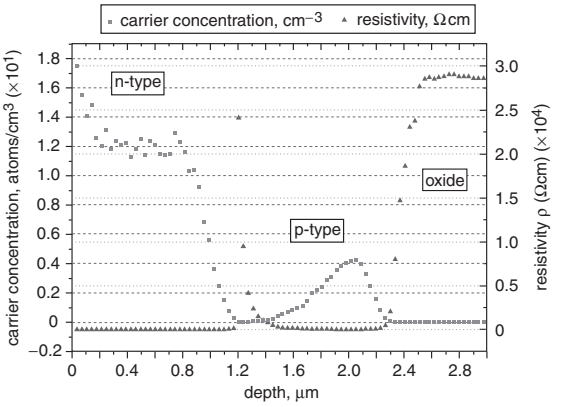

Fig. 14 *Spreading resistance data for p-type spin diffusion transistor*
These data were reported by Solecon Laboratories Inc. on a sample of the wafer used to make the p-type transistor. Notice that the doping is neither uniform nor of the same type throughout the device. In particular, note that there exists a weak p–n junction at a depth of 1.2 μm

4 First generation of spin diffusion transistors

4.1 Processing

The samples were fabricated using standard photolithography on n- and p-type silicon-on-insulator (SOI) wafers with a measured resistivity of 2–1000 Ω-cm. The details of the process are specified in [17, 18], so only the relevant aspects are provided here. The base contacts were heavily doped to form ohmic contacts. Tunnel barriers of Si_3N_4 were deposited on the collector and emitter contacts by low-pressure epitaxy. Then, all three contacts had 30 nm of Co and 1 μm of Al (for the electrical contacts) deposited by sputtering. The resulting structure is shown in Fig. 7.

4.2 Electrical characteristics in zero applied magnetic field

This device has been examined in detail in [17, 18], the main points are only summarised here for comparison with the second generation.

4.2.1 Two-terminal I–V characteristics: The I–V characteristics of the collector-to-emitter (CE) circuit and the collector-to-base (CB) circuit were performed at room temperature in the circuit configurations shown in Figs. 8*a* and *b*. Typical results are shown in Figs. 9 and 10, and differ slightly between the two types of transistors, although the overall form is the same in both. As shown previously [17, 18], these tunnel barriers conduct at low voltages ($< \sim 0.5$ V) by Mott's variable range hopping conduction [19, 20], and at higher voltages ($> \sim 0.5$ V) by Fowler–Nordheim tunnelling [21]. The existence of two different conduction methods is significant, because it has been well-established experimentally [22] that hopping conduction destroys the spin polarisation of carriers (as the time it takes to hop from one state to the next can exceed the spin lifetime of the carrier). Hence, no magnetic sensitivity should be observed in the hopping conduction regime.

4.2.2 Three-terminal I–V characteristics: When connected in common collector configuration (see Fig. 8*c*), the transistor exhibits similar characteristics (see Figs. 11, 12) to that of a conventional bipolar

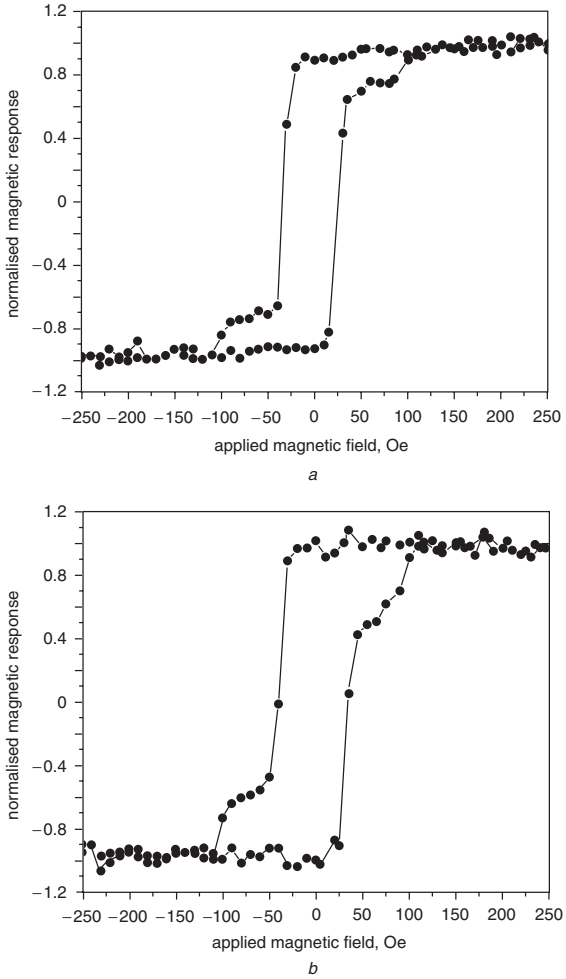

Fig. 15 *Normalised magnetic response minus Si background of spin diffusion transistors*
Owing to shape anisotropy, the collector switches at $\sim|30|$ Oe and the emitter and base at $\sim|115|$ Oe. This means that the magnetic moments of the emitter and collector Co layers are parallel for applied magnetic fields from –115 Oe to +30 Oe and greater than +115 Oe, and are antiparallel for positive applied magnetic fields between 30 Oe and 115 Oe
a p-type spin diffusion transistor
b n-type spin diffusion transistor

transistor: a dependence on both the base current and the emitter-collector voltage. However, the difference in the I–V characteristics between the n- and p-type transistors can be explained by either different doping in the silicon resulting in different minority carriers traversing the base or electron domination of the tunnelling process (due to the difference in effective masses for electrons and holes), causing one device to be a majority carrier device and the other to be a minority carrier device.

The emitter current as a function of base current and emitter-collector voltage is as high as −1.56 μA (−3.09 μA) for p-type (n-type) spin diffusion transistor, which occurs at $V_{EC} = -1$ V and $I_B = -1.0$ μA. Not only is this a higher output current than in the metal-based devices (by 3 orders of magnitude), but it also occurs at a lower voltage. At a slightly higher base current of −0.6 μA (see Fig. 13), the current gain (β) is 1.03 ± 0.03 (0.96 ± 0.03) for p-type (n-type). At a base current of −0.8 μA, the current gain (β) is 1.06 ± 0.05 for the p-type transistor. Furthermore, the

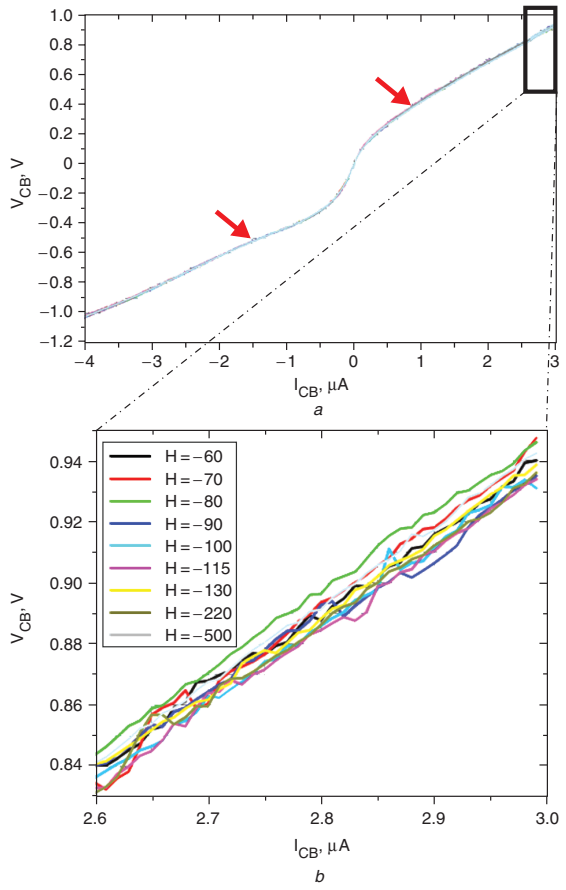

Fig. 16 *Two-terminal characteristics of p-type spin diffusion transistor as a function of applied magnetic field from collector to base*
Note the 'activity' (oscillations) around the coercive fields. (These samples were saturated at positive fields.)
a Full V–I curve where the arrows show the onset of Fowler–Nordheim tunnelling
b Blow-up of the highlighted regions in *a* to show the detail

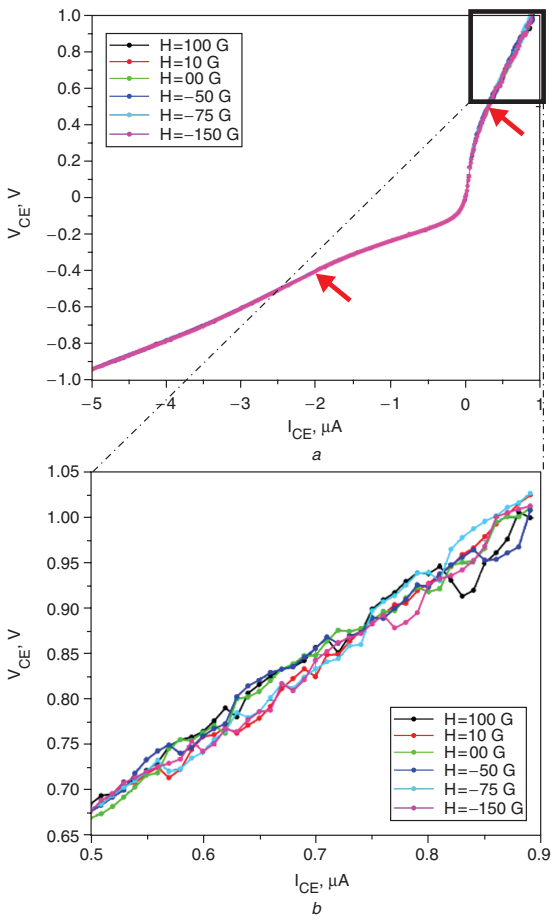

Fig. 17 *Two-terminal characteristics of p-type spin diffusion transistor as a function of applied magnetic field from collector to emitter*
a Full V–I curve where the red arrows show the onset of Fowler–Nordheim tunnelling
b Blow-up of the highlighted regions in *a* to show the detail. Note the 'activity' (oscillations) around the coercive fields. (These samples were saturated at positive fields.)

transfer ratio ($\alpha = I_E/I_C$) is calculated to be one within error for positive and negative V_{EC}, for both the p-type and n-type transistor at $I_B = 0\,\mu A$. This means that all of the emitter current is being transferred into the collector current. Hence, as the current gain is not identically equal to 1, the base current must be modifying either the amount of recombination in the Si, or the current injected into the Si from the emitter.

The transistor action is due solely to the presence of the silicon, because it occurs at any and all applied magnetic fields, and not to any spin transport in the silicon. It depends on a nonequilibrium condition (a surplus of minority carriers) being established at the first tunnel barrier, and continuing to the second barrier. In an ideal bipolar (tunnel) transistor, these minority carriers would diffuse across the base, as almost all of the applied voltage would be dropped over the depletion region of the p–n junctions (the tunnel barriers). However, this device does not have a uniform field in the base, resulting in a position dependence of the base minority carrier density. This is supported by the spreading resistance data (see Fig. 14), which indicate a nonuniform doping profile as well as a weak p–n junction in the silicon base. This inhomogeneity manifests itself as a parasitic resistance of 200 kΩ (980 kΩ) for the p-type (n-type) transistor. The presence of this parasitic base resistance limits the total output current and the current gain; in particular, the tunnel barrier ceases to dominate the output current at ~0.4 V (~0 V). This corresponds with the IV characteristics, which are a straight line above 0.4 V (~0 V) for the p-type (n-type) device, as well as with the location of the decrease in the current gain.

4.3 Electrical characteristics in an applied magnetic field

The magnetic response of the Co layers in the spin diffusion transistors was measured using a vibrating sample magnetometer (VSM). These hysteresis loops (see Fig. 15) indicate that differential switching is occurring in the devices, where the collector contact switches at the lower field of ~|30| Oe, and the emitter and base switch at the higher field of ~|115| Oe. Application of a magnetic field is expected to affect the I–V characteristics in two ways. First, the magnetisation of the emitter and collector Co contacts can be differentially manipulated, thereby introducing a spin-selective tunnelling magnetoresistance (TMR) effect that modulates the collector current. Secondly, the applied magnetic field decreases the mean free path in the silicon base via Lorentz magnetoresistance [23] (LMR) thereby

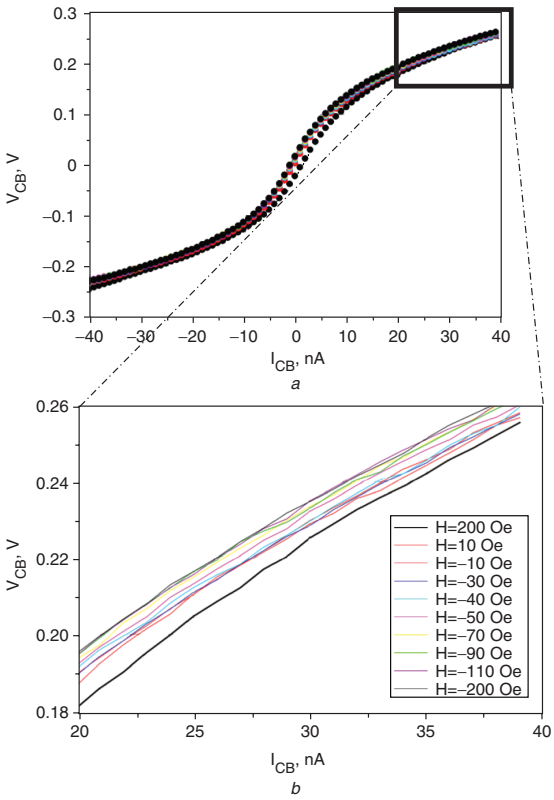

Fig. 18 *Two-terminal characteristics of n-type spin diffusion transistor as a function of applied magnetic field from collector to base*

Note the 'activity' (oscillations) or lack thereof around the coercive fields. (These samples were saturated at positive fields.)

a Full V–I curve

b Blow-up of the highlighted regions in *a* to show the detail

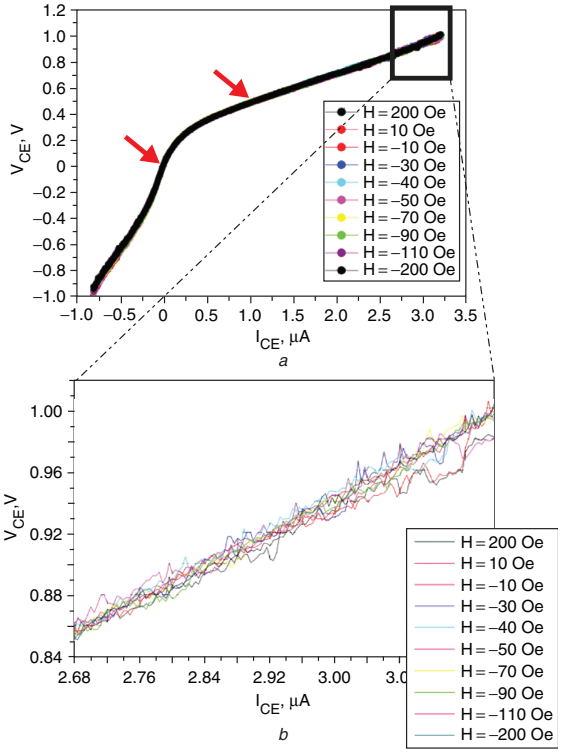

Fig. 19 *Two-terminal characteristics of n-type spin diffusion transistor as function of applied magnetic field from collector to emitter*

Note the 'activity' (oscillations) or lack thereof around the coercive fields. (These samples were saturated at positive fields.)

a Full V–I curve where the red arrows show the onset of Fowler–Nordheim tunnelling

b Blow-up of the highlighted regions in *a* to show the detail

also affecting the collector current. Both of these are observed in these devices.

4.3.1 Two-terminal magnetic I–V characteristics: The two-terminal measurements of Section 4.2.1 were repeated with a magnetic field applied in the plane of the transistor (perpendicular to the current). There are three important results (see Figs. 16–20) in these measurements. First, the I–V characteristics are a function of applied magnetic field. Secondly, no magnetic sensitivity is observed for voltages below the onset of Fowler–Nordheim tunnelling. This concurs with the claim that hopping conduction is occurring at low voltages. Thirdly, most of the 'activity' (shown in the inset of Figs. 16–20 as the ripples or deviations from a straight line) in the electrical characteristics occurs around the magnetic transition region, between −90 and −115 Oe. This suggests that the deviations may be due to magnetic domain formation and/or motion in the Co layers changing the magnetic state seen by different regions of the tunnel barrier.

4.3.2 Three-terminal magnetic I–V characteristics: The transistor was again operated in common-collector mode with the magnetic field applied in the plane of the transistor (perpendicular to the current). The results in Figs. 21–23 are typical and plot the emitter current as a function of applied emitter-collector voltage and magnetic field at $I_B = -0.6\,\mu A$. These results show a variation in the emitter current as a function of magnetic field, indicating that the transistor behaves as a magnetically tunable device with a field-dependent gain. The maximum variation of the average current gain (where β was averaged for all $V_{EC} > 0.4\,V$ and for each base current), relative to the current gain at $H = 0$ Oe, was $-11 \pm 3\%$ ($-15 \pm 2\%$) for p-type (n-type) which occurred at 75 Oe (110 Oe) and $I_B = -0.6\,\mu A$. On examination of the expanded graphs (see Fig. 24) for both n- and p-type at positive V_{EC}, it is clear that, when the magnetic moments of the emitter and collector Co layers are parallel, the emitter current is larger than in the antiparallel configuration. (From Fig. 21 it would appear that this magnetic sensitivity occurs in the region where the current gain is small. However, the current gain refers to I_C, the collector current and the magnetic sensitivity plotted in Fig. 18 refers to I_E the emitter current. Due to BJT definitions of positive current, one is turned 'on' in $+V_{EC}$ and the other is turned 'on' in $-V_{EC}$. Therefore, the region of large current gain is the same as the region of large magnetic sensitivity. The emitter current is plotted to show spin injection since the electrons actually flow from the collector to emitter. The same effect is apparent in the collector current due to conservation of charge.)

A detailed analysis of the origins of the magnetic sensitivity is explained in [17, 23], including other possibilities besides spin injection (or TMR) such as LMR, anisotropic magnetoresistance (AMR) and fringing fields from the magnetic elements. LMR is definitely measured, while AMR is eliminated, due to the size of the effect, and

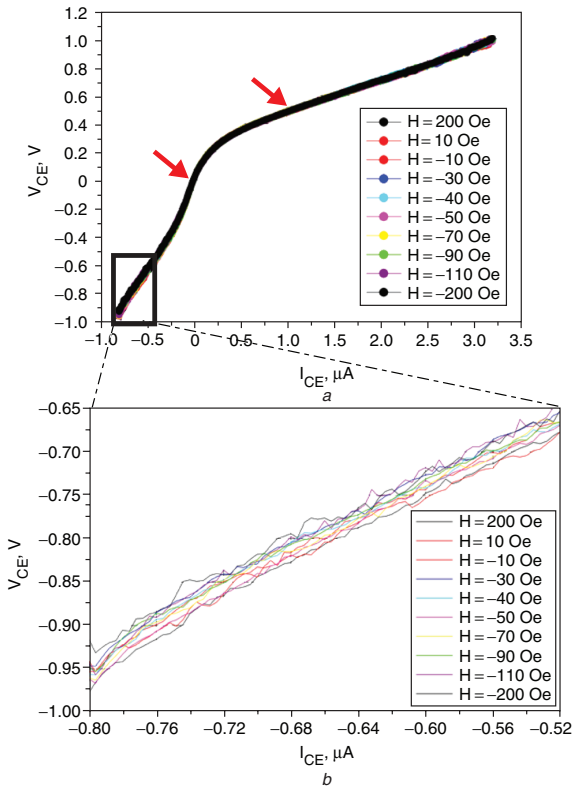

Fig. 20 *Two-terminal characteristics of n-type spin diffusion transistor as function of applied magnetic field from collector to emitter*
Note the 'activity' (oscillations) or lack thereof around the coercive fields. (These samples were saturated at positive fields.)
a Full V–I curve where the red arrows show the onset of Fowler–Nordheim tunnelling
b Blow-up of the highlighted regions in *a* to show the detail

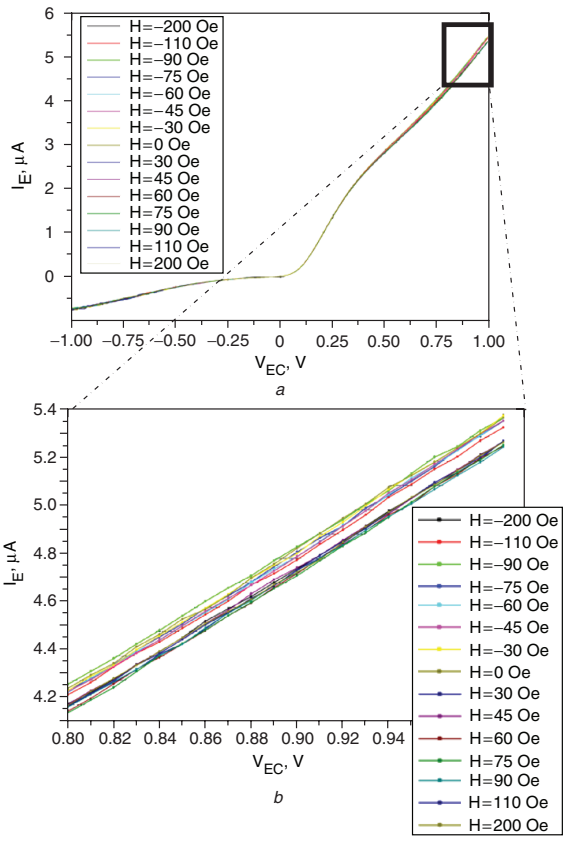

Fig. 21 *I_E characteristics as function of applied magnetic field of p-type spin diffusion transistors in common-collector configuration with $I_B = -0.6\,\mu A$*
The samples were saturated at negative fields
a Full V–I characteristics
b Blow-up of the black boxes from *a* for detail

the Hall Effect from fringe fields is eliminated by symmetry considerations. In particular, the percentage change as a function of field from LMR is 4% of the overall resistance at |200| Oe. This is a change of ~40 kΩ, which originates in part from the parasitic resistance of 200 kΩ (980 kΩ) for the p-type (n-type) device.

Assuming the existence of spin injection into Si (as presented in [24]), the spin polarisation can be estimated from Julliere's model [25] for spin tunnelling to be 2.5±0.5% for the p-type and 10±1% for the n-type (see Fig. 25). This value for the spin polarisation is significantly lower than the theoretical value of 38%, as well as being lower than typical values in the literature. This is to be expected as hopping conduction, though no longer dominant, is still active at high tunnel barrier bias and it destroys part of the injected spin polarisation.

5 Second generation of spin diffusion transistors

5.1 Processing

These samples were identical to the previous generation of devices except in the materials sputtered onto the Si. Tunnelling barriers of Al_2O_3 (1.5 nm) were deposited on the back of the wafer and tunnelling barriers of Al_2O_3 (1.0 nm) were deposited on the front of the wafer by sputtering of Al followed by plasma oxidation. Co (3 nm)/Fe (6 nm)/Cu (5 nm)/Cr (3 nm) were deposited on the emitter and base contacts, while CoFe (3–6 nm)/Cu (5 nm)/Cr (3 nm) were deposited on the collector. The resulting structure is shown in Fig. 26 and an actual device is shown in Fig. 27.

5.2 Electrical characteristics in zero applied field

5.2.1 Two-terminal I–V characteristics: I–V characteristics of the collector-to-emitter (CE) circuit and the collector-to-base (CB) circuit were performed at room temperature in the circuit configurations shown in Fig. 8*a* and 8*b*. Typical results on the stable barriers are shown in Fig. 28. However, although these VI characteristics show diode-like behaviour at low bias, they are not accurately represented by the equations for either an ideal diode or a nonideal diode as shown in Fig. 28. Instead, away from zero, the electrical characteristics of the tunnel barriers are linear in voltage and current, and are characterised by a resistance of 300 kΩ. This resistance is probably also due to the nonuniformity in the Si (as discussed in Section 4.2.2), with additional contributions from diffusion of the oxygen or Al into the surrounding Si, or Co or Fe into the Al_2O_3.

5.2.2 Three-terminal I–V characteristics: As seen in Fig. 29, these results closely resemble the results of the first generation p-type spin diffusion transistors for positive V_{EC}. However, there is negligible conduction in the negative V_{EC} regime, which results in a collector current

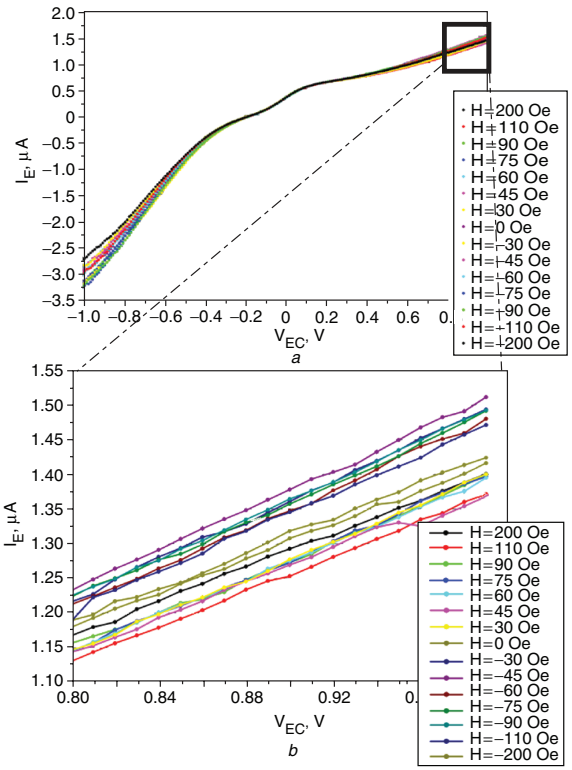

Fig. 22 *I_E characteristics as function of applied magnetic field of n-type spin diffusion transistors in common-collector configuration with $I_B = -0.6\,\mu A$*
The samples were saturated at negative fields
a Full V–I characteristics
b Blow-up of the black boxes from *a* for detail

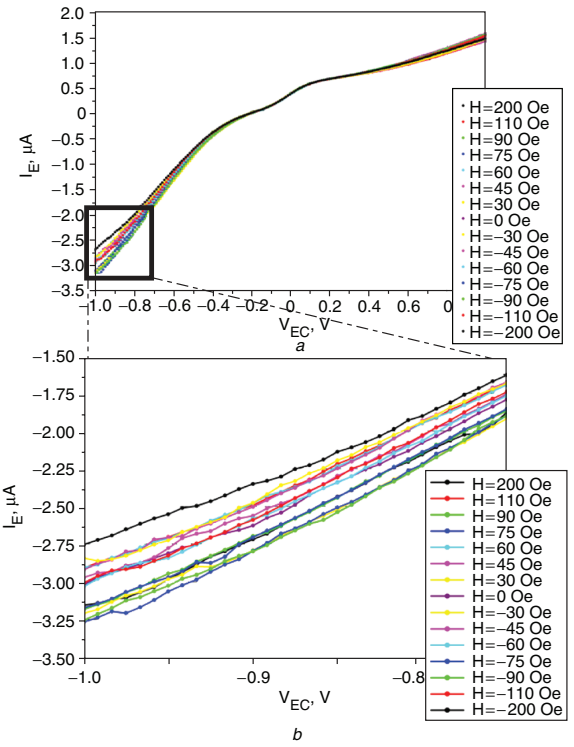

Fig. 23 *I_E characteristics as function of applied magnetic field of n-type spin diffusion transistors in common-collector configuration with $I_B = -0.6\,\mu A$*
The samples were saturated at negative fields
a Full V–I characteristics
b Blow-up of the black boxes from *a* for detail

gain for $V_{EC} < 0$ V, identical to 1. Hence, in this range, the base current does not modify the emitter current (which is zero), it simply adds to it. (For $V_{EC} > 1$ V, the current gain plateaued at an average of -0.933 ± 0.010. This plateau occurs when the contact resistance begins to exceed the tunnel barrier resistance at a voltage of ~ 0.9 V.)

5.3 Electrical characteristics in an applied field

The application of a magnetic field is expected to affect the I–V characteristics in the same ways as in the first generation of spin diffusion transistors. However, the primary expected differences are (i) that the cleaner switching will yield clearer parallel and antiparallel conditions and more stable electrical characteristics; (ii) that the larger separation between the coercive fields will yield more distinct parallel and antiparallel conditions and therefore larger TMR values; and (iii) that the new tunnel barriers will conduct spin better leading to a more highly spin-polarised current in the base which will yield greater magnetic sensitivity in the emitter current and larger TMR values.

The magnetic response, as measured by a SQUID Magnetometer, shows three coercivities (see Fig. 30). The base contact switches at $H_C \sim 10$ Oe, the emitter contact switches at $H_C \sim 85$ Oe, and the collector contact at fields > 100 Oe.

5.3.1 Two-terminal magnetic I–V characteristics: The two-terminal measurements of Section 5.2.1 were repeated with a magnetic field applied in the plane of the transistor (perpendicular to the current). There are three important results (shown in Figs. 31 and 32) from these measurements. First, the I–V characteristics are again a function of applied magnetic field. Secondly, as compared to the two terminal magnetic I–V characteristics of the first generation of devices, the I–V characteristics are much smoother, indicating cleaner magnetic switching than before. Thirdly, the variation in voltage at different applied magnetic fields is as large as 0.0934 V, for the collector to base measurement, and 0.0667 V, for the collector to emitter measurement, which is well outside the error in the measurement of ± 0.0001V (± 0.1 mV).

5.3.2 Three-terminal magnetic I–V characteristics: The transistor was again operated in common-collector mode with the magnetic field applied in the plane of the transistor (perpendicular to the current). The results (see Figs. 33 and 34) show a variation in the emitter current (of up to $0.672 \pm 0.006\,\mu$A in $|90|$ Oe) as a function of magnetic field, indicating that the transistor behaves as a magnetically tunable device with a field-dependent emitter gain. The maximum relative variation of the emitter current was $-14 \pm 0.3\%$ which occurred at -90 Oe, $V_{EC} = 1$ V and $I_B = 0.0\,\mu$A. Overall, the current variation shows a negative change; the emitter current is being decreased as a function of field.

Close examination of Fig. 34 shows that, although the emitter current for positive V_{EC} varies in an identical fashion to that expected for TMR-influenced data, there is a field-dependent distribution. Hence, the data do not show a simple TMR/spin injection signature (see Fig. 35): one current for parallel contacts and another for antiparallel

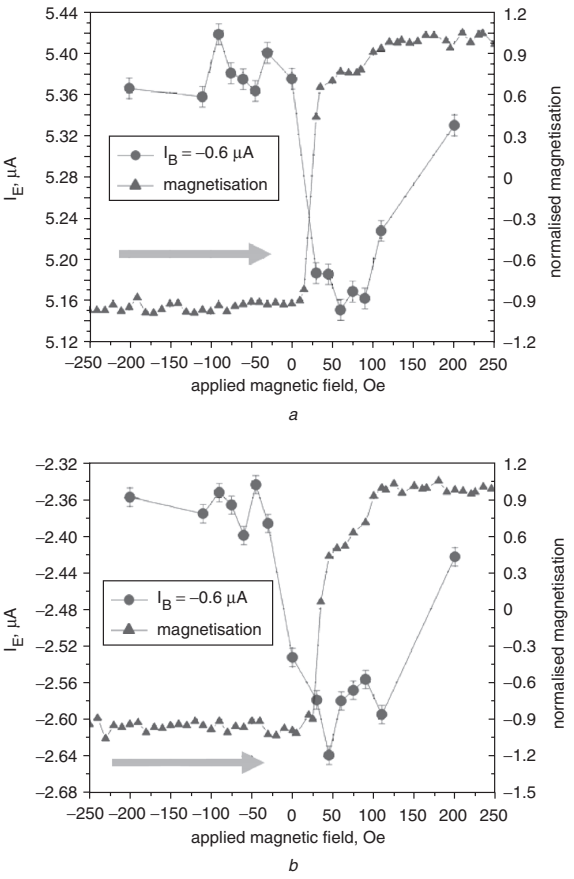

Fig. 24 *Emitter current as a function of applied magnetic field after correction for LMR at $V_{EC} = 1$ V and $I_B = -0.6$ μA*
Half of a hysteresis loop as measured on a VSM is shown by the circular symbols. The arrow indicates the direction of the magnetic field sweep of the measurements, following saturation at fields < -1 kOe. (These data points were simply taken from the common-collector configuration data in the previous graph above the HC/FNT threshold, corrected for Lorentz magnetoresistance, and plotted separately for clarity. Owing to the substantial additional noise associated with magnetic field sweeping (due to magnetocaloric effects combined with the temperature dependence of silicon), the data were measured by sweeping the voltage/current characteristics at a selection of fixed magnetic fields.)
a Emitter current (corrected for LMR) as a function of applied magnetic field through p-type Si ($V_{EC} = 1$ V)
b Emitter current (corrected for LMR) as a function of applied magnetic field through n-type Si ($V_{EC} = 1$ V)

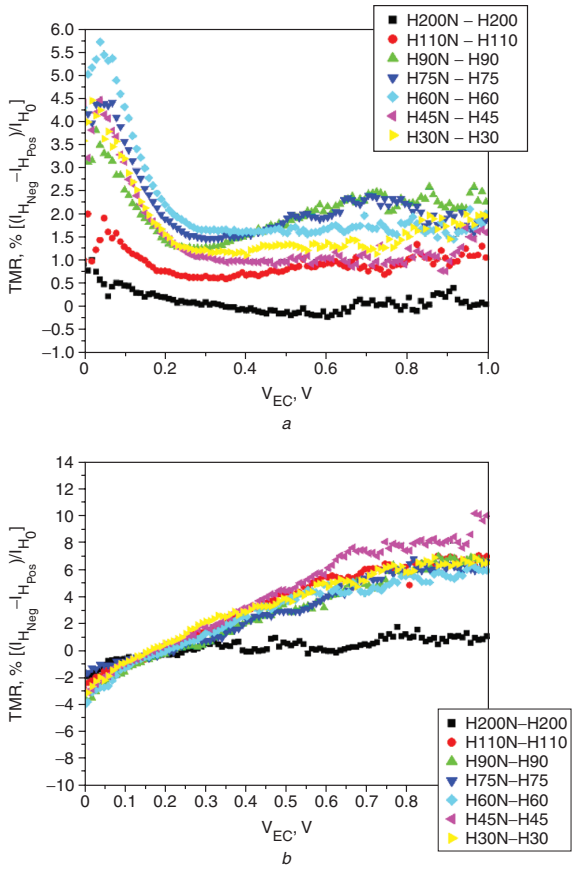

Fig. 25 *Calculated TMR of the emitter current for p-type and n-type spin diffusion transistor in common collector configuration and as function of both emitter-collector voltage and applied magnetic field at $I_B = -0.6$ μA*
The effect is zero for the ±200 Oe data since the magnetic elements are in parallel and the noise around $V_{EC} = 0$ V is the result of division by $I_C \approx 0$ A. The TMR is the difference between the positive and negative field signals, divided by the signal at zero field, and represents only the magnetic sensitivity from spin transport, not from LMR
a TMR percentage for p-type spin transistor (II-6), $I_B = -0.6$ μA
b TMR percentage for n-type spin transistor (II-8), $I_B = -0.6$ μA

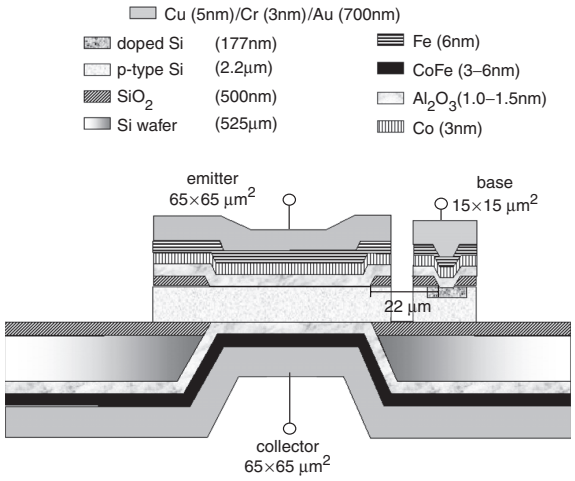

Fig. 26 *Schematic diagram of silicon-based spin diffusion transistor*
This geometry is identical to that of the first generation of spin diffusion transistors

contacts. The two groups have a symmetric contribution, which could be the result of any one of the symmetric contributions discussed in Section 4. Finally, it should be noted that, in both cases, the antiparallel fields yield a larger current than the parallel fields. This is due to Co and CoFe having a different majority spin carrier [26].

By removing these symmetric contributions, the maximum TMR is calculated (see Fig. 36) to be 13.3±0.2% at $I_B = -0.2$ μA. Close examination of the TMR shows their dependence on the magnetic response of the transistors. At |30| Oe, the base contact has switched. This introduces some spin-polarised current into the Si. (Recall that the base junction here is a tunnel junction and that the base current is predominantly additive, not recombinative.) Although, the emitter contact does not really start to switch until 75 Oe, the magnetisation is dropping slightly. This could lead to the decrease in TMR through 45, 60 and 75, as the

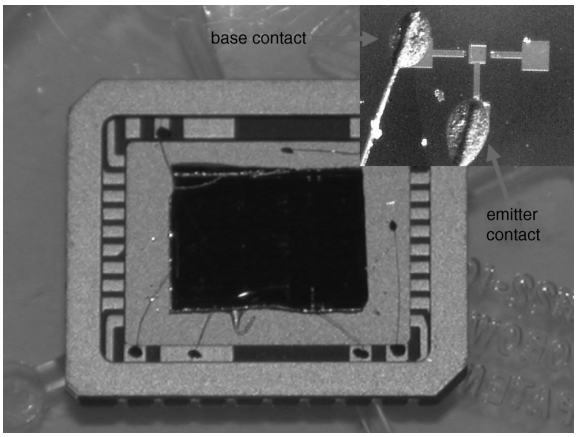

Fig. 27 *Actual spin diffusion transistor as mounted in chip package*
Inset: Close-up of carbon paste bonding where red arrows indicate the particular contact

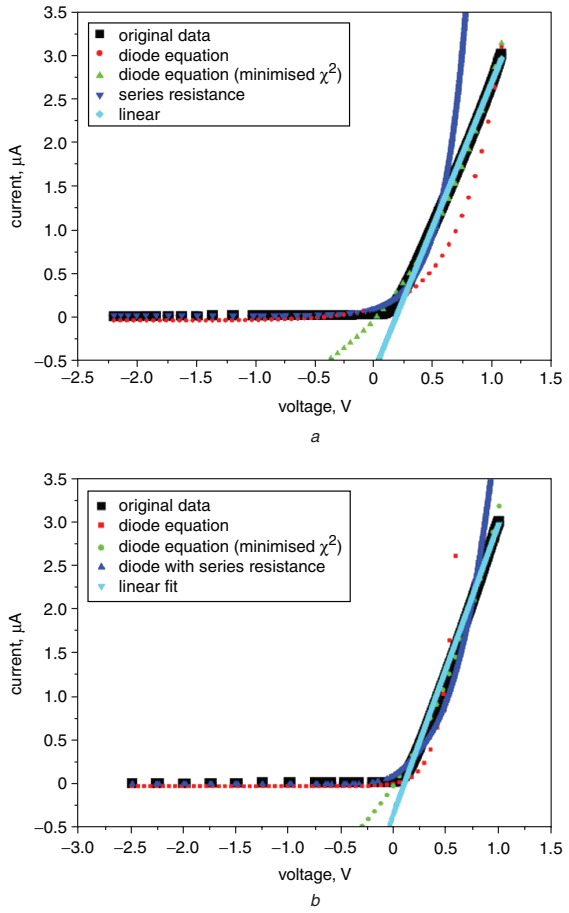

Fig. 28 *Two-terminal characteristics of the spin diffusion transistor*
The black dots indicate measured data points; the red and green dots are fits to the diode equation; the dark blue dots are fits to diode equation plus a series resistance; and the light blue dots are the linear fits
a V–I curves for Strasbourg transistor III-33: collector to base
b V–I curves for Strasbourg transistor III-33: collector to emitter

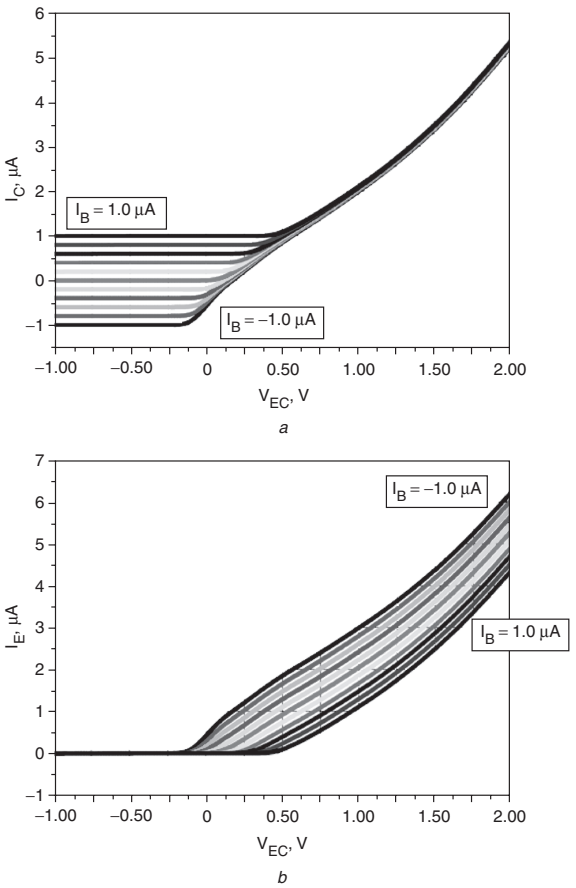

Fig. 29 *V–I characteristics of the p-type spin diffusion transistor in common-collector configuration and zero applied field*
The load resistor $R_L = 973\,\Omega$. The step size of I_B is 0.2 μA with the starting and ending currents as indicated in the boxes

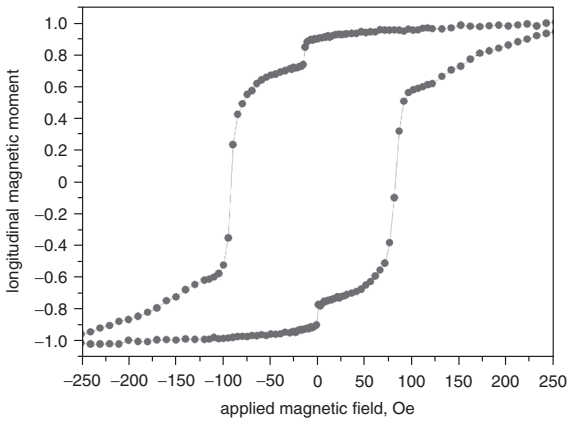

Fig. 30 *Magnetic characterisation with three coercivities at $H_C \sim 10$ Oe, $H_C \sim 85$ Oe and $H_C > 100$ Oe*
These are hypothesised to belong to the base, emitter and collector contacts, respectively. Magnetic data for Strasbourg transistor III-3 after NRL processing

emitter and base return to parallel alignment. By about 90 Oe, the emitter has almost completely switched, leading to antiparallel alignment of the emitter and collector, and the sudden jump in TMR. For the remaining fields, the collector undergoes a long reversal process, thereby

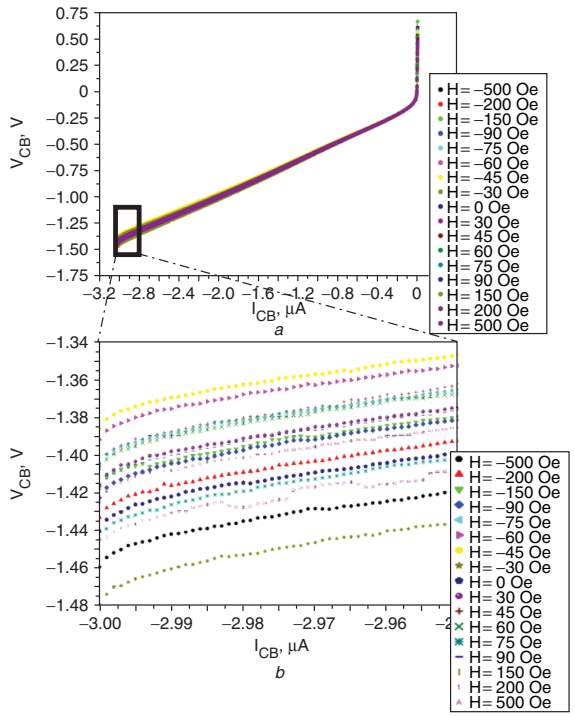

Fig. 31 *Two-terminal characteristics in an applied magnetic field of p-type spin diffusion transistor from collector to base*
These samples were saturated at positive fields
a Full I–V characteristics
b Blow-up of the highlighted regions in *a* to show the detail

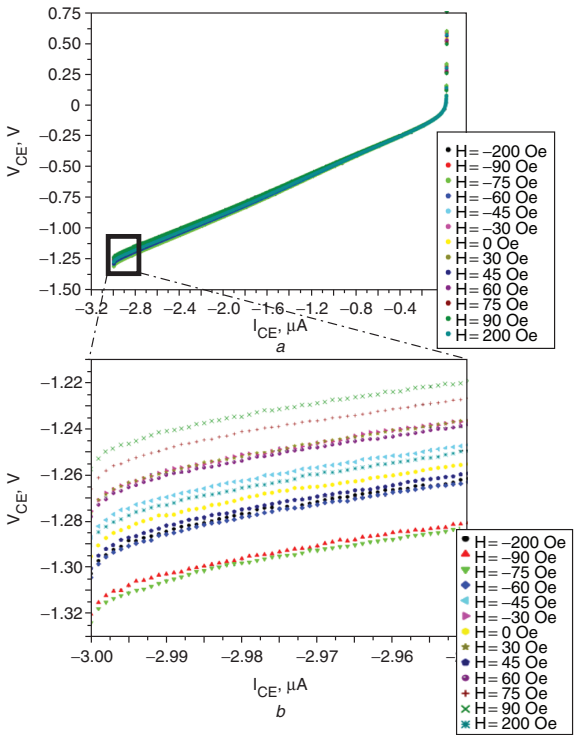

Fig. 32 *Two-terminal characteristics in applied magnetic field of p-type spin diffusion transistor from collector to emitter*
These samples were saturated at positive fields
a Full I–V characteristics
b Blow-up of the highlighted regions in *a* to show the detail

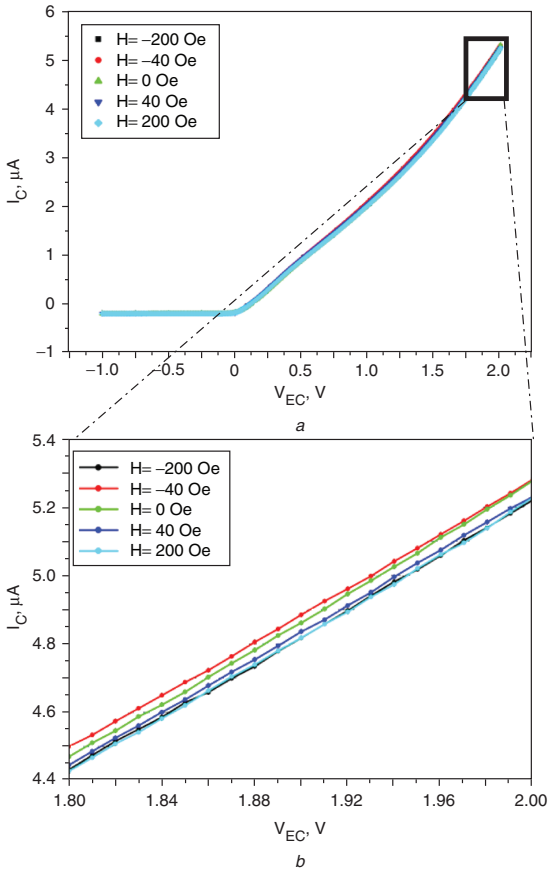

Fig. 33 *I_C characteristics as function of applied magnetic field of spin diffusion transistors in common-collector configuration with $I_B = -0.2\,\mu A$*
These samples were saturated at positive fields
a Full V–I characteristics
b Blow-up of the square regions in order to show the detail

decreasing the TMR effect. Hence, the TMR is nonzero for |150| Oe and |200| Oe, although the magnitude decreases with the increase in field. The effect is very close to zero for the ±500 Oe data because the magnetic elements are nearly all in parallel, as seen from the magnetisation curve shown Fig. 30.

6 Conclusions

Proof of concept has been established of a 'high' current gain (greater than unity), magnetically sensitive, silicon-base spin diffusion transistor. (The use of the word 'high' is with respect to other spin transistors.) This device has a current gain slightly greater than unity, which is 3 orders of magnitude larger than any other spin transistor, although it is still less than the typical bipolar junction transistor current gain of 100. However, as was shown in [14], it is possible for this design to achieve current gains comparable to the bipolar junction transistor. In zero magnetic field and at room temperature, the emitter I–V characteristics are similar to those of conventional transistors, and afford a current gain greater than unity and respectable emitter currents. The current gain of the device can be magnetically tuned (up to $-12\pm4\%$ ($-14\pm3\%$) for p-type (n-type) which occurred at -60 Oe and $I_B = -0.6\,\mu A$). Moreover, the base current and emitter-collector voltage control this

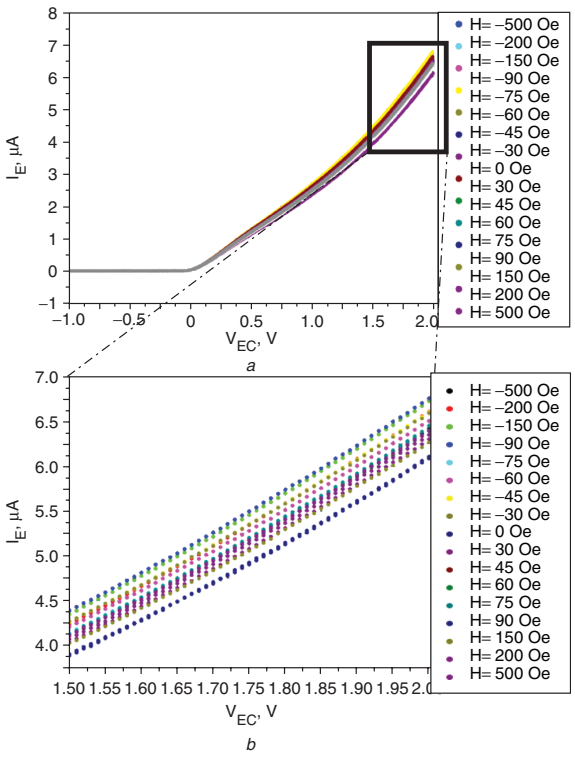

Fig. 34 *I_E characteristics as a function of applied magnetic field of spin diffusion transistors in common-collector configuration with $I_B = -0.2\ \mu A$*
These samples were saturated at positive fields
a Full V–I characteristics
b Blow-up of the square regions in order to show the detail

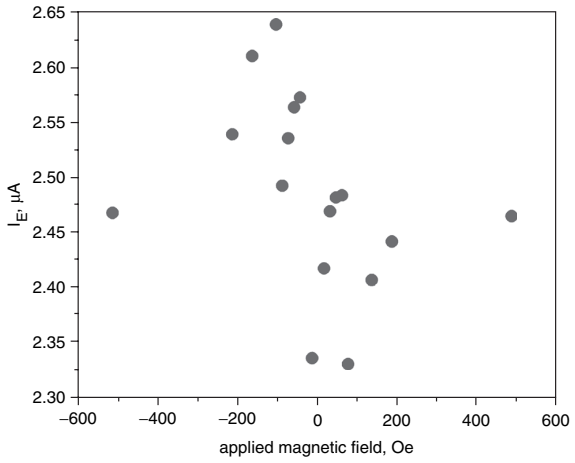

Fig. 35 *Emitter current as function of applied magnetic field in common-collector configuration with $I_B = -0.2\ \mu A$ and $V_{EC} = 1\ V$ for p-type spin diffusion transistor*
These data points were simply taken from the common-collector configuration data in the previous graph and plotted separately for clarity. (The samples were saturated at positive fields.)

field-dependent gain. However, the device described has a number of shortcomings, which, if eliminated, may provide improved performance. These include:

- *Nonoptimal tunnel barriers*: Si_3N_4 tunnel barriers conduct initially via hopping conduction, which is well known to

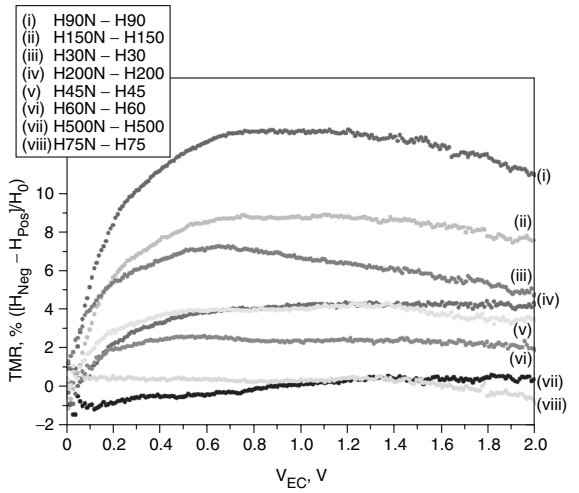

Fig. 36 *Calculated TMR of emitter current for the p-type spin diffusion transistor in common-collector configuration and as a function of both emitter-collector voltage and applied magnetic field at $I_B = -0.2\ \mu A$*

partially destroy the spin polarisation of the carriers. However, Al_2O_3 needs significant work as the deposition of Al directly onto Si results in the formation of AlSi. As was shown by Schmidt *et al.* [27], a metal-semiconductor contact will destroy the spin polarisation. It may also increase the contact resistance.

- *Implementing different magnetic materials on the collector and emitter*: There is insufficient magnetic switching differential (where each contact switches quickly at a particular field) between the three contacts. Furthermore, making the contacts small enough that they are mono-domain will sharpen up the magnetic switching behaviour of the device.
- *Existence of a contact resistance*: The existence of this ohmic contribution limits the output current of the device, thereby reducing the magnitude of current gain the device can produce, as well as affecting the magnetic characteristics. Further investigation on the fabrication of tunnel barriers on Si should remove this.
- *Nonoptimal electrode geometry*: Recent modelling [28–30] indicates that the emitter efficiency can be dramatically improved by implementing spin injection into a base with length (distance between the collector and base contacts) much greater than the thickness (distance between the emitter and collector contacts) and also by interposing the collector between the emitter and base contact. Tuning of the barrier resistances to optimise conduction in the region of positive current gain is necessary.
- *Nonoptimal doping profile*: The doping profile in these spin diffusion transistors is not optimal (see Fig. 14). The dopant changes sign in the middle of the silicon base, which creates a weak p–n junction that in turn dilutes the spin polarisation as the carriers cross it. This in turn reduces the maximum theoretical magnetic sensitivity.
- *The presence of Lorentz MR*: This is an intrinsic property of the silicon, but its magnitude may be reduced by careful device geometry. Furthermore, its effect will be rendered less significant by improvement in the spin-selective signal.

Finally, further work needs to be done to improve tunnel barrier fabrication on Si, to determine the correlation

between deposition parameters, Si doping and barrier resistance. Preliminary results can be found in [31, 32].

7 Acknowledgments

The authors thank the silicon processing team at the University of Southampton, M. Johnson and M. Hehn, for useful discussions, and the EPSRC (GR/L68643/01) and the EC contract SPINOSA (IST-2001-33334) for financial support.

8 References

1 Baibich, M.N., Broto, J.M., Fert, A., Dau, F.N.V., Petroff, F., Eitenne, P., Creuzet, G., Friederich, A., and Chazelas, J.: 'Giant magnetoresistance of (001)Fe/(001)Cr magnetic superlattices', *Phys. Rev. Lett.*, 1988, **61**, pp. 2472–2475
2 Johnson, M.: 'Bipolar spin switch', *Science.*, 1993, **260**, p. 320
3 Monsma, D.J., Lodder, J.C., and Popma, T.J.A. *et al.*: 'Perpendicular hot electron spin-valve effect in a new magnetic field sensor: the spin-valve transistor', *Phys. Rev. Lett.*, 1995, **74**, p. 5260
4 Sato, R., and Mizushima, K.: 'Spin-valve transistor with an Fe/Au/Fe(001) base', *Appl. Phys. Lett.*, 2001, **79**, p. 1157
5 van Dijken, S., Jiang, X., and Parkin, S.S.P.: 'Room temperature operation of a high output current magnetic tunnel transistor', *Appl. Phys. Lett.*, 2002, **80**, p. 3364
6 Ounadjela, K., and Hehn, M.: Patent Application Number FR9904227 (France, 2000)
7 Datta, S., and Das, B.: 'Electronic analog of the electro-optic modulator', *Appl. Phys. Lett.*, 1990, **56**, p. 665
8 Fabian, J., Zŭtić, I., and das Sarma, S.: 'Magnetic bipolar transistor', *Appl. Phys. Lett.*, 2004, **84**, p. 85
9 Fabian, J., and Zŭtić, I.: 'Spin-polarized current amplification and spin injection in magnetic bipolar transistors', *Phys. Rev. B, Condens. Matter Mater. Phys.*, 2004, **69**, p. 115314
10 Johnson, M.: 'The all-metal spin transistor', *IEEE Spectrum*, 1994, **31**, (5), p. 47
11 Gardelis, S., Smith, C.G., and Barnes, C.H.W. *et al.*: 'Spin-valve effects in a semiconductor field-effect transistor: A spintronic device', *Phys. Rev. B, Condens. Matter.*, 1999, **60**, p. 7764
12 Private communication, cited in [8]
13 Bandyopadhyay, S., Cahay, M.: 'Are spin junction transistors suitable for signal processing?' *Appl. Phys. Lett.*, 2005, **86**, p. 133502
14 Mead, C.A.: 'The tunnel-emission amplifier', *Proc. IRE.*, 1960, **48**, pp. 359–361
15 Kisaki, H.: 'Tunnel transistor', *Proc. IEEE.*, 1973, **61**, pp. 1053–1054
16 Gregg, J.F., and Sparks, P.D.: Patent Application Number US6218718, (USA, 2001)
17 Dennis, C.L., Siristhatikul, C., Ensell, G.J., Gregg, J.F., and Thompson, S.M.: 'A high-current gain silicon-based spin transistor', *J. Phys. D, Appl. Phys.*, 2003, **36**, pp. 81–87
18 Dennis, C.L.: 'A Silicon-based spin transistor'. PhD thesis, the University of Oxford, 2004
19 Mott, N.F.: 'Electrons in disordered structures', *Adv. Phys.*, 2004, **50**, pp. 865–945
20 Xu, Y., Ephron, D., and Beasley, M.R.: 'Directed inelastic hopping of electrons through metal-insulator-metal tunnel junctions', *Phys. Rev. B, Condens. Matter.*, 1995, **52**, p. 2843
21 Fowler, R.H., and Nordheim, L.W.: 'Electron emission in intense electric fields', *Proc. R. Soc. Lond A*, 1928, **119**, p. 173
22 Manoharan, S.S., Elefant, D., Reiss, G., and Goodenough, J.B.: 'Extrinsic giant magnetoresistance in chromium (IV) oxide, CrO2', *Appl. Phys. Lett.*, 1998, **72**, p. 984
23 Schwerer, F.C., and Silcox, J.: 'Electrical resistivity of nickel at low temperatures', *Phys. Rev. Lett.*, 1968, **20**, p. 101
24 Dennis, C.L., Gregg, J.F., Thompson, S.M., and Ensell, G.J.: 'Evidence for electrical spin tunnel injection into Si', submitted 2004
25 Julliere, M.: 'Tunneling between ferromagnetic films', *Phys. Lett.*, 1975, **54A**, p. 225
26 Coey, J.M.D.: 'Materials for spin electronics', in Thornton, M. and Ziese, M.: (Eds.).: 'Spin electronics' (Springer, New York, 2001), p. 278
27 Schmidt, G., Ferrand, D., Molenkamp, L.W., Filip, A.T., and van Wees, B.J.: 'Fundamental obstacle for electrical spin injection from a ferromagnetic metal into a diffusive semiconductor', *Phys. Rev. B, Condens. Matter.*, 2000, **62**, p. R4790
28 Borges, R.P., Dennis, C.L., Gregg, J.F., Jouguelet, E., Ounadjela, K., Petej, I., Thompson, S.M., and Thornton, M.J.: 'Comparative study of spin injection into metals and semiconductors', *J. Phys. D, Appl. Phys.*, 2002, **35**, pp. 186–191
29 Gregg, J.F., Borges, R.P., Jouguelet, E., Dennis, C.L., Petej, I., Thompson, S.M., and Ounadjela, K.: 'Spin injection efficiency in spin electronic devices', *J. Magn. Magn. Mater.*, 2003, **265**, pp. 274–287
30 Dennis, C.L., Tiusan, C.V., Gregg, J.F., Thompson, S.M., Ensell, G.J.: 'Characteristics of Si-based spin tunnel transistor: theory and experiment', in preparation, 2005
31 Dennis, C.L., Tiusan, C.V., Ferreira, R.A., Gregg, J.F., Ensell, G.J., Thompson, S.M., and Freitas, P.P.: 'Tunnel barrier fabrication on Si and its impact on a spin transistor', *J. Magn. Magn. Mater.*, 2005, **1383**, pp. 290–291
32 Dennis, C.L., Ferreira, R.A., Tiusan, C.V., Gregg, J.F., and Freitas, P.P.: 'Tunnel barrier fabrication on Si and its application to spintronics', in preparation, 2005

6.1 Résumé de chapitre en français

Transport polarisé en spin dans des structures complexes qui combinent des jonctions tunnel magnétiques et des matériaux semi-conducteurs, dédiés à l'injection de spin dans les semi-conducteurs

Un autre aspect de mon travail de recherche a visé le transport électronique dans des structures hybrides qui combinent les jonctions tunnel et des matériaux semi-conducteurs (SC). Les SC sont trés intéressants pour l'électronique de spin par la grande mobilité électronique, la longueur de diffusion de spin trés élevée et leur mécanisme de conduction ajustable en fonction du dopage, de la température etc. Le travail dans cette thématique est effectué en collaboration directe avec le groupe du Pr. J. Gregg (laboratoire Clarendon, Oxford) et concerne la réalisation d'un nouveau transistor de spin utilisant une base semi-conductrice. Le fonctionnement de la premiére génération de transistors repose sur l'injection directe d'électrons polarisés en spin à travers les barriéres Schottky d'une structure FM/SC/FM, le semi-conducteur étant alors composé de silicium dopé (n ou p). Ces transistors ont été fabriqués à l'Université de Southampton en ce qui concerne la base semi-conductrice et à l'IPCMS (Strasbourg) et au LPM (Nancy) en ce qui concerne les multicouches qui constituent l'émetteur et le collecteur. Les électrodes du transistor, structurées par lithographie optique, présentent des facteurs d'aspects différents afin d'exploiter l'influence de l'anisotropie de forme sur leurs propriétés magnétiques et ainsi de permettre le contrle de la réponse magnétorésistive du transistor. Des résultats prometteurs montrent des caractéristiques électroniques de type transistor, semblables aux transistors bipolaires classiques.

Part III

Spin filtering effects in single crystal magnetic tunnel junctions

Chapter 7

Spin tunneling phenomena in single crystal Fe/MgO/Fe magnetic tunnel junction systems

7.1 Introduction

The discovery in 1995 of a tunnel magneto-resistance (TMR) effect at room temperature in amorphous Aluminum oxide barrier based magnetic tunnel junctions (MTJ) [1] leads to large scale applications of MTJ in sensors and data storage devices [17].

The transport mechanisms in crystalline magnetic tunnel junctions (MTJ) attracted the interest of the international scientific community after the publication of several theoretical papers [10, 11, 12]. They show that a realistic description of the band structure makes the mechanisms of transport impossible to describe within the free electrons model. Indeed, in crystalline systems the Bloch electrons are not any more distinguished according to their orbital character but are classified with respect to the symmetry of their associated electronic wave function. This determines a symmetry dependent wave function attenuation within the insulator. Giant tunnel magnetorezistive effects, reaching several thousands of percents, are theoretically predicted in single-crystal MTJ employing bcc ferromagnetic electrodes and MgO insulating barriers.

The experimental study of tunnel magneto-resistance in the Fe/MgO like crystalline systems is relatively recent. The first unfruitful developments of single crystal MTJ were carried out in 1996 [70] and the first local spectroscopic studies reported in 2001 by the Kirschner's team [71]. In 2001, Bowen et al, obtained an encouraging magneto-resistance of 27% at room temperature [72].

Our team demonstrated experimentally that the physics of tunneling in single crystal Fe/MgO/Fe systems gets beyond the free-electrons model [73, 74]. On the other hand, in junctions employing amorphous MgO barriers and polycrystalline electrodes, we illustrated also that the tunneling phenomena are correctly described within the free electrons framework [75]. Moreover, in single crystal systems we illustrate the role of the interfacial electronic structure on the tunneling [76] and recently that Fe/MgO interface engineering is a powerful tool for high output voltage device applications [77]. Our experimental activity within this topics focused a large class of MTJ

systems employing MgO(100) insulating barrier and different bcc (100) electrodes such as Fe, Co, CoFe, Pd/Fe, Cr/Fe and their combination. In this chapter we report TMR ratios up to 180% at room temperature in simple and double barrier MTJs with standard Fe(001) electrodes and MgO(100) barrier. Our results are similar to those obtained by the group of Yuasa (AIST Japon) with TMR ratios in MBE grown systems below 200% [78]. The limited value of the TMR may be related to the structural quality of the epitaxial systems altered by the plastic relaxation induced by the epitaxial strains. In these circumstances a possible enhancement of the TMR ratio in epitaxial systems is still possible by increasing the polarization ratio of injected electrons. This has been already done using 'alternative' bcc ferromagnetic systems. A 410% TMR ratio has been recently reported in bcc-Co/MgO/Fe MTJ by Yuasa [79]. Another way to enhance the TMR ratio implicates the improvement of the structural quality of the MTJ stacks. This is motivated by recent experimental results obtained in the Kirschners group [80]. They illustrate by X-Ray diffraction experiments an oxygen induced symmetrization and improved structural coherency in Fe/FeO/MgO/Fe(001) and Fe/FeO/MgO/FeO/Fe(001) Magnetic Tunnel Junctions. Moreover, in the last class of systems the theory predicts TMR rations about ten times larger than in standard Fe/MgO/Fe systems.

Interestingly, the most important values of TMR have been experimentally reported for systems elaborated by sputtering. Here the MgO barrier is mainly grown on initially amorphous electrodes subsequently re-crystallized by annealing. The plastic relaxation of the barrier is 'eliminated': i.e. the ferromagnetic electrode adopts the structure of the insulator during the annealing. In 2004, the group of Parkin in IBM Almaden using an ANELVA sputtering plant reports 220% of TMR in sputtered CoFe/MgO MTJs [82] and Yuasa et al reported simultaneously [83] a TMR of 230%. Since these first results, the filtering efficiency reflected by the TMR ratio has been continuously enhanced. This was done by using different steocheometry CoFeB amorphous electrodes re-crystallized by subsequent annealing steps. It has been shown that the filtering efficiency is strongly related to the MgO barrier thickness and the annealing procedure. A record TMR ratio of 472% has been recently reported [89]. Other amorphous ferromagnetic materials elaborated by sputtering such as CoFeZr, CoZrNb, CoFeSiB, compatible with MgO(001) barriers are currently investigated by different groups.

Concerning the elaboration technique of the MgO barrier by sputtering several methods are commonly used: plasma oxidation of previously sputtered Mg metallic layers [81], direct sputtering from MgO target [82, 83, 85, 86, 88, 84, 89] or reactive oxygen sputtering from Mg target [85]. Finally, the best magneto-resistive results have been obtained when the MgO is directly sputtered from a MgO target. Depending on the elaboration technique, the TMR amplitude and the resistance area-product (RA) of the junctions may vary drastically. To satisfy the impedance-matching condition which is a major request in an electronic circuit for a high-speed operation the RA product of MTJs has to be carefully adjusted. MRAM applications require a RA in the range from 50 Ωm^2 to 10 kΩm^2, depending on the lateral MTJ size (i.e. areal density of MRAM). In this RA range, MR ratios of over 200% at RT can be easily obtained using MgO-based MTJs. On the other hand, the read head of a high-density HDD requires a very low RA product. MTJs with an amorphous AlO or TiO barrier are currently used in TMR read heads for hard disk drivers (HDDs) with areal recording densities of 100 up to 130

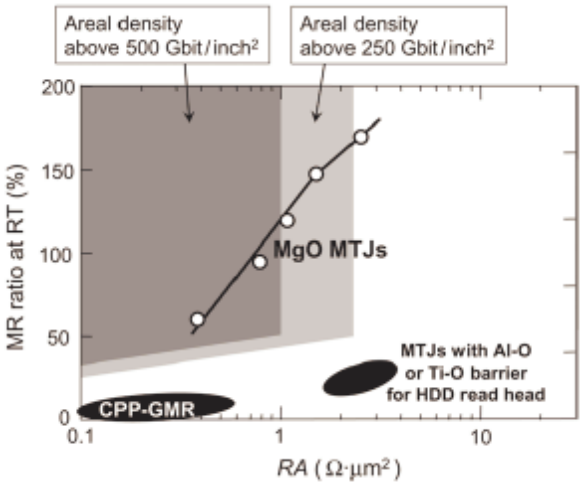

Figure 7.1: TMR ratio at RT versus resistance-area (RA) product. Open circles are values for CoFeB/MgO/CoFeB MTJs. Light grey and dark gray areas are the zones required for HDDs with recording densities above 250 and 500 Gbit/inch^2

Gbit/inch^2. These MTJs have low RA products ($23\Omega m^2$) and TMR ratios of $20-30\%$ at RT. Although these properties are enough for recording densities of $100-130$ Gbit/inch^2, even lower RA products and larger TMR ratios are needed for recording densities above 200 Gbit/inch^2. As example, a RA product below $1\Omega m^2$ for TMR ratios above 50% are required for areal recording densities above 500 Gbit/inch^2 (Figure 7.1). Such low RA products and large TMR ratios have never been obtained in a conventional MTJ with an amorphous AlO or TiO barrier (Figure 7.1). A current perpendicular to plane (CPP) GMR device, which is one of the candidates for the next-generation HDD read head, has an ultra low RA product (below 1 Ωm^2), but the GMR ratio of a CPP GMR device is too low (below 10% for a practical spin-valve structure) for a device used as a HDD read head (Figure 7.1). The MgO based single crystal MTJs opened a new area in the high density data storage technology, leading to new perspectives for large TMR and small RA devices.

The amplitude of the TMR ratio has been gradually enhanced by a better and better understanding and control of the basic transport/ spin filtering physics in single-crystal MgO based MTJ. The figure 7.2 points out the evolution of the TMR ratio measured at room temperature in magnetic tunnel junctions from its discovery in 1995 by Moodera to nowadays. One can observe the enhanced dynamics of this field brought by the single crystal MgO based MTJs. In this diagram, one can observe the place of our laboratory (LPM Nancy). Our single crystal Fe/MgO/Fe MTJ provide about 180% of TMR at room temperature, which is the record value for MTJ using epitaxial Fe and MgO electrodes (similar to the one obtained in AIST). As previously discussed, larger values (depicted in the figure 7.2), have been obtained using CoFeB electrodes.

Beyond of the TMR ratio enhancement in single crystal MTJs, new research directions emerge. Spin transfer switching and spin polarization experiments have been performed in magnetic tunnel junctions with MgO (150% TMR) and AlOx barriers [90, 88]. They explain the 3 to 4

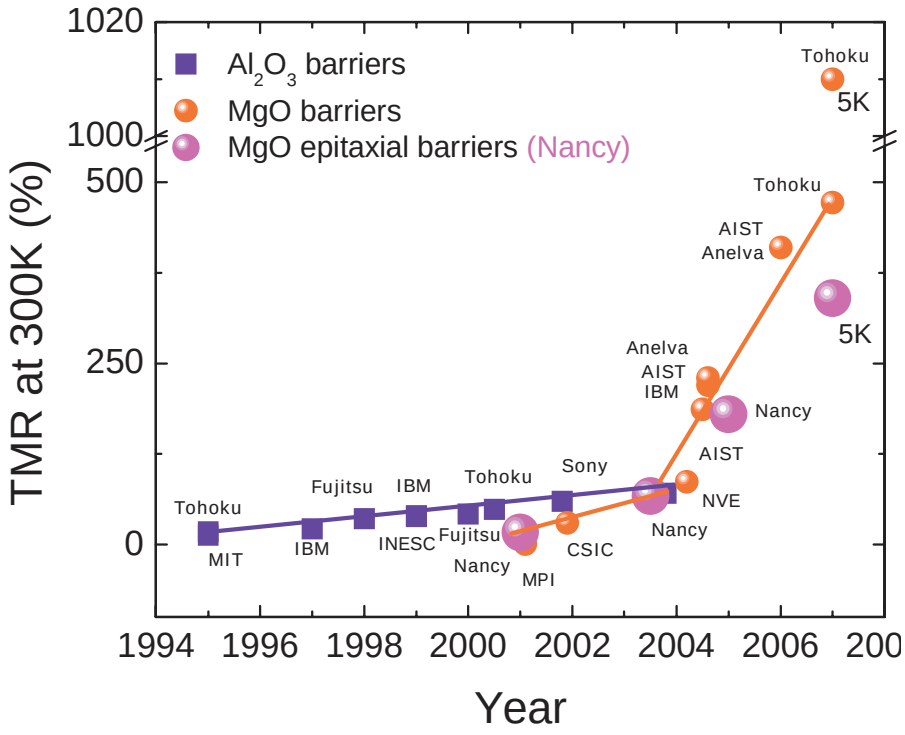

Figure 7.2: TMR ratio history in standard Al-O MTJs and 'new generation' single crystal MgO devices

times lower switching current density ($2-3\ 10^6\ A/cm^2$) for MgO based MTJs by the higher tunneling spin polarization in MgO MTJ. Radio-frequency diode effects have been recently reported [91] in single crystal Fe/MgO MTJs. A small RF current applied to a nanometer- scale MTJ generates a measurable direct-current (d.c.) voltage across the device when the frequency is resonant with the spin oscillations that arise from the spin-torque effect at resonance (which can be tuned by an external magnetic field). One of the last interesting effects reported in epitaxial junctions concerns the quantum oscillation of the tunneling conductance in fully epitaxial double barrier magnetic tunnel junctions, by Nozaki et al [92].

As previously mentioned, low resistance-area product in epitaxial magnetic tunnel junctions is required for integration of MTJ in read-heads or high-density MRAMs and in MTJ-MRAM devices where the magnetization is switched by a critical current by spin-torque mechanisms. However, in standard Fe/MgO/Fe MTJs when the MgO thickness is reduced the filtering efficiency within the MgO is reduced (other symmetries than Δ_1 and $k_{\|} \neq 0$ electrons gradually contribute to the tunneling - see the chapter 1). Recent results [86] report a reduction of TMR from 270 to 138% in 2.4 $\Omega\mu m^2$ low resistive junctions. Despite the progresses recorded during the last few years (especially in CoFeB based MTJs) the domain remain fully opened to the research. Concerning the epitaxial Fe based MTJs, the electronic structure engineering of the Fe/MgO interface remains one of the most promising strategies.

In this chapter we would like to address some fundamental aspects concerning the physics of spin and symmetry filtering in single crystal MTJ. They concern mainly the MTJs elaborated in our laboratory by Molecular Beam Epitaxy. However, one can consider that in textured sputtered samples the basic hypotheses still remain valid. Indeed, if one assume that in the

sputtered samples, one has single crystal grains with well defined (100) texture and possible lateral fluctuations of orientation of axes, each grain can determine a vertical single-crystal MTJ device. Recent in situ scanning tunneling microscopy observations of polycrystalline MgO(001) tunneling barriers grown on amorphous CoFeB electrode demonstrate that, surprisingly, the grain boundaries do not have strong influence on the tunneling properties [87].

In the first part of this HDR report I presented a brief theoretical review pointing out the specific aspects of the electronic transport in single-crystal magnetic tunnel junctions employing bcc(100) Fe electrodes and MgO(100) insulating barrier. These theoretical predictions are confronted here to the experimental reality in both equilibrium and out-of equilibrium regimes. The present chapter is organized as follows. The first section present the experimental results on spin polarized tunneling in Fe/MgO/Fe MTJs elaborated by Molecular Beam Epitaxy. The magneto-transport properties are investigated in two extreme regimes. First, for extremely thin MgO thickness, we show that the equilibrium tunnel transport in Fe/MgO/Fe systems leads to antiferromagnetic interactions mediated by the tunneling of the minority spin interfacial resonance state. Second, for large MgO barrier thickness, the tunnel transport in simple or double tunnel junction devices validates specific spin filtering effects in terms of symmetry of the electronic Bloch function and symmetry-dependent wave function attenuation in the single-crystal barrier. We emphasize the crucial role of the interfaces in the tunneling and on the spin filtering efficiency.

7.2 Sample elaboration

The MTJ multilayer stacks subjected to our studies have been elaborated by Molecular Beam Epitaxy (MBE), in a chamber with a base pressure of 5×10^{-11} Torr. The samples have been grown on (100) MgO substrates, previously annealed at 600°C for 20 min. This annealing stage does not remove completely the carbon impurities from the substrate. In order to trap the C on the substrate, a 10 nm thick seed MgO underlayer can be grown at 450°C on the substrate before the deposition of the 50-nm-thick Fe layer at 100°C. This Fe layer represents the bottom soft magnetic layer of the junction.

To improve its surface quality, the bottom Fe layer was annealed at 450°C for 20 min. The surface RMS roughness after annealing, estimated from Atomic Force Microscope analysis, was about 0.3 nm. However, the Fe top surfaces post-annealing are not equivalent for samples where the diffusion of carbon was not trapped by the MgO underlayer. This is highlighted in Figure 7.3 containing Reflecting High Energy Electron Diffraction (RHEED) patterns. For both sets of samples the RHEED patterns along the [110] direction (not shown here) are identical and they are characteristic of the cubic bcc Fe structure. However, along the [100] direction, the RHEED analysis of sample where the C is not trapped (type A), emphasizes a 2×2 reconstruction-related additional pattern, not present for sample where C is trapped (type B). A complete RHEED analysis concludes that in samples type A, the Fe surface post-annealing presents a $c(2 \times 2)$ superstructure. In agreement with results of previous Auger Electron Spectroscopy and quantitative Low-Energy Electron Diffraction (LEED) studies [96], we associate this reconstruction to the segregation of C at the Fe(001) surface. Using Auger analysis we checked the chemical nature

of the surface and we confirmed that for sample of type A, a carbon layer was segregated during the Fe annealing. Where does the C come from? We observed that the annealing stage of the MgO substrate at 600°C does not desorb all the C atoms from the surface. In case when the anti-diffusion 10nm MgO thick underlayer is not inserted (sample of type A), the residual C atoms diffuse and segregate to the Fe top surface and provide the surface reconstruction during the bottom Fe layer annealing. On the other hand, in the samples type B, the trapping under-layer of MgO provides a C free Fe top surface, post annealing. As it will be shown in the following, the chemical structure of the Fe surface has a strong impact on the magneto-transport characteristics of the junctions, mainly reflected by the TMR versus applied voltage behavior.

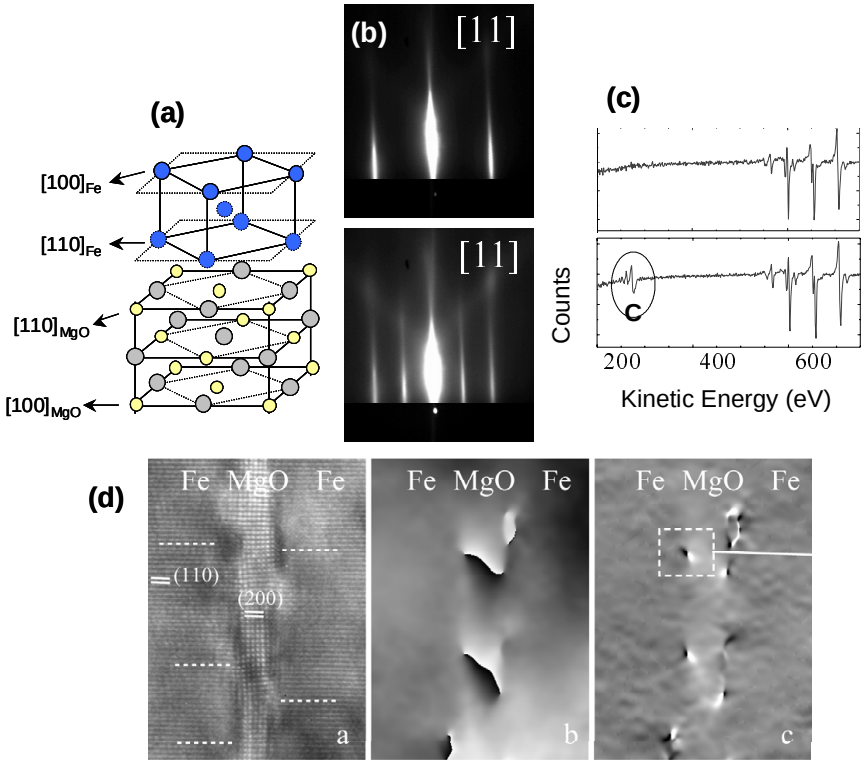

Figure 7.3: a) Schematic representation of the epitaxial growth of Fe on the MgO containing the specific epitaxy relations. The lattice of Fe is rotated by 45° with respect to the one of the MgO. This lets invariants the Δ_1 and Δ_5 symmetries. (b) RHEED patterns for the bottom Fe(100) surface along the [11] direction corresponding to a clean surface (top) and c(2x2) reconstructed surface (bottom). The Auger spectra depicted in (c) validate the absence of carbon impurities for clean samples and the presence of carbon for the reconstructed surfaces. (d) Cross Section High Resolution Transmission Electron Microscopy images for the Fe/MgO/Fe junctions (courtesy E. Snoeck - CEMES Toulouse (France)). One can remark the epitaxial growth of Fe/MgO system, the dark areas pointed by dashed lines indicating mismatch dislocations. The dislocations within the barrier are clearly identified in the phase image of the middle pannel, whereas the dislocations at the two interfaces are clearly depicted in the phase image from the right.

On the top of the bottom Fe layer, the MgO insulating layer was epitaxialy grown by means of an electron gun. A two-dimensional layer-by-layer growth was observed up to 5 monolayers by means of RHEED intensity oscillations [100]. After this critical thickness a plastic relaxation

occurs inducing dislocations within the barrier. These RHEED intensity oscillations have been used to control precisely the thickness of the barrier in the extremely thin thickness range, from 3 to 6 monolayers, used for magnetic coupling studies in equilibrium regime. For the systems used to study the magneto-transport properties out-of-equilibrium, the thickness of the insulating barrier was ranged from 2.5 to 3.0 nm. This thickness range should correspond to the asymptotic regime, where we expect (as predicted theoretically) large magneto-resistive effects.

A second magnetic 10-nm-thick Fe layer was epitaxially grown on the top of the insulating MgO barrier at 100°C. It was subsequently annealed for flattening at 380°C for 10 minutes. In standard single barrier MTJ systems, this top Fe layer is magnetically hardened by a 20nm Co over-layer. In agreement with the RHEED analysis and x-ray diffraction measurements the High Resolution Transmission Electron Spectroscopy experiments indicate a hexagonal compact packed (hcp) lattice for the cobalt layer, its sixfold axis being aligned along either the [100] or the [010] MgO direction. Therefore, two Co variants appear with the following epitaxial relation with respect to Fe: Co(11-20)[001]||Fe(001)[110] and Co(11-20)[0001]||Fe(001)[110].

When double barrier MTJ junction stack are elaborated the top hard Co over-layer is replaced by a second thin MgO barrier and a third Fe top layer. Their structure is then the following: MgO// MgO(10nm)/ Fe_I(50nm)/ MgO(2.5nm)/ Fe_{II}(10nm)/ MgO(0.6nm)/ Fe_{III}(20nm)/ capping. The structural quality of the Fe-II layer is illustrated in the RHEED patterns shown in the middle panel of Figure 7.4. The flatness of this layer is extremely important to insure the continuity of a 3 monolayer thin MgO-II barrier grown on top of the Fe-II. The MgO thickness is precisely monitored using RHEED intensity oscillations. The top Fe_{II}(10nm)/ MgO(0.6nm)/ Fe_{III}(20nm) subsystem behaves here as an artificial antiferromagnetic system. Its magnetic properties are driven by the exchange interactions between the two Fe layer across the barrier, as we will show in the next paragraph.

The MTJ stacks are capped with a Pd(10nm)/Au(10nm) protecting bilayer.

The structural quality of the tunnel junction stack is illustrated by the cross-section transmission electron microscopy picture depicted in Figure 7.3, using a CM30/ST microscope whose point resolution is 0.19 nm. The cross sectional specimens were cut along (100) MgO planes. One can first see the epitaxial growth of MgO on Fe. This is a key parameter for the conservation of symmetry from the Fe electrode through the MgO barrier (conservation of $k_{\|}$) and has a huge impact on the Bloch wave propagation in the stack. However, dislocations located either at the bottom or at the top Fe/MgO interface (indicated in the picture by dark zones pointed by white lines and clearly seen in the phase images) induce violation of symmetry conservation and have negative effects in the symmetry filtering efficiency and may reduce drastically the TMR amplitude.

After the MBE growth, all the MTJ multilayer stacks are patterned by UV lithography and Ar ion etching, step-by-step controlled in situ by Auger spectroscopy.

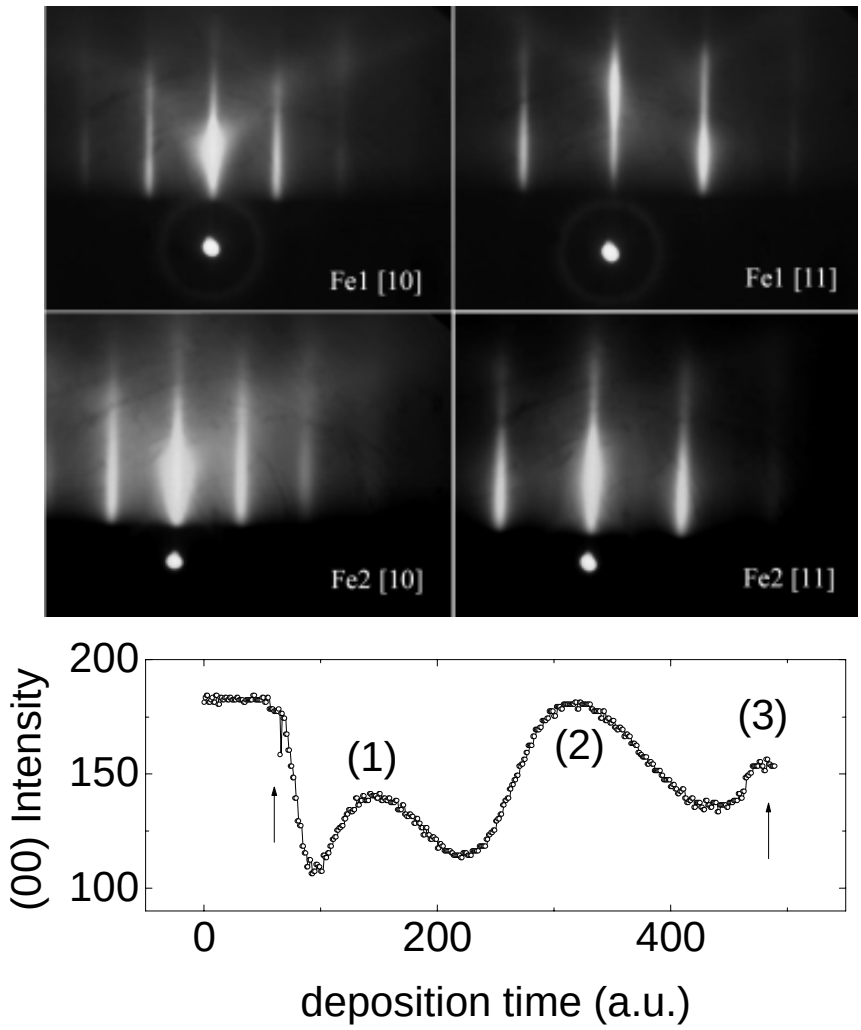

Figure 7.4: *Top panel:* RHEED patterns measured along the [10] and [11] azimuths of the square lattice of the bottom Fe-I. *Middle panel:* RHEED pattern measured along the [10] and [11] azimuths of the square lattice of the middle Fe-II. *Bottom panel:* RHEED oscillations observed on the (00) streak during the thin MgO barrier (of the AAF) grown at room temperature. The maxima denoted from (1) to (3) correspond to the completion of an atomic MgO layer.

7.3 Equilibrium tunnel transport - coupling regime

7.3.1 Non dissipative exchange coupling

In the extremely thin MgO thickness regime (3-5 monolayers), in continuous films (not patterned) we observe antiferromagnetic (AF) coupling interactions at room temperature between the two ferromagnetic (F) Fe layers separated by the thin insulating tunnel barrier. We associate these interactions to the transport of spin information across the insulating spacer by equilibrium quantum tunneling of spin polarized electrons [16]. Equilibrium tunneling implicates tunneling of majority and minority electrons from one side to the other of the junction. In the absence of any net bias, the total current across the insulating MgO barrier is zero.

The magnetic properties have been investigated from magnetization versus field loops, performed on continuous multilayer films of standard Fe/MgO/Fe/Co systems with lateral sizes above a few millimeters, in order to avoid spurious antiferromagnetic dipolar coupling, introduced by patterning of small size devices. This analysis has been already presented in detail in our paper concerning the interlayer coupling by spin polarized tunneling [16]. We only report here the main results. The interlayer magnetic coupling strength J is extracted from the shift of the minor hysteresis loops (Figure 7.5(a)), taken for the soft magnetic layer in a field window where the hard layer is magnetically 'locked' by an initial magnetization saturation. In Figure 7.5(b), we illustrate the variation of J with the thickness t_{MgO} of the insulating barrier. We notice that the AF coupling interactions have been observed in all types of junctions with and without carbon impurities at the interface Fe/MgO.

In a first step, the experimental points can be adjusted by the continuous line (Figure 7.5(b)) which represents the theoretical coupling strength computed in the simplified free-electron-like framework of Slonczewski [2]. More details about the coupling/spin torque phenomena can be found in the appendix E. The theoretical curve implicates effective parameters for the electronic transport, specific to the ferromagnetic Fe electrodes and the MgO insulator. Our experimental results are in good agreement with the predictions of Slonczewski (see the paragraph about theoretical introduction), where the equilibrium tunneling leads to non disipative exchange interaction (magnetic coupling). We explain the change of sign of the coupling (ferromagnetic coupling by the 'Orange Peel interactions) associated to the correlated roughness of the interfaces. The fluctuation length of the roughness (>10 nm) is determined by high resolution transmission electron microscopy and Atomic Force Microscopy. This leads to a basically constant orange peel coupling of 0.04 erg/cm^2 in the thickness range involved in our study.

The free-electron like model of Slonczewski does not take into account the specific aspects of the spin polarized tunneling in epitaxial systems i.e. the equilibrium propagation of different symmetry states for each spin channel, in each configuration of magnetizations: (i) in the parallel (P) configuration the $\Delta_{1,5,2'}$ states for the majority spin and $\Delta_{5,2,2'}$ states for the minority; (ii) in the anti-parallel configuration $\Delta_{5,2'}$ state for the majority and for the minority spin.

Moreover, recently Tsymbal et al [95] pointed out theoretically the implication of a resonance assisted tunneling mechanism in the AF coupling by spin polarized tunneling. In their model, they have shown that an additional resonant tunneling mechanism should exist in order to explain the sign of the coupling observed in our Fe/MgO/Fe junctions. Similar results concerning

the AF coupling by spin polarized tunneling have been recently reported by S. Yuasa et al [94]. In epitaxial Fe/MgO/Fe systems, if we neglect any impurity-associated resonant levels, the interfacial minority resonance of Fe(001) provides the resonant equilibrium tunneling mechanism, as shown in the ab-initio calculations of Dederichs et al [13]. Therefore, one can assume that the equilibrium tunnel transport in the anti-parralel configuration is dominated by the propagation of the interfacial resonance (related to the surface state of Fe(001)). By Scanning Tunneling Microscopy (STM) experiments performed on our Fe(100) samples we clearly specroscopically identified the Fe surface state. It has a d_{z^2} orbital character [93] belonging to the Δ_1 symmetry and is located in the minority spin channel. Moreover, our STM experiments show that the surface state of Fe is stable with respect to low-level disorder (it is not destroyed by terrace boundaries, carbon and oxygen contamination). One can imagine that some low-level disorder may even help for coupling of the surface state with the bulk bands (by elastic scattering changing the k), enhancing its contribution to the transport.

Theoretical calculations [10, 12] have shown that the interfacial resonance of Fe is preserved at the Fe(100)/MgO interface. Therefore, in a second step, we could assume that the resonant propagation of the interfacial resonance could be the main origin for the AF coupling observed in our Fe/MgO/Fe junctions. If we follow the ab-initio analysis of tunneling in epitaxial MTJ [10, 12], we see that the conductivity related to the propagation of the interfacial resonance manifests as sharp peaks located at specific values of $k_{\|}$. The contribution to the conduction of the surface state becomes significant when it lies within a bulk band becoming an interfacial resonance state (IRS).

In the thin MgO thickness regime, the carbon impurities at the Fe/MgO interface play no significant role in the tunneling. From magnetization curve measurements, describing the equilibrium (zero bias) transport properties, no significant effect of the C on the antiferromagnetic interactions has been observed (similar behavior of samples type A and B). If we consider the complex tunneling landscape in this regime, one can see that the C-Fe bonding does not affect the d_{z^2}-like resonance state of Fe, whose propagation dominates the equilibrium tunneling currents.

Moreover, recent results provided by noise measurements performed on our samples[1] illustrate that the $1/f$ noise is extremely small. These preliminary results show no clear signature of the oxygen vacancy or structural effects in the tunneling. They furthermore validate the high quality of the insulating barrier. However, these experiments have been performed on systems with large MgO barrier thickness (3 nm) beyond of the thickness range interesting for the coupling. Following the theoretical explanation of Tsymbal et al, other experimental studies are in progress in order to investigate the possible role of oxygen vacancies or other punctual defects within the barrier on the antiferromagnetic coupling. If the sign of the coupling would be determined by the contribution to the tunneling of vacancies/impurities one has to investigate the evolution of these effects as a function of the MgO thickness. Then, a possible explanation for the sign change of the coupling would be related to these aspects. However, it is important to notice that in our samples the change of sign for the coupling corresponds with the end of the pseudomorphical growth regime of MgO on Fe (critical thickness about 1 nm). It means that below 1 nm the growth is bi-dimensional layer by layer (as confirmed by the RHEED intensity oscillations). This

[1] within the collaboration with Prof. F. Aliev, University of Madrid

corresponds to atomically flat layers, where we can neglect the Orange Peel coupling. Above 1 nm, a plastic relaxation occurs and the roughness starts to increase during the growth (as confirmed by RHEED and atomic force microscopy). The estimated positive ferromagnetic 'Orange Peel' coupling (using experimental AFM data), corresponds to the coupling measured in the magnetization curves.

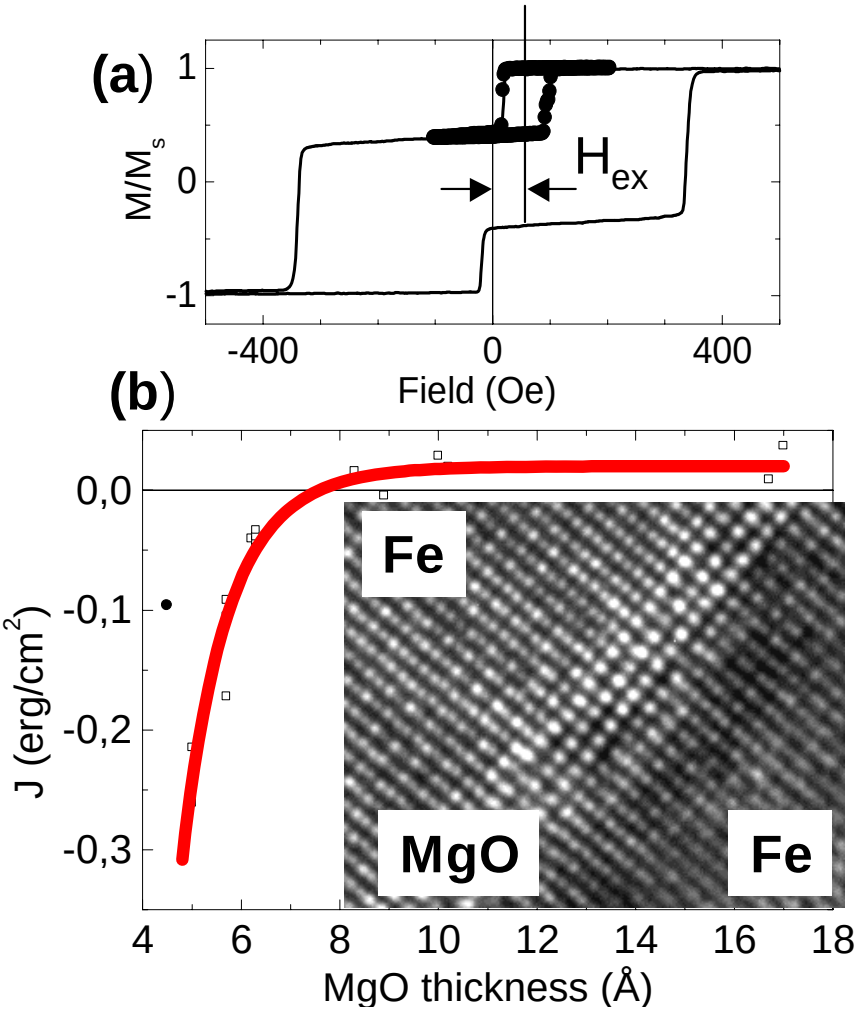

Figure 7.5: (a)Magnetization versus field curve for a Fe/MgO/Fe/Co system. The minor loop (-•-) represents the magnetization reversal of the bottom Fe layer, the top Fe/Co bilayer remaining locked along the positive field direction. From the positive shift of the minor loop H_{ex} we deduce the coupling strength J: $H_{ex} = J/(t_{Fe}Ms)$, where t_{Fe} is the thickness of the Fe bottom layer and Ms the saturation magnetization of Fe. **(b)** Variation of the coupling strength with the MgO thickness. The open square points represent experimental values and the continuous line a theoretical calculations within the Slonczewski model of coupling by spin-polarized tunneling. *Inset*: Cross section TEM picture illustrating the pseudomorphical epitaxial growth of MgO on Fe in the low thickness regime involved in magnetic studies for coupling by tunneling.

The physics of the equilibrium tunneling presented above looks complex, due to the implication in the coupling of Bloch states with different symmetry, and also of the interfacial resonance

of the Fe. Moreover, in the low thickness regime one has to take into account the significant contribution to the tunneling of electrons with $k_{\parallel} \neq 0$. These aspects would require a multi-channel tunneling model, each tunneling channel being associated to a specific symmetry or resonance state. A possible 'conciliation' with the simplified single-channel model of Slonczewski could be done, if one consider that the parameters used within this model are effective, and include the complex aspects of multi-channel tunneling landscape, mentioned upwards.
Recent calculations performed in the group of E. Tsymbal, either using the free-electron model or ab-initio techniques, show that the AF coupling could be explained by resonant tunnel transport mechanisms. We argue here that the resonant transport mechanism is provided by the minority spin interfacial resonance of Fe(001). However, the other resonant mechanisms cannot be excluded. They can be related to imperfections of the barrier (oxygen vacancies, impurities, structural defects, etc.). Up to now, the experimental spectroscopic studies performed on our samples to check the stoecheometry of the MgO barrier did dot provide clear evidence of oxygen vacancies or other impurities. Moreover, in the low thickness regime the growth of the barrier is pseudomorphic (layer by layer) on Fe, no dislocations being present within the insulator. However, other studies based on noise measurements are in progress to provide more insight on the complexity of the resonant transport mechanisms in our systems.

7.3.2 Artificial antiferromagnetic systems using spin polarized tunneling

Using the AF coupling by spin polarized tunneling we build artificial antiferromagnetic systems (AAF). These systems, are similar to the standard AAF [97] employing ferromagnetic layers separated by metallic nonmagnetic (NM) spacers where the coupling is provided by RKKY interactions. In standard AAFs the oscillations of the coupling strength with the NM spacer thickness may be explained by quantum interference effects of the propagative plane wave wave function in the NM spacer [19]. When an insulating spacer is involved, the non-oscillatory monotonous decay of the coupling strength with the spacer thickness reflects the evanescent character of the wave function within the barrier. The strength of the coupling and therefore the magnetic properties of the AAF can be experimentally adjusted by playing with the thickness of the MgO barrier. Typically, for a barrier thickness of 0.6nm a coupling strength of -0.2 erg/cm^3 is measured.
The magnetic properties of the AAF can be analytically explained using a Stoner-Wolfhart like model, presented in detail in the Appendix A. In order to simulate the magnetization versus field for an AAF one can perform the minimization of the total energy numerically (i.e. by steepest-descent, conjugated gradient, or Metropolis/Monte Carlo algorithms). Such kind of simulation, for the situation when the field is applied along one of the easy axes of the bcc Fe(001) is presented in Figure 7.6(a). If the field is larger than the saturation field H_S, the two magnetic layers of the AAF have the magnetization aligned along the field. When $H < H_S$ the magnetization of the thin layer starts to rotate dragged by the AF coupling which tends to reverse it in the antiparallel configuration to reduce the coupling energy. The complete reversal occurs for $H = H_P$. However, one can see during this reversal an intermediate plateau where the magnetization which reverses will remain trapped in a second anisotropy well corresponding to the second anisotropy axis for an angle $\theta_2 = \pi/2$. During the reversal of the thin layer from

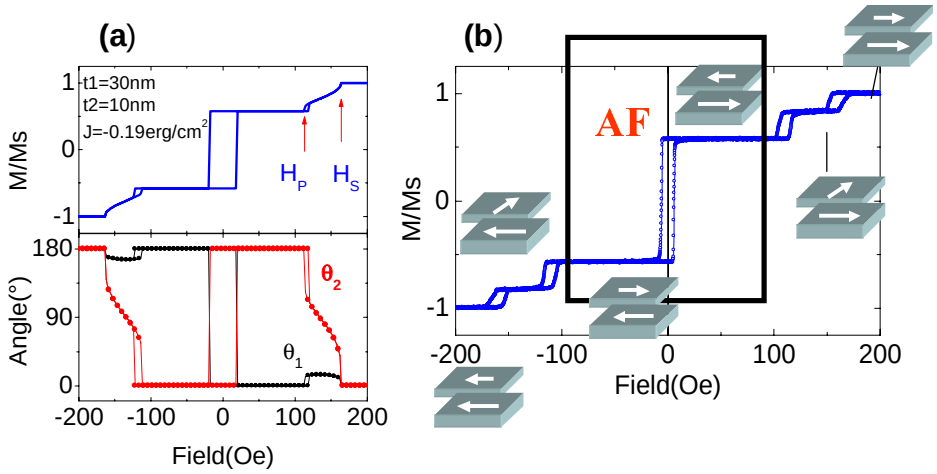

Figure 7.6: (a) Theoretical magnetization M-H curve along the Fe(100) easy axis calculated within a Stoner- Wolfhart macrospin model, using a numerical steepest-descent minimization procedure. The total magnetization is calculated by the equation $M(H) = (t_1 cos(\theta_1) + t_2 cos(\theta_2))/(t_1 + t_2)$. The field variation of the angles between and the magnetization and the external field ($\theta_1(H)$ and $\theta_2(H)$) is illustrated in the bottom panel. The parameters used for the calculation are: t_1 = 30 nm, t_2 = 10 nm and J= -0.19 erg/cm^3 (b) Experimental magnetization curve corresponding to a Fe(30nm)/MgO(0.6nm)/Fe(10nm), in good agreement to the theoretical simulation. We pointed out the magnetization configuration in the most important field windows. In the antiferromagnetic plateau, the systems behaves as a compact bloc of reduced magnetic moment ($M_1 - M_2$).

$\theta_2 = 0$ to π, the magnetization of the thick layer is only slightly deflected from the field direction, then in the AF plateau $\theta_1 \to 0$. The θ_i, $i = 1, 2$ represent the angles between the magnetization M_i and the field H. In the field window $-H_P < H < H_P$ the AAF behaves as a magnetically rigid mono-block with reduced magnetic moment $M_1 - M_2$.

The theoretical simulation is in perfect agreement with the experimental results presented in Figure 7.6(b). Here one can identify the different magnetic configurations from positive to negative saturation. The values of the plateau and the saturation field can be adjusted by playing with the thickness of the insulating barrier (which modulates exponentially the J) and with the thickness of the magnetic layers (affects the anisotropy and the Zeeman energies). In the last part of this section we will see that this special kind of AAF system can be successfully used as a brick to build double barrier MTJ systems. With respect to standard AAF employing metallic polycrystalline layers [98] the AAF with epitaxial layers can have specific advantages. The anisotropy of single crystal layers reduces the magnetic fluctuations (magnetic ripples or 360° domain walls structure). These fluctuations are responsible on parasitic magnetostatic interactions [99] and have negative effects on the magneto-transport characteristic of the MTJs. We also mention that this specific AAF which incorporates extremely thin oxide spacer layer, could be particularly interesting as a brick in spin valve metallic giant magnetoresistive devices. Indeed, the nano-oxide layer can enhance drastically the specular reflexions and confine the electrons in the active part of the device and therefore enhance the magnetoresistive effects.

7.4 Out-of-equilibrium tunnel transport regime

In the asymptotic regime, at large MgO thickness, the symmetry-dependent rate decay in the barrier reduces the number of the propagating Bloch states. The filtering effect in k of the MgO barrier [10] determines a strong reduction of conductivity for electrons with $k_{\|} \neq 0$ when the thickness of MgO increases. This is assisted by the vanishing of the equilibrium tunneling via the interfacial resonances, located at E_F for significantly large $k_{\|} \neq 0$, (Figure 1.4). However, if we follow the left panel of Figure 7.6, we see that the surface state of Fe may be 're-activated' by biasing the junction. Indeed, the interfacial resonance may assist the propagation of hot electrons with $E = E_F + eV$ around $k_{\|} = 0$. From the surface band diagram depicted in Figure 7.6 one one cans see that above E_F the surface state disperses toward $\bar{\Gamma}$ and at $k_{\|} = 0$ it behaves as interfacial resonance. Its coupling to the bulk allows a significant contribution to the conductivity.

However, it is important to mention that for large thickness, the structural quality of the MgO layer is slightly reduced. Indeed, after a pseudomorphical growth of MgO on Fe up to about 5 monolayers, the strains induce a plastic relaxation (see the Figure 7.3(d)). This will determine dislocations within the barrier. Moreover, we have to mention also the misfit dislocations at the bottom and top Fe/MgO interfaces due to the relaxation of thick Fe layers (electrodes) grown on MgO. All these local 'defects' determine a local symmetry breaking (the conservation of $k_{\|}$ is locally destroyed). Therefore, they are responsible on scattering events with negative re-mixing effects on the symmetry filtering. One can associate to each local defect a 'parasitic' conduction channel. This experimental reality draws aside the real transport mechanisms from

the theoretical framework of analysis valid for perfect mono- crystalline stacks where the $k_{\|}$ is fully conserved.
The analysis of the large MgO thickness regime is performed using magneto-transport measurements (non-equilibrium transport) on patterned tunnel junctions, with lateral size between 10-200μm.

7.4.1 MTJ with clean Fe/MgO interfaces

Lets us first consider the TMR(V) characteristics illustrated in Figure 7.7, measured on sample with carbon free Fe/MgO interface. In agreement with theoretical predictions [10, 12], the TMR ratio is large (around 180% at room temperature), as illustrated by Figure 7.7(a). For the thickness range of the barrier (here 2.5nm), the tunneling is expected to be dominated by the propagation of Δ_1 (and Δ_5) state the parallel (P) configuration and only the Δ_5 in the antiparallel (AP) configuration. The other symmetries should be completely attenuated in this thicknees regime.
Furthermore, the TMR ratio varies significantly with the voltage (Figure 7.7(b)), especially in the low voltage range. The slightly asymmetric bias-dependence can be explained by the asymmetric top and bottom Fe/MgO interfaces in terms of roughness, structural defects (dislocations) and the lattice distortions (the electronic structure of the top and bottom interfacial Fe may be slightly different due to difference in the lattice parameter). The limited maximum value of the TMR with respect to theoretical predictions implicates a reduction of the filtering efficiency possibly due to the structural imperfections and parasitic conductivity channels enumerated above, over our large area junctions[2].
In order to get more details on the conductivity channels which contribute to the transport we analyze the experimental conductance versus voltage illustrated in the top panel of Figure 7.8(a), associated to the parallel and the anti-parallel magnetization configurations. In all the figures presented below the conductance is defined as $G = I/V$. From the conductivity in the P configuration (see the zoom of Figure 7.8(a)) one identify at low voltage the contribution of two conductivity channels: the Δ_1 and the Δ_5. Indeed, from the band diagram depicted in Figure 7.8(b) one can see that the top of the Δ_5 band lies at about 0.2eV above E_F. It means that at low voltage (below 0.2V) this state may contribute to the transport. An injected Δ_5 state from the E_F of the right electrode finds an equivalent unoccupied state on the other side. The conductivity of the Δ_5 channel is added to the conductivity of the Δ_1, as is schematically represented in Figure 7.8(b). Indeed, at low voltage the contribution of Δ_5 enhances the parabolic conductivity associated to the Δ_1 state. This will lead to a total conductivity which presents two minima, around 0.2V. The contribution of the Δ_5 state in the parallel configuration implicates a reduction of the TMR. Indeed, in the AP configuration where the propagation of the Δ_1 state is forbidden, the ratio of filtering of Δ_5 state will determine the amplitude of the AP conductivity and therefore the conductivity contrast between P and AP configuration. Before to get dipper in

[2]Recent studies point out that some other mechanisms can be responsible on the reduction of filtering efficiency. They are related to the specific crystalline structure of the Co overrlayer used to harden the top Fe electrode. This Co layer is *hcp* with in-plane *c* axis and therefore there is a symmetry mismatch between the cubic Fe and the hexagonal Co for electrons (spins) whose coherence length is larger then the thickness of the top Fe. This will determine additional shunt channels in the small conductivity AP configuration, ad decrease the TMR effect.

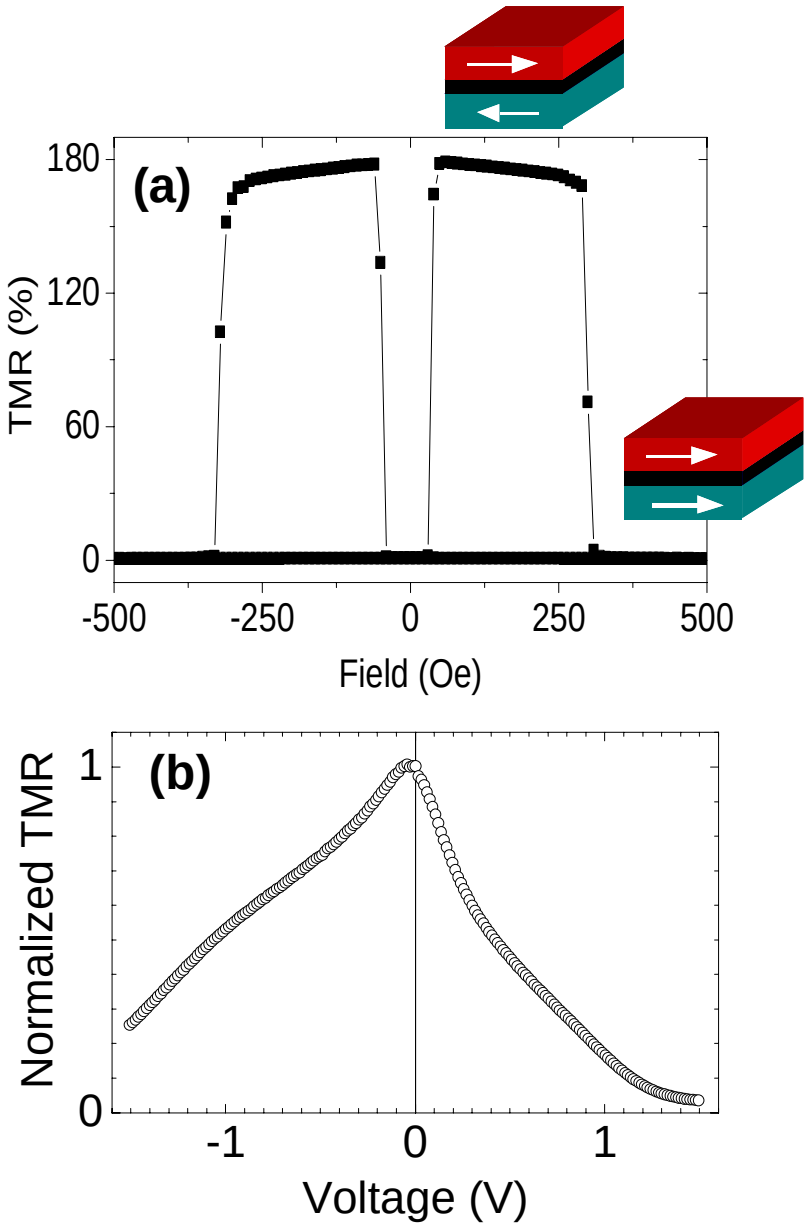

Figure 7.7: (a) Typical Tunnel Magneto-resistance curve for Fe(40nm)/ MgO(2.5nm)/ Fe(10nm)/ Co(20nm) MTJ measured for a 20 μm square junction. The area-resistance of the junctions for this MgO thickness is within the 10^6 $\Omega\mu m^2$ range. One can identify the two states of resistance corresponding to the parallel and antiparallel magnetization configuration. (b) Variation of the magnetization with respect to the bias voltage. In positive bias, the current flows from the top to the bottom electrode of the MTJ. The curve looks slightly asymmetric in positive and negative voltage.

the conductivity mechanisms in the AP configuration we would like to analyze the tunneling transport in MTJ systems where the bottom Fe/MgO interface is chemically modified. We will show that the chemical bonding at the interface plays in tunnel junctions a crucial role in the selection of tunneling electrons [102].

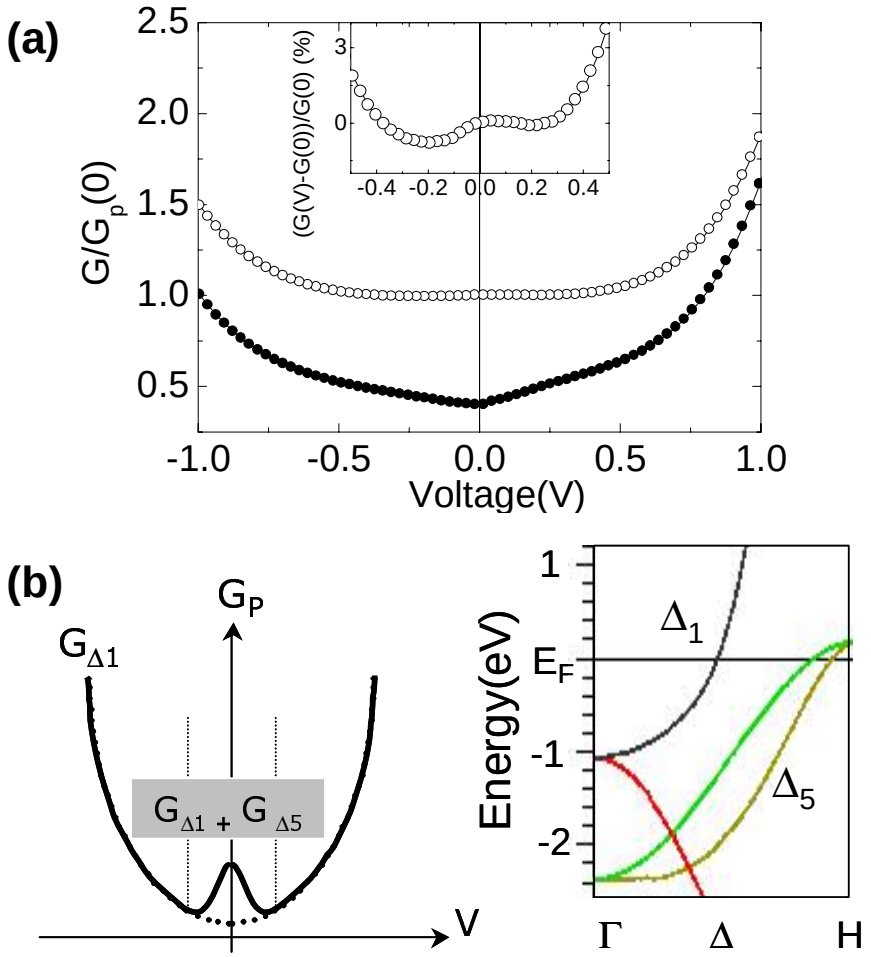

Figure 7.8: (a) Conductivity versus voltage curve, in the parallel (-○-) respectively anti-parallel (-●-) configuration of magnetization. *Zoom:* Relative variation of parallel conductivity in the small positive voltage regime, around the two local minima. (b) Schematic model used to explain the two local minima. Based on the multi-channel model of tunneling, they result from the superposition of a parabolic G(V) associated to the Δ_1 state conductivity channel and the Δ_5 channel available only at voltages < 0.2 eV, as clearly understood from the zoom on the majority spin band structure diagram of bulk bcc Fe. From the band diagram one can observe the top of the Δ_5 band lying at 0.2 eV above the Fermi level.

7.4.2 MTJ with carbon contaminated bottom interface

We remember that, by the growth technique we can elaborate Fe/MgO/Fe MTJs with C impurities at the bottom Fe/MgO interface (as illustrated by the RHEED images from Figure 7.8(b)). The TMR versus voltage characteristic measured on these samples appears strongly asymmetric (see the Figure 7.9(a)) with a maximum of TMR of 126% at room temperature. We explain this strong asymmetry by the enhancement of the contribution to the tunneling of the interfacial resonance of Fe [76, 14]. However, the interfacial carbon and the c(2x2) reconstruction should have a significant contribution to this enhancement. Normally, as seen in clean samples (Figure 7.9), the conductivity in the AP configuration remains always smaller than the parallel one, mainly related to the Δ_1 conduction channel.

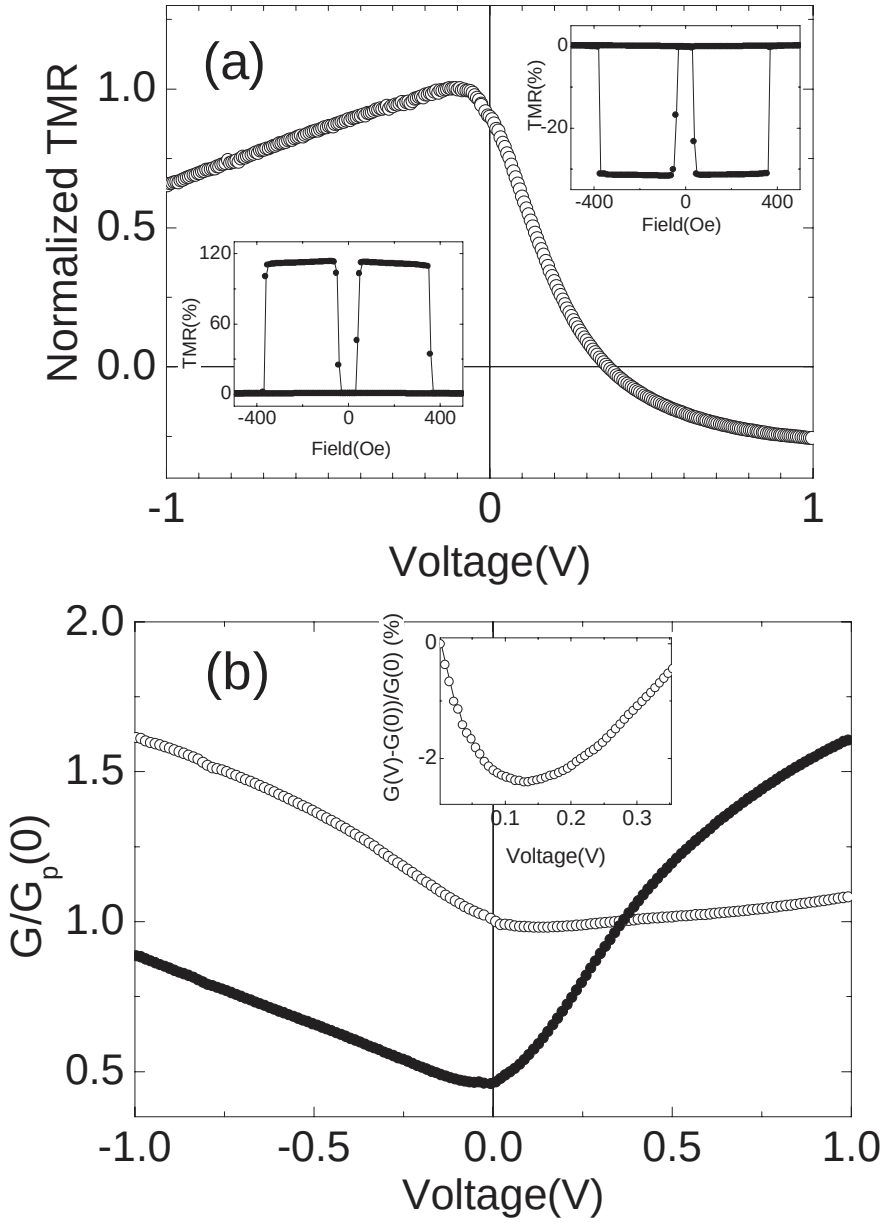

Figure 7.9: (a) Asymmetric magnetotransport TMR versus voltage for sample with carbon at the bottom Fe/MgO interface. In positive bias, the current flows from the top to the bottom electrode of the MTJ. *Bottom Inset*: Typical positive TMR-H loop measured -10mV, *Top Inset*: negative TMR-H curve measured at +0.6V, after the TMR sign reversal. (b) Conductivity versus voltage curve, in the parallel (-○-) respectively anti-parallel (-●-) configuration of magnetization. *Zoom:* Relative variation of parallel conductivity in the small positive voltage regime, around the local minima.

Theoretical studies are in progress to explain the effect of the interfacial carbon. However, few preliminary ideas can be already advanced. The bonding between C and Fe, (mainly via s, p-like orbitals) affects mainly the propagation of the Δ_1 symmetry, without affecting the interfacial resonance of Fe, located in a d_{z^2}-like orbital. Preliminary ab-initio calculations [103] of Fe-C/MgO electronic structure show that the main effect of C on the surface state of Fe is a slight shift upwards in energy, with respect to the carbon free interface[3]. Similar effects, concerning the localization of Δ_1 electrons in the interfacial bonding, have been reported by Butler et al, for oxygen impurities located at the interface Fe/MgO [105]. Moreover, as long as the associated-conductivity of the *sp*-like character state Δ_1 channel is reduced, one can expect an enhancement of the relative contribution to the tunneling of the *d*-like states of the bcc Fe(001) (within $\Delta_{1,5}$ symmetries). Therefore, the TMR(V) will be more sensitive to the spectroscopy of the density of *d*-like states of the bcc Fe(001). Moreover, one can also imagine that the periodical perturbation of the potential at the interface may determine scattering events (change in k), enhancing the contribution to the transport of the Fe minority interfacial resonance. This would lead to an increase of the conductivity in the AP configuration which can even overcome the P conductivity. This is reflected by the negative TMR ratio measured above few hundreds millivolts in positive voltage. Indeed, in positive voltage the electrons extracted from the top Fe(001) electrode tunnel across the barrier and 'scan' in energy the bottom 'flat' Fe(001) electronic structure. When the IRS is activated a strong enhancement of the antiparallel conductivity with respect to the parallel one occurs, via the enhancement of the wave function matching at the interface. This is directly reflected by the sign reversal of the TMR (Figure 7.9(a)) and by the antiparallel conductance which overcomes the parallel one (Figure 7.9(b)).

Here again, the P conductivity presents a minimum when the energy of the hot electrons overcomes the one of the Δ_5 band. The inset of Figure 7.9(b) illustrates a variation of the P conductivity of more than 2% between zero and the local minimum. Compared with the variation observed in samples with clean interfaces, one can observe that here the contribution of the Δ_5 electrons to the tunneling is more important. The reduction of the Δ_1 related conductivity by interfacial bondings between C and Fe explains also the reduction of the TMR ratio with respect to samples with clean interfaces (from 180 to below 130%).

7.4.3 Transport mechanisms

Tunnel spectroscopy analysis for both type of junctions with clean or carbon contaminated interfaces illustrate common features in the anti-parallel configuration. Indeed, from Figure 7.10 one can see that peaks in the second derivative of the current occur in both positive and negative voltage for both type of samples. These features determine the strong variation of the TMR with bias at low voltage. However, for samples with carbon the peak in positive voltage is significantly enhanced. This reflects the reversal of the TMR sign in positive voltage and the fact that G_{AP} become larger than G_P.

[3]We calculated the electronic structure of the Fe/Fe-C/MgO/Fe stack using the Full Potential-Linear Augmented Plane Wave (FP-LAPW) Wien2k code [104]. In our calculation, we used a supercell consisting of 10 Fe layers, sandwiched in-between 6 MgO layers. In order to describe the Fe-C/MgO interface a monolayer of C has been alternatively considered at 0.4Å above the interfacial Fe.

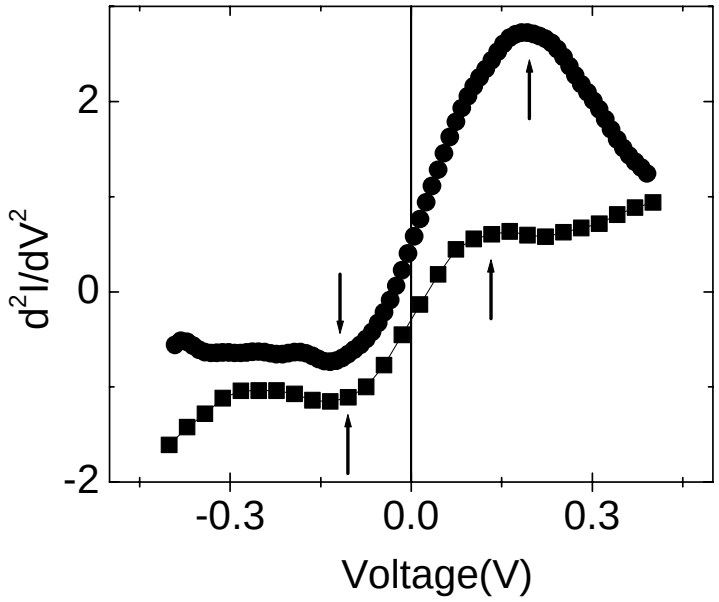

Figure 7.10: Second derivative of the current with respect to the voltage measured in the antiparallel configuration of magnetizations for MTJ with clean interfaces (black filled square) and carbon contaminated bottom Fe/MgO interface (-•-). The arrows indicated the local peaks in the second derivative.

Several mechanism may explain the voltage variation of the tunnel magneto-resistance. These mechanisms are: (i) incoherent tunneling due to scattering at impurities or defects located in the barrier [107]; (ii) quenching of TMR by hot electrons or spin excitation of magnons [109]. (iii) energy dependence of spin polarized DOS which affects the spin polarization [108]. In our single-crystalline MTJ, the 1st mechanism should be less important than in standard MTJ with poly-crystalline electrodes and amorphous barriers. In single crystal junctions, the quality of the insulating is rigorously controlled by the 2D epitaxial growth. However, the dislocations within the insulating barrier and at the interfaces will induce imperfect filtering effects and will complicate the analysis of tunneling in terms of symmetry/orbital character related channels. Concerning the 2nd mechanism, the analysis of the magnon spectra for the bcc Fe [110], and phonon spectra for MgO [111] shows no relevant peak in the magnon/phonon DOS, in the energy range where we analyze the voltage variation of the TMR. Therefore, we relate the observed TMR(V) in our junctions to the 3rd mechanism, which points out the signature of the electronic structure in the tunnel transport characteristics. This signature is different for samples with clean or carbon contaminated interfaces which, despite a similar bottom Fe electrode, have different bottom interface. If we take into account the IRS located in the minority band, with a d_{z^2} orbital character belonging to the Δ_1 symmetry, one can expect a resonant tunneling event when this IRS gets activated. This would explain an enhancement of the AP conductance via a resonant assisted mechanism, directly related to the interfacial resonance of the Fe(001). The contribution of the IRS to the tunneling is strongly enhanced by the carbon presence at the bottom interface which drives the conductance more sensitive to *d*-like electrons whose orbital character the IRS belongs.

In our explanation for the 'zero bias anomaly' observed in epitaxial Fe/MgO/Fe junctions, we excluded the implication of magnons. This, was done only based on theoretical calculations for magnon spectra, which show no peak in the magnon DOS in the relevant energy range. However, a complete proof for a dominant interfacial electronic structure origin of the zero-bias anomaly should be provided by further experiments concerning transport properties at low temperature, below the freezing temperatures of magnons in Fe. Moreover, our experimental results motivate further theoretical investigations which should confirm or invalidate the resonant transport mechanisms we propose here.

Studies are also in progress concerning the possible influence of the interfacial carbon on symmetry remixing effects (the cubic symmetry is locally broken at the interface) or symmetry change by diffusion on localized potential perturbation associated with the periodical interfacial superstructure. These could have significant effects on the conductance channels available for the transport. Indeed, the c(2x2) ordered superstructure of carbon at the Fe/MgO interface can be modeled by a localized perturbation in the potential profile seen by a propagating electrons. This additional potential will induce scattering events. Elastic scattering, combined with a certain disorder in carbon arrangement in realistic junctions, will determine a dispersion of k in the final state with corresponding increase of the available conductance channels. This is in agreement with the experimentally observed enhancement of the total conductance of the junction in systems with carbon contaminated interfaces. Moreover, (following the surface dispersion band schematically presented in figure 1.4) the dispersion in k for the final state can strongly enhance the contribution of the surface state to the tunneling. Indeed, the scattering enlarges the distribution of available k and enhance the coupling between the bulk and the interface (the scattering-induced change of k leads to states coupled to the bulk). Theoretical studies are in progress to validate these hypotheses.

Another interesting insight is provided by analysis of the variation of the resistance with the temperature in the parallel and the antiparallel configurations. This is illustrated in Figure 7.11. One can see that this variation is almost four time larger in the AP configuration then in the P one. This can be easily understood if one remember that in the AP configuration, for large MgO barrier thickness we expect a very low conductance regime. For perfect filtering, the conductance should be ideally almost zero, in our samples we showed that the AP conductance contains at least the Δ_5 state contribution.

Then, all the mechanisms which could provide additional transport channels when the temperature increases will have a major impact on the total conductance. We mention here few of them: the spin flip events which could allow the propagation of the Δ_1 state, the elastic/inelastic diffusion on phonons or local potential perturbations which may change the k and/or the energy and open a conduction channel forbidden at $k_{\|} = 0$. Moreover, the direct dependence of the conductance on the electronic structure features in single-crystal MTJ may implicate strong variations with the temperature if sharp feature appears in the DOS within the KT window (this is the case for the minority spin where the surface state provides a sharp peak above the E_F).

In the P configuration, the conductance is large, being dominated by the propagation of the Δ_1 channel which overwhelms any thermal activated conduction channels. This explain the smaller

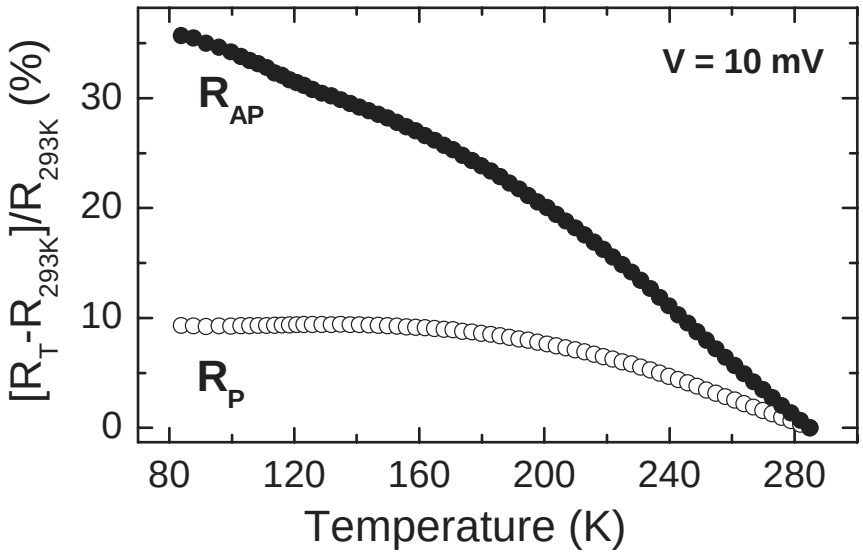

Figure 7.11: Typical relative variation of the junction resistance with the temperature, in the parallel (-○-) and the antiparalel (-●-) configuration of magnetization.

variation with temperature of the P conductance, measured in our samples.

7.4.4 Statistical aspects concerning the spin polarized tunneling in epitaxial MTJs

In a real junctions one can imagine fluctuations of the properties of the MTJ which will give rise to a specific statistical distribution of the tunnel currents over the surface of the junction. One of the most frequent fluctuation, already studied theoretically [112] and experimentally is the roughness related fluctuation in the barrier width or fluctuation related to the barrier height [61]. If one assume a Gaussian distribution of the barrier width (height), the statistical distribution of the tunnel currents will be log-normal: the broader is the Gaussian distribution, the broader is the log-normal distribution of tunnel currents. Interesting scaling effects can occur [112] when vary the size of the junction. From application point of view, if one wants to reduce the size dependence of the MTJ magneto-transport properties, one has to approach as close as possible a narrow Gaussian distribution for the tunnel currents. Experimentally, using conductive Atomic Force Microscopy experiments one can measure directly the tunnel barrier maps, extract the statistical distribution of the tunnel currents. The main purpose is to find the experimental elaboration conditions for the tunnel barriers (get homogeneous oxides, eliminate the current hot-spots) which reduce the width of the current distribution [61].
If we transpose now these concepts to single crystal systems, the situations becomes more complex. First, we can eliminate the large fluctuations of thickness, having in view the epitaxial control of the growth. However, even if one gets atomic layer roughness, the filtering effect in terms of symmetry will be extremely sensitive to any local defect related to symmetry breaking. We could mention here such kind of defects: terraces, the misfit dislocations at interfaces and in the MgO barrier. Each defect will lead to a local higher conductance conduction channel

being equivalent to a hot-spot in the classical approach. One has also to consider the fluctuation of the local electronic structure related to the specific local defect, having in view the extreme sensitivity of the magneto-transport to the electronic structure in the epitaxial MTJ.
Concerning the scaling, with respect to the micrometric size of our junctions, the effect of this kind of defect will be different. The period of dislocations is around one nanometer, therefore one consider that their effect is well averaged statistically and we have a good Gaussian distribution for junctions of micrometric size. This will provide a good scaling of the MTJ transport properties with respect to the size of the MTJ. The situation is completely different concerning the terraces whose size is several hundreds of nanometers. The statistical average effects over micrometric size surfaces is more drawn aside from a Gaussian and then one can expect large fluctuations of MTJ properties when the size of the junction varies.
The effect of the fluctuations is particularly important when one measure a low conductance state: i.e. the antiparallel configuration of a Fe/MgO/Fe MTJ. Here, each higher conductance channel associated to a defect will rise the low conductance having an electrical 'shortcut' effect. In the parallel state, the current is dominated by a low conductance channel, local fluctuation related rise of conductance being insignificant. Then we can deduce an interesting feature of the epitaxial MTJs: a statistical analysis of the magneto-transport properties distribution in the parallel and antiparallel configuration of the MTJ should be significantly different.
At the end of this paragraph, one can compare the epitaxially grown single crystal MTJs with similar systems grown by sputtering. Certainly, the statistical distribution of the local defects (grain boundaries) in the sputtered samples will be different to that of terraces in the epitaxial MTJs. Then, one can expect better average effects in sputter samples and better scaling of transport properties with the junction surface. However, an important source of magnetization fluctuations related to fluctuations of anisotropy is negligible in epitaxial samples with well defined magneto-crystalline anisotropy. The magnetization fluctuations can be more important in the sputtered textured samples. Here, in the AP low resistive state one can get fluctuations of magnetization in the sample related to local fluctuations of anisotropy from one magnetic grain to another. This may lead to mixed magnetic states (i.e. residual domain wall structure). A state which cannot propagate in a pure antiparallel magnetic state could then propagate via a channel associated to another magnetic configuration available (i.e. the core of a 360° wall will provide a local parallel magnetization high conductance channel with respect to adjacent antiparallel domains). Even if the magnetization fluctuations can be reduced by exchange anisotropy (when the exchange bias is used to pin the magnetization in sputtered MTJ samples), one still has to consider also another possible source of fluctuation which is related to fluctuation of the local crystalline quality.

7.4.5 Fe/MgO interface engineering for high-output-voltage device applications

For device application, the key parameter is the magnitude of the output signal modulation, namely the output voltage defined as: $V_{out} = V(R_{AP} - R_P)/R_{AP}$ where V is the applied voltage. From the TMR ratio as a function of the bias voltage (Figure 7.12(a)), the output voltage for device applications is plotted against the bias voltage in Figure 7.12(b) for Fe/MgO/Fe MTJs

with clean or carbon contaminated interfaces. For clean samples which provide the highest TMR amplitude, the V_{out} in positive bias voltages can exceed 300 mV. This value is already almost two times larger than the values measured for conventional MTJs with AlO barriers. However, as shown in Figure 7.12, we illustrate here that this V_{out} can be further increased (up to almost 1V) by interface engineering, namely the insertion of C at the Fe/MgO interface.

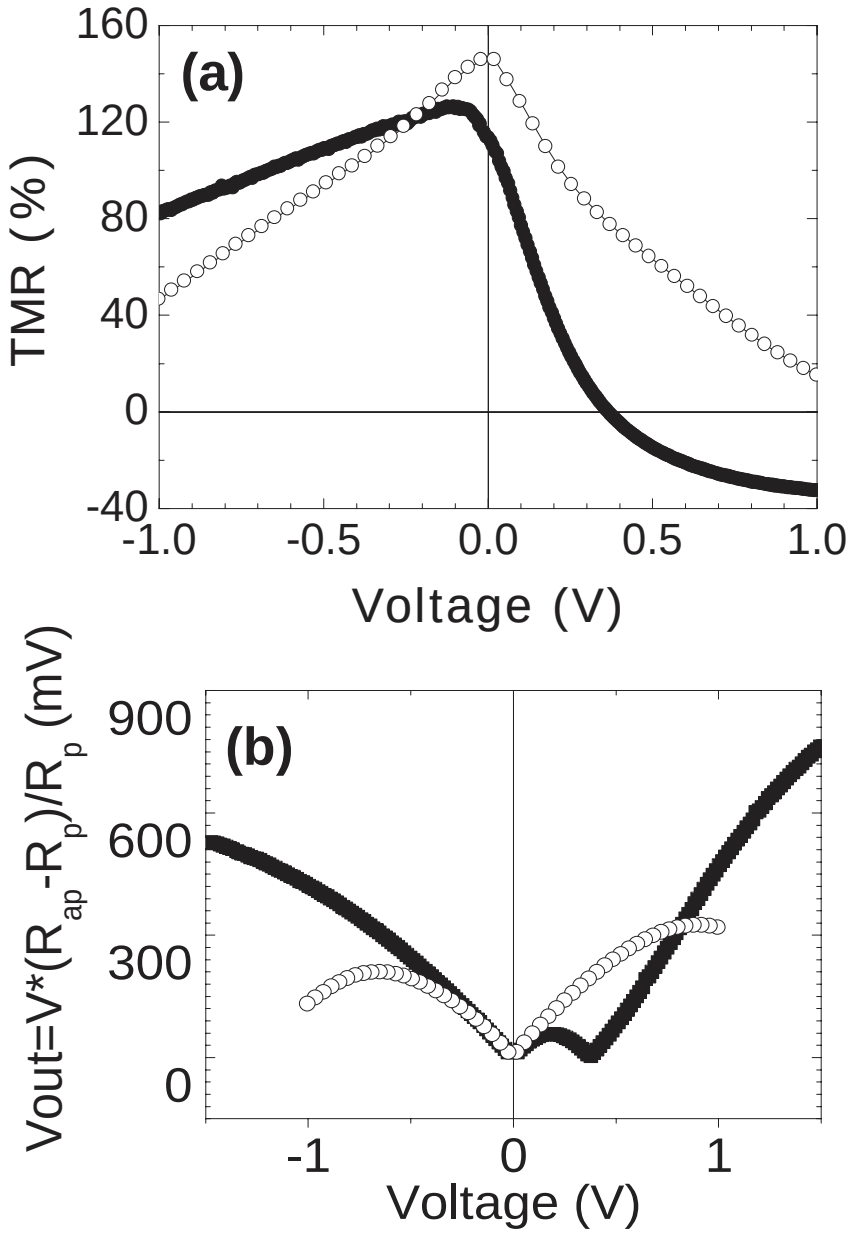

Figure 7.12: (a) Magnetoresistance as a function of applied voltage measured on a Fe/MgO/Fe tunnel junction (-○-) and on a Fe/C/MgO/Fe tunnel junction (-●-). (b) Output voltage versus applied voltage measured on a Fe/MgO/Fe tunnel junction (-○-) and on a Fe/C/MgO/Fe tunnel junction (-●-). In positive bias, the current flows from the top to the bottom electrode of the MTJ.

The conventional use of high values for both TMR and $V_{1/2}$ to provide large V_{out}, is replaced here by a new mechanism. The specific filtering effect related to C contaminated Fe/MgO interfacial

electronic structure, induces a change of the tunnel magnetoresistance sign. The inverse TMR, remains quasi constant at bias voltages beyond 1V, reaching values above -40%. This, combined with the small tunnel resistance of the junction biased beyond 1V, drives to large values of the junction output voltage and interesting features in view of integration of MTJs sensors or data storage in devices where low resistance is required. These results, illustrate how the interface engineering in Fe/MgO/Fe MTJs may be used as a key technology in engineering the properties of novel spintronic devices.

7.4.6 Effect of the IRS on the TMR: perspective studies

The bulk contribution of Δ_1 electrons provides a large positive tunneling polarization. As explain before, this is responsible on the large TMR effects expected for Fe/MgO/Fe MTJ systems. On the other hand, if we consider the interfacial resonance of Fe, we see that this state will provide a 100% negative polarization. Then, it is obvious that the larger is the contribution of the IRS to the tunneling, the smallest will be the TMR (the bulk and the interfacial tunneling polarization contributions have opposite sign). Two effects will contribute to the fast decrease of the TMR amplitude when reducing the thickness of the MgO. The first effect relates to the reduction of the MgO filterring efficiency (as shown in the theoretical bacground, other summetries than Δ_1 can propagate enhancing the AP conductance). The second effect is related to the enhancement of the IRS contribution to the conductance when the thickness of the insulator decreases. Therefore, for a critical MgO thickness one expects zero TMR effect (when the contribution of bulk and interface are balanced). If the thickness of the MgO is smaller than this critical value one expect negative TMR ratios, determined by the negative polarization of the IRS). In the small thickness regime, we expect large negative TMR ratios associated to extremely low junction resistance. These properties are extremely important for MTJ applications in read heads or high density data storage devices where low the low resistance-area become compulsory.

We assume that the IRS contribution to the tunneling in epitaxial MTJ can be also responsible on the lowest TMR amplitude in these systems with respect to sputtered samples, where the surface state does not exist[4]. A very interesting perspective of our study, currently in progress, consist in the study of these effects in samples where the IRS is quenched either by chemical bondings with interfacial ad-layers (as predicted theoretically by Tsymbal et col. [15]) or atomic level roughness (sub-monolayer ad-layer of Fe). The quenching of the IRS is expected to diminish also the voltage reduction of the TMR, especially in the low voltage regime.

Another experimental perspective consists in the analysis within the out-of-equilibrium regime (biased junctions), of the coupling observed at equilibrium. This implicated the patterning of submicronic pillars of MTJs with low thickness. On these objects which we would like to investigate the variation of the coupling strength with the bias. Theoretical models show that one can change the amplitude and the size of the coupling as a function of the voltage amplitude. On the same pillars we also plan to investigate the spin transfer effects (magnetization switching by the currents). In the part of this report concerning the projects, these last perspectives will be presented more in detail.

[4]One can assume that the in-plane disorder (i.e. fluctuations related to the grain boundaries) in sputtered samples quench the surface state

7.4.7 Double barrier MTJ devices involving AAF subsystems

Beyond the standard Fe/MgO/Fe MTJ, we also elaborated a new interesting class of double barrier epitaxial junctions. In these junctions, one electrode is a bottom Fe-I(100)(45nm) single-crystalline layer. It is separated by a 2.5nm thick MgO-I layer by the other electrode, constituted by the Fe-II(10nm)/MgO-II(0.7nm)/Fe-III(20nm) artificial antiferromagnetic (AAF) system. 'Standard' AAFs, using Ruderman-Kittel-Kasuya-Yosida (RKKY) interactions across a metallic nonmagnetic spacer, are commonly used in MTJ based devices such as read-heads or nonvolatile magnetic memories (MRAM) due to their advantages on the device magnetic properties [98]. Moreover, epitaxial Fe/MgO MTJ stacks using standard RKKY based AAF type Fe/Cr/Fe have been studied by Przybylski et al [113]. However, the particularity of the AAFs involved in our MTJs is that the coupling is achieved across the thin MgO spacer (about 3 monolayers) by quantum tunneling of electrons. The epitaxial growth of all the layers insures the conservation of the crystalline symmetry across all the stack and provides symmetry-dependent spin filtering effects.

Let us first consider the magnetic properties of the MTJ stack. The magnetization curve, measured on continuous film sample prior to lithography, is presented in the top panel of Figure 7.13. The field is applied along one of the easy axis of Fe which presents a four-fold anisotropy. The different magnetic configurations are detailed in the right panel sketch. At the saturation (state 1) all the Fe layers have their magnetization parallel to the field. Reducing the field, the AF coupling tends to stabilize the AF configuration within the AAF. Therefore, during its reversal, in (state 2) the magnetization of the Fe-II thinner layer of the AAF 'flips' to 90° with respect to the field, being 'temporary' trapped by the second, easy-axis-related, anisotropy quantum well of Fe. In the state (3) the AAF is stabilized in the AF configuration, with the net magnetic moment aligned along the positive field. Changing the sign of the field, the bottom Fe-I layer reverses its magnetization (state 4) following the field direction, then the net moment of the AAF switches along the field direction in the state (5). Increasing furthermore the field, the AAF will saturate (state 7) passing again through the intermediate 90° configuration of Fe-II (state 6).

The corresponding tunnel magnetoresistance curve is presented in the bottom panel of Figure 7.13. The curve is measured at a bias voltage of $10mV$ on a square $10\mu m$ lateral size MTJ with an areal resistance of $2.9 \times 10^5\ \Omega\mu m^2$. The field variation of the resistance validates the magnetic configurations described above in the macroscopic magnetization curve. Indeed, we observe the smallest resistance in (1) corresponding to the parallel configuration of magnetizations and a maximum of tunnel resistance in (3) corresponding to the anti-parallel configuration. In the intermediate states (2) and (6) one finds intermediate resistance stage related to the 90° configuration of Fe-II. In these steps one can also expect the subsistence of some magnetic inhomogeneities within the AAF layers created during the magnetization reversal [98]. Additional investigations by Magnetic Force Microscopy under applied field are in progress.

Having in view the thickness of the two tunnel barriers of the double junction, one can imagine that the voltage drop will mainly take place across the bottom thick MgO-I barrier. Therefore, here the measured resistance reflects the TMR effect of this barrier. However, coherent tunneling events within all the stack should be considered if the thickness of the intermediate Fe-II layer

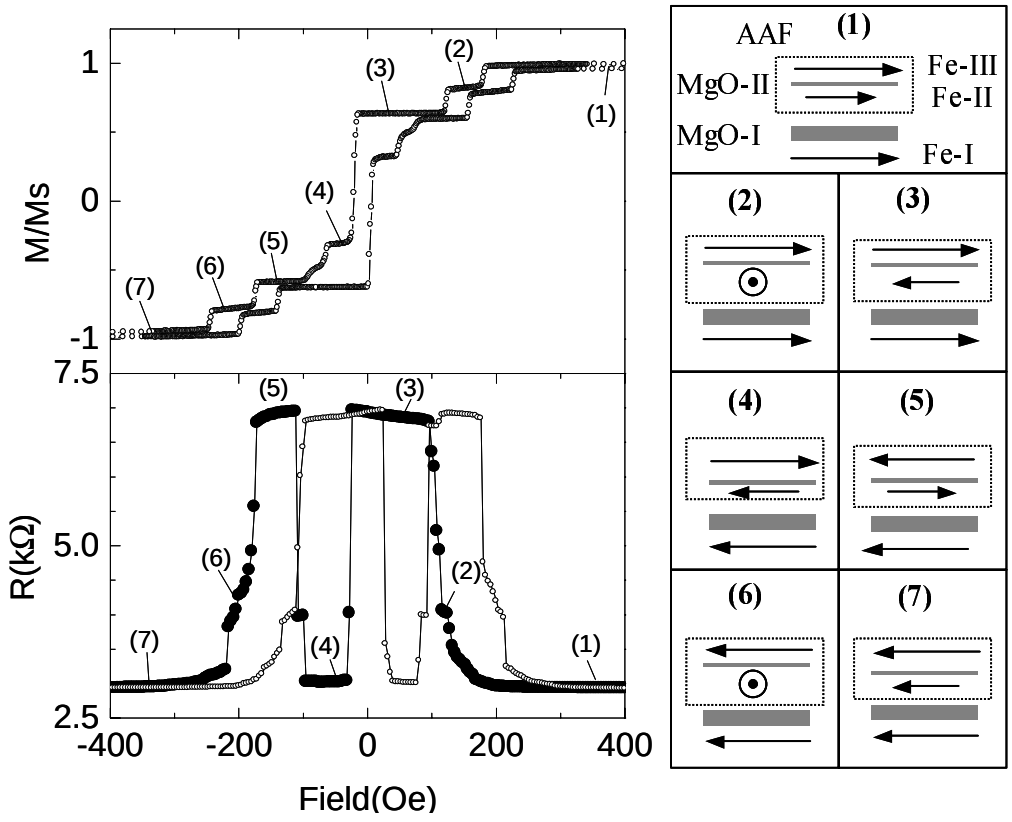

Figure 7.13: *Top Left panel:* Magnetization curve measured on a continuous film Fe(45nm)/MgO(2.5nm)/Fe(10nm)/MgO(0.7nm)/Fe(20nm) stack. *Bottom Left panel:* Resistance versus field curve, measured at 10mV positive bias, branch from the positive to negative field (-•-) and branch from negative to positive field (-○-). *Right panel:* Sketch indicating the magnetization configurations in the stack within different field windows from (1) to (7).

is decreased below 10nm (the reported coherence length for the majority spin in single-crystal Fe is above 10nm being 10 times smaller for the minority spin). All these aspects are currently under investigation.

7.5 Conclusion

In this chapter we confronted the theoretical predictions concerning the spin transport and the wave function filtering in terms of symmetry in single-crystal magnetic tunnel junctions. The experimental work is performed on Fe/MgO/Fe type MTJ systems elaborated by Molecular Beam Epitaxy.

In the equilibrium regime, when the junctions are not biased, the spin polarized tunnel transport leads to antifferomagnetic exchange interactions. An interesting class of artificial antiferromagnetic systems has been elaborated and studied.

The out-of-equilibrium regime is investigated for large MgO barrier thickness, where the filtering effect in k favor the tunnel propagation of electrons with k close to $k_{\|} = 0$. Moreover, the symmetry dependent attenuation rate in the barrier reduces the number of symmetry related conduction channels. This, simplifies the analysis of the multi-channel transport mechanisms. We illustrate that the chemical and electronic structure of the interface have a major role in the tunneling and filtering effects. Lastly, we present an interesting class of double barrier system combining a classic Fe/MgO MTJ and an artificial antiferromagnetic subsystem in which the magnetic properties are controlled by the coupling by spin polarized tunneling.

7.6 Résumé de chapitre en français

Effets de filtrage de spin dans des jonctions tunnel monocristallines

Dans ce chapitre, nous avons montré que, dans un système type JTM épitaxié, le transport tunnel polarisé en spin est gouverné par des effets complexes de structure électronique qui sortent du cadre du modèle des électrons libres. Ainsi, l'effet magnétoresistif dû au filtrage en spin des électrons est contrôlé par la structure électronique des électrodes ferromagnétiques mais également de la barrière isolante et des interfaces métal/isolant. Au-delà de la première vision considérant le système Fe/MgO/Fe comme une simple jonction tunnel magnétique susceptible de présenter une magnétorésistance tunnel (TMR) extrmement élevée, la croissance épitaxiale d'une telle structure en fait un système modèle autorisant la confrontation des prédictions théoriques avec les mesures expérimentales et permettant ainsi une meilleure connaissance de nombreux aspects de la physique fondamentale. Ce domaine de recherche est très concurrentiel de part les très forts enjeux économiques. En effet, en passant de l'isolant Al2O3 'classique', pressenti jusqu'à présent pour les applications industrielles, à l'isolant cristallin MgO, il est possible de multiplier par un facteur 5 le signal de sortie d'un dispositif utilisant les jonctions tunnel magnétiques.
Nous avons analysé le transport électronique dans deux régimes. A l'équilibre (system non polarisé électriquement) nous démontrons que le transport tunnel conduit à des interaction d'échange indirect par effet tunnel. Hors équilibre, nous avons étudié les propriétés de magnéto-transport des jonctions tunnel microscopiques polarisés par une tension externe.

Interactions magnétiques Depuis sa première mise en évidence, le couplage magnétique entre deux couches ferromagnétiques, à travers une couche séparatrice métallique ou semi-conductrice, a été amplement étudié expérimentalement et théoriquement. Des modèles théoriques ont prédit également la possibilité du couplage d'échange par l'effet tunnel à travers une fine couche isolante. Néanmoins, le couplage d'échange par effet tunnel d'électrons a été très peu abordé d'un point de vue expérimental, étant donné la décroissance extrmement rapide de l'intensité du couplage avec l'épaisseur de la couche isolante. La mise en évidence d'un tel couplage repose sur la possibilité de réaliser des couches continues d'isolant très minces ($< 1nm$) mais également sur la possibilité de discrimination entre le couplage par effet tunnel et le couplage direct par les trous d'épingle ferromagnétiques qui apparaissait lorsqu'on réduit l'épaisseur de l'isolant, en dessous d'une épaisseur critique. Le résultat marquant de notre travail de recherche est la mise en évidence, pour la première fois d'un point de vue expérimental, du couplage d'échange par effet tunnel entre des couches ferromagnétiques de Fe à travers une barrière tunnel de MgO. Les résultats originaux de ce travail ont été publiés dans Physical Review Letters. Nous avons exploité le couplage AF par effet tunnel entre deux couches ferromagnétiques séparées par une fine couche isolante pour construire des systèmes antiferromagnétiques artificiels (AAF) de type Fe (m_1)/MgO/Fe(m_2) où m_1 et m_2 sont les moments magnétiques des couches.

Transport hors équilibre Notre équipe a été la première à montrer expérimentalement que la physique du système Fe/MgO/Fe était au-delà du modèle classique des électrons libres. Des

mesures de transport électronique sous champ magnétique sur nos échantillons ont montré pour la première fois des magnéto-résistances de l'ordre de 100-180%, avec l'utilisation de métaux de transition. Les mesures de magnétotransport révèlent une forte corrélation entre la structure électronique et le transport tunnel polarisé en spin. Ceci est en bon accord les prédictions théoriques issues de calculs ab-initio. En effet, le courant tunnel est une sonde de la densité d'états interfaciale : lorsqu'on applique une tension à la jonction, les électrons injectés à partir du niveau de Fermi d'une des électrodes balaient en énergie la densité d'états de l'autre électrode. Ainsi, par l'influence de l'état de surface du spin minoritaire du Fe(001) localisé à 0.2V au-dessus de niveau de Fermi nous observons une augmentation de la conductance dans l'état AP liée au spin minoritaire par rapport à la conductance dans l'état P liée au spin majoritaire. Ceci est illustré également par l'inversion du signe de la TMR, lorsque la tension de polarisation de la JTM devient supérieure à 0.2 eV.

Du point de vue fondamental, nous avons déterminé les facteurs limitant la magnéto-résistance tunnel (les valeurs expérimentales sont bien inférieure aux 1000% attendus). Parmi ces facteurs nous pouvons cité les des défauts de la structure, l'impact des liaisons chimiques à l'interface Fe/MgO et l'influence de l'état de surface du Fe (spin minoritaire). De plus, nous avons montré l'importance des liaisons chimiques à l'interface et l'importance des contaminations d'interface. En effet, la forme de la variation de la magnéto-résistance avec la tension appliquée à la jonction tunnel dépend de la contamination d'interface. L'adjonction de C à l'interface Fe/MgO entrane une diminution de la magnéto-résistance à tension nulle mais de manière très intéressante déforme la courbe pour la rendre très asymétrique. Cette propriété, liée à la contribution dans le transport tunnel de l'état de surface du Fe (100), est tout particulièrement intéressante pour les applications et ne peut pas tre obtenue de manière simple avec des barrières amorphes.

Part IV

Recent results on spin filtering in complex magnetic tunnel junctions

Chapter 8

Spin polarized tunneling in hybrid [single crystal] / [polycrystalline] magnetic tunnel junctions

8.1 Introduction

This research topics implicates two thin film deposition techniques: the Molecular Beam Epitaxy and the Sputtering. Magnetic tunnel junctions combining single crystal bcc Fe bottom electrode and MgO barriers and polycrystalline top Co electrode have been elaborated. In these systems we demonstrate major filtering effects of the random distribution transport channels provided by the polycrystalline Co via the symmetry dependent attenuation rate in the MgO(100) barrier and the filtering in the single crystal Fe(001) electrode. Interestingly, this filtering ensures a high sensitivity of the tunnel characteristics to the cobalt density of states components which are the less attenuated in the barrier. Therefore, we observe a sign reversal of the tunnel magnetoresistance (TMR) in the positive voltage when the injected electrons scan the band structure of the top electrode. We explain this, by the sign reversal of the Δ_1 tunnel polarization in the Co. The larger amplitude of the TMR ratio in positive voltage reflects the large polarization of the single crystal [Fe/MgO] emitter, due to symmetry filtering effects which limit the available conduction channels. In negative voltage the polycrystalline emitter provides a larger number of propagating channels. This will enhance the conductivity of the junction in the antiparallel state and reduce the amplitude of the TMR. Our results highlight interesting aspects of tunneling in hybrid MTJ systems combining a single crystal electrode/barrier subsystem and polycrystalline counter-electrode. These results are compared to the spin filtering effects in standard single crystal MTJs.

8.2 Theoretical background of tunneling in hybrid systems

In order to describe the experimental results obtained in our hybrid single crystal [Fe/MgO]/ [polycrystalline Co] MTJs we propose here a simplified very intuitive insight on the complex tunneling phenomena. Our experimental results may be the starting engine for further theoretical

more sophisticated calculations.

Our model is based on the multichannel model presented before in this manuscript. The polycrystal, provides a random distribution of k, each one leading to a possible conduction channel. Then, one can use the Landauer formalism to compute the total conductivity. However, we assume here that the single crystal part of the MTJ plays its specific role in terms of electronic filtering with respect to the Bloch function symmetry. This leads to filtering effects: among all the possible propagating states with respect to the polycrystal only those which are the less attenuated in the barrier will be considered to contribute to conduction at large barrier thickness. Moreover, when the electrons are injected from the single crystal bottom electrode, this one fulfills the filtering task (i.e. only some specific Bloch states can be injected). However, due to the large spectra of crystalline orientations (distribution of k) the polycrystalline electrode will be less selective in terms of filtering than a single crystal. This will lead to an enhancement of the total conductivity. This enhancement is particularly important in the lowest conductivity state (typically in the AP magnetic configuration), and will determine a reduction of the amplitude of the TMR in hybrid junctions compared to the single crystal Fe/MgO/Fe systems.

Besides the transport channels related to the polycrystalline Co, one has to consider also the contribution of highly textured regions. Indeed, the structural characterization by High Resolution Cross Section Transmission Electron Spectroscopy validate the presence of *bcc* Co and also *hcp* regions constituted by domains with the in-plane c axis.

In the first part of this manuscript, we presented a more detailed analysis of the symmetrized basis functions belonging to each irreducible representation of the *bcc* structures. We showed that, related to the propagation direction of electrons in the Fe(100)/MgO/Fe MTJ, the Δ direction of the Brillouin plays an important role. Similarly, for the hexagonal crystalline layers with in-plane c axis, the relevant direction related to the tunneling transport in Fe(100)/MgO/(hcp-Co) will be the Σ high symmetry direction. The states Σ_i contain specific orbital basis functions[1]. For example, the basis of the Σ_1 symmetry contains s and d_{z^2} orbitals belonging to the Δ_1 state in the cubic structures. This is extremely important for the matching of these states in the Fe(100)/MgO/(hcp-Co) MTJ stack. However, in the Σ_1 state one can find other basis functions such as p_y (belongs to Δ_5 in the cubic symmetries) and $d_{x^2-y^2}$ (belongs to Δ_2 in the cubic symmetries). These states can match with the corresponding states in Fe and provide specific conduction channels. Nevertheless, as shown in the part consecrated to the theoretical background, one has to consider also the different attenuation rates in the crystal for the different in plane modulation of each orbital state: (i.e. an s state will be less attenuated than a $d_{x^2-y^2}$), etc... This, complicates the analysis of the propagating state in terms of symmetry, in a system where we pass from cubic to hexagonal lattice.

In order to give a simple, comprehensive picture of the transport we will consider here only the conduction channels corresponding to the cubic symmetry (related to the Fe/MgO/(bcc Co) channels). The other contribution are integrated in a term ΔG of additional conductivity related also to the dispersion in k in a polycrystal. Moreover, a 'misused language' is adopted, labeling the states with respect to the cubic symmetry and the corresponding Δ propagation

[1] A more detailed overview on the irreducible representation of the Σ line is presented in the appendix of the manuscript.

direction in the *bcc* Fe. A more detailed and accurate analysis of the conductivity within the Fe/MgO/(hcp Co) channels is in progress.

In positive voltage the electrons flow from the bottom bcc Fe(100) electrode toward the top polycrystalline Co. One can assume that the Fe(100) will filter in symmetry the injected electrons, and the single crystal MgO barrier will provide a symmetry dependent attenuation rate. As we already shown for standard Fe/MgO/Fe junctions, the less attenuated symmetries within the barrier are the Δ_1 then the Δ_5 [2]. Then, we expect that the highest conductivity channels in the parallel (P) and anti-parallel (AP) configurations will be given by $G^{\Delta_1} + G^{\Delta_5}$, if these states are available on each side of the barrier.

In negative voltage, the electrons are injected from the polycrystalline top electrode toward the bottom Fe(001) across the single crystal MgO barrier. One can assume that the polycrystal will provide a large spectrum of conduction channels. These channels can be discretized following the orbital decomposition of states: $s, p_z, d_{z^2}, p_x, p_y, d_{xz}, d_{yz}...$ However, the less attenuated states within the MgO barrier will be again those belonging to the Δ_1 and Δ_5 symmetries in Fe. Then, the conductivity can be written again as $G = \sum G^i = G^{\Delta_1} + G^{\Delta_5} + \Delta G$.

To get dipper in the conduction landscape, and to explain the term ΔG, we can use the multi-channel model. Each channel is associated to a path connecting an initial state i of an electron having a given $k_\parallel$, to a final state j and $k'_\parallel$.

Then, the transmission probability is given by:

$$T = \sum_{k_\parallel, i; k'_\parallel, j} T(k_\parallel, i; k'_\parallel, j)$$

We can suppose now that at large MgO barrier thickness in the asymptotic regime, the barrier filters the k of the propagating electrons around $k_\parallel = 0$. Then, $k'_\parallel = 0$ and one obtains:

$$T = \sum_{k_\parallel, i; 0, j} T(k_\parallel, i; 0, j) = \sum_{0, i; 0, j} T(0, i; 0, j) + \sum_{k_\parallel \neq 0, i; 0, j} T(k_\parallel, i; 0, j)$$

The first term, $T_0 = \sum_{0,i;0,j} T(0, i; 0, j)$ leads to a conductivity G_0 corresponding to the standard single crystal MTJ case with propagating $k_\parallel = 0$ electrons. The second term leads to a ΔG conductivity, related to the dispersion of crystalline orientations in the polycrystal (which can be modeled by a dispersion in $k_\parallel$). It represents the probability that a given $(k_\parallel, i)$ state provided by the polycrystal propagates in a final state $(0, j)$.

This term can be particularly important as a function of the magnetic configuration of the junction. Indeed, one can assume that in parallel configuration, the term G_0 is dominant with respect to ΔG (i.e. for Fe/MgO/Fe junctions this is related to the highly conductivity Δ_1 channel). On the other hand, in the AP configuration, when G_0 is extremely small $G_0 \approx 0$ (i.e. the Δ_1 cannot propagate in standard Fe/MgO/Fe MTJ) the amplitude of G is given by the ΔG which represents the contribution of $k_\parallel \neq 0$ paths provided by the polycrystal to the tunneling.

A particularly interesting experimental situation can be imagined when in the AP configuration one can also modulate the amplitude of G_0 with respect to ΔG. This may be done by

[2] The states are labeled with respect to the irreducible representation corresponding to the symmetry group of the single crystal bcc Fe bottom electrode. The epitaxial growth of MgO on Fe conserves the symmetry within the barrier.

the activation of the minority interfacial resonance of Fe(001) (see the chapter concerning the standard Fe/MgO/Fe MTJs). Let's denote by $G^{IRS} = G^{\star}_{\Delta_1}$ the corresponding contribution to the conductivity of this resonant channel. Two extreme interesting situations may be envisaged:

1. The enhancement of the conductivity in the AP configuration related to the interfacial resonance of Fe (G^{IRS}) is dominant with respect to ΔG

We have illustrated in a previous chapter the net signature of the surface state contribution to the conductivity in standard Fe/MgO/Fe MTJs. We consider here the case when the bottom Fe/MgO interface presents a c(2X2) reconstruction related to the interfacial carbon layer. This situation is extremely interesting because here the signature of the interfacial resonance is drastically enhanced with respect to the pure interface configuration.
From these previous results, one can deduce the tunneling polarization of the bottom Fe/MgO interface (within a generalized Julliere model):

$$P^{Fe-C/MgO}_{inf,\Delta_1} = \begin{cases} > 0 & \text{if} \quad V < 0.2V \\ < 0 & \text{if} \quad V > 0.2V \end{cases}$$

assuming that the interfacial resonance of Fe(001) arrives in $\bar{\Gamma}(k_{\parallel} = 0)$ at 0.2 eV above the Fermi level.
For the top electrode, we can roughly assume that at the interface with the MgO barrier (within few monolayers) the Co will have a bcc-like structure. Then, one can consider the corresponding tunneling polarization with respect to the Δ_1 symmetry:

$$P_{sup,\Delta_1} = \begin{cases} > 0 & \text{if} \quad V < 0.2V \\ < 0 & \text{if} \quad V > 0.2V \end{cases}$$

From the extended Jullière model, one expects the following bias variation of the TMR:
For both negative ($V < 0$) and positive ($V > 0$) bias,

$$TMR = \begin{cases} > 0 & \text{if} \quad V < 0.2V \\ < 0 & \text{if} \quad V > 0.2V \end{cases}$$

This is schematically illustrated in Figure 8.1(a).

2. The ΔG is dominant with respect to the enhancement of the conductivity in the AP configuration related to the interfacial resonance of Fe G^{IRS}

This situation will provide a monotonuous positive tunneling polarization of the bottom Fe-C/MgO interface $P^{Fe-C/MgO}_{inf,\Delta_1} > 0$ for all $V > 0$. This will lead to the voltage variation of the TMR schematically represented in Figure 8.1(b).
In hybrid junctions composed by single crystal [bottom electrode/barrier] and polycrystalline top electrode, the term ΔG can be significantly larger than the surface state related resonant conductivity. Moreover, the thickness of the MgO is particularly important in these junctions. Indeed, the amplitude of the term ΔG related to $\sum_{k_{\parallel},i;k'_{\parallel},j} T(k_{\parallel}, i; k'_{\parallel}, j)$ increases when the thickness of MgO decreases. This is due to the enhancement of the contribution to the tunneling

of states with $k_{\parallel} \neq 0$ in both initial and final states when the filtering effect in k of the MgO(100) is reduced. Then, one can experimentally expect different voltage variations of the TMR by controlling the ratio $G^{IRS}/\Delta G$.

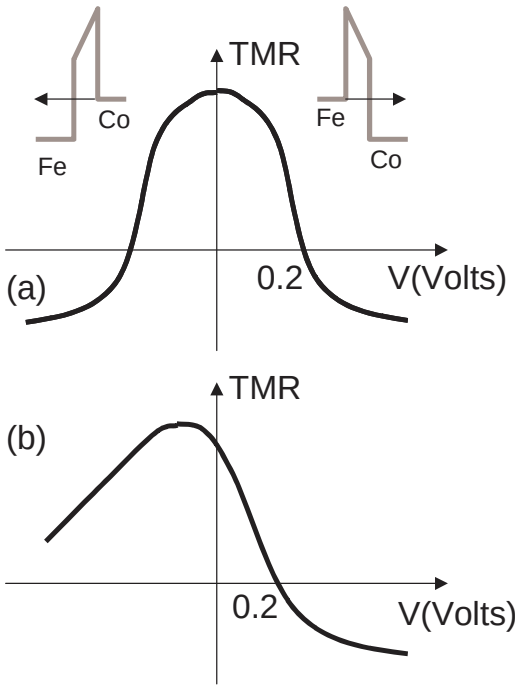

Figure 8.1: Schematic representation for the theoretical expectation of the tunnel magnetoresistance voltage variation in the hybrid junctions. In positive voltage the electrons are injected from the single crystal Fe toward the polycrystalline Co. In negative voltage, the electrons injected from the Co scan in energy the electronic structure of the Fe(001). (a) The conductivity enhancement in the AP configuration corresponds to the activation of the minority spin interfacial resonance of the Fe. (b) In this case the ΔG related to a larger dispersion in k of the propagating electrons overwhelms the contribution of the IRS. Then, the sign of the TMR does not change in negative voltage.

8.3 Experimental results

The MTJ stacks (see Figure 8.2) are elaborated in two steps. In a first step, using the Molecular Beam Epitaxy, the single crystal part of the junctions is grown. More details about the elaboration of this sub-systems have been described in the paragraph concerning th epitaxial Fe/MgO MTJ. Roughly, on top of a MgO(100) substrate a 45nm Fe layer is evaporated from a Knudsen cell, then annealed at 450° C for 20 minutes. Then, a 2.5 nm MgO barrier is epitaxially grown of the atomically flat Fe at about 100° C. Following the specific elaboration procedure, the Fe/MgO interface can be either clean or contaminated with half-monolayer of carbon. For the systems presented in this manuscript we only consider the structures with carbon contaminated interfaces where the Fe presents also a c(2x2) reconstruction. These systems are particularly interesting due to the net signature of the interfacial Fe electronic structure on the transport, as previously illustrated. In a second step a polycrystalline top electrode of the

MTJ is deposited using the sputtering technique. The structure of this electrode is the following: Co(2nm)/Ta(0.5nm)/Co(2nm)/IrMn(10nm). It represents the magnetically hard sub-system of the junction. The control of its magnetic properties is done using the exchange bias with the IrMn antiferromagnet. More details on the elaboration and the magnetic properties of this subsystem can be found elsewhere [115].

The Transmission Electron Microscopy analysis of the samples (see Figure 8.3) illustrates interesting structural features of the MTJ stack. One can distinguish: a bcc(100) bottom Fe electrode with an epitaxial MgO barrier on top of it, a textured Co electrode which 'tends' to conserve the structural coherence, an amorphous Ta layer covered by a (111) Co underlayer and lastly a highly textured IrMn. However, the most important for the tunnel transport related filtering mechanism is the structure of the first Co layer adjacent to the MgO epitaxial barrier. It is highly textured and a detailed analysis in high resolution shows that this layer contains either hcp regions[3] or (100) *bcc* (*bct*) epitaxially grown on Fe. These two specific structures of Co will have a strong impact on the spin filtering effects in the hybrid MTJ stack.

After the growth of the thin film structures, the tunnel junctions have been patterned by optical UV lithography and dry Ar ion etching. This lead to square MTJ elements with a lateral size between 10 to 100 μm. The magneto-electric measurements have been performed connecting always the top electrode of the junction to the positive voltage supply (bottom electrode to the negative).

The Figure 8.4 and Figure 8.5 illustrate the standard tunnel magnetoresistance versus field curves measured in two different MTJ samples. One can immediately see that they reproduce the sketched curves presented in Figure 8.1(a,b). Indeed, the curve presented in Figure 8.4 corresponds to the situation where the enhancement of the conductivity related to the interfacial resonance of Fe is higher then ΔG whereas the Figure 8.5 corresponds to the opposite situation.

In negative voltage, the tunneling electrodes scan the electronic structure of the bottom Fe electrode. The sign reversal of the TMR in negative voltage illustrated in Figure 8.4 reflects the conductivity enhancement in the AP configuration related to the surface state if this is higher then the ΔG. In the other sample, whose TMR(V) is illustrated in Figure 8.5, the ΔG dominates over the interfacial resonance related conductivity. This, explain the constant sign of the TMR in negative voltage.

On the other hand, in both type of MTJ samples in positive voltage the electrons are injected from the bottom single crystal Fe(001) electrode across the MgO(100) with a large positive tunneling polarization related to the Δ_1 states. The voltage variation of the conductivity will reflect the electronic properties of the top Co electrode. It means that the sign reversal of the TMR in positive voltage is related to the change of sign for the tunneling polarization of Co. The very first explanation we propose for this behavior assumes that the relevant polarization of Co is that related to the spin-dependent Bloch states which are the less attenuated within the barrier. These, are the states belonging to the Δ_1 symmetry (i.e. s, p_z, d_{z^2}). We consider here the contribution to the coherent tunneling related to the bcc Co conduction channels. This assumption is important if one wants to keep valid the symmetry related framework. Then, one

[3]These hcp regions are constituted by two domains with the c axis in plane at 90° one with respect to the other.

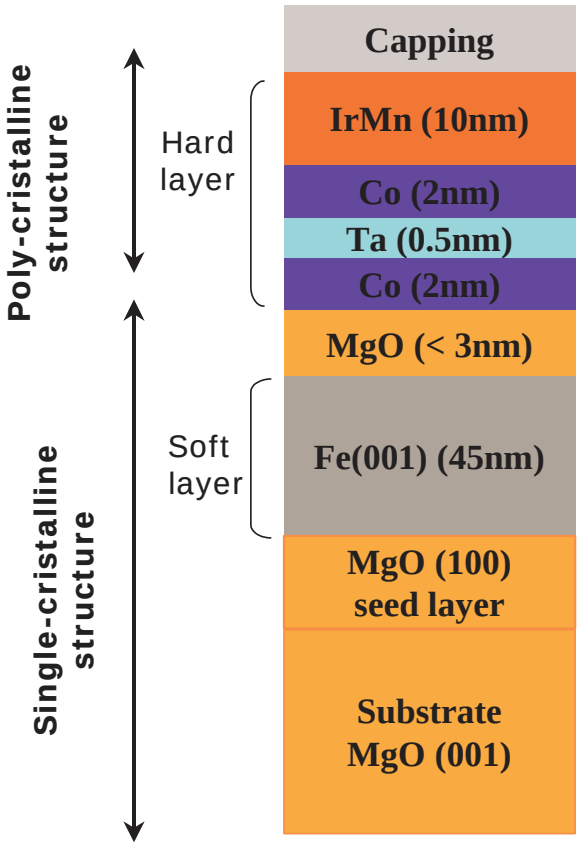

Figure 8.2: The multilayer stack structure of the hybrid magnetic tunnel junctions.

has to assume that the symmetry is not broken at the interface within a thickness sufficiently large with respect to the coherence length of the electron. Otherwise, one has to further discretize the propagating states and use a multichannel model where each state is associated to a given orbital projected component of the electron. However, we consider only those orbital projections which have the smallest attenuation rate within the MgO (s, p_z, d_{z^2} then p_x, p_y, d_{xz}, d_{yz} which are exactly the components of the $\Delta_{1,(5)}$ symmetries in a bcc structure). Then, both approaches should be equivalent to evaluate the tunneling polarization.

The change of sign for the polarization in the Co can be understood from the electronic structure of the bcc Co (see Figure 8.6). It is related to the bottom of the Δ_1 band of the minority spin appearing at about 0.2eV above the Fermi level. When the positive applied voltage reaches this value, in the AP configuration a strong enhancement of the conductivity is expected. Indeed, an injected Δ_1 state from the Fe finds an 'equivalent' available state at the top interface. Then G_{AP} may overcome G_P and the TMR becomes negative. Even if the Co is experimentally a poly-crystal, we consider this specific band structure diagram for two reasons:(i) the less attenuated components in the MgO(100) barrier, epitaxially grown on Fe(100) belong to the Δ direction; (ii) the Fe/MgO/(bcc Co) channels conserve the Δ_i symmetries. The two reasons implicate that the propagating density of states of Co will be mainly composed by the states belonging to the less attenuated symmetries (Δ_1, Δ_5). We remark again, that even if in the polycrystalline

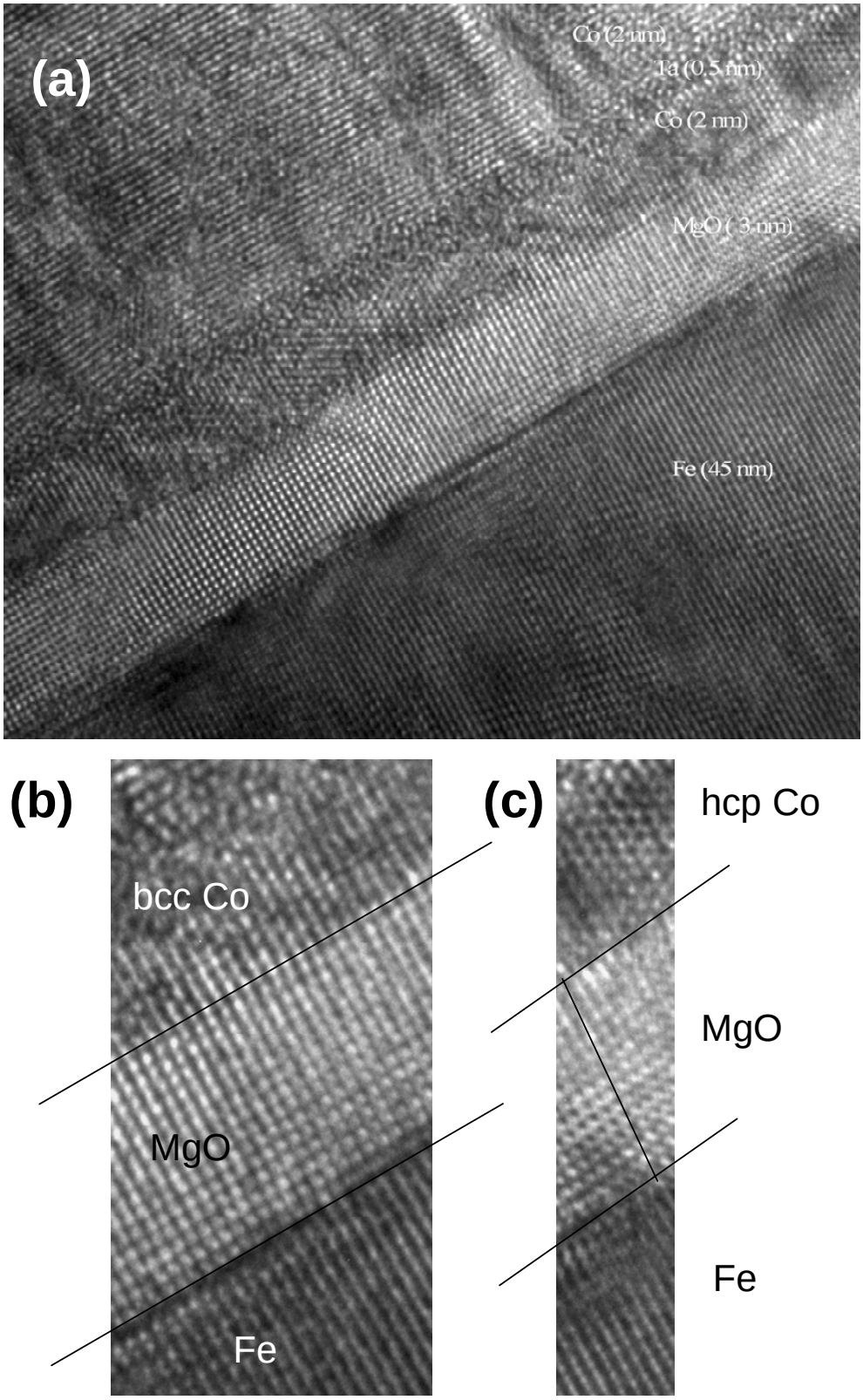

Figure 8.3: (a) High Resolution Cross Section Transmission Electron Microscopy of the MTJ stack. Zoom on hcp Co zones (b) and bcc (c)

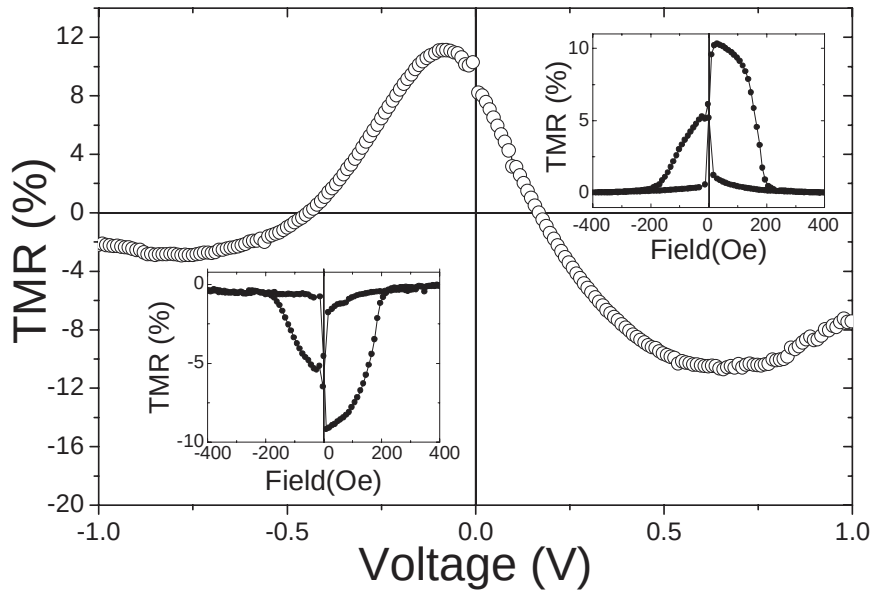

Figure 8.4: Experimental variation of the TMR in tunnel junctions in systems where G^{IRS} is dominant with respect to ΔG. *Top Inset*: Typical resistance versus field curve corresponding to positive TMR regime. *Bottom Inset*: Typical TMR(H) curve in the negative TMR regime.

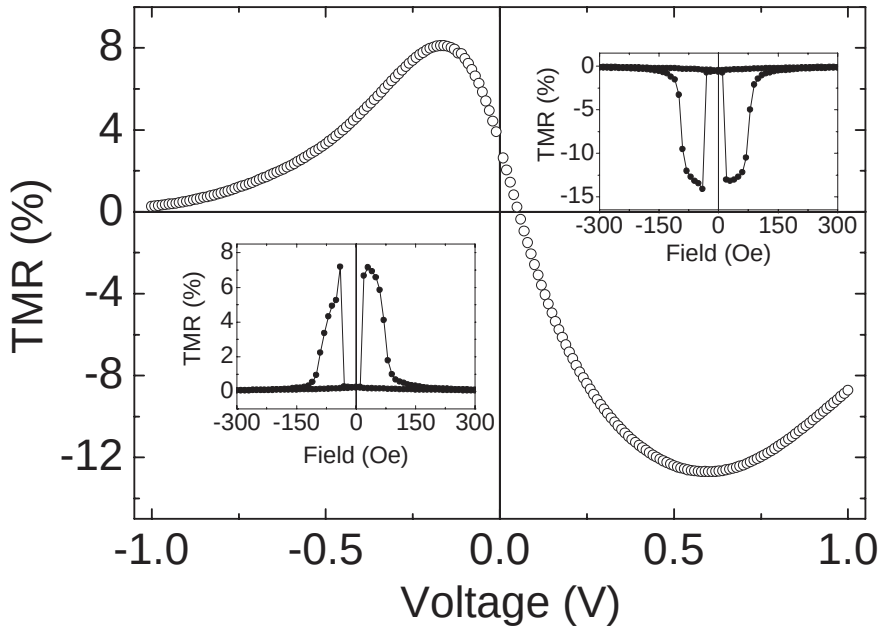

Figure 8.5: Experimental variation of the TMR in tunnel junctions where ΔG dominates the G^{IRS}. *Left Bottom Inset* Typical resistance versus field curve corresponding to positive TMR regime. *Top Right Inset*: Typical TMR(H) curve in the negative TMR regime.

Co the states cannot be anymore labeled in terms of the symmetry group of the Fe bcc, by a 'misused language' we call here Δ_1 state in Co a state composed by the superposition of the less

attenuated s, p_z, d_{z^2} in the MgO(100) (belonging to Δ_1 symmetry) [4].

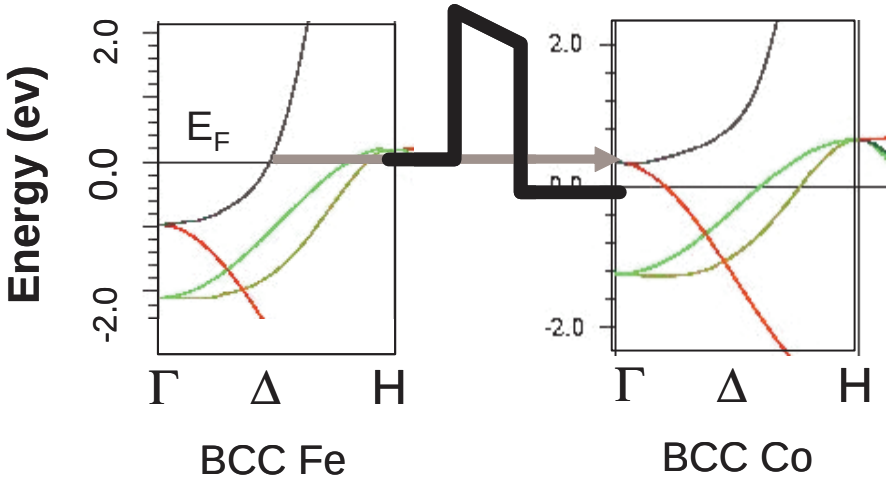

Figure 8.6: Sketch illustrating the bulk band structure diagram of bcc Fe (left) and bcc Co (right). This picture discretizes the conduction channel corresponding to $k_{\|} = 0$ for the majority spin in the anti-parallel configuration. One can see that above the Fermi level, an injected Δ_1 state from the bcc Fe can get in a similar symmetry state on the other side of the barrier. This can drastically enhance the AP conductivity and therefore reverse the sign of the TMR (when $G_{AP} > G_P$).

These assumptions are experimentally confirmed by comparing the conductivities of the two distinct samples. Indeed, for the sample one the conductivity is $G = 2.5\ 10^{-8}\ \Omega^{-1}\mu m^{-1}$, the contribution of the interfacial resonance to the conductivity in the AF configuration being estimated to about $10^{-7}\ \Omega^{-1}\mu m^{-1}$. On the other hand, in the other sample, the total conductivity is almost two order of magnitudes larger: $G = 10^{-6}\ \Omega^{-1}\mu m^{-1}$. This 'overwhelms' completely the IRS-related enhancement of the AP conductivity.

The experimental results presented in this section have been recently obtained. Therefore, more detailed experimental and theoretical approaches are necessary to explore all the magneto-transport aspects in this new class of hybrid MTJ systems. The electronic transport here has to be 'discretized' in different conductivity channels, associated to the structure of one of the MTJ electrode. This can be either epitaxial *bcc*, epitaxial *hcp* or disordered. Different level of studies are in progress. From the experimental point of view, the thickness of the insulating barrier will be varied in order to modulate the filtering efficiency of the MgO and then the relative ratio $G^{IRS} = G^{\star}_{\Delta_1}/\Delta G$. These studies will be performed also on samples with carbon free interfaces where the $G^{IRS} = G^{\star}_{\Delta_1}$ is smaller but ΔG related to the k dispersion in the polycrystal can be furthermore reduced by increasing the MgO thickness. Moreover, detailed structural analysis is in progress to get more insight on the structure of the interface between the polycrystal and the single-crystal barrier but also on the structure of the polycrystal itself. One of the very interesting perspectives consists in elaboration of hybrid systems where the 'crystalline level' of the top electrode can be gradually adjusted (i.e. one can use the CoFeB alloy, and play with the

[4]For hcp Co the labeling is also not correct because the s, d_{z^2} belong to the Σ_1 state and the p_z to the Σ_4 symmetry

annealing time and temperature). As a function of the crystallization degree, one can modulate the dispersion in k for the propagating electrons and therefore the ΔG. The detailed structural information will be used to elaborate a more sophisticated and complex theoretical model for the tunneling transport in the hybrid systems. Studies are in progress to elaborate a model which takes into account the propagation of a wave function from cubic to hexagonal symmetry. The tunnel barrier will provide specific attenuation rate for each basis function of the irreducible representation. This will lead to a complete tunneling model which will be able to include the conduction channel associated to the hcp Co regions.

8.4 Résumé de chapitre en français

Transport polarisé en spin dans des jonctions tunnel magnétiques hybrides type mono-cristal/ poly-cristal

En combinant l'épitaxie par jets moléculaires et la pulvérisation cathodique, nous avons élaboré des jonctions magnétiques à effet tunnel constituées par une électrode inférieure mono cristalline en Fe bcc (100), une barrière de MgO épitaxié par-dessus et une électrode supérieure poly-cristalline de Co. Dans ces systèmes, nous montrons d'importants effets de filtrage pour les canaux de transport de distribution aléatoire en k fournis par le cobalt poly-cristallin. Ceci s'explique par le taux d'atténuation dépendant de la symétrie dans la barrière de MgO (100) et par l'effet du filtrage en symétrie dans l'électrode de Fe mono-cristalline. Ce filtrage assure une grande sensibilité des caractéristiques tunnel aux composants de la densité d'état du cobalt qui sont les moins atténués dans la barrière tunnel. Ainsi, nous observons un changement de signe de la magnétorésistance tunnel au-delà d'une certaine tension positive qui force les électrons à sonder en énergie la structure de bande du cobalt. Nous expliquons ceci par le changement de signe de la polarisation tunnel des électrons de symétrie Δ_1 dans le cobalt au-delà d'une certaine énergie supérieure au niveau de Fermi .
L'amplitude plus importante de la magnétorésistance tunnel en tension positive par rapport à celle en tension négative, traduit la forte polarisation du système émetteur [Fe/MgO], grâce aux effets de filtrage en symétrie et en vecteur d'onde k qui limitent le nombre des canaux de transport accessibles. En tension négative, l'électrode poly-cristalline fournit un grand nombre de canaux de propagation disponibles. Ceci se traduit par l'augmentation de la conductivité dans l'état antiparallèle et ainsi par la réduction de l'amplitude de la magnétorésistance tunnel. Nos résultats mettent en avant des aspects intéressants concernant le transport électronique dans des systèmes hybrides qui combinent des parties mono et poly-cristallines. Ces résultats sont comparés avec les effets de filtrage en spin et en symétrie dans des systèmes purement mono-cristallins.

Chapter 9

Spin polarized tunneling in single crystal Fe/Cr/MgO/Fe junctions

9.1 Introduction

This research topics is performed within the framework of a common scientific project involving the Spintronics team of our laboratory and the Institute of Physics and Chemistry of Materials (IPCMS) from Strasbourg. All the results presented here are recently obtained. Magnetic tunnel junctions (MTJ) combining single crystal bcc Fe and MgO barriers have been elaborated. We investigated the effect of a thin Cr layer with variable thickness, intercalated at the bottom interface between the Fe and the MgO. For standard Fe/MgO/Fe MTJ, without Cr, we obtain typical large TMR effects of 180% at room temperature. When a thin Cr layer is inserted between the Fe and the MgO barrier we observe a reduction of the TMR ratio related to the decrease of the conductivity in the parallel magetization configuration. This, demonstrates that the Cr layer behaves as an additional barrier for the propagation of the Δ_1 state in the parallel configuration of the magnetization. The quenching of the Δ_1 conductivity channel will lead to a higher sensitivity of the tunnel transport to the Δ_5 symmetry state propagation, as illustrated by our magneto-transport results. Moreover, by increasing the thickness of the Cr, we modulate the amplitude of the polarization for the propagating states across the barrier. For large Cr thickness the parallel and anti-parallel configurations of the MTJ become equivalent in terms of magneto-transport. The propagation of the Δ_1 state in these Fe/Cr/MgO/Fe MTJs can be alternatively modulated by the voltage across the junction. This will enable to change the sign of the Δ_5 associated tunnel polarization and explains the sign reversal of the TMR in positive voltage. Using the Cr as a symmetry dependent barrier we build quantum well structures in Fe/Cr/Fe/MgO/Fe MTJ systems. In these structures, our experiments demonstrate clear signature of quantum confinement for the Δ_1 electrons in the thin Fe layer sandwiched between the Cr and the MgO. Our theoretical approach used to explain the experimental results is pretty simple with respect to the complex reality of the tunneling in single crystal devices. However, its figure of merit is to remain very intuitive and to provide a satisfactory qualitative description of experimental results. Recent more sophisticated ab-initio calculations, within a ballistic framework for the tunneling, show a good agreement with the experimental results.

9.2 Multi-channel tunneling model

In order to explain the electronic transport in the single crystal Fe/Cr/MgO/Fe system we use a multi-channel tunneling model. As already discussed in case of standard Fe/MgO/Fe MTJs, each channel is associated to a given wave function symmetry. The Fe and Cr are bcc with an almost similar lattice parameter which insures the conservation of symmetry by the epitaxial growth. The available propagating symmetries can be easily identified from the band structure diagrams of the bcc Fe and Cr. We mention here that this analysis is extremely rough. It takes only into account the propagating electrons with $k_{\|} = 0$. This is mainly valid at large barrier thickness in the asymptotic regime which corresponds to our experimental samples. Moreover, we are fully aware that the band structure used to identify the symmetry depended channel is calculated at equilibrium without any bias on the sample. However, one can assume that in a first order the bulk electronic structure of the electrodes is not perturbed too much by the bias, having in view that the voltage drop within the MTJ is mainly localized on the insulating barrier. Then, in a very rough first order approach we consider that the only effect of the bias consists in a shift in energy of the band structure. Applying an external voltage V to the junction the chemical potential of the electrodes μ_L and $\mu_R = \mu_L + eV$ are shifted with respect to each other which means that the potential and the corresponding bands are shifted. In the small transmission regime, one can consider that the voltage drop in the barrier is linear, as demonstrated by ab-initio calculations [114]. Moreover, in our intuitive model we use the bulk band structure diagrams, and we are fully aware about the difference of the electronic structures of the thin Cr layer and also of the interfaces. Despite the apparent simplicity of our modeling it has the figure of merit to be able to describe qualitatively a large class of experimental data measured in our realistic MTJs.

In Figure 9.1 we depicted the band structure diagrams corresponding from left to right to the bulk bcc Fe, bulk bcc Cr, for the majority and the minority spins in the parallel and the anti-parallel configuration of magnetizations. They correspond to the $\Delta = \Gamma - X$ high symmetry direction which corresponds to propagating electrons perpendicular to the (100) plane of the MTJ stack ($k_{\|} = 0$). From these diagrams one can extract important information about the available wave function symmetries around the Fermi level in the left Fe emitter, in the Cr and in the right Fe collector. From this analysis we propose the multichannel model illustrated in Figure 9.2. Our qualitative model considers a rectangular barrier. The barrier height and the effective mass in the insulator are symmetry dependent.

In both parallel and anti-parallel configuration, for each spin we illustrate in Figure 9.2 the symmetry dependent potential profile (using intuitive free-electron like potential profile diagrams). We limit here our analysis only to the Δ_1 and Δ_5 symmetries related channels, considering that experimentally we are in the asymptotic regime where all the other symmetries are completely attenuated by the MgO barrier.

In the diagrams we illustrated the potential profile at equilibrium (zero bias). As mentioned before the effect of the bias V consists in the shift of the potentials with eV and a linear variation of the potential profile within the insulator. Moreover, for biased junctions the electrons contributing to the tunneling come from an energy range $E_F - eV$ under the Fermi level. Conventionally, in positive voltage we consider that the electrons flow from left to right.

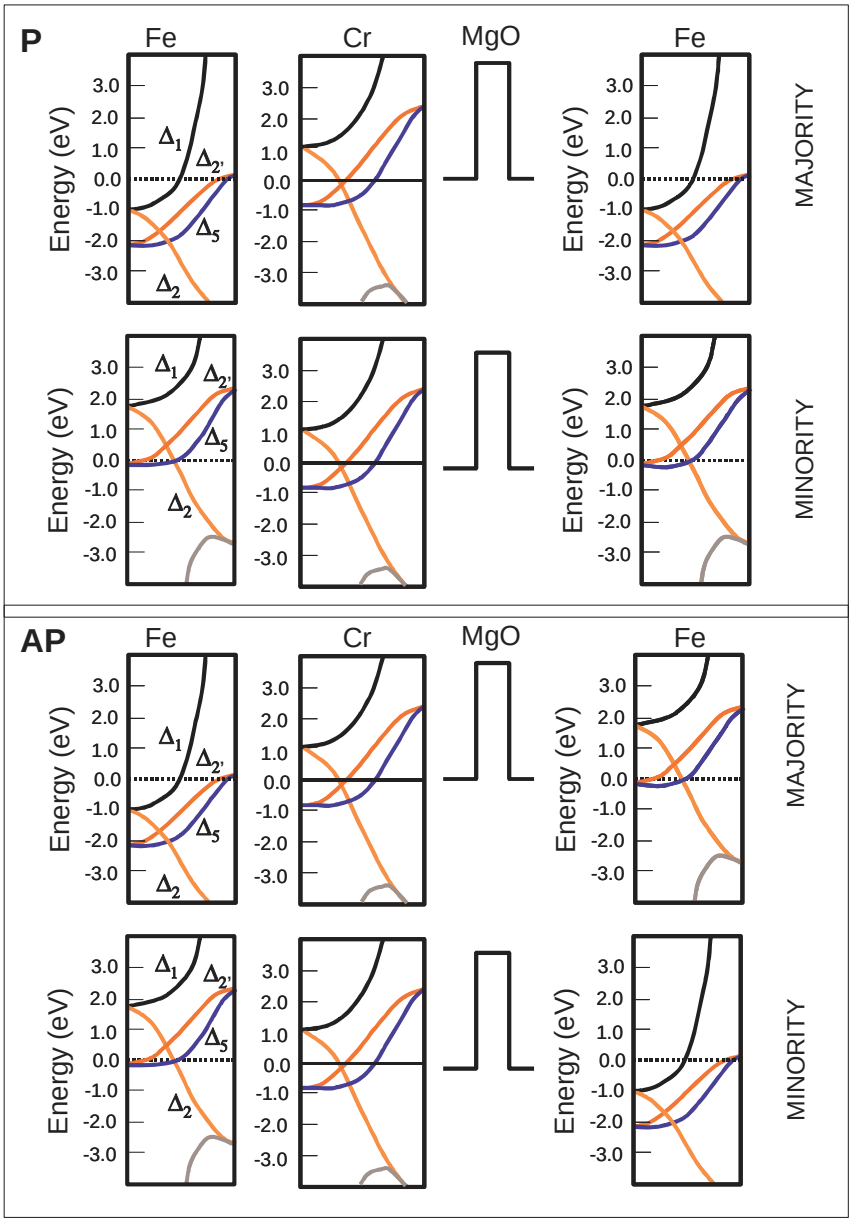

Figure 9.1: Bulk band structure diagram for bcc Fe and Cr, in parallel (P) and antiparallel (AP) magnetization configuration of the Fe/Cr/MgO/Fe MTJ. The top and bottom panels present the P and AP configurations, for the majority and the minority spins. From left to right, one can distinguish the band structure corresponding to the $\Gamma - X$ directions for the left Fe, Cr, and right Fe electrodes

PARALLEL CONFIGURATION

Majority spin

At the Fermi level a propagating Δ_1 state from the Fe will find no available state in the Cr. Then, as seen from the band structure diagram of Cr, we can model the Cr by a barrier of $1eV$ height and d_{Cr} thickness with respect to the Δ_1 symmetry. Then, the next rectangular barrier corresponds to the barrier height of MgO for Δ_1 electrons. One can immediately see that the

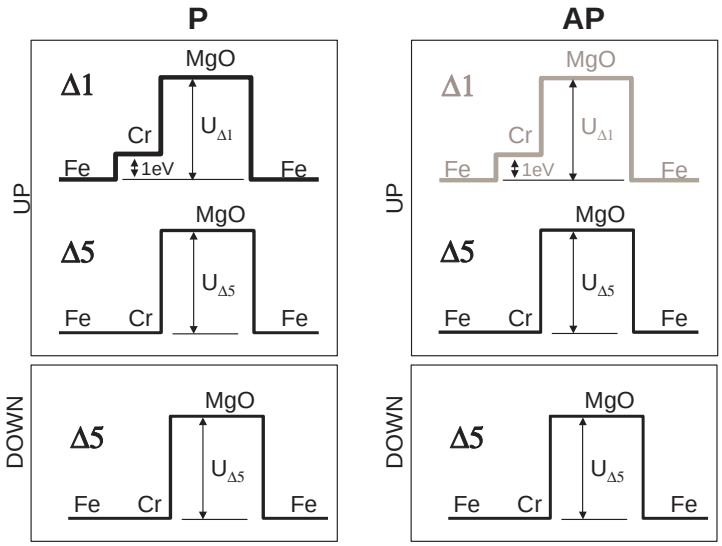

Figure 9.2: Potential profile seen by electrons corresponding to parallel and antiparallel configurations of the magnetizations, in a multichannel model, each channel being associated to a given symmetry and a given spin. U_{Δ_1} and U_{Δ_5} represents the corresponding barrier heights of the MgO for the $\Delta_{1,(5)}$ electrons. The Cr constitute a barrier of $1eV$ for the Δ_1 electrons comming from the Fe.

conductivity of this channel will exponentially decrease when the thickness of the Cr increases. The Δ_5 symmetry injected from Fe can 'freely' propagate in Cr (no additional barrier). The MgO will provide then a barrier height $U_{\Delta_5} > U_{\Delta_1}$ which will give a smallest conductivity of Δ_5 (in case when the thickness of Cr is zero). From the band structure one can see that when biasing the junction, above 0.2V (which corresponds to the energy of the top of the Δ_5 band) the conductivity of the majority spin Δ_5 channel will vanish.

Minority spin

The Fe left emitter has no available Δ_1 electrons at Fermi level. Consequently, this conduction channel is not activated.

The minority Δ_5 electrons can freely propagate. However, above 0.2 eV their associated conductivity will saturate, because the bottom of the Δ_5 band is at -0.2 eV under E_F (if one takes into account the contribution of the tunneling of electrons under E_F when the junction is biased).

ANTIPARALLEL CONFIGURATION

Majority spin

In the AP configuration, the Δ_1 symmetry injected from the left electrode finds no available state in the right electrode. Then, the only possible propagation will be via spin-flip events or via interfacial resonance states (as mentioned in the section consecrated to the standard Fe/MgO/Fe junctions). However, here again the associated conductivity will rapidly vanish when the thickness of Cr increases.

On the other hand, the conductivity associated to the Δ_5 electrons channel will be important. From the bands structure diagrams one can see that this conductivity gradually increases with the bias voltage. When the conductivity of the Δ_1 channel is quenched for larger Cr layer thickness, the Δ_5 contribution becomes dominant.

Minority spin

For the minority spin in the AP configuration, the only propagating symmetry available in the metallic electrodes Fe and Cr is the Δ_5. However, its related conductivity channel will vanish above 0.2eV which corresponds again to the top of the Δ_5 band in the right Fe electrode.

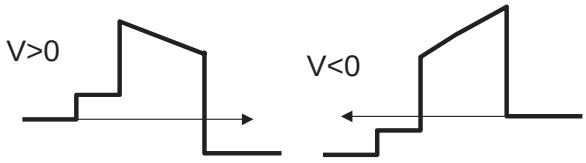

Figure 9.3: Potential profile corresponding to the Δ_1 channel of the majority spin under positive (left) and negative (right) applied bias.

In Figure 9.3, we illustrate the shape of the potential profile corresponding to the biased junction for the majority Δ_1 electrons. From these diagrams we expect, firstly, asymmetric conductivity versus voltage curves in positive and negative voltages. Moreover, one can see that the conductivity of the Δ_1 channel can be drastically increased in negative voltage when the energy of the hot electrons arriving in the left electrode overcomes the barrier height of Δ_1 electrons in Cr (bottom panel of Figure 9.3).

9.3 Experimental results

Following these 'rough' theoretical considerations and expectations we address now the experimental results.

9.3.1 Sample elaboration and structural properties

The samples are elaborated by Molecular Beam epitaxy, following the procedure described for single crystal Fe/MgO/Fe MTJ. On the MgO(100) substrate degassed at 600° a first underlayer of MgO is used to trap the residual carbon impurities. A 26 nm thick Fe buffer layer is then epitaxially grown at room temperature then annealed at 450° for 20 minutes. A wedge shaped Cr layer with a variable thickness from zero to 0.9 nm is intercalated between the bottom Fe electrode and the 3nm thick MgO barrier epitaxially grown on top. The Cr grows on Fe layer by layer, leading to atomically flat films. On the barrier, the magnetically hard top electrode of the junction, constituted by Fe(6nm)/Co(20nm) is grown. A capping layer protects the multilayer stack for further ex-situ processing of the samples. The Figure 9.4 illustrates the complete multilayer structure of the MTJ stack.

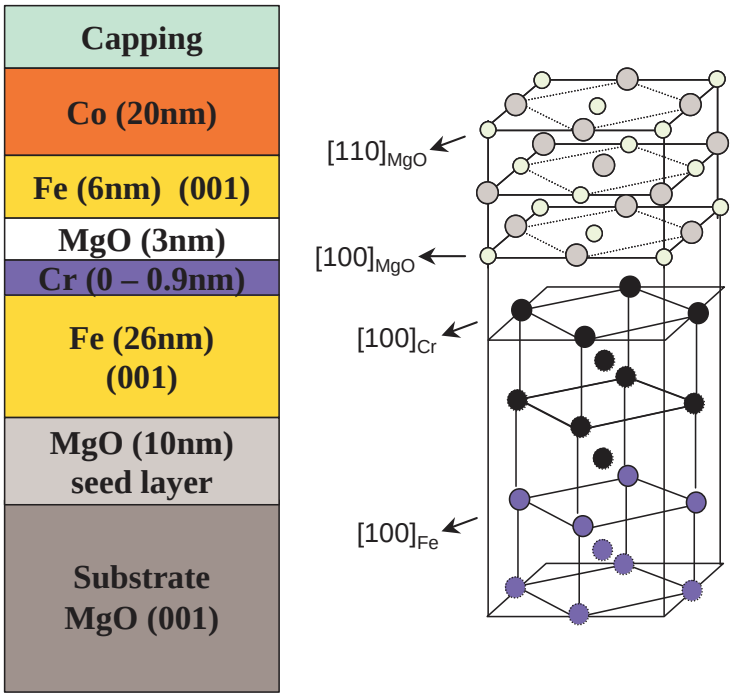

Figure 9.4: Structure of the multilayer stack (left) and epitaxy relations for the Fe/Cr/MgO system.

After the epitaxial growth of the continuous layers, micrometric sized magnetic tunnel junctions are patterned by optical lithography and ion etching techniques. The magneto-electric measurements presented here have been performed on a single sample. The wedge shape of the Cr insured a variable Cr thickness in MTJ devices having the same bottom electrode, barrier and top counter-electrode. Different Cr thickness can be addressed on the wafer by the choice of the lateral position of the patterned MTJ .

One of the most important aspects concerning the electronic transport in the Fe/Cr/MgO/Fe/Co MTJ is related to the crystallographic structure of this system. Due to the almost similar lattice parameter of the bcc Fe and Cr, a perfect epitaxy insures the conservation of the symmetry across the stack. Similarly to the standard Fe/MgO MTJs, the MgO will grow epitaxially on Cr, via a lattice rotation by 45°. All the aspects related to symmetry of the Bloch functions valid in standard single crystal junctions will remain valid here. The conservation of the symmetry insure the conservation of the propagation vector $k_{\|}$. The theoretical framework of tunneling remains close to the Landauer ballistic model. Like in standard junctions, the local defects where the symmetry is broken will affect the statistics of the spin dependent tunnel transport in the junction. Among these structural defects we can mention again the terraces and the dislocations in Fe, within the MgO barrier and at the interfaces.

9.3.2 Magneto-transport properties

The magneto-electric measurements have been performed on micrometric MTJs, using the following convention. In positive voltage the electrons flow from the bottom Fe/(Cr) to the top

Fe/Co electrode.

In Figure 9.5 we illustrate the evolution of the dynamic conductivity with the thickness of the Cr, in both parallel and anti-parallel configurations. The first panel corresponds to a standard Fe/MgO/Fe sample, the second one to a sample with an intermediate 0.6nm Cr layer and the third one to a 0.9nm Cr thickness. The area resistance $R \times A$ of the junction measured at 10mV in the parallel configuration, doubles from the standard sample (47 k$\Omega\mu m^2$) to the 0.9m Cr sample (90 k$\Omega\mu m^2$). This would indicate an additional filtering effect of electrons related to the Cr layer, assuming that the MgO barrier is the same for all the samples with variable Cr thickness. However, we are aware that this is an only rough assumption. Differences concerning the growth of MgO on Fe or Cr with different thickness cannot be excluded, leading to possible structural differences in the MgO. More detailed studies using cross-section Transmission Electron Microscopy are in progress to check these aspects.

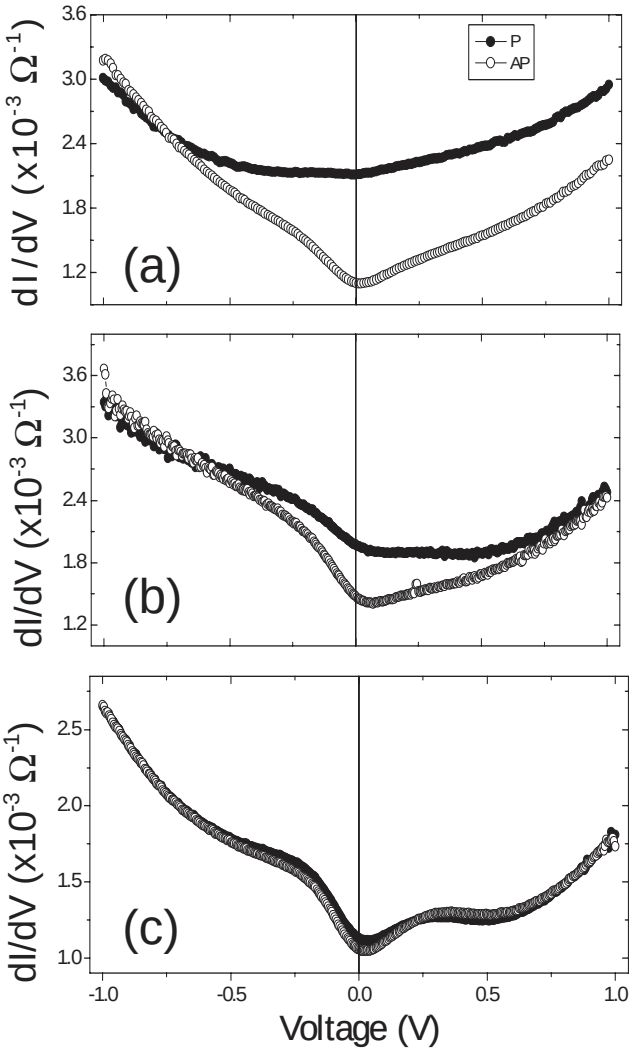

Figure 9.5: Dynamic conductivity versus voltage in parallel (-●-) and antiparallel (-○-) configuration of magnetization. (a) Standard Fe/MgO/Fe MTJ; (b) Fe/Cr(0.6nm)/MgO/Fe MTJ; Fe/Cr(0.9nm)/MgO/Fe MTJ.

A visual rough comparison between the three samples indicates that the effect of Cr is dramatic with respect to the parallel dynamic conductivity. One can see that the shape of this conductivity evolves toward the anti-parallel conductivity shape for the thicker Cr sample. Using the multi-channel model from the previous paragraph we will explain this evolution of shape by the vanishing of Δ_1 majority spin channel contribution to the conductivity when the Cr thickness increases.

In Figure 9.6 we illustrate schematically the expected shape of the conductivity in standard MTJs (a) and in Fe/Cr/MgO/Fe MTJs (b). As explained in a previous chapter, in standard MTJs at low voltage an additional conductivity term related to the Δ_5 electrons is superimposed to the parabolic Δ_1 related G(V). This will lead to a total conductivity versus voltage curve showing two minima around 0.2V, corresponding to the top of the Δ_5 band of the majority spin electrons. On the other hand, for the samples Fe/Cr/MgO/Fe, from the electronic structure diagrams depicted in Figure 9.1 one can remark the absence of the Δ_1 symmetry in Cr. This implicates that this symmetry will be evanescent in both Cr and MgO. An additional barrier of 1eV for only the Δ_1 electrons, with the thickness equal to the Cr thickness, is added to the standard MgO barrier. This explains the reduction of the Δ_1 associated conductivity when the Cr thickness increases. However, this conductivity can be increased by biasing the junction. This is show in Figure 9.5(b). At low voltage, the Δ_1 related conductivity is small, and it increases abruptly with the voltage. The inflection point around 1V corresponds to the barrier heights seen by the Δ_1 electrons in Cr. Here again, the Δ_5 electrons will provide an additional conductivity channel at small voltages ($< 0.2V$). The total conductivity will have a shape presenting a strong dip at small voltages (related to the strong reduction of the Δ_1 channel) and two local minima related to the vanishing of the Δ_5 contribution above 0.2eV.

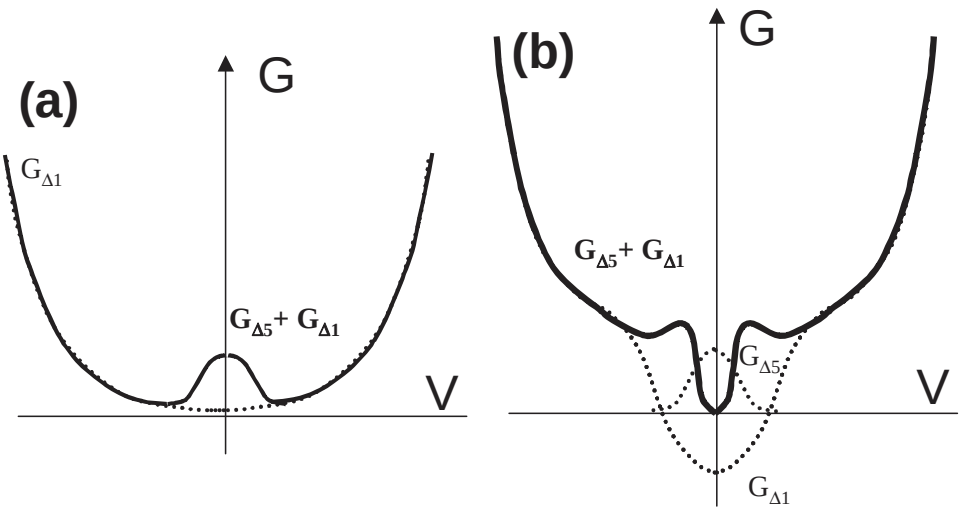

Figure 9.6: Representation of the conductivity G versus voltage V in standard Fe/MgO/Fe junctions (a), and Fe/Cr/MgO/Fe junctions (b). The two local minima correspond to the vanishing of the Δ_5 conduction channel above 0.2eV, and the dip observed at low voltages in the P configuration for the Fe/Cr/MgO/Fe system (b) corresponds to the strong attenuation in Cr of the Δ_1 symmetry.

From the models depicted in the Figure 9.1 and Figure 9.2 one can discretize the conductivity in the parallel and the anti-parallel configuration.

$$G_P = G^{\uparrow}_{\Delta_1} + G^{\uparrow}_{\Delta_5} + G^{\downarrow}_{\Delta_5} \tag{9.1}$$

$$G_{AP} = G^{\star\uparrow}_{\Delta_1} + G^{\uparrow}_{\Delta_5} + G^{\downarrow}_{\Delta_5} \tag{9.2}$$

Following the band structure diagrams depicted in Figure 9.1, one can qualitatively evaluate the voltage variation of the parallel and the antiparallel conductivities. The term $G^{\uparrow}_{\Delta_1}$ vanishes when the Cr thickness increases. Its contribution can be increased by biasing the junction to overcome the additional barrier height in Cr. The $G^{\uparrow}_{\Delta_5}$ vanishes above 0.2V and $G^{\downarrow}_{\Delta_5}$ saturates above 0.2eV (contribution of states below the Fermi level). In the antiparallel conductivity the channel $G^{\star\uparrow}_{\Delta_1}$ is related to the interfacial resonance assisted mechanisms or spin-flip events. It vanishes again when the Cr thickness is increased. The dominant term in the AP conductivity is $G^{\uparrow}_{\Delta_5}$ which, following the band structure diagrams, increases when the voltage increases. The last term $G^{\downarrow}_{\Delta_5}$ will vanish above 0.2V. From this rough analysis one can observe that at small voltage for large Cr thickness $G_P \to G_{AP}$, the conductivities being in both configurations related to the Δ_5 channels. Moreover, having in view the increase with the voltage of $G^{\uparrow}_{\Delta_5}$ in the AP configuration, one can expect that above a given voltage $G_P < G_{AP}$ which will lead to a sign reversal of the TMR.

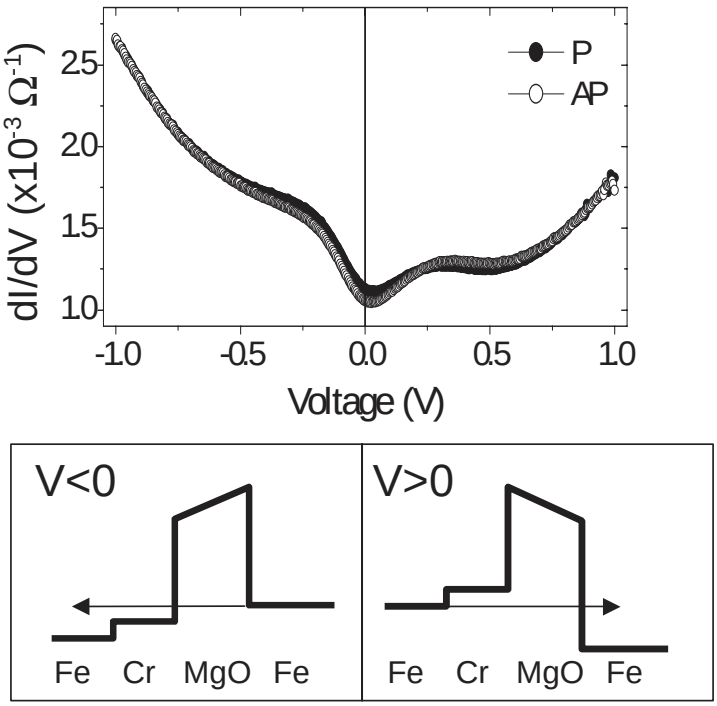

Figure 9.7: Conductivity versus voltage curve (top panel) and corresponding potential profile model for Δ_1 channel for Fe/Cr(0.9nm)/MgO/Fe MTJ. In positive voltage the electrons are injected from the bottom Fe/Cr toward the top Fe electrode.

The Figure 9.7 validates the potential model from Figure 9.2. It corresponds to the 0.9nm Cr

One can observe that the G(V) is asymmetric in positive and negative voltages. In negative voltages, the conductivity is larger and increases more quickly with the voltage which reduces the barrier height of the Δ_1 electrons. In positive voltage, the electrons see continuously two barrier heights: one related to the MgO and the one related to the Cr.
The fact that the Cr layer behaves as an additional barrier with respect to the Δ_1 symmetry is clearly demonstrated in the Figure 9.8. This figure presents the exponential decrease of the parallel conductivity as a function of Cr thickness. We have already pointed out that the main contribution to the conductivity across the MgO barrier corresponds to the Δ_1 channel. One can observe the exponential decay of G_P with the Cr thickness which corresponds to the evanescent propagation of the Δ_1 symmetry across the Cr metallic layer. On the other hand, in the same picture we depict the conductivity in the antiparallel configuration. In contract to G_P, this conductivity remains constant when the Cr thickness increases. This result is consistent with the fact that G_{AP} is dominated by the Δ_5 symmetry channel, whose propagation is not affected by the Cr (see the model from Figures 9.1 and 9.2).

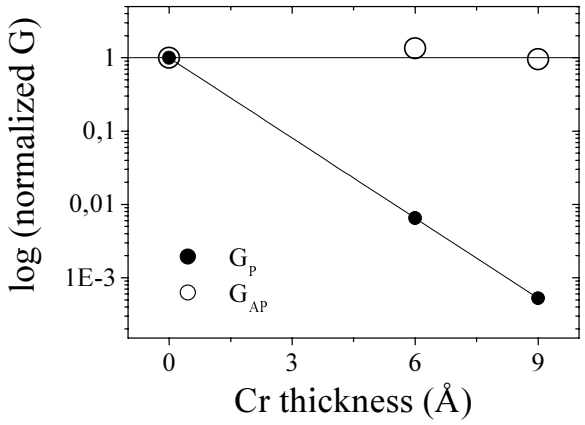

Figure 9.8: Variation of the normalized conductivity with the Cr thickness in logarithmic scale.

The tunnel magnetoresistance versus voltage curves for the extreme situations (0nm and 0.9nm of Cr) are illustrated in Figure 9.9. The curves are measured at room (RT) and liquid nitrogen (80K) temperatures. The left panel corresponds to the standard Fe/MgO/Fe MTJ. The reduced value of the TMR amplitude with respect to the maximum TMR value reported in standard Fe/MgO/Fe junctions (180%) is explained by a reduced structural quality of the top Fe/Co electrode. Here, on the same sample we have a variable Cr thickness provided by the Cr wedge. In order to avoid some Fe/Cr mixing effects, we did not annealed the top Fe/Co to enhance its structural cristalline quality and provide larger TMR. Then, the assymetry between the positive and the negative branch of the TMR reflects the different structural quality and electronic properties of the bottom and top Fe(001) electrodes of the MTJ. The large positive TMR measured in these junctions is related to the large positive tunneling polarization of Fe provided by the Δ_1 electrons. It is trivial that by reducing the conductivity of the Δ_1 channel, when the Cr is intercalated between Fe and MgO, the TMR amplitude will be reduced. This is clearly illustrated in the right panel of the Figure 9.8. Moreover, we observe here that in positive voltage the sign of the TMR reverses. As explain before, this is related to the situation when

the $G_{AP} > G_P$ (when the $G^{\uparrow}_{AP\Delta_5}$ term becomes dominant) in a regime where $G^{\uparrow}_{\Delta_1}$ is drastically reduced by the Cr. On the other hand, in negative voltage, the sign of the TMR remains positive. This validates again the potential profile model from Figure 9.7 (Figure 9.2) where we see that the barrier height of Δ_1 is lowered by the negative voltage and therefore the $G^{\uparrow}_{\Delta_1}$ term will dominate providing a $G_P > G_{AP}$.

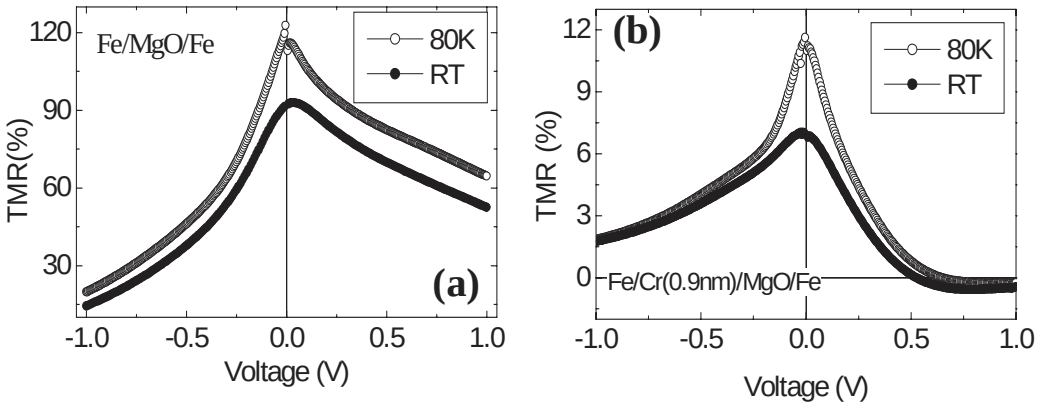

Figure 9.9: Tunnel magneto-resistance versus voltage curve at room temperature and 80K for Fe/MgO/Fe MTJs (a) and Fe/Cr(0.9nm)/MgO/Fe MTJs (b).

We conclude that, in a coherent tunneling regime where the tunneling electrons are selected in the Fe(001) single crystal electrodes, the Cr acts as an additional metallic potential barrier for the Δ_1 Bloch states. Based on this results and on the electronic structure of bcc Fe and Cr along the Γ direction (Figure 9.1), we build symmetry dependent quantum-well (QW) structures: an Fe(001) ad-layer with variable thickness d = 7-21ML is introduced between Cr(6ML) and MgO. This interfacial layer behaves as a QW structure for the propagating Δ_1 electrons which will be confined between the Cr and MgO barriers (Figure 9.10(a)). In negative voltage the electrons injected from the E_F from the top (right) Fe layer may scan in energy the resonant levels in the bottom Cr/Fe/MgO well ((Figure 9.10(b))). In positive voltage, the electrons arrive always at E_F in the Cr/Fe/MgO QW (Figure 9.10(b)) and therefore no resonant level can be activated/scanned. The first effect of the Fe interfacial ad-layer is to completely restore the TMR ratio compared to pure Fe/MgO/Fe MTJs. Interesting features related to the quantum confinement of the Δ_1 electrons in the Cr/Fe/MgO QW are demonstrated by tunnel spectroscopy experiments ($G(V) = dI/dV$ and $dG/dV = d^2I/dV^2$). These measurements are compared to those measured on standard Fe/MgO/Fe MTJs (Figure 9.11). An oscillatory behavior of G_P (sensitive to the Δ_1 channel) is observed in negative voltage (Figure 9.11(a)), whereas no change appears for G_{AP} and $V > 0$. These oscillations are highlighted on the d^2I_P/dV^2 curves in negative voltage (Figure 9.11(b)) for variable Fe d thickness. A clear dependence of the distance between the resonant levels and their position in energy is observed as a function of the Fe well thickness (Figure 9.11(b)). As expected for a standard QW, when the well thickness increases the levels get closer and the energy of the first level is decreased ($E(n) \sim n^2/d^2$, n indexing the level).

Another interesting aspect is related to the temperature variation of the TMR in the two different

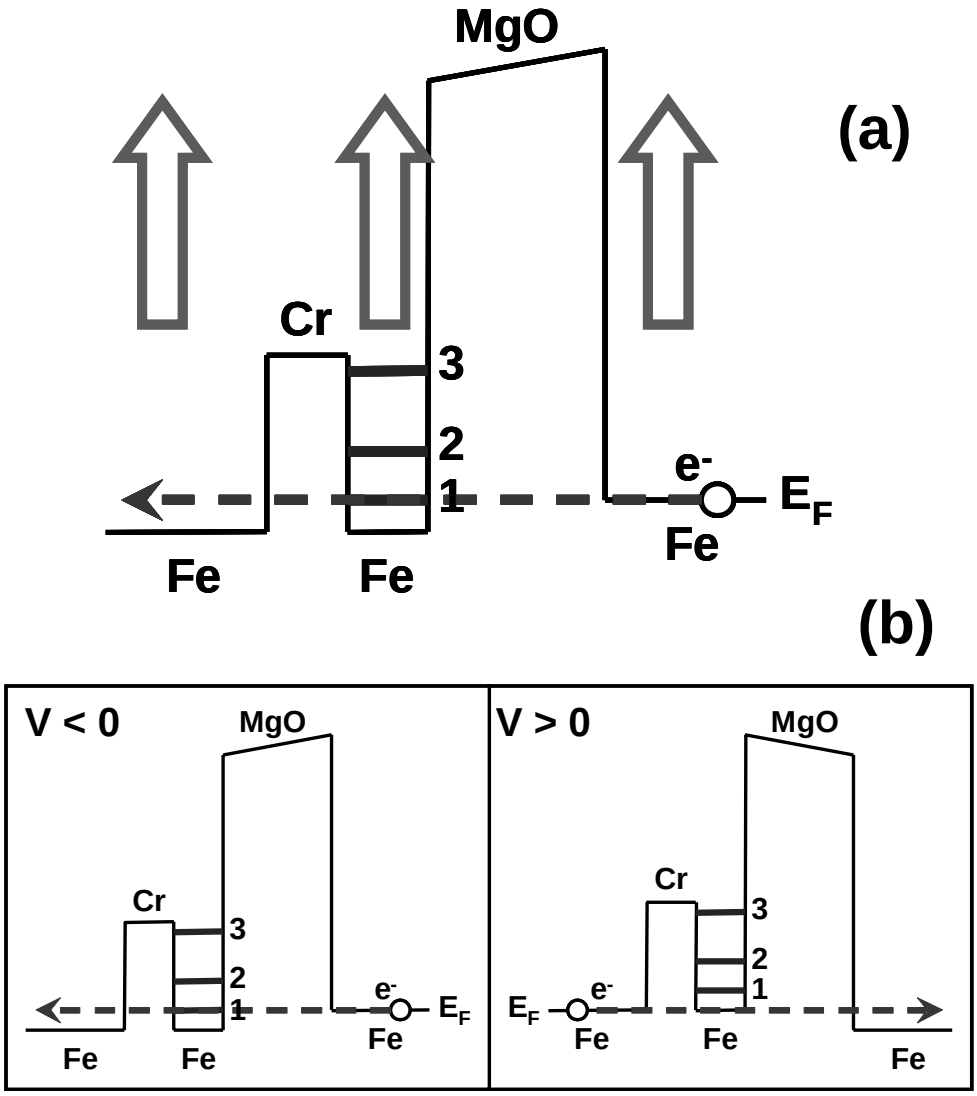

Figure 9.10: (a) Schematic representation of the potential profiles seen by Δ_1 electrons in parallel magnetization configuration in Fe/Cr/Fe/MgO/Fe MTJs. (b) Potential profile in negative and positive bias voltage.

systems. In standard Fe/MgO/Fe junctions (left panel) the TMR variation with voltage is almost equivalent within all the voltage range. The $R \times A$ in the P configuration varies slightly with temperature (4% variation) from 47 $k\Omega\mu m^2$ (RT) to 49 $k\Omega\mu m^2$ (80K). On the other hand, in Fe/Cr0.9nm/MgO/Fe MTJ (right panel) one can see a completely different behavior. A strong variation of TMR amplitude (100% variation) is measured from RT to 80K. The $R \times A$ in the P configuration records a 18% variation, from 90 to 107 $k\Omega\mu m^2$. Moreover, the variation with the temperature of the TMR is not constant with the voltage. It decreases with the voltage, especially in the negative voltage range where the barrier height of the Δ_1 electrons is lowered by the bias and their contribution to the tunneling is enhanced. At low voltages, the thermal variation of the $G^{\star\uparrow}_{AP\Delta_1}$ (interfacial resonance assisted tunneling, spin-flip events) may be significantly important and explain the strong variation of G_{AP} within this voltage

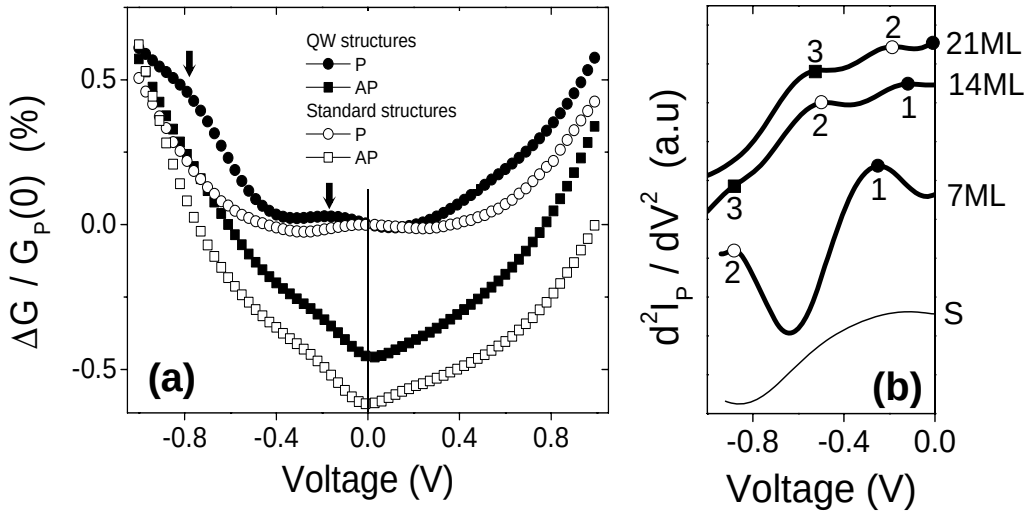

Figure 9.11: (a) Relative variation of $G_{P(AP)}(V)$ in standard Fe/MgO/Fe MTJs and in QW Fe/Cr(6ML)/Fe(7ML)/MgO/Fe MTJs. The arrows point local maxima in the P conductivity. (b) $d^2I_P/dV^2(V)$ curves in Fe/Cr(6ML)/Fe(d)/MgO/Fe MTJs for variable d = 7, 14, 21ML thickness compared to the derivative of the parallel conductivity in standard (S) Fe/MgO/Fe MTJs. The numbers point maxima of the parallel dynamic conductivity in negative voltage. They correspond to the position of the resonant levels in the QW. For d = 21ML the first level is too close to $V = 0$ within the resolution of our experiment.

range. Further experimental and theoretical investigations have to be performed to explain this interesting behavior.

In the analysis of the results presented in this section we neglected the possible quantum well effects in the Cr layer, of finite small thickness. The investigation of this kind of effects represents future interesting perspectives of the current study. From an experimental point of view, this new analysis will require a dense network of adjacent junctions which should provide a gradual variation of Cr thickness from junction to junction, on the same wafer. In the current study, we have been limited by a network of MTJ allowing to investigate only three thickness zones. Moreover, here again a more detailed theoretical investigation (i.e.) can be performed, in order to describe more quantitatively the physics of tunneling in the Fe/Cr_{thin}/MgO/Fe magnetic tunnel junctions.

Recent theoretical calculations, using ab-initio techniques, performed in IPCMS Strasbourg confirm our simple theoretical approach. They illustrate the Cr thickness dependence of the tunnel conductivity. We present in Figure 9.12(a) the conductance G for each spin channel (P↑, P↓, AP↑ and AP↓) as a function of Cr thickness x. We see that $G_{\mathrm{P}\uparrow}$ decreases with increasing x and reaches the low conductance of the other spin channels for x=6, which remain broadly constant for all x. This confirms the filtering effect of the Cr layer.

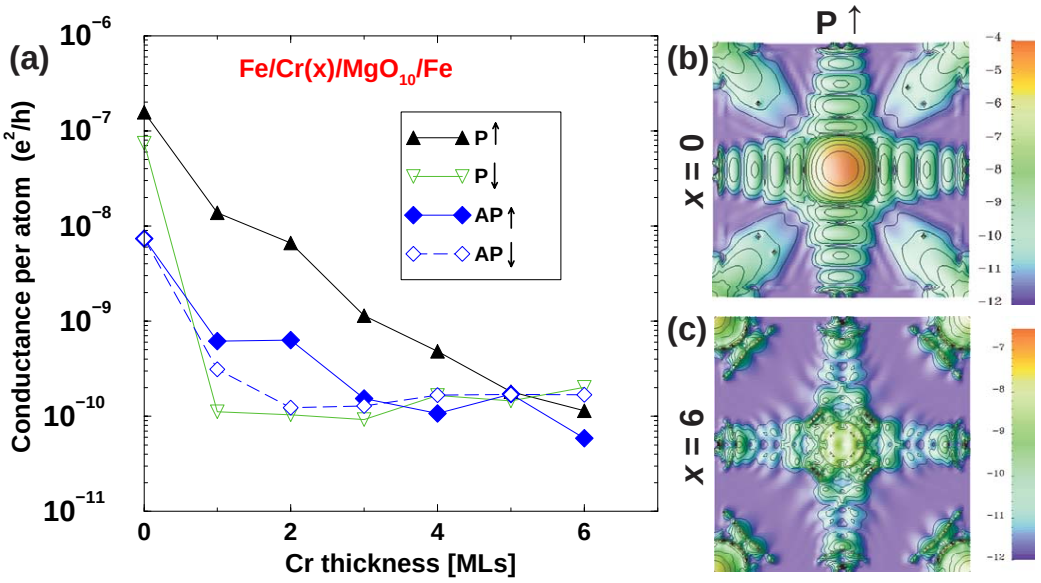

Figure 9.12: Fe / Cr (x ML) /MgO (10 ML) / Fe: (a) evolution of the P↑, P↓, AP↑ and AP↓ conductance channels with increasing Cr thickness x. Transmission probability of the dominant P↑ conductance channel as a function of $k_{||}$ for (b) x =0 and (c) x =6. The calculation has been performed by O. Bengone (IPCMS) using a surface Green's function technique implemented within the framework of a tight-binding linear muffin-tin orbital approach.

9.4 Résumé de chapitre en français

Transport tunnel polarisé en spin dans des jonctions monocristallines de type Fe/Cr/MgO/Fe.

Ce travail s'effectue en collaboration directe avec l'Institut de Physique et Chimie des Matériaux de Strasbourg. Des échantillons qui combinent des couches monocristallines de Fe et MgO sont élaborées par la technique d'épitaxie par jet moléculaire. Nos avons étudié l'effet d'une fine couche de Cr (épaisseur variable inférieure à 1nm) intercalée entre le Fe et la barrière de MgO. Les jonctions classiques sans Cr de type Fe/MgO/Fe présentent des fortes valeurs de magnétorésistance tunnel, jusqu'à 180% à la température ambiante.

Le premier effet qu'on observe lorsqu'on rajoute la couche de chrome est la réduction de l'amplitude de la magnétorésistance tunnel. Ceci nous prouve le fait que le Cr constitue une barrière de potentiel supplémentaire pour la propagation de l'état Δ_1 dans la configuration parallèle de l'aimantation. En effet, les mesures de magnéto-transport effectuées sur les échantillons, temoignent d'une plus grande sensibilité du transport tunnel par rapport à la propagation de la symétrie Δ_5.

De plus, en augmentant l'épaisseur de la couche de chrome, nous pouvons ajuster l'amplitude de la polarisation tunnel pour les états qui se propagent par effet tunnel à travers la barrière. Pour des épaisseurs de Cr qui tendent vers 1nm les configurations magnétiques parallèle et antiparallèle de la jonction deviennent équivalentes en termes de propriétés de magnéto- transport.

La propagation de l'état de Bloch de symétrie Δ_1 peut être alternativement modulée par la tension électrique appliquée sur la jonction. Ceci permet de changer également le signe de la polarisation tunnel des états Δ_5 ce qui explique le changement de signe de la TMR avec la tension appliquée.
Ces résultats montrent que l'adjonction de Cr à l'interface Fe/MgO agit comme une barrière de potentiel additionnelle pour les états de symétrie Δ_1. L'avancé majeure de cette étude a été de montrer qu'un métal pouvait être utilisé comme barrière de potentiel de par la grande sensibilité des jonctions tunnel monocristallines à la structure électronique et ses symétries. Cette interprétation a été confirmée par une série d'échantillons additionnels type jonctions tunnel monocristallines bcc Fe(001) / Cr(001)/ Fe$\star$(001) /MgO(001)/Fe(001). La couche de Fe$\star$(001) adjacente à la barrière de MgO constituera un puits de potentiel pour les électrons de symétrie 1 qui seront ainsi confinés entre la barrière métallique de Cr et la barrière classique de MgO. Les effets de confinement dans ce puits de potentiel ont été étudiés en faisant varier l'épaisseur de bcc Fe $\star$(001) de 0 à 21 monocouches (ML). Dans les courbes de conductance différentielle représentés nous observons très clairement apparatre des oscillations dans les conductances dans l'état parallèle lorsque les électrons sont injectés du Fe supérieur dans la tricouche Fe/Cr/Fe.
Afin d'expliquer les résultats expérimentaux nous proposons un modèle très simple de type multicanal, qui est validé par des calculs ab-initio récentes.

Chapter 10

Magneto-transport in single crystal Fe_3O_4/MgO/Co magnetic tunnel junctions

10.1 Preliminary results

This research topics is developed within a research project between our research team and the CEMES laboratory from Toulouse. Within this project, the single crystal Fe_3O_4/ MgO(100) based magnetic tunnel junctions (MTJ) are elaborated in CEMES by ultra-high vacuum sputtering system. The patterning of the samples by UV lithography/ion etching and the magneto-transport experiments are performed in Nancy.

The Fe/Fe_3O_4/MgO/Co films were epitaxially grown on MgO(001) substrates by sputtering in a UHV chamber whose base pressure is 10^{-8} Torr. The Fe layer was deposited at room temperature using a magnetron system. The Fe_3O_4 was grown at 400°C with a radio frequency power under a 5.10^{-3} Torr Ar plasma pressure starting from Fe_2O_3 facing targets which is reduced in the plasma. Then MgO was grown at 100°C and Co at RT. An Au capping layer was then deposited to protect the whole stack from oxydation. The flatness of each layer and the epitaxial relationship between them have been checked by in-situ Reflection High Energy Electron Diffraction (RHEED).

The cross-sectional specimens for TEM studies were cut along (100)MgO planes, glued face to face then thinned by mechanical grinding and ion-milling to the electron transparency. The structures of the different layers and interfaces were investigated in CEMES by TEM both in conventional and in high-resolution mode (HRTEM) using a FEI-F20 microscope fitted with a spherical aberration (Cs) corrector (CEOS) whose point resolution is 0.13nm.

Figure 10.1 shows a low magnification TEM bright field image of the multilayer. The insulating barrier appears to be continuous over a long distance. An HRTEM micrograph of the stacking is reported in Figure 10.1(b) together with its corresponding Fourier Transform (Figure 10.1(c)). Both clearly evidence the good quality of the epitaxial growth separated by reasonably flat interfaces. Table I gathers the lattice parameters and effective misfits (roughly not exceeding 3%) between the neighbor relaxed layers. Co_1 and Co_2 notation depicts the

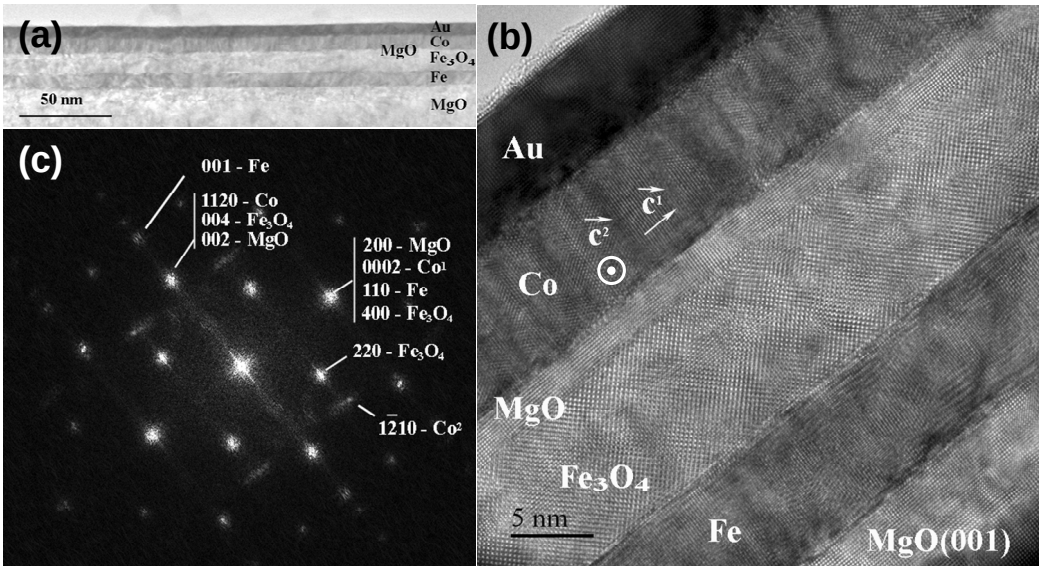

Figure 10.1: (a) low magnification TEM bright field image of MgO(001)/Fe/Fe_3O_4/MgO/Co/Au. (b) HRTEM image of the same stacking. (c) Fourier Transform of the 1(b) HRTEM image.

occurence of two variants in the *hcp* Co layer i.e. the hexagonal axis lying parallel to the interface plane and being parallel to the [100] or [010] direction of MgO. The two variants for the total epitaxial relationship are therefore : MgO-substrate(001)[100]//Fe(001)[110]// Fe_3O_4(001)[100]//MgO(001)[100]//Co_1(11-20)[0001] and Co_2(11-20)[1-100].

	crystal direction	lattice parameter	effective misfit
MgO subst.	[200]	0.21nm	
Fe (bcc)	[110]	0.203nm	+3.3%
Fe_3O_4 (fcc)	[400]	0.21nm	-3.4%
MgO (fcc)	[200]	0.21nm	<1%
Co_1 (hcp)	[0002]	0.203nm	+3.3%
Co_2 (hcp)	[1-100]	0.19nm	+9.5%

Table 10.1: Effective misfits between adjacent layers.

The spin polarized tunnel transport in this systems validates the filtering effects related to the symmetry dependent attenuation rate within the MgO(100) tunnel barrier. The Fe_3O_4 selects typically the *d*-like electrons to contribute to the tunneling and provides a negative polarization of electrons at the Fe_3O_4/MgO interface. Moreover, the MgO(100) barrier will have the smallest attenuation rate for the density of states components which belongs to Δ_1 symmetry. Therefore, the tunneling polarization of the Co will be mainly related to the *d* component of the Δ_1 symmetry. Following the electronic structure of the bcc Co(100), this polarization will change the sign at 0.2eV above the Fermi level.
These electronic structure characteristics are validated by the experimental magneto-transport measurements. In negative voltage, the TMR decreases and reaches its maximum value at -0.2V

(-8.5% at 300K and -22% at 80K). In positive voltage, one can notice a rapid increase of the TMR and a net change of its sign at 80K at +0.3V, this latter being more reserved at 300K. At +0.6V, the positive TMR achieves a maximum value (+5%) as shown by the inset in Figure 10.2.

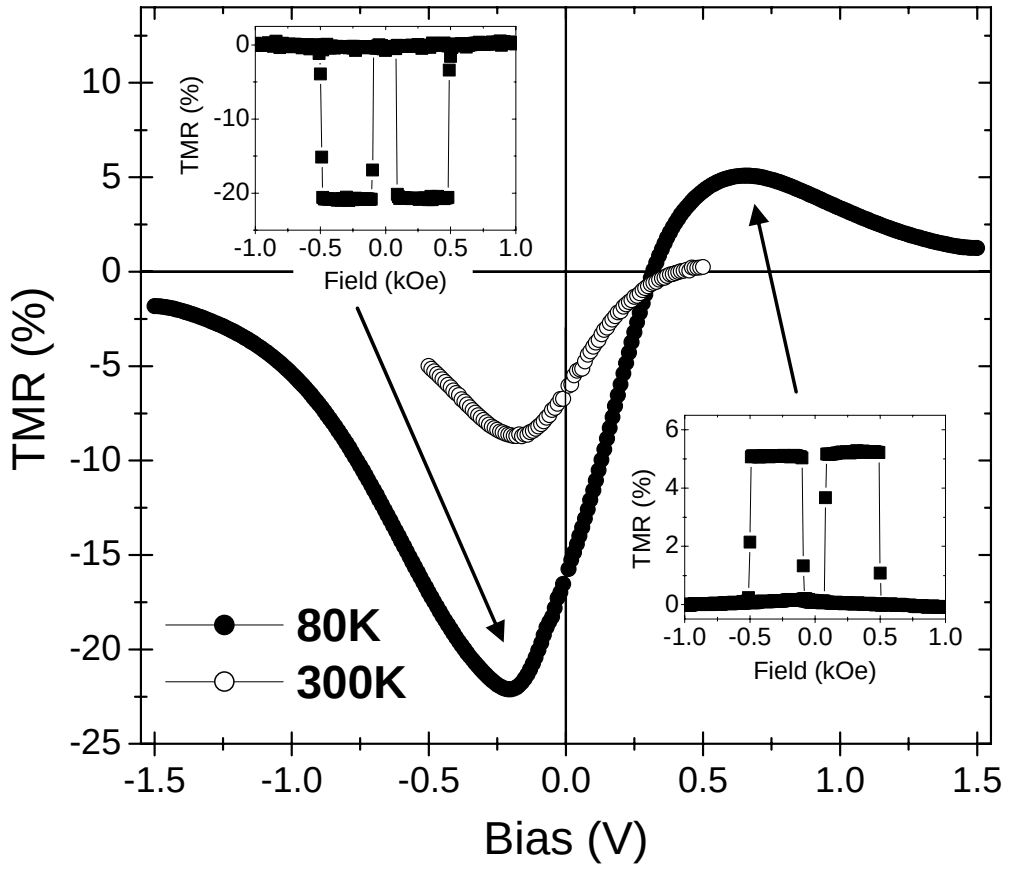

Figure 10.2: TMR versus bias curves in $Fe/Fe_3O_4/MgO/Co$ MTJs at 300K (open circles) and 80K (full circles). Inset : TMR versus field curves at 80K for V = -0.2V (-22% TMR) and V = +0.6V (+5% TMR).

Interestingly, our magneto-transport measurements depict an abrupt switching of the Fe/Fe_3O_4 bilayer at small applied magnetic fields (see insets in Figure 10.2). This leads to a flat and enduring plateau of 500 Oe where the Fe_3O_4 magnetization remains homogeneous. This behavior highlights better magnetic properties of the Fe_3O_4 layer. Indeed, the Fe_3O_4 magnetization has been previously reported to be hard to saturate because of the occurrence of anti-phase boundaries (APBs)[130]. Therefore, in our samples, we argue a drastic reduction of the APBs because of the abrupt switching of the soft bilayer followed by full saturation leading to a large operating field window.

Understanding the specific bias dependence of the TMR remains difficult. The negative spin-polarization of the Fe_3O_4[131, 132, 133] is widely accepted and has been experimentally proved for Fe_3O_4(001)[134, 135]. Bataille *et al*[136] have also found a negative spin-polarization at Fe_3O_4/γ-Al_2O_3 using spin-resolved photoemission. However, their spin-dependent tunneling

experiments in Fe_3O_4/γ-Al_2O_3/Co MTJ suggests a negative Co tunnel polarization. In our samples, according to the negative TMR, a positive polarization of Co is suggested. Moreover, this polarization changes with applied voltage as shown by the change in sign of the TMR. The influence of the barrier on the spin-polarization of the tunneling current has already been highlighted by DeTeresa *et al*[137]. In their study, the authors have demonstrated that the barrier can induce a reverse of the tunneling current. Our results show again that the relevant parameter to describe the spin polarized transport in MTJs is the tunneling polarization and not only the electrode polarization. Furthermore, in MgO epitaxial based MTJs, the role of the barrier has already been demonstrated to be symmetry dependent[74]. This makes impossible the analysis of transport using such a simple model. Thus, to have a complete understanding of the observed phenomenon, calculations on the interfacial polarization for both Fe_3O_4/MgO and MgO/Co(hcp) are needed.

10.2 Résumé de chapitre en français

Propriétés de magnéto transport des jonctions tunnel de type Fe_3O_4/MgO/Co

Cet axe de recherche s'effectue dans le cadre d'une collaboration qui vient de démarrer entre notre group et le laboratoire CEMES (Toulouse). Des échantillons monocristallines de type Fe(100)/Fe_3O_4/MgO(100)/Co(100) sont élaborés à Toulouse à l'aide d'un bti de pulvérisation cathodique sous ultra- vide. Leur qualité monocristalline est validée par des analyses détaillées en utilisant la microscopie électronique en transmission. Le transport tunnel polarisé en spin dans ces systèmes valide les effet de filtrage liés à l'atténuation dépendante en symétrie des fonctions d'onde de Bloch dans les barrières de MgO(100).
Le Fe_3O_4 sélectionne typiquement les électrons de type *d* pour contribuer au transport tunnel et fournit une polarisation de spin négative à l'interface Fe_3O_4/MgO. La barrière de MgO, quant à elle, aura le taux d'atténuation le plus faible pour les électrons qui appartiennent aux symétries $\Delta_{1(5)}$. Ainsi, la polarisation tunnel du cobalt sera aussi principalement liée à la composante *d* de la symétrie $\Delta_{1(5)}$. Selon l'analyse de la structure de bande du cobalt bcc (100) nous observons que cette polarisation change de signe au-delà de 0.2eV au dessous de niveau de Fermi.
Les propriétés électroniques du système sont directement validées par les mesures de magnéto-transport. En tension négative les électrons sont injectés à partir du cobalt, qui à une polarisation tunnel positive au niveau de Fermi, vers le Fe_3O_4 qui à une polarisation négative. Ceci conduit à une TMR négative (-20 % à 80K, -10% à 300K). En tension positive, les électrons sont injectés à partir du Fe_3O_4 avec une polarisation négative vers Co dont la polarisation change de signe au dessous de 0.2eV. Ceci explique le changement de signe de la magnétoresistance observé en tension positive.

Part V

Perspective studies and scientific projects

Chapter 11

Research projects

This chapter summarizes the research projects which I would like to develop in the next future. They integrate directly the context of the scientific expertise acquired during the last years in the field of magnetism and spin electronics. The projects have two orientations: the first is experimental and the second theoretical.

11.1 Experimental activity

11.1.1 Spin and charge transport in magnetic tunnel junctions

This work is scheduled to be developed within a collaboration framework with several laboratories: SPINTEC (Grenoble), IPCMS (Strasbourg), CEMES (Toulouse), SP2M (CEA Grenoble). In or laboratory it implicates a close collaboration with other researchers (S. Andrieu, C. Bellouard, Mr. Hehn, F. Montaigne, B. Kierren).
The objectives of the project can be classified in two categories: those turned toward the fundamental comprehension of the tunnel magneto-resistance in MTJ systems based on crystalline barriers (MgO) and those turned toward the use of the large magneto-resistance properties of these systems to build new spin electronics devices. The overall objective of the upstream studies turned toward the fundamental aspects is to understand the complex physics of the tunnel transport in systems with a specific crystallographic symmetry. Standard ab-initio calculations will model the consequences on the transport of the crystallographic and chemical quality of interfaces and the tunnel barrier. Then, we will confront these theoretical results with those obtained in experiments. In this purpose, we envisage the elaboration of nanometric sized MTJ with low surface resistance, i.e. thickness of MgO lower than 1 nm in which we modulate the spin filtering efficiency via the chemical bonds at the interface metal/insulating barrier. Two distinct directions are envisaged: different 'chemical doping' (oxygen, carbon, etc...) and the quantum wells consisting in thin metallic layers (Ag, Cr).
Another particularly interesting research axis concerns the study of the effects related to the spin-orbit coupling on the tunnel transport spatial anisotropy. The spin-orbit interaction 'is introduced' by the use of Pd and Au active layers or some magnetic or non-magnetic alloys where the inversion symmetry is broken. This type of studies will be carried-out via tunnel magneto-resistance angular anisotropy measurements.

A special effort will be devoted to study in detail the surface electronic properties of the systems involved in the realization of the tunnel junctions. The spin polarized surface state of Fe(100) will be studied in detail by Scanning Transmission Spectroscopy to elucidate the respective influence of structural defects (dislocations, terraces) and different adsorbed atoms. Moreover, another interesting phenomena which will be addressed relates to the confinement of the surface state. In this sense we envisage two types of structures. The first class involves the lateral confinement in small dimensionality objects, obtain by self-assembled growth. The second class implicates the realization of magnetically modulated structures (samples with up-down stripe domain structures). Here, the idea would be to confine the 2D electronic gas in the quantum well related to the exchange splitting in the ferromagnet. Some theoretical investigations of the last concept are in progress to estimate the effects of this kind of confinement. All these studies dedicated to the electronic properties of the surface represent important tracks for the engineering of new magneto-electrical characteristics of the tunnel junction device.
The control of the fundamental aspects such as the ballistic transport via the interfacial resonance states or quantum coherence phenomena will allow further studies on magnetic coupling and spin-torque effects in nanometric structures. The investigated tunnel junction devices will be elaborated by three techniques: Molecular Beam Epitaxy, sputtering and their combination. Hybrid systems will be elaborated in the new MBE/Sputtering elaboration complex whose experimental realization is in progress in our laboratory. The development of the elaboration procedure for crystalline MgO by sputtering is of primary importance. It will allow the technological transfer of the current know-how toward the technology of the electronic components.

The spin transfer in magnetic tunnel junctions

Low resistance-area product in epitaxial magnetic tunnel junctions is required for integration of MTJ in read-heads or high-density MRAMs and in MTJ-MRAM devices where the magnetization is switched by a critical current by spin-torque mechanisms. However, typically when the MgO thickness is reduced, the filtering efficiency within the MgO is reduced. Therefore, other filtering mechanisms have to be used on order to achieve one of the important milestones of our project: the optimization of MTJ devices with large TMR and low RA. We will addresse few of them: the filtering by the chemical bonding at the interface between the ferromagnetic metal and the MgO barrier, impurities in the barrier, resonant tunnel transport mechanisms. The understanding of spin transport mechanisms and related magnetic interactions represent an extremely important milestone towards the spin-torque/ magnetic switching implementation in MRAM devices. One of our objectives is the control of the resonant ballistic tunnel transport. This would make possible the development of MTJ having simultaneously low RA and high TMR, i.e. the ideal characteristics for devices based on the spin-transfer phenomenon. One of the important milestones of our project concerns the current-driven magnetic switching by spin-torque.
When the thickness of the tunnel barrier is reduced, interesting phenomena of magnetic coupling and spin-torque appear. The study of the TMR evolution with the voltage and with the current density, for different RA junctions, will allow the differentiation between the coupling and spin-torque phenomena.

The magnetic coupling is a torque effect created by the equilibrium tunnel currents. The following phenomena related to the coupling will be addressed in detail:

- The influence of the coupling on the magnetization reversal mechanisms.
- The variation of the coupling with the voltage (out-of-equilibrium coupling), the sign reversal of coupling (F /AF) in the voltage window where the TMR is reversed.
- The effect of the Fe(001) interfacial resonance on the AF coupling in Fe/MgO and Co(bcc)/MgO MTJ, the role of the interfacial impurities (C, O), etc...
- The effect of MgO bulk resonance on the coupling (O vacancies, metallic impurities: Fe, Cr...).

Specific studies on coupling will be carried out in junctions with a large RA (micron sized junctions).
The spin-torque is an out-of-equilibrium phenomenon which represents the transfer of moment between a net spin polarized current and the magnetization of a layer where the current flows [116, 117]. To induce spin-torque effects, a critical current density is required (about $10A/cm^2$). This implicates the nano-patterning of the MTJ objects of sizes below 150 nm by electronic lithography techniques. Among the planned studies concerning the spin-torque we enumerate:

- The commutation by current injection (magnetization reversal).
- The relationship between the amplitude of the TMR and the amplitude of the spin-torque spin. The critical current being inversely proportional to the TMR the larger he TMR is the smaller the critical current will be.

The spin transfer effects can be alternatively studied in 'lateral' device systems. Here, the electronic transport takes place in the plane of the film. The spin polarized current transfers a moment to a domain wall which can therefore be moved [118]. The specificity of our study would be the study lateral devices where the ferromagnetic layer has a surface state which is 100% spin polarized (i.e. Fe(100)). This would provide a large polarization of the current which should enhance a lot the torque efficiency. The studies will be performed in filiforme structures, pattened by electronic lithography, containing constrictions. The propagation of walls will be confirmed by magnetic force microscopy imaging.

11.1.2 Hybrid epitaxial magnetic tunnel junctions: synthesis, magnetotransport and low frequency noise

This project represents the kernel of the recent collaboration started with Prof. F. Aliev from the University of Madrid. Within this project we address the study of spin polarized transport in simple and hybrid MTJ devices by two complementary techniques: static magneto-transport measurements and dynamic noise measurements.
As shown in this manuscript, we have demonstrated the role of the interfacial electronic structure on the tunneling. The Fe/MgO interface engineering was shown to be a powerful tool for to

engineer high output voltage device applications. Special magneto-electric characteristics can be alternatively engineered in different ways. The TMR amplitude and its variation with voltage can be engineered by inserting a nonmagnetic metallic layer inside the barrier layer [119], the control of the TMR sign by choosing an appropriate ferromagnet/insulator barrier combination [108]. One can also list the possibility to control the characteristics of TMR devices by controlled doping of structures [120] or by intercalation of quantum wells structures [91]. A particularly interesting topics within the field of MTJs physics, from both fundamental and applied points of view, concerns the double barrier systems in which two tunnel barriers are separated by an intermediate thin metallic layer. This third electrode allows to control independently the voltage drop on the two tunnel barriers and adds an additional degree of freedom to adjust the magnetic tunneling characteristics. Theoretical studies in such hybrid double barrier TMR devices predict that by applying an external potential to the third electrode [121] one can control the TMR and the shot noise and optimize the signal to noise ratio.

From a fundamental point of view, the simultaneous study of nonequlibrium tunneling phenomena both via electron transport and current fluctuations is expected to provide new detailed information about the tunneling mechanisms. For example, the shot noise allows to distinguish between sequential or co-tunneling processes by comparing the measured shot noise with the one expected for Poissonian statistics [122]. This information is not accessible from the transport data only where average current is measured.

This project proposes collaborative research in the growth, structural characterization and electron transport measurements including low frequency noise of the hybrid epitaxial MTJs with MgO barrier. We plan to control the MgO barrier parameters by doping it with impurities or via insertion of the third electrode to which an external voltage could be applied to control both TMR and noise. The motivation from the fundamental point of view is to manipulate and investigate the electron tunneling statistics in TMR devices. This knowledge could provide new tracks to optimize the main parameters of the novel hybrid magnetic tunnel devices and possibly add new functionalities.

Our group, which has already demonstrated their expertize in realization of single crystal Fe/MgO/Fe junctions, will grow, pattern and characterize MTJs based on insulating MgO based barrier. The investigated systems concern simple 'non-structured' MTJ (control samples) and 'structured' (MTJ doped with impurities or double MTJ with a third electrode). The group at *Universidad Autonoma de Madrid*, which recently gained expertise in noise studies on MTJs, will carry out electric transport characterization: TMR and inelastic electron tunneling spectroscopy (IETS) down to 0.3K, as well as 1/f and shot noise measurements on these structures.

11.1.3 Microwave emission and detection using spin-transfer nano-oscillators

This project will be performed within a collaboration with T. Dimopoulos and H. Brueckl from the *Nano-System Technologies/ ARC-Seibersdorf Research GmbH (Vienna, Austria)* and Prof. F. Aliev from *University of Madrid*.

The project aims for the study and manipulation of a nano-scale magnetic object that can emit and detect microwave radiation, based on the spin-transfer effect. This object will have the form of a giant or tunnel magnetoresistance multilayer, patterned in nano-scale dimensions, i.e. below

100nm of lateral size. Only at these reduced dimensions is the spin-transfer effect significant. Our first goal is to tune the frequency and amplitude of the emitted radiation by modifying material and geometrical characteristics of the object. Our next goal will be to set an array of individual nano-oscillators into a coherent precession mode, so as to enhance the radiation power ouput. Finally we target on the possibility to detect a microwave field by such a device, by monitoring changes of the dc voltage between its electrodes that are predicted to appear whenever the external microwave field couples to the magnetization's precession mode. It has been recently shown that two closely situated, current excited, nanoscale oscillators can be self-tuned to coherent radiation emission, with amplitude that scales with the square of the number of devices [123]. After tailoring the dynamic response of the single oscillator, it will be challenging to obtain self-tuning for a close-packed array of oscillators, achieving therefore high power output of microwave radiation. The next challenge will be to see whether the microwave field from such an array can be detected by another oscillator, through monitoring the aforementioned d.c. Berger voltage. In this manner we could study both the energy flow from the current to the precessing spins and vice versa. The nano-oscillator will also be used for detection of microwave fields produced via an inductive technique, i.e. with the use of a patterned coplanar waveguide transmitting high frequency voltage pulses [124, 125] at the vicinity of the magnetic multilayer.

The dynamic response of the device depends on its geometric characteristics, the current density and the magnetic field values, as well as on the currents spin polarization and the magnetic properties of the FM electrodes (saturation magnetization, Gilbert damping, magnetic anisotropy). In view of the above, our first goal will be to optimize and manipulate the structural and electronic properties of the critical interfaces of the GMR and TMR multilayers in order to achieve a high degree of the currents spin polarization and therefore an efficient spin-transfer effect. A focal point will be to study the spin-transfer effect as a function of the orbital character of the electrons. In tunnel junctions this can be achieved by proper combinations of tunnel barriers and FM electrodes. Another idea is to obtain further spin-filtering of the tunneling current by inducing spin-dependent resonant levels inside the barrier, by means of a proper doping profile. To realize these ideas we need a large flexibility on sample elaboration techniques.

For this, both sputter PVD (in ARCS, Vienna) and molecular beam epitaxy (MBE) (in our laboratory) will be used. For the sputtered multilayers, the FM electrodes will include polycrystalline $Ni_{80}Fe_{20}$ and CoFe alloys, as well as amorphous CoFeB. These will be combined with Cu spacer for the CPP GMR stacks and thin MgO sputtered barriers for the tunneling junctions. MgO is a good candidate for inducing a very high spin polarization and a low resistance-area product (therefore allowing large current densities) for the junctions. The magnetization of the fixed FM electrode can be set by exchange biasing with an antiferromagnet (IrMn) or simply by adjusting its thickness and saturation magnetization relative to the free layer. MBE grown stacks will be deposited in our laboratory which has a long-standing experience and already achieved record magnetoresistance values for Fe/MgO/Fe single crystal multilayers as well as demonstration of coupling effects through spin transfer. In the epitaxial systems we expect a better control of the physical and chemical properties of the interfaces. This will enable us to better manipulate the orbital character of the tunnelling electrons and the doping profile of the barrier, as we discussed earlier. We also plan to deposit films with in-plane and out-of-plane

anisotropies (e.g in Co/Pt systems) to tailor the dynamic response of the nano-magnet through the anisotropy field.

As mentioned before, the geometric characteristics of the spin-transfer devices influence the magnetizations dynamic response. The coherence of the stimulated emission of spin-waves can be achieved by lateral confinement in the presence of a nanoscale patterned boundary. In this manner the excitation of discrete spin-wave modes will be favoured. Additionally, the spin-transfer effect dominates over the current-induced magnetic field response (Oersted field) only for nanoscale samples. Patterning becomes therefore a critical issue. The challenge here would be to down-scale the lateral dimensions of the elements below 100 nm without degradation of the multilayer structure. Since the quality of interfaces is so decisive in GMR and TMR systems, patterning should be done after the complete multilayer stack is deposited. E-beam lithography (at ARCS, LPM) will be used in order to define elements for individual addressing. Additionally, we are planning to use a subtractive lithography process that will enable us to further shrink the devices dimensions in the range below 50 nm and create arrays of nano-oscillators, that can be collectively excited. To achieve this we will deposit on the multilayer surface a hard mask consisting of either perpendicular grown nanowires (at ARCS) or metallic pillars grown by focused ion beam (FIB) technique (at the TU, Vienna). Subsequently we will use ion milling, equipped with secondary ion mass spectroscopy (in ARCS), to etch the multilayer structure to the desired depth and SiO2 deposition to isolate the different nano-elements. Bottom and top electrical contacts for electrical addressing will be defined by optical lithography (at ARCS and LPM). As mentioned above, one of our targets will be to achieve a short of communication between the oscillators so as to study both emission and detection of microwaves on the same sample.

The spin-transfer induced magnetizations dynamic response will be monitored by the high frequency, magnetotransport set-up of the partner UAM in Madrid, whose expertises include magnetic dynamics, tunnel spectroscopy and noise measurements on magnetic multilayers as mentioned in the previous subsection. With this set-up, at present, experimental control is obtained over reflection-transmission measurements below 1 GHz for temperatures down to 1.5K and magnetic fields to 9 Tesla by using an Agilent Network analyzer with maximum frequencies to 8.5GHz. In addition to this, room temperature static and relatively low frequency (up to 1 MHz) magnetotransport measurements can be also realized in ARCS and LPM.

In conclusion, we propose to study, control and manipulate spin-transfer induced oscillators for emission and detection of microwaves. Such a study is related to the ever-growing field of spin-dependent transport and is situated today at the frontier of knowledge. The project is planned to proceed in the following manner: Firstly we will study the frequency and amplitude response of single GMR and TMR nano-pillars upon d.c. current excitation. Then we will investigate the conditions to set an array of current-excited devices into coherent spin-wave emission in order to enhance the power output of the microwave field. Last objective will be to detect the external microwave field by measuring the Berger voltage between the two electrodes of the nanopillar.

11.1.4 Studies concerning the spin injection and transport in semiconductors and other materials

By spin injection one understand the injection of a spin polarized current from a ferromagnetic materials to a semiconductor. Motivated by the promising results obtained in our group concerning the large efficiency of the spin filtering in Fe/MgO/Fe MTJ, we envisage to elaborate systems where the spin injection in SC is done across a single crystal tunnel junction. The filtering effects in terms of symmetry of the couple ferromagnetic metal/ barrier open the way toward a new transport physics. We also expect a strong enhancement of the injection efficiency. The first step on this research topics is the study of the growth of epitaxial barriers on Si.
The injection or the spin polarized detection from a ferromagnetic metal toward a semiconductor across a tunnel barrier can also be used to study the transport of hot or ballistic spin polarized carriers in semiconductors. In fine, this research field could lead to the realization of a spin transistor operating with a semiconductor base. This invention is the subject of two patents which I co-signed [Patents WO 97/41606 and GB0006142.4 deposited by Clarendon Laboratory]. The transistor uses a structure type $FM_1/I_1/SC/I_2/FM_2$, where FM_i (i = 1, 2) is a ferromagnetic metal, I_j (j = 1 or 2) an insulating barrier and SC is an intrinsic or doped semiconductor. The spin-polarized electrons from FM_1 are injected by tunnel effect through I_1 in SC. In SC, they behave either like conduction electrons with large spin-diffusion length or like hot or ballistic electrons.
After passing the SC their spin polarization is analyzed by tunnel effect through I_2 by the FM_2 detector. On the other hand, depending on the characteristics of I_1 and I_2, the spin asymmetry and the character of the electrons injected by FM_1 can be modified in a selective way. In addition, by playing with the doping of the SC it would be possible to modify the type of carriers (electron or hole) and thus the mobility of the species carrying the spin.
This research topics will be carried out in collaboration with the group of Pr J. Gregg from Clarendon Laboratories Oxford and Dr. C. Denis (NIST, Gaithersburg).
The next step after the injection of spin in the semiconductor will consist in the study of the spin transport and interaction mechanisms. The injection by tunneling will allow the modulation in energy of the electron injected into the SC. The spin relaxation and decoherence mechanisms, particularly important in spintronics will be then studied as a function of electron energy. This kind of studies will be oriented to investigate the characteristic lengths of the electronic transport in another large class of materials. We mention here the magnetic semiconductors (SCM) and the magnetic oxides (MO). After their elaboration, in these systems we plan to investigate the aspects concerning the spin transport (decoherence /relaxation) in parallel with their magnetic/ micromagnetic properties.

11.1.5 Studies concerning the realization of spin electronic devices

This research program is performed in close collaboration to Prof. M. Hehn, Dr. F. Montaigne and Dr. D. Lacour. It relates to the study of spin-dependent coherent transport in metallic structures with multiple barriers and constitutes the central point of the thesis of F. Greullet, thesis for which I am co-adviser.
We have shown that in single-crystal junctions, the anisotropy of the crystal leads to additional

filtering effects of electrons in terms of their symmetry. In order to give an additional impulse to this work, we would like to study the injection of spin and symmetry polarized electrons in complex systems made up of one or several tunnel junctions. One of our main goals is to understand better the filtering phenomena and to introduce the elementary single-crystal MTJ brick into more complex devices like the hybrid multiple junctions with crystalline, amorphous and poly-crystalline subsystems.

The realization of hybrid systems Sputtering/ MBE/in the new experimental setup will open the way toward the development of more complex systems. This will make possible to multiply the number of available materials. A second tunnel barrier can be therefore easier obtained by sputtering. The use of alternative barriers with different intrinsic parameters (height and/or width, effective mass) within the same multiple barrier structure will allow us to study the spin dependent transport phenomena with a large degree of freedom and to carry out new and original micro-electronics devices.

Here again, the study of the spin transport in double-barrier systems type $FM_1/I_1/X/I_2/FM_2$ (where X is a magnetic or nonmagnetic layer) is particularly important because it allows to analyze in energy the spin relaxation and spin coherence phenomena. The injection by tunneling across a first tunnel junction (FM_1/I_1) allows the modulation in energy of the electrons injected into the intermediate layer (X). The analysis is carried out by a second tunnel junction tunnel (I_2/FM_2). The same technique can be used to study the effects of spin precession/relaxation in a magnetic layer (X). Thus, the angle of spin precession/relaxation in the layer X can be calculated from the analysis of the tunnel characteristics measured for selected combinations of magnetization geometries in the FM_1, FM_2, X layers.

These new devices are integrated within a most general research framework. It concerns the development of a new generation of magneto-electronic components. These actions point out the realization of magnetic transistors and nonvolatile magnetic memories (MRAM). This research is supported by the European 'BLUEBERRIES' MEDEA+ Project (Building-up Embedded Memories). From a fundamental point of view, the magnetic transistor represents a powerful tool to study the characteristic lengths of the spin polarized hot carriers.

11.2 Theoretical activity

11.2.1 Ab-initio modeling of spin dependent tunnel transport

This project implicates close collaborations with D. Stoeffler (Institut de Physique et Chimie des Matériaux, Strasbourg) and Dr. M. Chshiev (University of Alabama, USA).

The transport properties of the multilayer systems are directly related to their electronic properties. As we already illustrated in the introduction of this report, one of the simplest models describes the tunnel magnetoresistance as a function of the spin polarization. This last quantity is directly related to the spin dependent density of states of electrons: $P(E) = \left(n^{\uparrow}(E) - n^{\downarrow}(E)\right) / \left(n^{\uparrow}(E) + n^{\downarrow}(E)\right)$. By ab-initio band-structure calculation techniques, in a super-cell model, one can model the tunnel junction devices. From these calculations one can obtain the spin dependent orbital projected density of states which leads to the interfacial polarization. From the comparison between the calculated polarization at the metal/oxide interface

and the experiments one can get the first indications about the spin filtering via the interfacial chemical bonding. On the other hand, from the calculations one can get other spin dependent or not intrinsic parameters such as the effective mass, the barrier height and the barrier width. These values can be subsequently injected in a free-electrons model which provides the transmission of spin by tunnel effect. Using a conduction model based on independent channels one can calculate the tunnel magnetoresistance. This very simple approach has been successfully used in the pioneering of the spin electronics, when the most of the studied systems have been polycrystalline or amorphous. The free-electrons model described correctly these systems which are spatially isotropic and the potential seen by the propagating electrons has no periodicity. This kind of model still remains valid in systems with rough interfaces or with amorphous barriers.

On the other hand, the experimental realization of systems with crystalline order drives the above theoretical description inappropriate. Recent theoretical works take into account the effect of the crystal periodicity on the electronic transport using Bloch functions to describe the electrons. When the propagation vector $k_{\|}$ is conserved, one can calculate the total conductivity by summing the respective conductivity associated to each $k_{\|}$. This is described by the Landauer-Buttiker equation: $G = \frac{e^2}{h} \sum_{k_{\|}} T(k_{\|})$ where G is the total conductivity and $T(k_{\|})$ the transmission coefficient; the summation takes place over the whole Brillouin zone. Usually, the calculation of the transmission coefficients in performed by ab-initio techniques (i.e. Layered Korringa-Kohn-Rostoker (LKKR)). This kind of calculation illustrates the influence of the wave function symmetry on the electronic transport. This symmetry characterizes the behavior of the wave function with respect to a rotation around an axis parallel to the z direction, perpendicular to the interfaces. Moreover, the ab-initio calculations demonstrate also the specific role of the interfaces on the tunnel transport. Experimentally, this kind of effects have been also addressed by the tunnel transport experiments performed by our group.

However, the calculation by the LKKR technique are timely expansive and these tools are note available in our laboratory. Recently, Chshiev et al [126] demonstrated that classical calculation codes can be successfully used to describe correctly the transport in single crystal tunnel junctions. Therefore, in a first step I would like to orient my theoretical research activities, following this kind of approach.

The studied system is modeled by a supercell. Then, one can classically modulate the chemical an the cristalographical structure of the interfaces. In a first step standard calculations will provide the band structure of the studied system. Then, one has to build on the wave functions on each atomic site, for energies around the Fermi level. Each wave function is projected on a symmetry state obtained from the decomposition of the Bloch function along the irreducible representation. Furthermore, one can calculate the amplitude of the probability $|\Psi^{\star}\Psi|$, layer by layer, in the supercell which model our system. Such kind of calculations, performed by Chshiev et al, is illustrated in Figure 11.1 which illustrates the dependence of the attenuation rate on the wave function symmetry.

From the band structure, one can depict the dependence of the k^2 as a function of energy, for the propagation direction which is interesting for experiments (i.e. the (100) for Fe/MgO). In the vicinity of the gap, the $k^2(E)$ curves can be fitted par the equation: $\frac{1}{k^2(E)} = \frac{\hbar^2}{2m_v^*(E-E_v)} + \frac{\hbar^2}{2m_c^*(E-E_c)}$, with E_v, E_c the top of the valence band and the bottom of the conduction band.

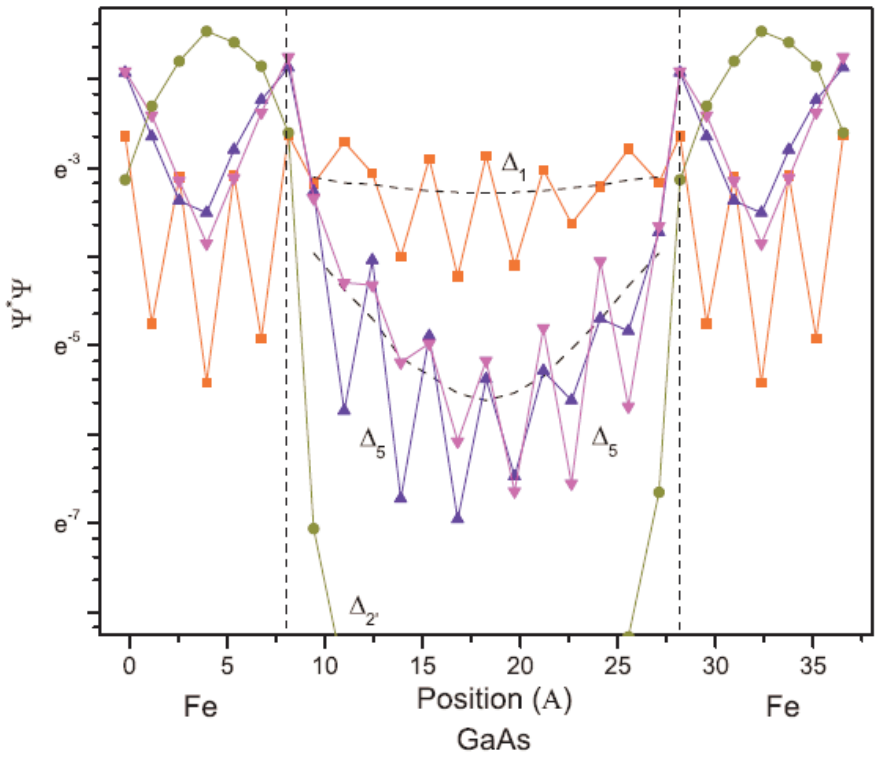

Figure 11.1: Absolute square of $|\Psi^{\star}\Psi|$, layer by layer for the, Δ_1 (squares), $\Delta_{2'}$ (circles) and Δ_5 (triangles) wave functions in a Fe—GaAs supercell. The dashed lines without data points indicate the expected decay rate based on the fit with the equation $k^2(E)$.

From this fit one can extract the effective mass of the electron for each band and each symmetry. The attenuation of $|\Psi^{\star}\Psi|$ for a given symmetry can be fitted then by the equation: $\exp(-2\,|k|\,z)$ where k is calculated from the previous equation.

The calculation technique described above will be used in combination with the *Wien*2*k* (FP-LAPW) code available in our laboratory. Among the phenomena we would like to investigate we mention here the effect of the interfacial chemical bondings on the spin filtering (the specific influence of different metallic or non-metallic impurity atoms).

A second step, the Landauer-Buttiker formalism will be used to calculate the conductivity, after a first ab-initio calculation of $T(k_{\|})$ (Green function formalism).

11.2.2 Modeling of spin transfer effects in magnetic tunnel junctions

In the electronic transport, the particle density: $n(r) = \sum_{i\sigma} \Psi^*_{i\sigma}(r)\Psi_{i\sigma}(r)$ and the current density $j(r) = \sum_{i\sigma} \Psi^*_{i\sigma}(r)\left[-\frac{i\hbar}{m}\nabla\right]\Psi_{i\sigma}(r)$ are conserved and verify the continuity equation: $\nabla j + \frac{\partial n}{\partial t} = 0$. On the other hand, the spin density $m(r) = \sum_{i\sigma\sigma'} \Psi^*_{i\sigma}(r)s_{\sigma\sigma'}\Psi_{i\sigma'}(r)$ and the spin current density $Q(r) = \sum_{i\sigma\sigma'} \Re e\left[\Psi^*_{i\sigma}(r)s_{\sigma\sigma'} \otimes \left(\frac{-i\hbar}{m}\nabla\right)\Psi_{i\sigma'}(r)\right]$ are quantities which are not conserved. The quantity s is relates to the Pauli matrix by the equation: $s = \hbar\sigma/2$. The non-conservation, intuitively illustrated in figure 11.2, is described by two terms the continuity equation: $\nabla \cdot$

$Q + \frac{\partial m}{\partial t} = -\frac{\delta m}{\tau_{\uparrow\downarrow}} + n_{ext}$. The first term in the right side of the equation represents the spin accumulation and the second term the total external torque. Then, one can write: $\frac{\partial m}{\partial t} = n_c + n_{ext}$, where $n_c = -\frac{\delta m}{\tau_{\uparrow\downarrow}} - \nabla \cdot Q$ represents the current-induced contribution to the torque density [127]. The other term represents all the external torques (i.e. the Landau-Lifshitz-Gilbert torque density $n_{ext} = -(g\mu_B/\hbar)m \times B_{eff} + \alpha \hat{m} \times \dot{m}$. The B_{eff} is the effective field related to exchange, anisotropies, external fields and α is the damping.
The main purpose of my project within this topics is to calculate the torque produced by the current in magnetic tunnel junctions. The specific point of this calculation will be the use of a multichannel model, each channel corresponding to a given symmetry. This will allow to take into account the characteristic aspects of electronic transport in the single crystal systems experimentally studied in our team. In a first step, the calculation will be performed within the free-electrons formalism, including channel dependent parameters for the junction, extracted from ab-initio calculations, as described in the previous paragraph. Finally, a most accurate approach will be a provided by complete ab-initio calculations. This ultimate approach is scheduled to be performed via scientific collaborations with theoretical groups already involved in this topics.

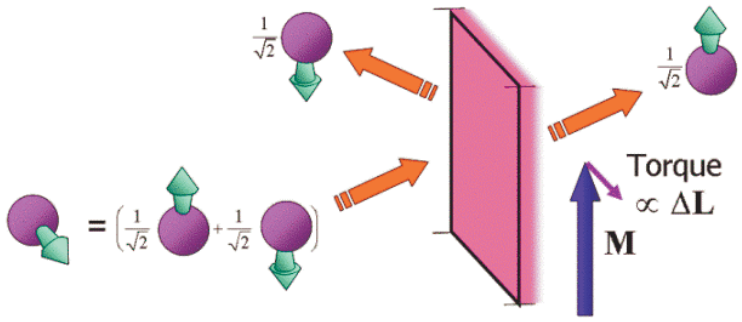

Figure 11.2: Intuitive representation for the non-conservation of the spin transverse component during the injection of the spin to a ferromagnet (FM) having the orientation of the magnetization **M** perpendicular to the initial spin direction. The spin component identical with that of magnetization is transmitted in the FM, while the other component is totally reflected

11.3 Other projects and activities

In parallel to the scientific research activities enumerated before, I would like to continue and diversify the teaching activity which already I carry out.
Moreover, within the framework of the International Collaboration Convention between the Henri-Poincaré University and the Technical University of Cluj-Napoca, I intend to intensify the scientific and technical exchanges between the two educational establishments in order to: define joint new research programs and topics, facilitate exchange/mobility of the students, researchers, professors, allow students and post-docs to carry out training courses, develop common teaching modules, organize specific cycles of formation, support the exchange and the communication
I will also continue the activities concerning the advising of theses and research stages, taking

an active part in activities of scientific animation and management of research (animation of French and international research programs).

11.4 Résumé de chapitre en français

Projets de recherche

Ce paragraphe résume les projets de recherche que je voudrais mener dans les années à venir. Ils s'insèrent directement dans le contexte de l'expérience scientifique acquise lors des dernières années dans le domaine du magnétisme et de l'électronique de spin. Mes projets de recherche se déroulent selon deux volets, l'un expérimental et l'autre théorique.

ACTIVITE EXPERIMENTALE Un premier volet de l'activité expérimentale est dirigé vers la continuation des études concernant le transport de charge et de spin dans les jonctions tunnel. Les objectifs du projet peuvent être classés en deux catégories : ceux tournés vers la compréhension fondamentale de la magnétorésistance tunnel à travers les barrières cristallines (MgO) et ceux tournés vers l'utilisation des propriétés de magnétorésistance exceptionnelle de ces barrières dans des dispositifs d'électronique de spin. L'objectif global des études en amont, tourné vers les aspects fondamentaux, est de comprendre la physique complexe du transport tunnel dans des systèmes avec une symétrie cristallographique spécifique. Par des techniques de calcul type ab-initio nous modéliserons le rôle des interfaces et de la barrière tunnel aussi bien au niveau de la qualité cristallographique que chimique. Par la suite, nous confronterons ces résultats théoriques à ceux obtenus expérimentalement. La ma îtrise des aspects fondamentaux que sont les processus de transport balistique via des états de résonance interfaciale de m ême que les phénomènes de cohérence quantique permettra l'étude du couplage magnétique et des effets de spin torque dans ces structures nanométriques. Les JTMs seront élaborées suivant trois techniques : Epitaxie par Jet Moléculaire, pulvérisation cathodique et leur combinaison dans le complexe MBE/Pulvérisation cathodique que nous construisons actuellement au LPM. Le développement de la procédure d'élaboration de barrières de MgO cristallin par pulvérisation cathodique est primordial car il permettra un transfert des connaissances acquises vers la technologie de l'industrie des composants électroniques. Des études spécifiques de bruit à basse fréquence seront effectuées sur les jonctions dans le cadre d'une collaboration avec l'Université de Madrid. Un axe de collaboration avec le Centre de Recherche Nano-System Technologies/ ARC-Seibersdorf de Vienne sera orienté vers la réalisation et l'études des oscillateurs à haute fréquence basés sur le transfert de spin.
Un deuxième volet de l'activité expérimentale est constitué par l'injection et le transport de spin dans les semi-conducteurs. Motivé par les résultats très prometteurs obtenus dans notre équipe sur l'efficacité de filtrage en spin dans les jonctions mono cristallines Fe/MgO/Fe, j'envisage l'élaboration de systèmes qui permettent l'injection de spin dans un semi-conducteur à travers une barrière isolante mono-cristalline. Les effets de filtrage en symétrie dans le couple électrode ferromagnétique/ barrière cristalline ouvriront la voie vers une nouvelle physique et vers une forte amélioration de l'efficacité d'injection. L'injection ou la détection polarisée en spin d'un ferromagnétique métallique vers un semi-conducteur à travers une barrière tunnel peuvent également

être utilisées pour l'étude du transport de porteurs chauds ou balistiques polarisés en spin dans les semi-conducteurs. In fine, ce domaine de recherche pourrait se concrétiser par la fabrication d'un transistor de spin à base semi-conductrice. L'étape suivante après l'injection de spin dans le SC consistera dans l'étude du transport et des mécanismes d'interaction du spin dans le semi-conducteur. L'injection par effet tunnel permettra la modulation en énergie de l'électron injecté dans le SC. Les mécanismes de relaxation et de décohérence du spin (Elliot-Yaffet, D'yakonov-Perel, Bir-Aronov-Pikus, interaction hyperfine), particulièrement importants dans la spintronique, seront ainsi étudiés en fonction de l'énergie. Un projet plus lointain vers lequel je voudrais m'orienter dans les années à venir concerne la physique des oxides et semi-conducteurs magnétiques sur les aspects suivants : transport (décohérence /relaxation) de spin et propriétés magnétiques/ micromagnétiques.
Un autre axe selon lequel je voudrais continuer mes recherches concerne l'étude et la réalisation de dispositifs à électronique de spin: capteurs, diodes et transistors magnétiques, mémoires non volatiles. Il concerne l'étude du transport cohérent dépendant du spin dans des structures métalliques à barrières tunnel multiples. L'utilisation de barrières alternatives dotées de paramètres intrinsèques différents (hauteur et/ou largeur de barrière, masse effective) au sein d'une m ême structure à barrières multiples permettra d'étudier les phénomènes de transport dépendant du spin avec un grand degré de liberté et de réaliser des dispositifs microélectroniques nouveaux et originaux. L'étude du transport de spin dans les systèmes à double barrière tunnel sera particulièrement importante pour analyser les mécanismes de relaxation et de décohérence du spin dans les métaux en fonction de l'énergie. Ces nouveaux dispositifs s'intègrent dans le cadre plus général du développement d'une nouvelle génération de composantes magnéto-électroniques.

ACTIVITE THEORIQUE Le premier volet de mes projets théoriques est orienté vers la modélisation ab-initio du transport dépendant du spin. Les propriétés de transport des systèmes multicouches sont directement liées à leurs propriétés électroniques. L'un des modèles les plus simples décrit la magnétorésistance d'une jonction tunnel magnétique en fonction de la polarisation de spin, directement liée à la densité d'états. Par des techniques ab-initio, dans un modèle type super cellule on peut envisager des calculs de densité d'états résolue en spin et en caractère orbital. Ainsi, après une confrontation entre l'expérience et le calcul de la polarisation d'interface pour une structure métal/oxyde nous pouvons sortir des premiers indices sur le filtrage de spin via les liaisons chimiques à l'interface. Par ailleurs, le calcul de structure électronique pourra nous fournir des paramètres intrinsèques résolus en spin et en caractère orbital comme la masse effective, la largeur et la hauteur de la barrière tunnel. Ces valeurs peuvent être ultérieurement injectées dans un modèle type électrons libres afin de calculer la transmission du spin par effet tunnel. Dans un modèle de la conduction par des canaux indépendants on peut ainsi estimer la magnétorésistance. Pour décrire les propriétés de transport dans les systèmes mono-cristallins on modélise le système par une super-cellule. Ainsi, on peut de manière classique moduler la nature chimique et la structure cristallographique des interfaces. Dans une première étape, des calculs classiques seront effectués pour fournir la structure de bande du système étudié. Par la suite, on va construire les fonctions d'onde projetées par site, au voisinage du niveau de Fermi, pour les différentes symétries à partir de la décomposition des fonctions de Bloch selon les

représentations irréductibles. Ensuite, on peut calculer directement la probabilité de présence plan par plan, dans la super-cellule qui modélise notre système. Ceci nous fournit la dépendance du taux d'atténuation dans la barrière de la symétrie de la fonction d'onde. L'analyse des relations de dispersion peut nous donner les valeurs des masses effectives des électrons pour chaque bande et chaque symétrie. La technique décrite ci-dessus sera utilisée en combinaison avec le code de calcul dont nous disposons déjà au laboratoire : Wien2k (FP-LAPW). Parmi les effets que je voudrais étudier, je mentionne l'effet des liaisons chimiques aux interfaces sur le filtrage de spin : l'influence des impuretés métalliques ou non-métalliques adsorbées.
Le deuxième volet de mes activités théoriques concerne les calculs des effets de transfert de spin dans les jonctions tunnel magnétiques. L'objectif vise le calcul du torque par injection de courant dans les jonctions tunnel magnétiques. Dans une première étape ce calcul sera effectué en utilisant un modèle de type électrons libres avec les paramètres intrinsèques des jonctions tunnel issus des calculs type ab-initio. Le point spécifique de ce calcul sera la prise en compte du caractère orbital des électrons qui transportent le spin par effet tunnel dans un modèle de transport multi-canal. Evidemment, l'étape ultime à plus long terme sera constituée par un calcul complet type ab-initio.

AUTRES ACTIVITES Parallèlement aux activités de recherche scientifique énumérées auparavant, je voudrais continuer et diversifier l'activité d'enseignement que j'effectue déjà. Par ailleurs, je compte intensifier les échanges scientifiques et techniques avec d'autres établissements. Je veux continuer également les activités concernant l'encadrement de thèses et stages de recherche, en participant activement à des activités d'animation scientifique et du management de la recherche (animation de programmes de recherche français et internationaux).

Part VI

Appendix

Appendix A

Micromagnetic aspects

A.1 Analysis of MFM contrast for a 360° wall

The MFM tip, magnetized only in the z perpendicular direction, probe the second derivative of the stray field z component [43, 44] in a phase detection mode [42]. Figure A.1(a) presents a MFM image of a 360° circular wall that separates uniformly magnetized regions (see Figure 2.5(e), corresponding to CoFe single layer). From the associated magnetization loop (Figure 2.5), we observe that the magnetization is mostly reversed at the field which corresponds to this wall profile, so all the domains have the magnetization oriented along the negative field direction. The contrast is given only by the stray field of the wall that subsists after the magnetization reversal. The magnetic structure of the wall, proposed by Heyderman *et al* [45], Gillies *et al* [46] and Cho *et al* [49] is shown in Figure A.1(b), and can be used to explain all types of expected contrast for different 360° walls orientation, relative to the field direction and domain magnetization.
We have simulated the MFM contrast for two particular situations concerning the orientation of the wall: the wall is parallel or perpendicular to the field direction. Each configuration is defined by a certain magnetization profile [47, 48] $\vec{M}(x,y,z)$.

$$\vec{M}^{\parallel}(x,y,z) = \frac{c_1^2}{c_1^2+\left[(x-\mu_1)/\Delta)\right]^2} + \frac{c_2^2}{c_2^2+\left[(x-\mu_2)/\Delta)\right]^2} \tag{A.1}$$

$$M^{\perp}(x,y,z) = c_1 \arctan\left[(x-\mu_1)/\Delta\right] + c_2 \arctan\left[(x-\mu_1)/\Delta\right] \tag{A.2}$$

Parameters c_1, c_2, μ_1, μ_2, Δ are adjusted to fit the corresponding wall profile of width Δ. In each case, the z component of the stray field H_d^z was calculated from the density of magnetic charge $\rho(x,y,z)$ corresponding to a 360° wall.

$$\rho(x,y,z) = -\nabla \cdot \vec{M}(x,y,z) \tag{A.3}$$

A scalar potential ϕ, obtained from the Poisson equation:

$$\Delta\phi(x,y,z) = -4\pi\rho(x,y,z) \tag{A.4}$$

allow to compute the stray field:

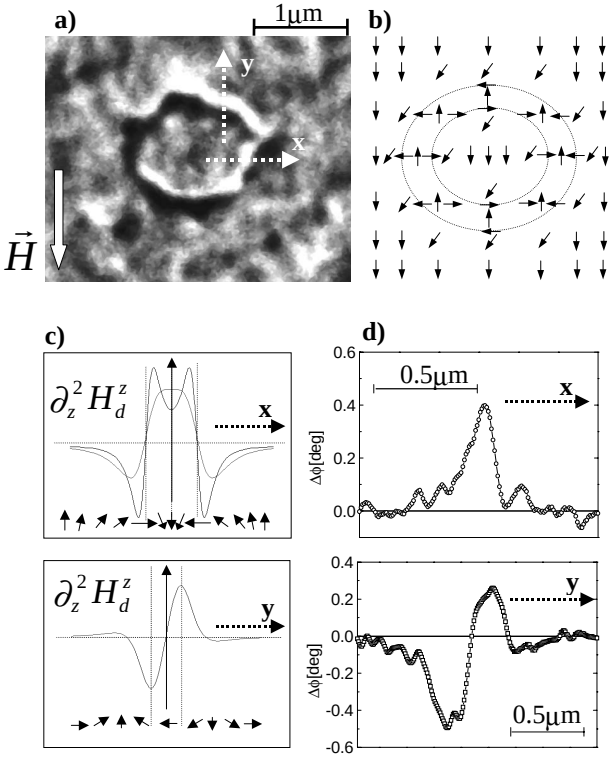

Figure A.1: Measured MFM contrast (a) and the magnetization configuration (b) for a 360° circular wall. The simulated MFM contrast, computed in two situation where the wall is either parallel, or perpendicular to the field direction (c) are in good agreement with line sections on the measured MFM images (d).

$$H_d(x, y, z) = -\nabla\phi(x, y, z) \tag{A.5}$$

and subsequently, the MFM signal proportional with $\partial^2 H_d^z/\partial z^2$.
Results of the simulation (Figure A.1(c)) show a good agreement with line sections on the MFM images (Figure A.1(d)).

A.2 Stability of 360° walls in the artificial ferrimagnet layers

This section provides the analysis concerning the stability of 360° Nèel type walls, in an artificial ferrimaget system.
The total energy in an antiferromagnetically coupled system, with in-plane magnetization, submitted to an external field H, can be expressed as [50, 51]:

$$\varepsilon(H) = \int \left\{ A \left[t_1 \left(\frac{d\theta_1}{dx} \right)^2 + t_2 \left(\frac{d\theta_2}{dx} \right)^2 \right] + K_L \left[t_1 sin^2\theta_1 + t_2 sin^2\theta_2 \right] \right\} dx +$$

$$\int \{J\left[\sin\theta_1\ \sin\theta_2 + \cos\theta_1\cos\theta_2\right] - MH[t_1\cos\theta_1 + t_2\cos\theta_2]\}\,dx \tag{A.6}$$

where θ_1, θ_2 describe the orientation of the magnetization in each layer relative to the field direction. The first set of terms contains the intralayer exchange (A) and local anisotropy (K_L), that determine the shape and the energy of the uncoupled domain walls in the system. The magnetostatic energies due to the divergence of the magnetization in the film plane, varying as $\sin^2\theta$ are included in K_L. The second set of terms contains the interlayer coupling energy and the Zeeman energy in an applied field H. For example, in a static configuration without any magnetic field or exchange AF coupling, the energies of independent 180° walls are $\sigma_{1,2} = 4\sqrt{AK_L}$.
During the reversal of the net magnetic moment, antiferromagnetically mirrored 360° walls appear in each layer of the AFi system. To estimate the stability of these walls, a simplified model is proposed. Centered one above another, antiferromagnetically mirrored volumes in the thin and in the thick layer of the artificial ferrimagnet, are considered. In each volume we suppose a 360° wall. λ_1 and s_1 are the perimeter and the surface of the wall in the thick AFi layer (thickness t_1), and λ_2 and s_2 are the perimeter and the surface of the wall in the thin layer (thickness t_2). In the thick layer the domain magnetization is oriented along the field direction and the magnetization of the center of the wall opposite to the field direction. In the thin layer the domain magnetization is opposite to the field direction, while the center of the wall has the magnetization along the field direction. The total energy of this "two walls" configuration $\varepsilon_2(H)$ is calculated and compared with the energy for the "one wall" configurations for which: (i) the wall disappears in the thick layer and subsists in the thin layer $\varepsilon_1^1(H)$ or (ii) the wall disappears in the thin layer and subsists in the thick one $\varepsilon_1^2(H)$.

$$\begin{aligned}
\varepsilon_2(H) &= -MHS[t_1 - t_2 - 2(s_1t_1 - s_2t_2)] + \\
&\quad +\sigma(\lambda_1t_1 + \lambda_2t_2) - 2J(S/2 - s_1 + s_2) && \text{(A.7)}\\
\varepsilon_1^1(H) &= -MHS(t_1 - t_2 + 2s_2t_2) + \sigma\lambda_2t_2 - 2J(S/2 - s_2) && \text{(A.8)}\\
\varepsilon_1^2(H) &= -MHS(t_1 - t_2 - 2s_1t_1) + \sigma\lambda_1t_1 - 2J(S/2 - s_1) && \text{(A.9)}
\end{aligned}$$

The difference in energy between the "two wall" and "one wall" configurations is:

$$\begin{aligned}
\Delta\varepsilon_1(H) &= \varepsilon_2(H) - \varepsilon_1^1(H)\\
&= 2MHs_1t_1 + \sigma\lambda_1t_1 - 2J[2s_2 - s_1] && \text{(A.10)}
\end{aligned}$$

if the wall disappears in the thick layer and subsists in the thin layer, at a given value of the applied field H. This process becomes energetically favorable when $\Delta\varepsilon_1 > 0$, true at applied fields:

$$H > \frac{J[2s_2 - s_1] - \sigma\lambda_1t_1/2}{Ms_1t_1} = H_{xc} - H_{anisotropy} \tag{A.11}$$

The stability of the wall is determined by the balance between Zeeman + domain wall energy (which tend to annihilate the wall in the thick layer) and the AF coupling energy (which tends

to preserve the wall acting as a pinning source). The higher is the coupling strength J, the higher is the critical field where the wall disappears in the thick layer. The higher is the local anisotropy, for a given value of J, the smaller is the critical field. The larger is the magnetic moment of the thick layer, the smaller is the critical field, (higher pressure exerted on the wall). The values of the critical fields, (extracted from MFM images by analyzing the disappearance of walls as a function of the applied field) give local measures of coupling strength and anisotropies. If hypothetically, the wall would disappear in the thin layer and would subsist in the thick one, the variation of energy would be:

$$\begin{aligned} \Delta\varepsilon_2(H) &= \varepsilon_2(H) - \varepsilon_1^2(H) \\ &= -2MHs_2t_2 + \sigma\lambda_2 t_2 - 2Js_2 \end{aligned} \tag{A.12}$$

This process is energetically unfavorable, leading to a magnetic state with a higher energy, in the field range at which 360° walls are supposed to collapse.
In conclusion, at the end of domain magnetization reversal, 360° walls exist in the two layers of the AFi system. By increasing the applied field, walls disappear in the thick layer by shrinking their center part. This occurs at a critical field which depends on the local antiferromagnetic coupling (which acts as an additional pinning parameter) and on the local anisotropy. The walls located in the thin layer are stable, having their center aligned along the field direction. For these stable walls, the Zeeman and the AF coupling energy act both as pinning sources.

A.3 Quantitative analysis of field dependent domain structure in magnetic tunnel junctions

Micromagnetic features appearing during the reversal of an artificial ferrimagnet used as a hard layer of a magnetic tunnel junction are quantitatively analyzed using the high sensitivity of the spin polarized tunnel current to magnetization fluctuations in the electrodes of the magnetic junctions. We propose an analytical model which takes into account different tunneling paths associated with local magnetization configurations. The model allows a quantitative correlation between the spin polarized transport characteristics and the field-dependent domain structure. The results extracted from the tunnel magnetoresistance measurements are found to be in good agreement with the magnetic domain wall density extracted from magnetic force microscopy experiments. We used this technique to study selectively the micromagnetic-reversal mechanism in an artificial ferrimagnetic system. These aspects are summarized in the following review papers.

JOURNAL OF APPLIED PHYSICS VOLUME 89, NUMBER 11 1 JUNE 2001

Spin polarized tunneling as a probe for quantitative analysis of field dependent domain structure in magnetic tunnel junctions

C. Tiusan[a)]
Institut de Physique et de Chimie des Matériaux de Strasbourg, 23 rue du Loess, F-67037 Strasbourg Cedex, France

M. Hehn
Laboratoire de Physique des Matériaux, UMR CNRS 7556, BP 239, 54506 Vandoeuvre lès Nancy Cedex, France

T. Dimopoulos and K. Ounadjela
Institut de Physique et de Chimie des Matériaux de Strasbourg, 23 rue du Loess, F-67037 Strasbourg Cedex, France

Micromagnetic features appearing during the reversal of an artificial ferrimagnet used as a hard layer of a magnetic tunnel junction are quantitatively analyzed using the high sensitivity of the spin polarized tunnel current to magnetization fluctuations in the electrodes of the magnetic junctions. We propose an analytical model which takes into account different tunneling paths associated with local magnetization configurations. The model allows a quantitative correlation between the spin polarized transport characteristics and the field-dependent domain structure. The results extracted from the tunnel magnetoresistance measurements are found to be in good agreement with the magnetic domain wall density extracted from magnetic force microscopy experiments. © *2001 American Institute of Physics.* [DOI: 10.1063/1.1361044]

Micromagnetic domain structures within the ferromagnetic layers have been shown to have a large effect on the transport properties of the hard/soft magnetic tunnel junction (MTJ) architecture.[1–6] The understanding as well as the control of the magnetization reversal in the magnetic electrodes is the key parameter for optimizing the field response of the microelectronic devices. We present here a powerful technique for quantitatively investigating field-dependent micromagnetic features in thin magnetic layers. The technique uses the extreme sensitivity of the spin polarized tunneling in MTJs to the local magnetic configuration of each magnetic layer in contact with the tunnel barrier. The investigated magnetic layer is used as a magnetically hard electrode and it acts as a spin polarizer. The electrons which tunnel across the insulating layer are then analyzed by the magnetically soft electrode. We have used this technique for a quantitative study of the micromagnetic reversal mechanism in an artificial ferrimagnetic system (AFi), widely used nowadays as a hard subsystem in magnetic devices. The studied AFi is composed of a Co (2 nm)/Ru (0.8 nm)/CoFe (3 nm) trilayer separated by a 1 nm thick Al oxide barrier from the Co (1 nm)/Fe (6 nm) magnetically soft bilayer or detection layer (DL).[5,7] In the present work, the CoFe (3 nm) layer is interfaced with the barrier. We have developed an appropriate analytical model to demonstrate the use of the TMR signal as a probe for investigating the field dependent domain wall density and the average angle of domain magnetization. These values extracted from the TMR measurements are found to be in good agreement with the magnetic domain wall images analysis.

A typical magnetization versus field, $M-H$ curve, correlated with a tunnel magnetoresistance versus field, TMR$-H$ curve, for a Co/Ru/CoFe AFi based junction is shown in Fig. 1(a). The curves are measured in a ± 1 kOe field window where the AFi behaves as a single block of reduced moment (M_1-M_2) due to the strong antiferromagnetic coupling between its magnetic layers M_1 and M_2. We analyze Fig. 1(a) starting from positive maximum field. In a positive field the AFi net moment and the DL are parallel leading to a minimum value of the resistance. When reversing the external field, the DL switches at a field of about -30 Oe, illustrated in Fig. 1(a) by the drop (jump) in the $M-H$ (TMR) curve. The antiparallel configuration between the DL and the net moment of the AFi is reflected by the higher resistive state of the junction. For fields lower than -100 Oe, the DL remains in a single domain state, saturated along the negative field direction. The resistance of the junction for fields lower than this value is only modulated by the magnetization configuration in the AFi.

By further decreasing the negative applied magnetic field, the AFi net magnetic moment reverse by rotation of magnetizations in each layer leading to a decrease of the MTJ resistance. When the reversal of the net moment is completed [Fig. 1, state (3)], the magnetization of the AFi topmost layer becomes again parallel with the DL. However, since the two AFi layers rotate by 180° for the reversal of the net AFi moment, creation and annihilation of 360° domain walls in both thick and thin magnetic layers have been shown to appear.[5] In this field range, the intermediate reversal states [Fig. 1, states (1) and (2)] are constituted by multidomain configurations as shown by magnetic force microscopy (MFM) measurements. The MFM images illustrate how the wall structure starts to form [Fig. 1(b), state 1], how 360° walls are stabilized when domains completely reverse

a)Electronic mail: tiusan@ipcms.u-strasbg.fr

0021-8979/2001/89(11)/6668/3/$18.00

J. Appl. Phys., Vol. 89, No. 11, 1 June 2001

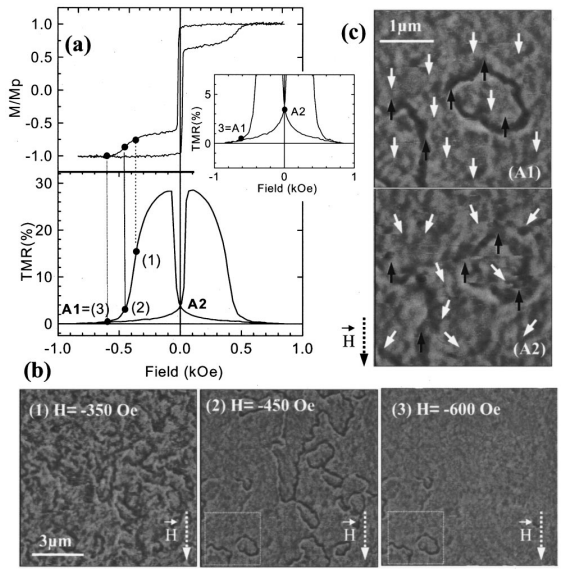

FIG. 1. (a) $M-H$ and TMR$-H$ curves for a Co/Ru/CoFe AFi based MTJ. States (1)–(3) define significant magnetization configurations during the AFi magnetization reversal. These configurations are illustrated by the associated MFM images (b) *state 1*: domain magnetization reversed by about 90°, the TMR reaches half of its maximum value, MFM wall contrast becomes enhanced; *state 2*: domain reversal is completed, stable domain wall structure is clearly resolved by MFM; *state 3* domain walls are almost annihilated, only isolated very stable walls persist. Inset: Zoom on the TMR$-H$ curve corresponding to low resistance range. (c) MFM images illustrating relaxation of magnetization in domains due to local anisotropies in the polycrystalline layers when reducing the external field from -600 Oe to zero. The Arrows sketch domain and domain wall magnetization orientation with respect to the external field.

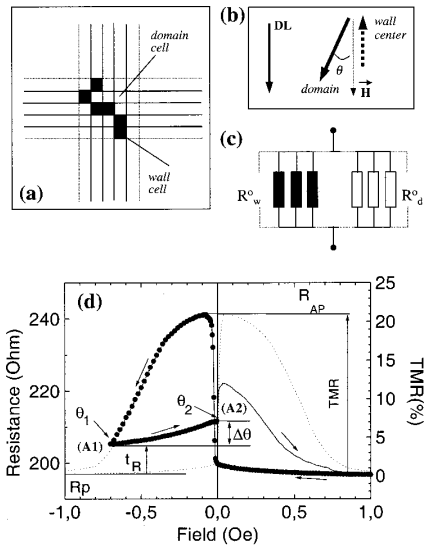

FIG. 2. Model for a MTJ in a multidomain state. (a) Elementary grid dividing the surface of the junction in elementary domain and wall cells. (b) Sketch illustrating magnetization orientation in a domain (straight arrow) and a domain wall (bold dotted arrow) with respect to the field direction in an intermediate state during the AFi net moment reversal. (c) Electrical model for the MTJ in a multidomain configuration: network of in-cascade resistances, corresponding to domain and domain wall associated tunneling paths. (d) Typical TMR$-H$ curve containing the main parameters used in our analytical model: $t_R(H)$, TMR, R_P, and R_{AP}. Legend: (·····): symmetric TMR loop taken in a field range where the domain reversal is completed ($t_R=0$); (-·-): ''minor'' TMR loop where the reversal in negative field in state (A1) is not yet completed ($t_R^{A1}\neq 0$).

along the field direction (state 2) and how the walls are annihilated at high fields (state 3). The MFM images shown in Figure 1(c): states (A1), (A2) illustrate the magnetization relaxation processes inside domains when reducing the negative fields from state A1 to A2.

In order to proceed to a quantitative analysis of the domain wall contribution to the tunnel magnetoresistance response, we have developed an analytical model which can be applied to junctions in a multidomain configuration. The total surface S of the junction is divided in a grid of n_w elementary wall cells and n_d elementary domain cells, each cell having an elementary surface s_0 [see Fig. 2(a)]. The total surface occupied by the walls is $S_w=n_w\times s_0$ whereas the total surface occupied by the domains is $S_d=n_d\times s_0$.

As discussed previously, during the magnetization reversal of the AFi, 360° domain walls are created.[5] The center of these walls is constituted by regions which magnetization remains blocked along the initial positive saturation direction, antiparallel to the DL, whereas the magnetization of adjacent domains makes an angle θ with respect to the external field direction and so to the DL. Assuming that in this field window the DL is in a single domain state, the resistance of the conduction channels associated to elementary domain R_d^0 and elementary wall R_w^0 cells is calculated as a function of the total resistance of the MTJ corresponding to perfect parallel R_P and antiparallel R_{AP} magnetic configurations:[5]

$$R_d^0=\frac{1}{2}\frac{S}{s_0}[R_P+R_{\mathrm{AP}}+(R_P-R_{\mathrm{AP}})\cos\theta]. \tag{1}$$

In this model, the center of the 360° wall is considered as a small ''domain'' of inverse magnetization. Tail related effects, when taking into account an analytical wall profile, are included in the angle θ which quantifies the average angle of the wall adjacent magnetization of the domain. Therefore, the resistance of the elementary wall can be written as:

$$R_w^0=\frac{S}{s_0}R_{\mathrm{AP}}. \tag{2}$$

The total resistance R of the MTJ in a multidomain configuration can be calculated as the equivalent resistance of a network of in-cascade resistances associated to domain, respectively domain wall elementary segments [Fig. 2(c)].

$$\frac{1}{R}=\sum_i\frac{1}{R_w^0}+\frac{1}{R_d^0}=\frac{n_w}{R_w^0}+\frac{n_d}{R_d^0} \tag{3}$$

$$=\frac{1}{s_0}\left[\frac{S_w}{R_w^0}+\frac{S-S_w}{R_d^0}\right]. \tag{4}$$

Lets consider the successive intermediate state occurring during the magnetization reversal [i.e., state (A1), Fig. 2(d)].

Here, the residual domain wall structure subsisting in the hard subsystem is reflected by the higher resistive state of the MTJ than the one corresponding to the perfect parallel configuration. Indeed, the center of the residual 360° walls being oriented opposite to the detection layer [see Fig. 2(b)] gives rise to high resistance tunneling channels, compared with tunneling channels associated to adjacent domains (low resistance). This high resistive state is ''quantified'' by a residual magnetoresistance t_R^{A1} and so a resistance $R(A1)$:

$$R(A1)=R_P(1+t_R^{A1}). \tag{5}$$

From Eq. (1)–(4), we can write:

$$\frac{1}{R_P(1+t_R^{A1})} = \frac{1}{s_0}\left[\frac{s_0}{S}\frac{S_w^{A1}}{R_{AP}}+\frac{2s_0(S-S_w^{A1})/S}{(R_P+R_{AP}+(R_P-R_{AP})\cos\theta^{A1}}\right]. \tag{6}$$

Using the definition of the tunnel magnetoresistance: $TMR=(R_{AP}-R_P)/R_P$, one can deduce from the Eq. (6), the surface of the walls with respect to the total surface of the junction responsible for a residual magnetoresistance t_R^{A1}:

$$\omega^{A1}=\frac{S_w^{A1}}{S}=\frac{t_R^{A1}-\dfrac{TMR(1-\cos\theta^{A1})}{2}}{\dfrac{TMR(1+\cos\theta^{A1})}{2}}\frac{1+TMR}{1+t_R^{A1}}. \tag{7}$$

From state (A1) when decreasing the field towards zero, the resistance of the junction increases to state (A2). Since ω remains unchanged when the magnetic field is decreased, the variation of the MTJ resistance is only related to the relaxation of the magnetization in the domains as shown in the MFM images of Fig. 1(c). Here again, the variation of the wall profile with the field, such as tails effects for instance, are included in the angle θ of wall adjacent domain magnetization. By measuring the residual t_R^{A2} from the TMR curve, one can calculate the angle of domain magnetization θ^{A2} corresponding to a given density of domain walls ω^{A1}.

$$\cos\theta^{A2}=\frac{t_R^{A2}-\dfrac{TMR}{2}\left[\omega^{A1}\dfrac{1+t_R^{A2}}{1+TMR}+1\right]}{\dfrac{TMR}{2}\left[\omega^{A1}\dfrac{1+t_R^{A2}}{1+TMR}-1\right]}. \tag{8}$$

This equation, applied for the states (A1) and (A2), gives the relaxation angle

$$\Delta\theta=\theta^{A2}-\theta^{A1}. \tag{9}$$

This analytical model is used for quantitative analysis of the AFi magnetization reversal, illustrated by the (1)–(2)–(3) branch of the $M-H$ and TMR$-H$ curves in Fig. 1. As shown by MFM measurements, in states (2) or (3), the domain magnetization is practically reversed ($\theta\simeq 0$) but domain wall structure persist ($\omega\neq 0$). From the residual magnetoresistance t_R in a given state and considering $\theta=0$, the density of walls (ω) can be calculated from Eq. (7). In state (2) of Fig. 1, the calculated residual density of walls is $\omega\simeq 17.2\%$ corresponding to a residual $t_R\simeq 4\%$ and a TMR$=28.8\%$. This value becomes slightly smaller (15.3%) when considering a contribution of magnetization angle in domains described by an angle $\theta=15°$. These values are in good agreement with the value extracted from analysis of the MFM image Fig. 1(b), state (2), $\omega_{MFM}\simeq 15\%$. Similar analysis performed for state (3) of Fig. 1 gives values for the density of walls $\omega\simeq 2\%$ for $t_R=0.5\%$. This result is also in good agreement with the value extracted from the MFM image analysis. The relaxation of domain magnetization, reflected by the increase in the junction resistance between the states (3)$=$(A1) and (A2) Fig. 1(a) and illustrated by the MFM images of Fig. 1(c), is quantified using the set of Eqs. (8) and (9). Indeed, between the state (A1) defined by $t_R^{A1}=0$ and $\theta^{A1}=0$, and the state (A2) ($H=0$ Oe) defined by $t_R^{A2}=3.4\%$, we estimate a relaxation angle of $\Delta\theta\simeq 38°$ when reducing the field. The extracted value quantifies the local anisotropy distribution in the AFi layers, key factor in magnetization reversal of a polycrystalline system.[5]

In conclusion, a good agreement is found between results extracted from the TMR analysis and the data extracted from the analysis of the MFM images. This suggest that the analytical model used for this study and adapted to tunnel junctions in a multidomain state, is a useful tool to quantify both domain wall density and local anisotropy distributions.

The authors are grateful for illuminating discussions with H. van den Berg, V. da Costa, and experimental support of C. Meny, Y. Henry, M. Acosta, and G. Wurz. This work was supported by the European Framework IV Materials Technology Programme, Contract No. BRPR-CT98-0657, the *Dynaspin* program, *Training and Mobility of Researchers* network, under Contract. No. FMRX-CT97-0147 and the Nanomem Program (IST-1999-13741). One of the authors (K.O.) also acknowledges NSF Grant No. CNRS-9603252.

[1] S. Gider, B.-U. Runge, A. C. Marley, and S. S. P. Parkin, Science **281**, 797 (1998).
[2] K. S. Moon, R. E. Fontana, and S. S. P. Parkin, Appl. Phys. Lett. **74**, 3690 (1999).
[3] A. Anguelouch, B. Shrang, G. Xiao, Y. Lu, P. Trouilloud, W. J. Gallagher, and S. S. P. Parkin, Appl. Phys. Lett. **76**, 622 (2000).
[4] L. Thomas, M. G. Samant, and S. S. P. Parkin, Phys. Rev. Lett. **84**, 1816 (2000).
[5] C. Tiusan, T. Dimopoulos, K. Ounadjela, M. Hehn, H. A. M. van den Berg, Y. Henry, and V. Da Costa, Phys. Rev. B **61**, 580 (2000).
[6] M. Hehn, O. Lenoble, D. Lacour, C. Fery, M. Piecuch, C. Tiusan, and K. Ounadjela, Phys. Rev. B **61**, 11643 (2000).
[7] C. Tiusan, M. Hehn, K. Ounadjela, Y. Henry, J. Hommet, C. Meny, H. A. M. van den Berg, L. Baer, and R. Kinder, J. Appl. Phys. **8**, 5276 (1999).

PHYSICAL REVIEW B, VOLUME 64, 104423

Field-dependent domain structure evolution in artificial ferrimagnets analyzed by spin-polarized tunnel transport in magnetic tunnel junctions

C. Tiusan, T. Dimopoulos, and K. Ounadjela
Institut de Physique et Chimie des Materiaux de Strasbourg, 23 rue du Loess, F-67037, Strasbourg Cedex, France

M. Hehn
Laboratoire de Physique des Matériaux, CNRS (UMR 7556), Université H. Poincaré, F-54506 Nancy, France
(Received 5 July 2000; revised manuscript received 6 February 2001; published 23 August 2001)

A powerful technique for investigating field-dependent micromagnetism in thin magnetic layers is presented. The technique uses the spin-polarized tunnel-transport mechanism in magnetic-tunnel junctions. We used this technique to study the micromagnetic-reversal mechanism in an artificial ferrimagnetic system, which consists of two ferromagnetic layers strongly antiferromagnetically coupled through a nonmagnetic interlayer. We show that the high sensitivity of the spin-polarized current to the fluctuations of magnetization allows to probe the magnetic-domain structure in the magnetic electrodes. As a contrast to standard *M-H* and giant-magnetoresistance measurements, which are only able to probe the global magnetic state of this artificial ferrimagnet, we show here that the tunnel magnetoresistance discriminates the field-dependent evolution of the domain phases in selective magnetic layers. Furthermore, we demonstrate the capability of a tunnel-magnetoresistance signal to be used as a quantitative probe for investigating residual walls during the reversal process.

DOI: 10.1103/PhysRevB.64.104423 PACS number(s): 75.60.−d, 73.40.Gk, 73.40.Rw, 77.80.Dj

I. INTRODUCTION

Extensive experimental work has been done on magnetotransport properties of magnetic tunnel junctions (MTJ) since the discovery of the large tunnel magnetoresistance (TMR) at room temperature.[1,2] Up to now, studies were especially focused on transport properties, such as bias voltage and temperature dependence of tunnel resistance and magnetoresistance. Recently, magnetism in ferromagnetic electrodes has defined a new exciting research area in this field.[3–9] The key factor is that the spin-polarized tunneling is sensitive to the local magnetic configuration of each magnetic layer in contact with the tunnel barrier.[6] Extreme resistive states of the MTJ are then observed for ferromagnetic and antiferromagnetic alignment of the magnetizations of the electrodes. However, intermediate situations may exist for which the magnetic layers include domain-wall structures. The correlation between domain-structure and magnetic-field-dependent-transport properties can be done taking into account different tunneling paths associated with local magnetization configurations.[6] According to this model, domains and domain walls give rise to tunneling channels with different resistances determined by the lateral fluctuations of the angle between the magnetic moment of the magnetic layers in contact with the tunnel barrier.

The technique described in this work uses an MTJ as a powerful *tool* to investigate micromagnetic properties of a magnetic thin film. The design of that device has an optical analog: the *polarizer-analyzer* system. The investigated magnetic layer is used as a hard layer in the MTJ and it acts as a *spin polarizer*. It is separated by an insulating barrier from a magnetically soft subsystem, having a small coercive field and a sharp magnetization reversal. When this soft layer is in a single-domain state, it acts as a *spin analyzer* (detection layer) for electrons injected across the barrier from the hard subsystem (spin polarizer). Then, all features that appear in the field-dependent resistance of the MTJ are due to domain walls or fluctuations in domain magnetization located in the hard magnetic layer, *interfaced* with the tunnel barrier. The strength of this technique is to selectively analyze the magnetism of layers in contact with the tunnel barrier in contrast with imaging techniques that integrate the signal over several layers.

In this paper, we have investigated the magnetic-domain-structure evolution in an artificial ferrimagnet (AF) trilayer. This system[6,10,11] is constituted by two ferromagnetic metals, having unequal magnetic moments antiferromagnetically coupled across a nonmagnetic spacer. They are widely used nowadays as magnetically hard electrodes in MTJ and spin-valve devices due to their high thermal stability and magnetic rigidity.[10,12] Their small net magnetic moment reduces the parasitic coupling with the soft layer, which in general could be detrimental in MTJ and giant-magnetoresistance (GMR) sensor capabilities. Typical GMR measurements performed in spin-valve systems or multilayers using artificial antiferromagnetic systems[13] are only able to probe the global domain structure of the entire device without being able to discriminate the individual magnetic-field evolution of domain phases in each magnetic layer of the hard subsystem. In contrast, by building a magnetic-tunnel junction based on an AF, having either the thicker or the thinner magnetic layer in contact with the tunnel barrier, we show here that the magnetic behavior of each layer can be extracted selectively. This is performed by analyzing the magnetoresistive signal shape and amplitude corresponding to each stacking sequence of the AF. Furthermore, quantitative information on the evolution of the domain-wall density with the external field has been extracted from the TMR signal in agreement with values obtained from magnetic-force-microscopy (MFM) mea-

0163-1829/2001/64(10)/104423(8)/$20.00

surements, performed in the operational field window of the MTJ device.[6]

This paper is organized as follows. Section II describes the stack design and sample preparation as well as measurement conditions. Section III provides the analytical description of the field-dependent magnetic behavior of an artificial ferrimagnet without introducing any domain structure. Then analysis of data involving experimental magnetization curves and current in-plane GMR on the AF are compared to the analytical description to illustrate the presence of domain walls. How selective is the current-perpendicular to plane-tunnel MR measured on the MTJ stack is described in Sec. IV together with a clear analysis of the field-dependent magnetic features of the hard subsystem in the entire field window.

II. SAMPLE PREPARATION, MEASUREMENTS

Tunneling junctions are constituted from complex stacks defined as follows. First, a Cr(1.6 nm)/Fe(6 nm)/Cu(30 nm) buffer layer is grown on a previously sputter-etched 3 in. diameter Si(111) wafer.[10] On the top of the buffer, the AF trilayer Co(1.8 nm)/Ru(0.8 nm)/Co(3 nm) (denoted by *N*-AF) or the ''reversed'' configuration Co(3 nm)/Ru(0.8 nm)/Co(1.8 nm) (denoted *R*-AF) is stacked. The Al-oxide barrier was formed by a rf Ar/O_2 plasma oxidation of a previously sputtered Al metallic layer.[10,15] A magnetically soft bilayer [the so-called detection layer (DL)] is sputtered on top of the Al-oxide tunnel barrier and consists of Co(1 nm)/Fe(6 nm). Finally, the multilayer stack is capped for protection with Cu(5 nm)/Cr(3 nm).

Magnetic properties of as-deposited multilayer films were studied at both macroscopic and microscopic scales. Macroscopic magnetization curves were measured using an alternating gradient-field magnetometer at room temperature. At a microscopic scale, the domain structure has been observed by MFM, in a tapping-lift phase-detection mode, in zero and in-plane applied fields up to $|H| = 800$ Oe, available in our experimental setup.

As-deposited 3-in. wafers, containing the stack described above, were patterned by UV lithography into arrays of squared junctions with tunnel-barrier surface areas of $10 \times 10\ \mu m^2$. The junctions, measured using a conventional four-point technique, present a large (25–30 %) tunnel magnetoresistance at room temperature.

III. ANALYTICAL RESPONSE OF TUNNEL JUNCTIONS USING ARTIFICIAL FERRIMAGNETS

How an artificial ferrimagnet system behaves when submitted to a magnetic field can be simply calculated under the assumption that the magnetization reversal in the magnetic layers occurs via a coherent-rotation mechanism. Because of the strong torque created by the antiferromagnetic coupling on the magnetization of the two coupled layers, a coherent rotation of the magnetization should be favored with respect to a mechanism based on nucleation and propagation of walls in the antiferromagnetically coupled subsystem. This type of magnetization reversal can be calculated using the

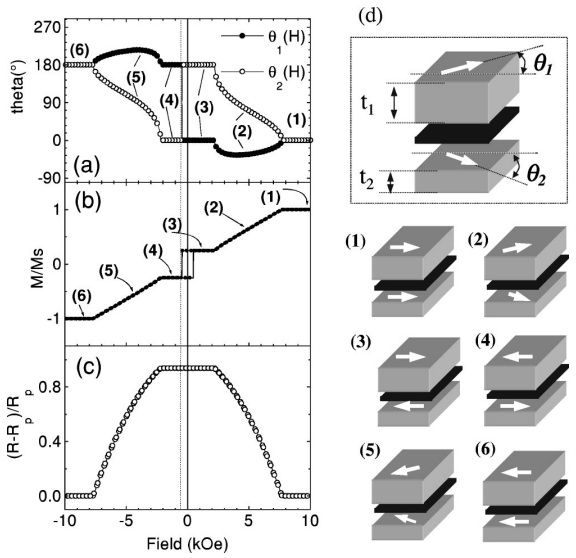

FIG. 1. Theoretical calculation of field-dependent magnetic behavior of an AF system, by using the Stoner-Wolfarth model (Ref. 18). (a) Variation of angle between the magnetizations of the ferromagnetic layers constituting the AF hard subsystem and the external applied field direction. (b) Magnetization versus field (M-H) curve using the expression $M(H) = M_s[t_1 \cos\theta_1(H) + t_2 \cos\theta_2(H)]/(t_1 + t_2)$. (c) Theoretical magnetoresistive response (GMR) of the AF using an expression of the type $(1 - \cos[M(H)/M_s]^2)$. The sketch in the right-hand side of the (d) shows the ideal micromagnetic configuration of the AF at critical field values [states (1)–(6)].

energy functional, reported in Eq. (1), of an antiferromagnetically coupled trilayer with in-plane magnetization submitted to an external field H,[16,17]

$$\varepsilon(H) = J\cos[\theta_1 - \theta_2] - M_s H[t_1 \cos\theta_1 + t_2 \cos\theta_2] + K_1 t_1 \sin^2\theta_1 + K_2 t_2 \sin^2\theta_2, \quad (1)$$

where θ_1, θ_2 describe the orientation of the magnetization relative to the field direction in each layer of thickness t_1 and t_2, respectively. The first two terms contain the interlayer coupling energy and the Zeeman energy in an applied field H. The second two terms describe the in-plane uniaxial anisotropy energies of the two magnetic layers. The values taken for the modeling have been set close to the measured experimental data extracted from the magnetization curves ($t_1 = 3$ nm, $t_2 = 1.8$ nm, $J = -1.1$ erg/cm^2, $K_1 = K_2 = 10^5$ erg/cm^3, $M_s = 1430$ emu/cm^3).

The magnetization-angle variation as a function of field, $\theta_1(H)$, $\theta_2(H)$ shown in Fig. 1(a), can be calculated by minimizing numerically the energy functional. Figures 1(b) and 1(c) show field-dependent magnetization $M(H)$ and magnetoresistance $R(H)$ curves, respectively, deduced from the angle variation.

Let us consider the $\theta(H)$, M-H, and R-H curves counterclockwise from the positive high-field saturation, where all magnetic moments are parallel and oriented in the positive field direction [Fig. 1, state (1)].

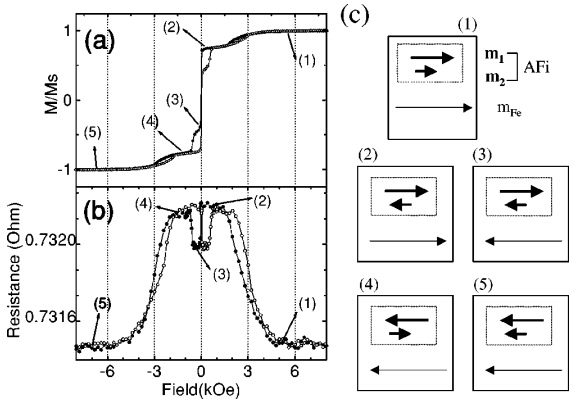

FIG. 2. Experimental *M-H* (a) and magnetoresistance GMR (*R-H*) curve with the current-in-plane (b) for the Si/Cr/Fe/Cu/Co/Ru/Co stack. In the figures the branch measured from positive to negative field is (−●−) while the branch measured from negative to positive field is (−○−). The sketch in the right-hand side of the (c) shows the micromagnetic configuration of the states (1)–(5) as predicted by the theoretical calculations. Hysteresis effects in the flank of both MR and *M-H* curves, not present in the theoretical curves, are related with domain structure developed in the AF layers during the magnetization reversal in the saturation-plateau [states (1)–(2)] region.

By decreasing the applied field in the flank region of the *M-H* curve [field window between (1) and (3)], the angle of the thinner layer of the AF varies continuously from 0 to π with respect to the positive high-field saturation direction. At the same time, the moment of the thicker layer starts to rotate up to a maximum deflection angle, then it is dragged back to its initial state by the strong AF coupling. This field region corresponds to a transition from a parallel configuration (saturated state) to an antiparallel configuration [plateau shown in Fig. 1, state (3)] of the magnetizations of the two layers strongly antiferromagnetically coupled. As expected from the angle dependence of the magnetizations in the two layers, it is shown from the *M-H* and *R-H* curves that the net moment decreases from the parallel state (1) to the antiparallel state (2) while the resistance increases. The width of the plateau depends on the strength of the antiferromagnetic (AFM) coupling with respect to the Zeeman energy. In this region, the AF behaves like a magnetic rigid body of reduced moment $(m_1 - m_2)$ and switches in a reversed magnetic field, which depends on the intrinsic properties of the material and the strength of the AFM coupling.[11] The reversal of the AF is shown in Figs. 1(a) and 1(b) for which an abrupt 180° change occurs for the angles of both layers [transition from state (3) to state (4)]. However, the MR curve [Fig. 1(c)] indicates no change in the resistance at the coercive field since the relative angle remains unchanged.

These results, showing features corresponding to pure rotation of magnetization, are compared with experimental data extracted from *M-H* [Fig. 2(a)] and magnetoresistance (GMR) [Fig. 2(b)] measurements. In this case, measurements are performed on a continuous Cr/Fe/Cu/Co(1.8 nm)/Ru(0.8 nm)/Co(3 nm)/Al multilayer stack with the current in plane using a conventional four-point technique. The experimental data show general features similar to those predicted by the theoretical curves, which indicate that the reversal mechanism follows mainly a rotational process. Indeed, from positive saturation down to an AFM plateau, the gradual decrease of magnetization in the *M-H* curve and the related increase of resistance in the *R-H* curve both indicate the variation of the relative angle of magnetizations of the two layers of the AF. The magnetic contribution of the 6-nm Fe buffer layer separated from the AF by the 30-nm-thick Cu layer is shown as a sharp reversal at low field (20 Oe). Interestingly, the presence of the Fe seed layer gives rise to an additional small MR contribution (0.02%), shown by a decrease of the resistance when the Fe magnetization switches [transition from state (2) to state (3), Fig. 2(b)] and an increase of resistance when the net moment of the AF reverses [transition from state (3) to state (4), Fig. 2(b)]. In this way, the Fe seed layer is used to probe the AF net-moment behavior at low field.

However, this simplified energy functional does not take into account aspects related to random distribution of anisotropy,[14] which is a key factor for the formation of domain-wall structures. In the flank region (1),(2) and (4),(5), irreversible processes give rise to hysteretic behavior illustrated in both GMR and *M-H* curves [Figs. 2(a) and 2(b)] and are attributed to a domain phase transformation in the AF magnetic layers. Indeed, for the same applied field, the magnetization configuration is strongly affected by the magnetic history of the AF. A reasonable assumption is to attribute the existence of the phase transformation in the AF thinner layer, since this layer reverses by 180° according to the theoretical prediction [Fig. 1(a)]. However, several questions remain unanswered. Will this domain phase transformation be duplicated in the thicker layer by the AFM coupling? How stable are the magnetic walls in each of the layers and in which field regions are they created and annihilated? The GMR and *M-H* measurements provide evidence of a domain phase transformation without being able to discriminate which layer of the AF is involved. In the next section, we will show that using tunnel-transport and MFM experiments, we are able to selectively analyze the field-dependent evolution of the domain-wall structure in each layer of the AF subsystem.

IV. TUNNEL TRANSPORT AS A PROBE FOR INVESTIGATING FIELD-DEPENDENT DOMAIN STRUCTURES

As already mentioned, the magnetic-tunnel junctions consist of an artificial ferrimagnet as a hard subsystem (Co/Ru/Co) separated by an Al-Oxide layer from a Co/Fe soft subsystem. The soft DL presents a square magnetization loop, with a coercive field of about 20 Oe and a magnetization reversal in a field range smaller than 2 Oe.[10] Therefore, for applied fields above 30 Oe, the DL can be considered as being in a single-domain state. It will act as a spin analyzer for electrons injected from the hard magnetic subsystem (spin polarizer) across the tunnel barrier. Two stacking sequences will be discussed in this paper: (i) The thicker layer of the AF interfaced with the tunnel barrier (*N*-AF), which will determine the direction of the net moment in the opera-

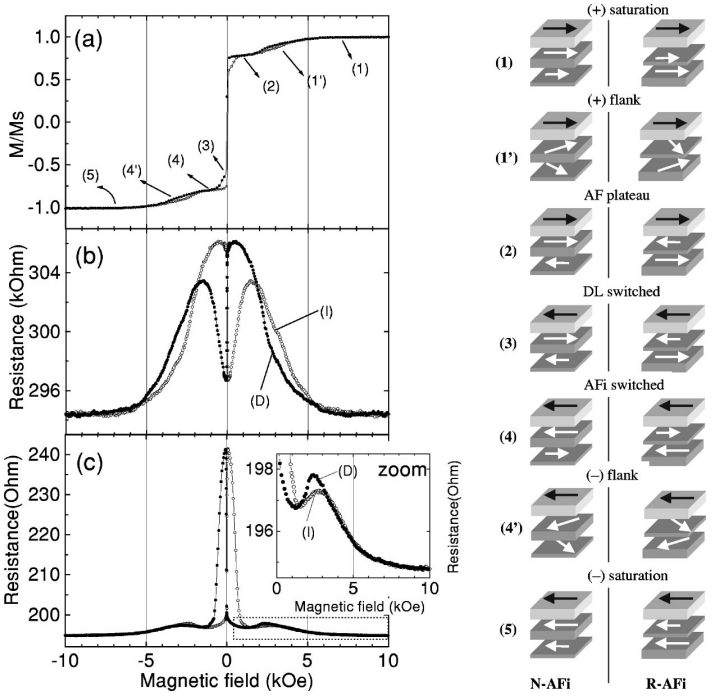

FIG. 3. Magnetization versus field *M-H* (a) and *R-H* curves (b,c) for a magnetic-tunnel junction using an AF hard subsystem. The *R-H* curves are taken in the current-perpendicular-to-plane (CPP) geometry being then only sensitive to the tunnel current. (b) and (c) are the TMR curves for the junctions with the thin and thick magnetic layers of the AF in contact with the tunnel barrier, respectively. The inset of (c) shows a zoom in the low resistive state. The sketch in the right-hand side of the figure shows the ideal micromagnetic configuration of the MTJ at critical field values [states (1)–(5)].

tional field window, (ii) the thinner layer of the AF interfaced with the tunnel barrier (*R*-AF), in which magnetization will be opposite to the direction of the net moment.

Tunnel-magnetoresistance curves were measured on MTJ's with AF having either the thin [Fig. 3(b)] or the thick Co layer [Fig. 3(c)] in contact with the tunnel barrier. This allows to selectively analyze their domain structure. As expected, there are no significant differences in the *M-H* loops [Fig. 3(a)] for the *N*-AF and *R*-AF because of the averaging signal over the entire stack. However, the *R-H* loops are completely different for the two stacking sequences, reflecting different field-dependent domain-phase evolutions in the thick and the thin magnetic layer of the AF.

A. Selective analysis of micromagnetic features at high field (flank region) in the artificial ferrimagnet

Let us first consider the *M-H* and *R-H* curves counterclockwise from the positive high-field saturation, where all the magnetic moments are parallel and oriented in the positive field direction [Fig. 3, state (1)]. The resistance of the MTJ based either on an *N*-AF or on an *R*-AF is the lowest, and corresponds to electrons that tunnel across the insulator between two ferromagnets in a parallel configuration (all magnetic moments are aligned).

By decreasing the applied field in the flank region of the *M-H* curve [field window between states (1) and (2)], a continuous gradual increase of the MTJ resistance is observed when the thinner Co layer is in contact with the barrier [*R*-AF, Fig. 3(b)]. However, for the *N*-AF junction, a small increase of resistance followed by a decrease towards the end of the flank can be observed [Fig. 3(c)]. This is in agreement with the expected variation of magnetization angles shown in Fig. 1(a) and confirms that only the thinner layer has the large magnetization rotation. As a result, in the positive part of the AFM plateau [Fig. 3, state (2)], the thicker AF layer has its magnetization aligned along the field direction (parallel with the DL) while the thinner AF layer is oriented opposite. This corresponds, in the *R-H* curves, to a low resistance state in the case of the *N*-AF [Fig. 3(c)] and to a high resistance state in the case of *R*-AF [Fig. 3(b)] after completion of the reversal occurring at field. A first evidence of the formation of domain structure in the thinner layer of the AF is shown in Fig. 3(b). In the flank region (3–5 kOe field window), the *R-H* curve of the *R*-AF, which probes the thinner magnetic layer, is hysteretic [Fig. 3(b)]. Starting from positive saturation and decreasing the field, the magnetization of the thinner layer of the AF experiences a 180° rotation giving rise to 360° Néel domain walls. These walls originate at regions where the local anisotropy coincides with the direction of the saturation field and they will constitute the core of the future walls, when adjacent regions relax their magnetization by rotating in antiphase. Indeed, when the field is reduced, these regions will rotate clockwise and anticlockwise, while the magnetization in the core region will remain blocked,[18] aligned with the direction of the field and the detection layer. In terms of tunnel resistance, in branch (*D*) these regions constitute local channels of low tunnel resistance compared to adjacent regions that have their moments misaligned with respect to the detection layer. These low-resistance channels are reflected in the *R-H* curve in Fig. 3(b): for a given applied field between 3 and 5 kOe, a significant change of the resistance is observed when comparing branch (*D*), measured when decreasing the field from

positive saturation, with branch (*I*), measured when increasing the field towards positive saturation. Indeed, when measuring branch (*I*), the initial state of magnetization of the thin layer is antiparallel to the field direction. In this case, the nucleated walls would have their center antiparallel to the detection layer and act as high-resistance state. So, the overall resistance is now higher induced by the contribution of the additional resistance of the blocked regions.

B. Duplication of domain walls in the artificial ferrimagnet: Lower-field region, end of the flank—AF plateau

How the presence of 360° walls in the thin AF layer affects the thicker layer is shown in the inset of Fig. 3(c). From the absence of hysteresis at high fields in the flank when the thicker AF layer is interfaced with the tunnel barrier (3.5 to 5 kOe), no domain structure is built in the thick layer in this field region. This is related to a limited rotation of the magnetization with respect to the field direction [limited to 45° as shown in Fig. 1(a)]. In contrast, below 3.5 kOe, the competition between the AFM coupling, local anisotropy, and Zeeman energies allows the walls to be duplicated from the thinner to the thicker layer. Duplication of the walls from the thin layer can take place due to the strong AFM coupling that tends to locally flip the magnetic moments to overcome the frustration sensed by the walls in the thin layer. These walls have their center parallel with both the external field and the magnetization of the thicker layer of the AF. This makes them energetically favored by the external field but the AFM exchange coupling tends to annihilate them when reducing the field. An estimation of the AFM exchange field ($H_{ex} = 3-4$ kOe) indicates that this duplication should take place at a field in the range of 3 kOe. Above this field range, the Zeeman energy prevents the walls from being duplicated in the thicker layer. These walls act as high-resistance channels and are reflected in the inset of Fig. 3(c) as high-resistance states compared to the reversed branch of the loop where no domain walls subsist at the end of the plateau (see next section).

At the end of the flank, the angle of the walls in the AF layers will be large enough to make their existence energetically unfavorable (the wall energy increases with the angle of the adjacent domains). Therefore, the walls are annihilated, corresponding to the closure of the hysteresis in Figs. 3(b) and 3(c). Magnetization features in the AF layers in the AFM plateau are reflected in the TMR loops for the *R*-AF-based [Fig. 3(b)] and *N*-AF-based [Fig. 3(c)] MTJ's. Indeed, fluctuations of magnetization angle in the thicker AF layer, due to local anisotropies, determine a resistive state in the plateau higher than in the saturation state (perfect parallel alignment) as shown in the inset of Fig. 3(c). Moreover, a gradual increase of the junction's resistance, when reducing the field towards zero, is determined by the relaxation of magnetic moments in both AF layers towards their local anisotropy axes [see Figs. 3(b) and 3(c)].

C. Negative low-field-reversal domain structures and the flank towards negative saturation

By reversing the magnetic field in the negative direction, the magnetically soft DL reverses its magnetization [Fig. 3, transition from state (2) to state (3)]. This will induce a magnetization configuration between the magnetic layers interfaced with the tunnel barrier, antiparallel in the case of *N*-AF-based MTJ responsible for a high-resistance state [Fig. 3(c)], and a parallel magnetization configuration in the case of R-AFi-based MTJ, responsible for a low-resistance state [Fig. 3(b)]. By further increasing the negative applied magnetic field, the Zeeman energy will then overcome the coupling energy and the AF net magnetic moment reverses spontaneously by rotation of magnetizations in each layer, leading to a rapid increase (*R*-AF) or decrease (*N*-AF) of the MTJ resistance. As soon as the reversal of the net moment is completed [Fig. 3, state (4)] , the magnetization of the AF topmost layer becomes either parallel (small-resistance configuration in the case of *N*-AF-based MTJ) or antiparallel with the DL (high-resistance configuration of the *R*-AF-based MTJ).

However, since the two Co layers rotate by 180° for the reversal of the net AF moment, creation and annihilation of 360° domain walls in both thick and thin magnetic layers are expected.[6,18] Furthermore, as a consequence of the strong interlayer AFM coupling, walls nucleated in one layer are mirrored in the other. The AFM coupling has a strong impact on the walls stability. Indeed, during the reversal, the thick layer develops walls having their centers opposite to the negative field direction. This situation is energetically unstable, as the core of the wall has its magnetization direction antiparallel to the field. However, this instability is further maintained by the AFM exchange, which couples the walls in the thick and thin layers since the walls in the thin layer are energetically stable (their center is oriented along the field direction). So, the AFM coupling acts as an additional source of pinning for the walls located in the thick layer up to fields for which the Zeeman energy overcomes the AFM coupling energy.

This particular domain-phase evolution and the stability of the walls in each layer is reflected in the *R-H* curves (Fig. 3) and confirmed using field-dependent MFM with *in situ* applied field. After reversal of the DL, the cores of the 360° walls act as high-resistance tunnel channels in the *N*-AF configuration and as low-resistance tunnel channels in the *R*-AF configuration. The stability of the walls in the thin AF layer is evidenced on the TMR curve [Fig. 3(b)] by the fact that the highest-resistance state is never achieved (maximum resistance 304 kΩ as compared to 306 kΩ) after the AF reversal. In this magnetic configuration, the core of the walls is parallel to the DL acting as highly conducting channels, reducing as a consequence the resistance of the MTJ. These stable walls will gradually disappear only when, at high fields, the domains adjacent to the walls will start reversing by rotation, annihilating eventually the large-angle walls. This effect is shown on Fig. 3(b) by the slow decrease of the resistance at the negative flank towards saturation. In contrast, the walls are less stable in the thick AF layer and can vanish at lower fields in the negative AFM plateau, soon after the AF's net-moment reversal. This effect is clearly indicated in the TMR curve by reaching the low-resistance state in the negative AFM plateau, as shown in Fig. 3(c).

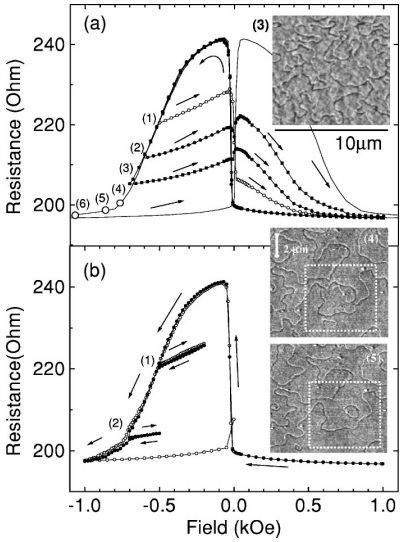

FIG. 4. (a) Minor *R-H* loops (CPP), taken in the AF plateau, for a MTJ using an AF having the thick magnetic layer in contact with the tunnel barrier (*N*-AF configuration). Asymmetric loops start for all curves at + 1 kOe and are reversed at different negative field values: −500 Oe (1), −600 Oe (2), −700 Oe (3), −800 Oe (4), −900 Oe (5), −1 kOe (6). These curves illustrate the existence of 360° walls in the thick AF layer up to fields of −1 kOe. (b) Minor *R-H* loop (CPP) taken in the AF plateau (+1/−1 kOe) starting at +1 kOe, reversed at some negative-field values during the magnetization reversal of the AF: −500 Oe (1), −700 Oe (2) decreased up to fields of −200 Oe and −500 Oe, respectively, and then increased again up to −1 kOe. This reversible phenomenon, which shows that the walls are not propagating, is aimed to emphasize the rotation mechanism of the magnetization reversal. Inset: Magnetic-force-microscopy images showing the 360° residual domain structure in state (3) and the evolution of the domain structure between two magnetic states (4) and (5). The MFM images corresponding to the states (4) and (5) illustrate the annihilation of wall segments with the applied field.

D. Stability of the 360° walls using minor TMR loop features

Details of the magnetization reversal and domain-wall stability are reflected in Figs. 4 and 5 for the *N*-AF- and *R*-AF-based MTJ junctions, respectively. These figures represent measurements of minor *R-H* curves for the *N*-AF between +1 and −1 kOe (Fig. 4) and for the *R*-AF between +2 and −2 kOe (Fig. 5) after saturation in a positive field. Starting from the positive field, the MTJ is in a low(*N*-AF)- or high(*R*-AF)-resistance state depending on which of the AF's layers is in contact with the barrier. These resistance states are inverted when the DL switches at low negative field.

Before negative saturation, the field sequence is inverted at some states denoted by states (1), (2), (3), or (4) in Figs. 4 and 5. Reversing the field towards positive values, the resistive jump occurring when the DL switches at positive field depends on the degree of reversal of the AF net magnetization and therefore on the residual domain-wall structure. The jump even changes sign when a particular point has been

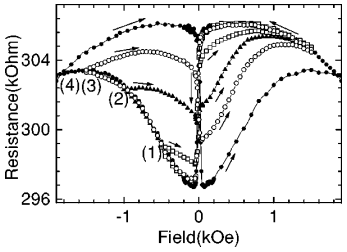

FIG. 5. Minor *R-H* loops (CPP), taken in the AF plateau, for an MTJ using an AF having the thin magnetic layer in contact with the tunnel barrier (*N*-AF configuration). Asymmetric loops are taken between +1 kOe and different negative field values, defined by the states −500 Oe (1), −1 kOe (2), −1.5 kOe (3), −2 kOe (4), during the net AF moment reversal. This figure is aimed to emphasize the stability of the walls in the thin layer of the AF. It is interesting to note that the walls are more stable in the thin layer up to fields of 2 kOe, compared with lower-field annihilation in the thick layer (Fig. 4).

overcome upon reversal. The amplitude and especially the sign of the jump in the *R-H* curve has a particular importance. In Fig. 4 (Fig. 5), corresponding to *N*-AF (*R*-AF)-based MTJ's, respectively, when the reversal is stopped in state (1) a steep drop (increase) of the MTJ resistance after the DL reversal in the positive field indicates that the switch of the DL has activated predominant low (high) conduction channels, associated with the network of walls, which contribute to the resistance along with the high- (low-) conduction channels provided by the domains. Interestingly, the reversed effect, an increase (drop) of the resistance when the DL switches, shown in Fig. 4 (Fig. 5) after previously stopping in state (3), is due to the activation of predominant domain conduction channels. The two contributions in the resistance from domains and walls, almost balance in the case when the reversal is stopped at state (2). This will not give rise to any jump in the resistance when the DL switches, as we can see from Figs. 4 and 5.

The stability of the walls is given through the field range needed to get a symmetric TMR curve. In the *N*-AF case, the field range between −1 and 1 kOe was sufficient to completely reverse the thicker AF layer, which indicates that most of the 360° walls have been annihilated. This is confirmed by the symmetry of the TMR curve when increasing the field towards saturation. In contrast, the experiments performed on the *R*-AF system show that the stability of the domain walls in the thinner AF layer exceeds the previous field range, where the layers were supposed to have completely reversed as shown from the asymmetric shape of the curves for fields below 2 kOe, Fig. 5 [states (1), (2), (3)]. In this states the subsistence of walls in the thinner layer is responsible for the asymmetric TMR signal of the junctions incorporating the *R*-AF. Interestingly, the asymmetry vanishes only for fields beyond 2 kOe [Fig. 5, state (4)], which indicates that the walls have been annihilated for fields larger than 2 kOe.

Quantitative analysis of the AF net magnetization reversal[17] and the domain-wall stability features has been made by using an analytical model for the MTJ in a multi-

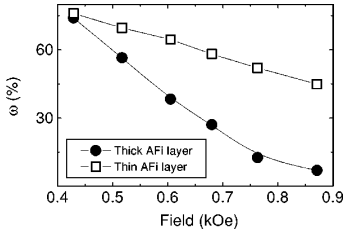

FIG. 6. Variation of the density of walls in external field in the thicker and the thinner AF magnetic layers.

domain configuration.[19] In this model, domain and domain walls constitute tunneling channels having different resistances. The domain magnetization makes an angle θ with respect to the field direction, while the magnetization in the center of the wall remains aligned along the initial positive saturation direction. Therefore, the total resistance R of the MTJ in a multidomain configuration is calculated as the equivalent resistance of a network of in-cascade resistances associated with domain and domain-wall elementary segments.

The residual domain-wall structure subsisting in the AF in a state (i) (i$=1, \ldots, 5$, Figs. 4 and 5) is reflected by a higher (for an *N*-AF) or a lower (for an *R*-AF) resistive state of the MTJ than the one corresponding to the configuration where the walls are completely annihilated (R_0). We quantify this wall-related resistive state by a residual magnetoresistance $t_R^{(i)}=[R(i)-R_0]/R_0$. Therefore, the surface of the walls with respect to the total surface of the junction $\omega^{(i)}$, responsible for a residual magnetoresistance $t_R^{(i)}$, can be deduced from the equation[19]

$$\omega^{(i)}=\frac{t_R^{(i)}-\dfrac{T_{MR}(1-\cos\theta^{(i)})}{2}}{\dfrac{T_{MR}(1+\cos\theta^{(i)})}{2}}\,\frac{1+T_{MR}}{1+t_R^{(i)}} \qquad (2)$$

where $T_{MR}=(R_{AP}-R_P)/R_P$; R_{P} and R_{AP} represent the tunnel resistance corresponding to the parallel (*P*) and antiparallel (AP) configuration, respectively, of the MTJ barrier-adjacent magnetic layers.

As shown by the MFM measurements, in the state (3) (inset of Fig. 4), the domain magnetization is practically reversed. So $\theta(i>3)\simeq 0$ and ω can be easily calculated for the *N*-AF and *R*-AF from Eq. (2).

The variation of ω as a function of the applied field is reported in Fig. 6. The results are in agreement with values extracted from the analysis of the MFM images (inset of Fig. 4).

The results presented in Fig. 6 are of particular importance because they illustrate the relative stability of the walls in the thick and thin layer of the AF. For relatively small negative applied fields ($|H|<0.5$ kOe), ω is high and almost similar in both layers. This result confirms the fact that in this field range the domain-wall structure is antiferromagnetically mirrored in both AF layers. However, we have to specify that the calculated values are slightly overestimated since for $H<0.5$ kOe, the angle of the magnetization in the AF layers with respect to the external field ($\theta^{(i)}$) cannot be neglected.

For higher fields ($H>0.6$ kOe), $\theta^{(i)}$ can be reasonably considered zero. In this field range, no significant change in the evolution of ω with the applied field was found when taking into account a nonzero value of $\theta^{(i)}$.

From Fig. 6 we can clearly see that the variation of the density of walls with respect to the field $[\omega(H)]$ is strongly different in the thicker and the thinner AF layers. Domain walls located in the thin AF layer are more stable than those located in the thicker one. For an applied field of 0.9 kOe, the walls are completely annihilated in the thick layer while almost 45% of the thin-layer surface area is still occupied by residual walls.

Another interesting phenomena that can be ''probed'' using the high sensitivity of the spin-polarized tunnel transport is the reversible character of the AF's net magnetic-moment reversal by coherent rotation. This is illustrated by the *R-H* minor-loop measurements shown in Fig. 4(b). In this case the external field was stopped in an incomplete AF reversal state after the switching of the DL in negative field, then reduced and finally increased back again. Repeating this process for two points [Fig. 4(b), points (1) and (2)], fully reversible features have been observed. This implies that the magnetization reversal is a fully reversible process that can only be explained through a fully magnetization-rotation mechanism, directly related to the angular distribution of local anisotropies in polycristalline materials.

For preventing all their negative effects on the magnetoresistive response of potential spin-electronics devices, the creation of the 360° walls has to be inhibited. This can be achieved by inducing an anisotropy in an AF system, i.e., by exchange coupling the AF structure with a standard antiferromagnet (IrMn, PtMn) or by growing the magnetic layers in an external field.

V. CONCLUSION

By analyzing the tunnel-magnetoresistive signal shape and amplitude, micromagnetic features in each layer of an artificial ferrimagnet system have been selectively studied. This is made possible by the high sensitivity of the spin polarized current to fluctuations of magnetization in one of the magnetic layers of the magnetic-tunnel junctions. We propose a simple analytical model for the MTJ in a multidomain state, which takes into account different tunneling paths associated to local magnetization configurations. The model allows a quantitative correlation between the spin-polarized transport characteristics and the field-dependent domain structure. The results extracted from the tunnel-magnetoresistance analysis are found to be in good agreement with the data extracted from the analysis of the magnetic-force-microscopy images.

The magnetic state versus field of the magnetic layers constituting the AF was probed selectively in the field window from positive to negative saturation. Hysteretic features were analyzed and attributed to domain-wall creation and annihilation in the AF layers. These effects were interpreted

in the framework of randomly distributed anisotropy axes in polycrystalline films. From our understanding of the magnetic behavior of the AF, it appears that a key parameter to avoid the formation of domain walls during the reversal process would be to induce a uniaxial anisotropy in the hard subsystem to force the magnetization to rotate uniformly. Therefore, to control and optimize the field response of magnetic thin-film devices, hard magnetic AF subsystems are nowadays used with adjacent antiferromagnets or uniaxial anisotropy.

ACKNOWLEDGMENTS

The authors thank illuminating discussions with V. da Costa, Pierre Panissod, H. van den Berg, and Ursula Ebels and experimental support of Yves Henry, Cristian Meny, and Gerard Wurz. This work was supported by the European Framework IV Materials Technology Program, Contract No. BRPR-CT98-0657, the *Dynaspin* program, *Training and Mobility of Researchers* network under Contract. No. FMRX-CT97-0147, and the Nanomem Program (IST-1999-13741). K.O. also acknowledges NSF Grant No. CNRS-9603252.

[1] J.S. Moodera, L.R. Kinder, T.M. Wong, and R. Meservey, Phys. Rev. Lett. **74**, 3273 (1995); T. Miyazaki and N. Tezuka, J. Magn. Magn. Mater. **139**, L231 (1995).

[2] W.J. Gallagher, S.S.P. Parkin, Y. Lu, X.P. Bian, A. Marley, K.P. Roche, R.A. Altman, S.A. Rishton, C. Jahnes, T.M. Shaw, and G. Xiao, J. Appl. Phys. **81**, 3741 (1997).

[3] E. Nowak, R.D. Merithew, M.B. Weissman, I. Bloom, and S.S.P. Parkin, J. Appl. Phys. **84**, 6195 (1998).

[4] S. Gider, B.-U. Runge, A.C. Marley, and S.S.P. Parkin, Science **281**, 797 (1998).

[5] K.S. Moon, R.E. Fontana, S.S.P. Parkin, Appl. Phys. Lett. **74**, 3690 (1999).

[6] C. Tiusan, T. Dimopoulos, K. Ounadjela, M. Hehn, H.A.M. van den Berg, Y. Henry, and V. Da Costa, Phys. Rev. B **61**, 580 (2000).

[7] M. Hehn, O. Lenoble, D. Lacour, C. Fery, M. Piecuch, C. Tiusan, and K. Ounadjela, Phys. Rev. B **61**, 11 643 (2000).

[8] A. Anguelouch, B. Shrang, G. Xiao, Y. Lu, P. Trouilloud, W.J. Gallagher, S.S.P. Parkin, Appl. Phys. Lett. **76**, 622 (2000).

[9] L. Thomas, M.G. Samant, and S.S.P. Parkin, Phys. Rev. Lett. **84**, 1816 (2000).

[10] C. Tiusan, M. Hehn, K. Ounadjela, Y. Henry, J. Hommet, C. Meny, H.A.M. van den Berg, L. Baer, and R. Kinder, J. Appl. Phys. **8**, 5276 (1999).

[11] H.A.M. van den Berg, W. Clemens, G. Gieres, G. Rupp, M. Vieth, J. Wecker, and S. Zoll, J. Magn. Magn. Mater. **165**, 524 (1997).

[12] T. Dimopoulos, C. Tiusan, K. Ounadjela, M. Hehn, and H.A.M. van den Berg, J. Appl. Phys. **87**, 4685 (2000).

[13] N. Persat, H.A.M. van den Berg, K. Cherifi-Khodjaoui, and A. Dinia, J. Appl. Phys. **81**, 4748 (1997); N. Persat, H.A.M. van den Berg, and A. Dinia, J. Magn. Magn. Mater. **165**, 446 (1997).

[14] D.V. Berkov and N.L. Gorn, Phys. Rev. B **57**, 14 332 (1998).

[15] J. Nassar, M. Hehn, A. Vaures, F. Petroff, and A. Fert, Appl. Phys. Lett. **73**, 698 (1988).

[16] E.C. Stoner and E.P. Wohlfarth, Philos. Trans. R. Soc. London, Ser. A **240**, 559 (1948).

[17] R.L. Stamps, A.S. Carrico, and P.E. Wigen, Phys. Rev. B **55**, 6473 (1997).

[18] The polycrystalline Co layers, constituted of small magnetic grains coupled by exchange interactions, are macroscopically magnetically isotropic due to a random orientation of the easy magnetic axis of each grain. For the thickness range and weak intergrain coupling involved in our samples, the reversal of the layer magnetization proceeds mainly by individual grain magnetic-moment rotation (Ref. 14). During the magnetization reversal, moments inside areas presenting the smallest coupling (direct lateral-exchange coupling and/or indirect AF interlayer coupling) start to rotate, and drag in rotation the magnetization inside neighbor areas with stronger coupling. The sense of rotation is determined by a local effective anisotropy. Therefore, separate domains with rotating magnetization turn clockwise or counterclockwise leading to the appearence of 360° Néel domain walls.

[19] C. Tiusan, M. Hehn, T. Dimopoulos, and K. Ounadjela, J. Appl. Phys. **89**, 6668 (2001).

Appendix B

Analytical model for an artificial anti-ferromagnetic system

In this appendix we propose an analytical model which describes the behavior of an artificial antiferromagnetic system in magnetic fields. The model leads to analytical expression for the critical parameters such as the saturation field H_S and the plateau field H_P, as a function of the AAF's intrinsic parameters: thickness of layers, anisotropies, coupling strength.
We consider here the situation where the magnetic layers present a fourfold anisotropy: K_1, K_2 being the anisotropies of layers 1 and 2 of thickness t_1 and t_2 and magnetizations M_1 and M_2. The bilinear coupling is J, $\theta_{1,2}$ represent the angles between the magnetizations $M_{1,2}$ and the field H, φ the angle between one of the easy axis (A) and the field H, the other easy axis (B) is perpendicular to (A) (fourfold anisotropy). The Figure B.1 presents schematically the macrospin Stoner-Wolfhart model used in our modeling.
Within this model the total energy of the AAF is given by:

$$\mathrm{E_{total}} = -\mathrm{H}\times(\mathrm{M_1 t_1 cos}\theta_1+\mathrm{M_2 t_2 cos}\theta_2)-J\cos(\theta_1-\theta_2)+\frac{K_1 t_1}{4}\sin^2 2\,(\theta_1-\varphi)+\frac{K_2 t_2}{4}\sin^2 2\,(\theta_2-\varphi)$$

The first term represents the Zeeman energy, the second the bilinear coupling energy and the last two terms the anisotropy energy.
The minimization of the total energy $\frac{\partial E}{\partial \theta_1}=0$ and $\frac{\partial E}{\partial \theta_2}=0$ leads to the following equations:

$$\begin{cases} \sin(\theta_2-\theta_1)=\frac{1}{J}\left[MHt_1\sin\theta_1+K_1t_1\sin 2(\theta_1-\varphi)\cos 2(\theta_1-\varphi)\right] \\ -\sin(\theta_2-\theta_1)=\frac{1}{J}\left[MHt_2\sin\theta_2+K_2t_2\sin 2(\theta_2-\varphi)\cos 2(\theta_2-\varphi)\right] \end{cases}$$

These equations can be solved in several specific situations.

B.1 Easy axis ($\varphi = 0$)

In order to compute the saturation field H_s and the plateau field H_P one can rewrite the general equations for $\varphi = 0$ in the form:

$$\begin{cases} \frac{\sin\theta_1}{\sin(\theta_2-\theta_1)}=\frac{J}{t_1}\frac{1}{[MH+2K_1\cos\theta_1\cos 2\theta_1]} \\ -\frac{\sin\theta_2}{\sin(\theta_2-\theta_1)}=\frac{J}{t_2}\frac{1}{[MH+2K_2\cos\theta_2\cos 2\theta_2]} \end{cases}$$

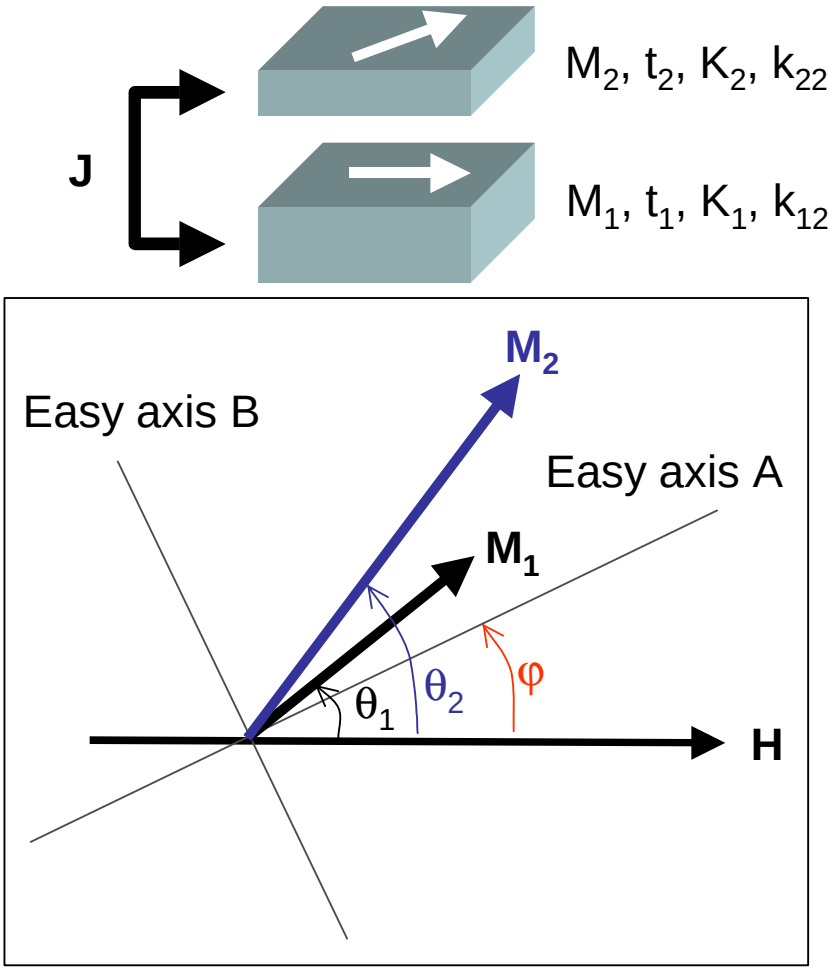

Figure B.1: Schematic representation for the macrospin Stonel-Wolfhart model. The four-fold easy axis are denoted by A and B. The field H is applied at an angle φ with respect to the A easy axis. In an arbitrary configuration, the magnetization M_i of the layer i of thickness t_i, anisotropy K_i, k_{i2} makes the angle θ_i with respect to the field. The magnetic coupling between the two layers is denoted by J.

By summing the two equations we obtain:

$$\frac{\sin\theta_1 - \sin\theta_2}{\sin(\theta_2 - \theta_1)} = \frac{J}{t_1}\frac{1}{[MH + 2K_1\cos\theta_1\cos 2\theta_1]} + \frac{J}{t_2}\frac{1}{[MH + 2K_2\cos\theta_2\cos 2\theta_2]}$$

The saturation field for the easy axis denoted by H_S^E corresponds to the saturation of both magnetic layers: i.e. $\theta_1 \to 0^-$ and $\theta_2 \to 0^+$. Moreover, we have:

$$\frac{\sin\theta_1 - \sin\theta_2}{\sin(\theta_2 - \theta_1)} = \frac{2\cos(\frac{\theta_1+\theta_2}{2})\sin(\frac{\theta_1-\theta_2}{2})}{2\cos(\frac{\theta_2-\theta_1}{2})\sin(\frac{\theta_2-\theta_1}{2})} = -\frac{\cos(\frac{\theta_1+\theta_2}{2})}{\cos(\frac{\theta_2-\theta_1}{2})}$$

the limit $\theta_1 \to 0^-$ and $\theta_2 \to 0^+$ gives:

$$-1 = \frac{J}{t_1}\frac{1}{[MH_S^E + 2K_1]} + \frac{J}{t_2}\frac{1}{[MH_S^E + 2K_2]}$$

which leads to a second order equation with respect to H_S^E whose resolution gives:

$$H_S^E + \frac{K_1 + K_2}{M} = -\frac{J}{2M}\left(\frac{1}{t_1} + \frac{1}{t_2}\right)\left[1 \pm \sqrt{1 + \frac{4t_1t_2(t_1 - t_2)}{(t_1 + t_2)^2}\frac{(K_2 - K_1)}{J} + \frac{4t_1^2t_2^2}{(t_1 + t_2)^2}\frac{(K_2 - K_1)^2}{J^2}}\right]$$

In order to determine the plateau field we use now the equations:

$$\frac{\sin\theta_1 + \sin\theta_2}{\sin(\theta_2 - \theta_1)} = \frac{J}{t_1}\frac{1}{[MH + 2K_1\cos\theta_1\cos 2\theta_1]} - \frac{J}{t_2}\frac{1}{[MH + 2K_2\cos\theta_2\cos 2\theta_2]}$$

combined with:

$$\frac{\sin\theta_1 + \sin\theta_2}{\sin(\theta_2 - \theta_1)} = \frac{2\cos(\frac{\theta_1-\theta_2}{2})\sin(\frac{\theta_1+\theta_2}{2})}{2\cos(\frac{\theta_2-\theta_1}{2})\sin(\frac{\theta_2-\theta_1}{2})} = -\frac{\sin(\frac{\theta_1+\theta_2}{2})}{\sin(\frac{\theta_2-\theta_1}{2})}$$

The determination of the plateau field H_P^F implicates the limit situation: $\theta_1 \to 0^-$ and $\theta_2 \to \pi^-$ which leads to:

$$1 = \frac{J}{t_1}\frac{1}{[MH_P^E + 2K_1]} - \frac{J}{t_2}\frac{1}{[MH_P^E - 2K_2]}$$

which corresponds again to a second order equation in H_P^E. The solution of this equation gives the plateau field along the easy axis:

$$H_P^E - \frac{K_2 - K_1}{M} = -\frac{J(t_1 - t_2)}{2t_1t_2M}\left[1 \pm \sqrt{1 - \frac{4t_1t_2(t_1 + t_2)}{(t_1 - t_2)^2}\frac{(K_1 + K_2)}{J} + \frac{4t_1^2t_2^2}{(t_1 - t_2)^2}\frac{(K_1 + K_2)^2}{J^2}}\right]$$

In these expressions the sign $\pm$ implicates two possible solutions for the saturation and the plateau fields. The analysis of the solution in the limit case when $K_1 = K_2 = 0$ allows to chose only the physical valid solutions:

$$H_S^E + \frac{K_1 + K_2}{M} = -\frac{J}{2M}\left(\frac{1}{t_1} + \frac{1}{t_2}\right)\left[1 + \sqrt{1 + \frac{4t_1t_2(t_1 - t_2)}{(t_1 + t_2)^2}\frac{(K_2 - K_1)}{J} + \frac{4t_1^2t_2^2}{(t_1 + t_2)^2}\frac{(K_2 - K_1)^2}{J^2}}\right]$$

and:

$$H_P^E - \frac{K_2 - K_1}{M} = -\frac{J(t_1 - t_2)}{2t_1t_2M}\left[1 + \sqrt{1 - \frac{4t_1t_2(t_1 + t_2)}{(t_1 - t_2)^2}\frac{(K_1 + K_2)}{J} + \frac{4t_1^2t_2^2}{(t_1 - t_2)^2}\frac{(K_1 + K_2)^2}{J^2}}\right]$$

B.2 Hard axis ($\varphi = \pi/4$)

We can proceed in a similar way:

$$\begin{cases} \frac{\sin\theta_1}{\sin(\theta_2-\theta_1)} = \frac{J}{t_1}\frac{1}{[MH-2K_1\cos\theta_1\cos 2\theta_1]} \\ -\frac{\sin\theta_2}{\sin(\theta_2-\theta_1)} = \frac{J}{t_2}\frac{1}{[MH-2K_2\cos\theta_2\cos 2\theta_2]} \end{cases}$$

The limit $\theta_1 \to 0^-$ and $\theta_2 \to 0^+$ for the saturation field H_S^H and $\theta_1 \to 0^-$ and $\theta_2 \to \pi^-$ for the plateau field H_P^H along the hard axis give:

$$-1 = \frac{J}{t_1}\frac{1}{[MH_S^H - 2K_1]} + \frac{J}{t_2}\frac{1}{[MH_S^H - 2K_2]}$$

and

$$1 = \frac{J}{t_1}\frac{1}{[MH_P^H - 2K_1]} - \frac{J}{t_2}\frac{1}{[MH_P^H + 2K_2]}$$

The resolution of these equations lead to the analytical solutions:

$$H_S^H - \frac{K_1+K_2}{M} = -\frac{J}{2M}\left(\frac{1}{t_1}+\frac{1}{t_2}\right)\left[1 \pm \sqrt{1 + \frac{4t_1t_2(t_1-t_2)}{(t_1+t_2)^2}\frac{(K_2-K_1)}{J} + \frac{4t_1^2t_2^2}{(t_1+t_2)^2}\frac{(K_2-K_1)^2}{J^2}}\right]$$

and:

$$H_P^H + \frac{K_2-K_1}{M} = -\frac{J(t_1-t_2)}{2t_1t_2M}\left[1 \pm \sqrt{1 + \frac{4t_1t_2(t_1+t_2)}{(t_1-t_2)^2}\frac{(K_1+K_2)}{J} + \frac{4t_1^2t_2^2}{(t_1-t_2)^2}\frac{(K_1+K_2)^2}{J^2}}\right]$$

The physical valid solutions are then:

$$H_S^H - \frac{K_1+K_2}{M} = -\frac{J}{2M}\left(\frac{1}{t_1}+\frac{1}{t_2}\right)\left[1 + \sqrt{1 + \frac{4t_1t_2(t_1-t_2)}{(t_1+t_2)^2}\frac{(K_2-K_1)}{J} + \frac{4t_1^2t_2^2}{(t_1+t_2)^2}\frac{(K_2-K_1)^2}{J^2}}\right]$$

and

$$H_P^H + \frac{K_2-K_1}{M} = -\frac{J(t_1-t_2)}{2t_1t_2M}\left[1 + \sqrt{1 + \frac{4t_1t_2(t_1+t_2)}{(t_1-t_2)^2}\frac{(K_1+K_2)}{J} + \frac{4t_1^2t_2^2}{(t_1-t_2)^2}\frac{(K_1+K_2)^2}{J^2}}\right]$$

B.3 Limit situations

We can consider first the case of isotropic magnetic layers ($K_1 = K_2 = 0$). This limit gives the following simplified expressions for the saturation and the plateau fields:

$$\begin{aligned} H_S &= -\frac{J}{M}\left(\frac{1}{t_1}+\frac{1}{t_2}\right) \\ H_P &= -\frac{J}{M}\frac{(t_1-t_2)}{t_1t_2} \end{aligned}$$

Note that the isotropic limit all the directions are equivalent which is also validated by the limit equal values of $H_S^E = H_S^H = H_S$ and $H_P^E = H_P^H = H_P$.
We can define the factor Q given by:

$$\frac{H_S}{H_P} = \frac{t_1+t_2}{t_1-t_2} = Q$$

One can demonstrate that the Q factor represents also the amplification factor for the coercive field of the AAF[97]. For an AAF in the AF plateau the net magnetic moment is reduced $(M_1 - M_2)$ which reduces the sensitivity in external fields by the factor $t_1 - t_2$. Moreover within the mono-bloc strongly AF coupled the total friction of the magnetization with respect to external fields is increased by a factor proportional to $t_1 + t_2$. Then, roughly the coercive field of an AAF is the coercive field of one of its single layers multiplied by the factor Q.
If $K_1 = K_2 = K$ then we obtain:

$$\begin{array}{l} H_S^E + \frac{2K}{M} = -\frac{J}{M}\left(\frac{1}{t_1} + \frac{1}{t_2}\right) \\ H_S^H - \frac{2K}{M} = -\frac{J}{M}\left(\frac{1}{t_1} + \frac{1}{t_2}\right) \end{array}$$

$$H_P^E = -\frac{J(t_1 - t_2)}{2t_1 t_2 M}\left[1 \pm \sqrt{1 - \frac{8t_1 t_2(t_1 + t_2)}{(t_1 - t_2)^2}\frac{K}{J} + \frac{16t_1^2 t_2^2}{(t_1 - t_2)^2}\frac{K^2}{J^2}}\right]$$

and:

$$H_P^H = -\frac{J(t_1 - t_2)}{2t_1 t_2 M}\left[1 \pm \sqrt{1 + \frac{8t_1 t_2(t_1 + t_2)}{(t_1 - t_2)^2}\frac{K}{J} + \frac{16t_1^2 t_2^2}{(t_1 - t_2)^2}\frac{K^2}{J^2}}\right]$$

If the AAF is compensated $(t_1 = t_2)$ then:

$$\left\{ \begin{array}{l} H_S^E + \frac{2K}{M} = -\frac{2J}{Mt} \\ H_S^H - \frac{2K}{M} = -\frac{2J}{Mt} \end{array} \right.$$

B.4 Inequivalent anisotropy axes

In epitaxial systems the growth of the samples in oblic geometry may give rise to inequivalent anisotropy values for the fourfold axes. In order to include this inequivalent anisotropy for the fourfold axes one can simply add a second order anisotropy for each easy axis (φ and $\varphi + \pi/2$). We denote this two fold anisotropies by k_{12} and k_{22}. This will add some additional second order anisotropy terms in the total energy:

$$\begin{array}{l} \mathrm{E_{totale}} = -\mathrm{H} \times (\mathrm{M_1 t_1 cos}\theta_1 + \mathrm{M_2 t_2 cos}\theta_2) - J\cos(\theta_1 - \theta_2) + \frac{K_1 t_1}{4}\sin^2 2(\theta_1 - \varphi) \\ + \frac{K_2 t_2}{4}\sin^2 2(\theta_2 - \varphi) + k_{12} t_1 \sin^2(\theta_1 - \varphi) + k_{22} t_2 \sin^2(\theta_2 - \varphi) \end{array}$$

Along the easiest axis (A) whic corresponds to $\varphi = 0$ the energy minimization leads to:

$$\left\{ \begin{array}{l} \frac{\sin\theta_1}{\sin(\theta_2 - \theta_1)} = \frac{J}{t_1}\frac{1}{[MH + 2K_1\cos\theta_1\cos 2\theta_1 + 2k_{12}\cos\theta_1]} \\ -\frac{\sin\theta_2}{\sin(\theta_2 - \theta_1)} = \frac{J}{t_2}\frac{1}{[MH + 2K_2\cos\theta_2\cos 2\theta_2 + 2k_{22}\cos\theta_2]} \end{array} \right.$$

whereas along the other easy axis (B) which corresponds to $\varphi = \pi/2$ one obtain:

$$\left\{ \begin{array}{l} \frac{\sin\theta_1}{\sin(\theta_2 - \theta_1)} = \frac{J}{t_1}\frac{1}{[MH + 2K_1\cos\theta_1\cos 2\theta_1 - 2k_{12}\cos\theta_1]} \\ -\frac{\sin\theta_2}{\sin(\theta_2 - \theta_1)} = \frac{J}{t_2}\frac{1}{[MH + 2K_2\cos\theta_2\cos 2\theta_2 - 2k_{22}\cos\theta_2]} \end{array} \right.$$

Similarly to the previous analysis, the limit situations lead to the following expressions: For the easiest axis (A):

$$H_S^A + \frac{K_1+k_{12}+K_2+k_{22}}{M} = -\frac{J}{2M}\left(\frac{1}{t_1}+\frac{1}{t_2}\right)\left[1+\sqrt{1+\frac{4t_1t_2(t_1-t_2)}{(t_1+t_2)^2}\frac{(K_2+k_{22}-K_1-k_{12})}{J}+\frac{4t_1^2t_2^2}{(t_1+t_2)^2}\frac{(K_2+k_{22}-K_1-k_{12})^2}{J^2}}\right]$$

and:

$$H_P^A - \frac{K_2+k_{22}-K_1-k_{12}}{M} = -\frac{J(t_1-t_2)}{2t_1t_2M}\left[1+\sqrt{1-\frac{4t_1t_2(t_1+t_2)}{(t_1-t_2)^2}\frac{(K_1+k_{12}+K_2+k_{22})}{J}+\frac{4t_1^2t_2^2}{(t_1-t_2)^2}\frac{(K_1+k_{12}+K_2+k_{22})^2}{J^2}}\right]$$

For the other easy axis (B)

$$H_S^B + \frac{K_1-k_{12}+K_2-k_{22}}{M} = -\frac{J}{2M}\left(\frac{1}{t_1}+\frac{1}{t_2}\right)\left[1+\sqrt{1+\frac{4t_1t_2(t_1-t_2)}{(t_1+t_2)^2}\frac{(K_2-k_{22}-K_1+k_{12})}{J}+\frac{4t_1^2t_2^2}{(t_1+t_2)^2}\frac{(K_2-k_{22}-K_1+k_{12})^2}{J^2}}\right]$$

and:

$$H_P^B - \frac{K_2-k_{22}-K_1+k_{12}}{M} = -\frac{J(t_1-t_2)}{2t_1t_2M}\left[1+\sqrt{1-\frac{4t_1t_2(t_1+t_2)}{(t_1-t_2)^2}\frac{(K_1-k_{12}+K_2-k_{22})}{J}+\frac{4t_1^2t_2^2}{(t_1-t_2)^2}\frac{(K_1-k_{12}+K_2-k_{22})^2}{J^2}}\right]$$

If we suppose now that $k_1 = K_2 = K$ and $k_{12} = k_{22} = k$ we obtain the following equations:

$$H_S^A + \frac{2(K+k)}{M} = -\frac{J}{M}\left(\frac{1}{t_1}+\frac{1}{t_2}\right)$$
$$H_S^B + \frac{2(K-k)}{M} = -\frac{J}{M}\left(\frac{1}{t_1}+\frac{1}{t_2}\right)$$

whose resolution gives:

$$k = \frac{M}{4}\left(H_{S_1} - H_{S_2}\right)$$

This means that by measuring the saturation field along each of the two easy axis one can extract information about the second order anisotropy.

The above analytical model has been used to extract exact analytical expressions for the critical fields (saturation and plateau). It may be useful to calculate the values of the $\theta_1(H)$ and $\theta_2(H)$ for each value of the field H from positive saturation field to negative saturation field. This implicates the minimization of the total energy, point by point $\frac{\partial E(H)}{\partial \theta_1(H)} = 0$ and $\frac{\partial E(H)}{\partial \theta_2(H)} = 0$. This can be performed numerically (i.e. by steepest-descent, conjugated gradient, or Metropolis/Monte Carlo algorithms).

Appendix C

Symmetrized bases for wave functions in hexagonal close packed crystal

This appendix contains some elements about the basis of function belonging to each irreducible representation of groups of the hexagonal close packed structures.

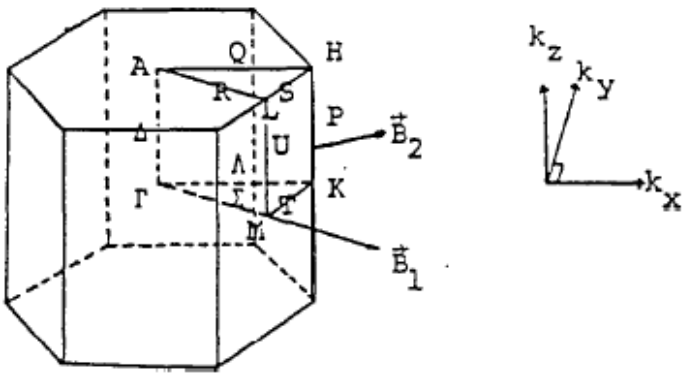

Figure C.1: Basis functions for the irreducible representations of the Σ line

A detailed analysis has been performed by Chang et al [129] using the Herring method and Altmann-Cracknell simplified scheme for finding the irreducible representations of nonsymmorphic space groups. They derived a general result including phase factors induced by a symmetry operator of a nonsymmorphic space group acting on a Bloch sum formed with atomic-like orbitals in the commonly used cubic harmonic basis.
The electronic wave function is represented in the form of a linear combination of atomic orbitals (LCAO). The set of atomic orbitals is set up with reference to the three axes of a rectangular system transforming like x, y, z for p orbitals, xy, xz, yz, $(x^2 - y^2)$, z^2 for d orbitals, etc.
The first Brillouin zone and the corresponding high symmetry directions are represented in the Figure C.1.

The space group of the *hcp* lattice is D^4_{6h}. The basis functions for the irreducible representation of the Σ line are represented in the table here below.

Rep.	Basis Functions
Σ_1	s, y, $x^2 - y^2$, z^2
Σ_2	x, xy
Σ_3	xz
Σ_4	z, yz

Appendix D

Spin transport - spin torque effects

An easy way to get into the theory of the spin transport is to have a look to the particle transport. One can define the particle density:

$$n(\mathbf{x},t) = \Psi^*(\mathbf{x},t)\Psi(\mathbf{x},t)$$

where Ψ is defined by the spinor:

$$|\Psi\rangle = C_\uparrow |\uparrow\rangle + C_\downarrow |\downarrow\rangle = \begin{pmatrix} C_\uparrow \\ C_\downarrow \end{pmatrix}$$

Then, the current density is given by:

$$j(\mathbf{x},t) = \frac{\hbar}{2im}\left[\Psi^*(\mathbf{x},t)\nabla\Psi(\mathbf{x},t) - (\nabla\Psi^*)(\mathbf{x},t)\Psi(\mathbf{x},t)\right]$$

One can write down a continuity equation:

$$\nabla \cdot j + \frac{\partial n}{\partial t} = 0$$

which expresses the conservation of the particle density and the current density.
For the spin degree of freedom, the analogous of the particle density will be represented by the spin density:

$$\rho^S(\mathbf{x},t) = \mathbf{\Psi}^*(\mathbf{x},t)\sigma\mathbf{\Psi}(\mathbf{x},t)$$

The Ψ is a spinor in a Hilbert space and the spin is:

$$\mathrm{S} = \frac{\hbar}{2}\sigma$$

where σ is a vector whose Cartesian components are the Pauli matrices $\sigma_x, \sigma_y, \sigma_z$.

$$\sigma_x = \begin{pmatrix} 0 & 1 \\ 1 & 0 \end{pmatrix} \sigma_y = \begin{pmatrix} 0 & -i \\ i & 0 \end{pmatrix} \sigma_z = \begin{pmatrix} 1 & 0 \\ 0 & -1 \end{pmatrix}$$

The spin current density is a tensor quantity whose Cartesian components are given by:

$$j^S_{\alpha\beta}(\mathbf{x},t) = \frac{\hbar}{2im}\left[\Psi^*(\mathbf{x},t)\sigma_\beta\frac{\partial\Psi(\mathbf{x},t)}{\partial x_\alpha} - \frac{\partial\Psi^*(\mathbf{x},t)}{\partial x_\alpha}\sigma_\alpha\Psi(\mathbf{x},t)\right]$$

where $\nabla \cdot \mathbf{j}^S = \partial_\beta j_{\alpha\beta}$.
The left index $\alpha = x, y, z$ is in the spin space and the right index $\beta = x, y, z$ is in the real space. In a complete system where the spin is coupled with the magnetization, the spin and the spin density current are not conserved so the analogous of the continuity equation has nonzero terms in the right hand side.

$$\frac{\partial \rho^S(\mathbf{x}, t)}{\partial t} + \nabla \cdot j^S(\mathbf{x}, t) = -\frac{\delta m}{\tau_{\uparrow\downarrow}} + n_{ext}$$

The first term in the right hand side represents the transfer of angular momentum spin-lattice by spin flips. The term $\delta\mathbf{m} = (|\mathbf{m}| - \mathbf{m}_{eq})\hat{\mathbf{m}}$ represents the spin accumulation and $\tau_{\uparrow\downarrow}$ the spin relaxation time related to spin flip events. The second term in the right hand side n_{ext} represents the total external torque that act to change the direction of magnetization. For example, the Landau-Lifshitz-Gilbert torque density:

$$\mathbf{n}_{ext} = -(g\mu_B/\hbar)\mathbf{m} \times \mathbf{B}_{eff} + \alpha\hat{\mathbf{m}} \times \dot{\mathbf{m}}$$

which includes the precession around an external effective field B_{eff} and a phenomenological damping α.
One can rearrange the continuity equation in a form that points out the contribution of the current to the torque density:

$$\mathbf{n}_c = -\nabla \cdot \mathbf{j}^S - \frac{\partial \mathbf{m}}{\partial t}$$

which represents the torque on the net magnetization induced by net flux of spin current.

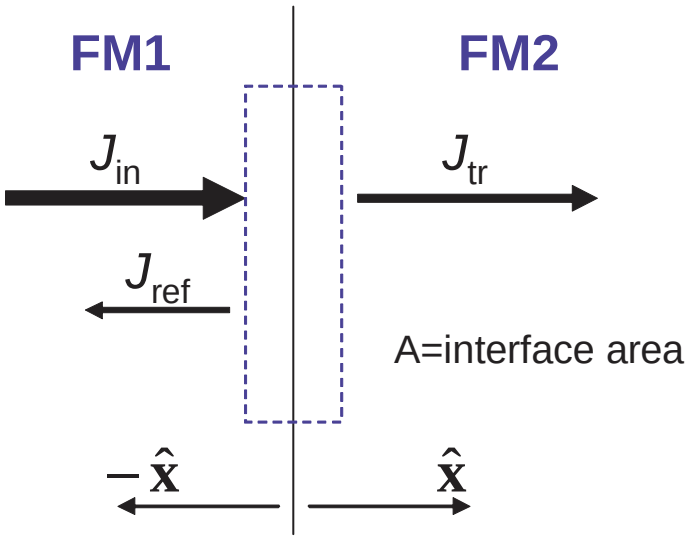

Figure D.1: Interfacial pillarbox used as integration volume when the divergence theorem is applied to the continuity equation

The divergence theorem can be applied to the continuity equations, defining an interfacial volume as a pillarbox. One can then integrate the steady state of the continuity equations over the

pillbox (see figure D.1). For the charge current, one can find the conservation equation for the particle current density:

$$0 = (\mathbf{j}_{in} + \mathbf{j}_{ref} - \mathbf{j}_{tr}) \cdot A\hat{\mathbf{x}}$$

This equations say that the incoming flux $\mathbf{j}_{in} \cdot A\hat{\mathbf{x}}$ minus the outgoing flux $\mathbf{j}_{tr} \cdot A\hat{\mathbf{x}} + \mathbf{j}_{ref} \cdot (-A\hat{\mathbf{x}})$ equals zero.
Neglecting the spin-flip one can find a similar equation for the spin current density:

$$\mathbf{N}_c = (\mathbf{j}^S_{in} - \mathbf{j}^S_{tr} + \mathbf{j}^S_{ref}) \cdot A\hat{\mathbf{x}} \approx \mathbf{j}^S_{\perp} \cdot A\hat{\mathbf{x}}$$

which demonstrates that the torque is proportional to the transverse part of $\mathbf{j}$. The torque $\mathbf{N}_c$ is a vector in the spin space.

D.1 Spin torque in magnetic tunnel junctions

We consider a MTJ which can be modeled within a free electron model by the potential profile represented in the figure D.2 (rectangular barrier). We consider here the simplified situation where the electrons flow along the x direction. M_1 and M_2 are the magnetization of the two ferromagnetic layers of the junction. The quantization axes are not the same in the FM layers (1) and (2) and θ defines the angle between the spin quantization axes z and z'.

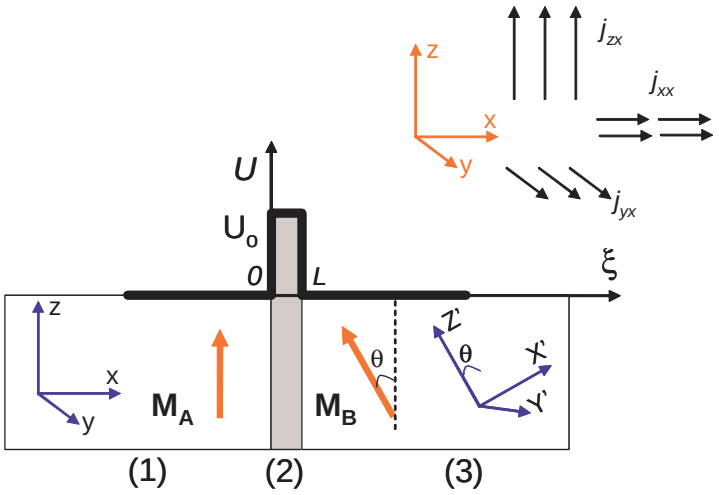

Figure D.2: Potential profile describing a magnetic tunnel junction

A standard Scrodinger equation projected to the three regions leads to the standard solutions:

$$\Psi^{(1)}_{in} = A_1 e^{ik_1^{\uparrow} x} |\uparrow\rangle + B_1 e^{ik_1^{\downarrow} x} |\downarrow\rangle$$
$$\Psi^{(1)}_{re} = R_{\uparrow} e^{-ik_1^{\uparrow} x} |\uparrow\rangle + R_{\downarrow} e^{-ik_1^{\downarrow} x} |\downarrow\rangle$$

for the incident and the reflected wave in the region (1),

$$\Psi^{(2)} = \left(A_2^{\uparrow} e^{\kappa x} + B_2^{\uparrow} e^{-\kappa x}\right) |\uparrow\rangle + \left(A_2^{\downarrow} e^{\kappa x} + B_2^{\downarrow} e^{-\kappa x}\right) |\downarrow\rangle$$

for the evanescent wave in the barrier and:

$$\Psi'^{(3)} = T^{\uparrow} e^{ik_3^{\uparrow}(x-L)} |\uparrow\rangle + T^{\downarrow} e^{ik_3^{\downarrow}(x-L)} |\downarrow\rangle$$

for the transmitted wave in the FM2.
The continuity of functions and derivatives in x=0 and x=L have to be completed with the spinor transformation at the interface $x = L$ due to the change of the quantization axis:

$$\begin{pmatrix} \Psi_3'^{\uparrow} \\ \Psi_3'^{\downarrow} \end{pmatrix}_{x=L} = U \begin{pmatrix} \Psi_2^{\uparrow} \\ \Psi_2^{\downarrow} \end{pmatrix}_{x=L}$$

and

$$\begin{pmatrix} \frac{\partial}{\partial x}\Psi_3{}'^{\uparrow} \\ \frac{\partial}{\partial x}\Psi_3{}'^{\downarrow} \end{pmatrix}_{x=L} = U \begin{pmatrix} \frac{\partial}{\partial x}\Psi_2{}^{\uparrow} \\ \frac{\partial}{\partial x}\Psi_2{}^{\downarrow} \end{pmatrix}_{x=L}$$

where

$$U = \begin{pmatrix} \cos\frac{\theta}{2} & -\sin\frac{\theta}{2} \\ \sin\frac{\theta}{2} & \cos\frac{\theta}{2} \end{pmatrix}$$

represents the rotation matrix.
This set of continuity equation will provide the probability amplitude coefficients from the wave functions which have to be determined. Knowing the $\Psi(\mathbf{r}, t)$ one can calculate the spin current density $j^S_{\alpha\beta}(\mathbf{x}, t)$ and therefore the current induced torque: $\mathbf{n}_c = -\nabla \cdot \mathbf{j}^S$.
If the current flows along the x direction one can easily demonstrate that:

$$\mathrm{j}_{\mathrm{zx}}^{\mathrm{S\,in}} = \mathrm{j}_{\mathrm{zx}}^{\mathrm{S\,tr}} + \mathrm{j}_{\mathrm{zx}}^{\mathrm{S\,ref}}$$

which represents the conservation of the longitudinal (with respect to M) components. This is trivial at equilibrium, when the net charge current in the junction is zero (left to right current equals to the right to left).
However, the transverse components are not conserved:

$$j^S_{\mathrm{xx}} \neq 0, j^S_{\mathrm{yx}} \neq 0$$

which give rise to a torque effect.

D.1.1 Equilibrium transport- Free electron approach

At equilibrium, the net charge current is zero $I = 0$ (left to right current equals to right to left). However, the spin current will be nonzero:

$$\begin{cases} j^S_{zx} = 0 \\ j^S_{xx} = 0; j^S_{yx} \neq 0 \end{cases}$$

The term $j^S_{yx} \neq 0$ will give rise to a torque having the direction parallel to $\mathbf{M}_A \times \mathbf{M}_B$.
The equilibrium torque determines an effective interfacial exchange coupling (Heinsenberg) $Jcos\theta$.
If one write the energy of the exchange coupling phenomenologically [128] as:

$$E_c = J(1 - m_1 \cdot m_2) + (1/2)J_{BQ}[1 - (m_1 \cdot m_2)^2]$$

where m_1 and m_2 are the unit vectors of magnetic moments M_1 and M_2, J the bilinear and J_{BQ} the biwuadratic coupling constants. Additionally with $m_1 \cdot m_2 = cos\theta$ one can define the torque as being proportional to:

$$\frac{\partial Ec}{\partial \theta} = (J + J_{BQ}\cos\theta)\sin\theta = \frac{\partial \langle S(t) \rangle}{\partial t}$$

These equations allow to calculate the Heisenberg coupling intensity J. The above formalism has been used by Slonczewski [2] within the free electron model and gives the following expression for the Heinsenberg like coupling (see the part 1):

$$J = \frac{(U - E_F)}{8\pi^2 d^2} \frac{8\kappa^3(\kappa^2 - k_\uparrow k_\downarrow)(k_\uparrow - k_\downarrow)^2(k_\uparrow + k_\downarrow)}{(\kappa^2 + k_\uparrow^2)^2(\kappa^2 + k_\downarrow^2)^2} e^{-2\kappa d}$$

The sign of the coupling is given by the term $(\kappa^2 - k^\uparrow k^\downarrow)$. Then, it can be ferromagnetic ($J > 0$) or antiferromagnetic ($J < 0$).

D.1.2 Equilibrium tunnel transport - beyond the free electrons approach

We argue here that the sign of the coupling is related to the sign/amplitude of the tunneling polarization. A rigorous demonstration of this property (hypothesis) represents one of the perspectives of the current study.
Then, if the tunneling polarization for the down electrons is larger then the one corresponding to the up electrons $T^\uparrow/T^\downarrow << 1$ the Heisenberg like coupling will be antiferromagnetic.
This situation can be experimentally achieved in Fe(001)/MgO/Fe(001) MTJ systems, where ab-initio calculations demonstrate a resonant ballistic transport for down electrons in contrast with tunnel transport for the up electrons (see figure D.3). This is related to the resonant transport of the minority spin interfacial resonance state (IRS) [13]. Then, we can argue here that the sign of the coupling observed in Fe/MgO/Fe MTJs is related to the resonant transport of the IRS.

D.1.3 Out of equilibrium spin transfer

If the magnetic tunnel junction is biased, in the out-of-equilibrium regime, the net charge current is nonzero. Moreover, one can demonstrate that all the spin density current components are not conserved (longitudinal and transverse).

$$\begin{cases} j_{zx}^S \neq 0 \\ j_{xx}^S \neq 0; j_{yx}^S \neq 0 \end{cases}$$

The free electron model can be used again to calculate the current induced torque. One finds [2] a dissipative exchange term which has the form:

$$\frac{\partial \langle \mathbf{S} \rangle_t}{\partial t} = D(V_B - V_A)\mathbf{S}_A \times (\mathbf{S}_A \times \mathbf{S}_B)$$

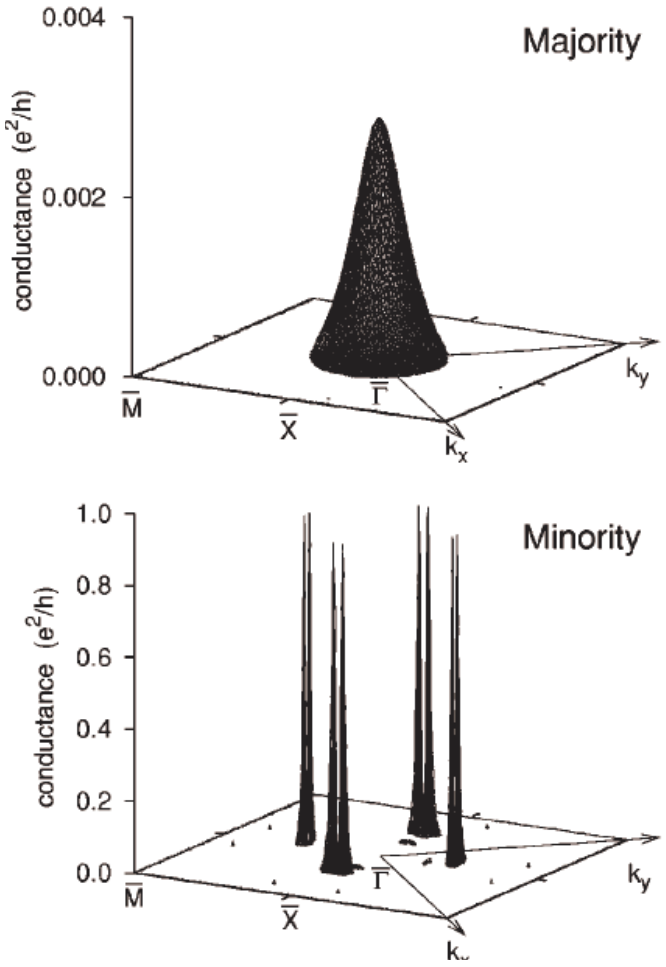

Figure D.3: Conductivity projected on the Brillouin zone for up and down spins in epitaxial MTJs (after Dederichs and al). One can observe that the amplitude of minority (down) spin conductivity is three order of magnitudes larger than the one corresponding to the majority spin (up).

where D is a constant (see [2]) V_A and V_B is the potential applied to the electrodes (1) and (2). As a function of the voltage sign $V_A - V_B$ this term represents either a **relaxation type Landau Lifshitz** ($V_A - V_B > 0$) or a **pumping action (negative damping)** when ($V_A - V_B < 0$).

One of the most important experimental perspectives of this study is to look at the out-of equilibrium coupling in Fe/MgO/Fe MTJs. The main goal is to investigate the influence of the net charge current:

- on the AF coupling: change of amplitude/sign.
- on the magnetization reversal dynamics (LLG, nanopillars)

and to develop specific models for spin torque in single crystal MTJ which take into account the symmetry filtering effects and the interfacial electronic structure.

Appendix E

Selection of papers on spin polarized tunneling in single crystal Fe/MgO tunnel junctions

This appendix contains few review papers on the topics regarding the spin polarized tunneling transport in tunnel junctions implicating the magnesium oxide as tunnel barrier.

The first paper summarizes the physics of tunnel transport in Fe/MgO/Fe systems in the equilibrium regime, where we demonstrate the existence of an antiferomagnetic coupling across the extremely thin MgO epitaxial barrier.

The second paper illustrates the signature of the interfacial electronic structure on tunneling characteristics in single crystal Fe/MgO/Fe magnetic tunnel junctions. In this paper we demonstrate the influence of the spin polarized interfacial resonant state of the Fe in the out-of-equilibrium tunneling.

The third paper summarizes the results obtained in our group[1] concerning the spin polarized tunneling in tunnel junctions which implicates amorphous MgO oxide in combination with standard Al_2O_3 barriers. This class of systems is not analyzed in detail within the present manuscript. However, with the review paper presented here, we want to illustrate the net difference between the spin filtering effects in single-crystal MgO based tunnel junctions and MTJ systems with amorphous oxide barriers. We show that in this last class of systems which does not present crystalline order, the physics of tunneling is satisfactory described within the free electrons model. These results motivate further interesting perspectives regarding the elaboration and the study of hybrid systems combining single crystalline and poly-crystalline or amorphous subsystems.

The fourth paper represents recent results issued from the collaboration with the University of Madrid, concerning low frequency noise experiments on single crystal Fe/MgO magnetic tunnel junctions.

The fifth paper concerns the result of a scientific collaboration with E. Popova (GEMac Versailles) and N. Lesnik (University of Kiev). It presents the temperature dependence of the interlayer exchange coupling in epitaxial tunnel junctions using X-band ferromagnetic resonance

[1] This work represents the PHD thesis work of C. de Buttet (2003-2004) advised by M. Hehn in a collaboration framework between LPM Nancy and CROLLES 2, FREESCALE-PHILIPS-STMICROELECTRONICS.

(FMR) in the range 2300 K.

These two last papers represent additional content with respect to the HDR manuscript version submitted to the HDR jury in November 2006. Their place in the present compilation of the manuscript is justified by the fact that they bring important additional information on the physics of spin polarized tunneling transport in single crystal Fe/MgO MTJs.

Interlayer Magnetic Coupling Interactions of Two Ferromagnetic Layers by Spin Polarized Tunneling

J. Faure-Vincent, C. Tiusan, C. Bellouard, E. Popova, M. Hehn, F. Montaigne, and A. Schuhl

Laboratoire de Physique des Matériaux, BP 239, 54506 Vandoeuvre lès Nancy, France

(Received 6 May 2002; published 20 August 2002; publisher error corrected 8 October 2002)

Magnetic interactions involving ferromagnetic layers separated by an insulating barrier have been studied experimentally on a fully epitaxial hard-soft magnetic tunnel junction: Fe/MgO/Fe/Co. For a barrier thickness below 1 nm, a clear antiferromagnetic interaction is observed. Moreover, when reducing the MgO thickness from 1 to 0.5 nm, the coupling strength increases up to $J = -0.26$ erg·cm^{-2}. This behavior, well fitted by theoretical models, provides an unambiguous signature of the interlayer exchange coupling by spin-polarized quantum tunneling.

DOI: 10.1103/PhysRevLett.89.107206 PACS numbers: 75.70.–i, 73.40.Rw, 73.43.Jn, 75.30.Et

After the first observation of an antiferromagnetic (AF) interaction of Fe films separated by a Cr spacer [1], the interlayer exchange coupling (IEC) has been subsequently studied with a large variety of metallic spacers [2]. In these systems the oscillation of the coupling strength with spacer thickness has been observed and attributed to the topology of the spacer metal Fermi surface. Theoretically, various models based on either a total energy calculation or models of a Ruderman-Kittel-Kasuya-Yosida–type have been elaborated [2]. Furthermore, a generalization of the IEC theory to nonmetallic (insulating) spacers has been proposed [3–5] by introducing the concept of a complex Fermi surface. However, in the latter case, the IEC, either ferromagnetic or antiferromagnetic, should show a monotonic nonoscillatory variation of its strength with spacer thickness. Experimentally, in the case of nonmetallic spacers, the IEC has been reported for only one system [6,7], namely, a Si based spacer between Fe magnetic layers. In this system for which both a bilinear and a biquadratic coupling are observed [8], the analysis of the contradictory results is rather complex. Moreover, with a semiconductor spacer, the coupling can be related directly to the conduction charge carrier in the Fe-Si spacer layer thermally or optically generated, which may communicate spin information between the Fe layers. Finally, the formation of metallic silicide could explain the observation of oscillatory coupling [9].

In this Letter we provide experimental evidence of room temperature antiferromagnetic coupling between two ferromagnetic (F) layers across a very thin insulating tunnel barrier. Here the spin information and the coupling are carried out across the spacer by equilibrium quantum tunneling of spin-polarized electrons. Our study is performed on the hard-soft magnetic tunnel junction architecture, namely, MgO(100)/Fe/MgO/Fe/Co/V. The materials and the thickness of the layers of our multilayer system were chosen in order to achieve a net AF coupling, as estimated theoretically. The sign of the IEC is a major condition for performing an unambiguous analysis of the interlayer exchange coupling variation when reducing the spacer thickness. Otherwise, a corresponding strong augmentation of a ferromagnetic coupling would be difficult to decorrelate from the direct coupling effects associated with ferromagnetic pinholes in ultrathin spacers.

Theoretically, several model types have been developed to explain the IEC effects, relating to the charge and spin-current transmission between the ferromagnetic (F) layers across an insulating spacer. In the spin-current Slonczewski's model [3,4], the coupling is derived from the torque produced by rotation of the magnetization from one F layer relative to another and is described in terms of a spin-flip current probability calculated from the stationary wave functions of the free-electron Schrödinger equation. The quantum interference model of Bruno [5], associates the coupling with the interferences of the electron waves in the barrier due to the spin reflections at the interfaces. The coupling is expressed in terms of the spin asymmetry of the reflections. This model extends for both metallic and insulating spacers by introducing the concept of complex Fermi surface in the case of insulators. It predicts the temperature variation of the coupling which reduces to the Slonczewski's spin-current model for $T = 0$ K. In addition, we may cite the more sophisticated models implicating the nonequilibrium Keyldysh formalism [10,11] developed to calculate the spin-polarized tunnel current and its connection to the interlayer exchange interaction in thin planar junctions out of equilibrium. They have shown that a nonequilibrium bias across a tunnel junction system may significantly alter the amplitude and the sign of the coupling and that there is a component of the interaction energy between the ferromagnets proportional to their thickness. However, in the absence of external bias, when the ferromagnetic/insulator/ferromagnetic trilayer lies in the equilibrium state, these models reduce again to the equilibrium Slonczewski's spin-current model. Indeed, within the framework of this last model, which has a high physical transparency, the coupling strength J is directly correlated to intrinsic physical parameters of the insulating

VOLUME 89, NUMBER 10 PHYSICAL REVIEW LETTERS 2 SEPTEMBER 2002

barrier (width d, height u) and to the free-electron band structure parameters of the ferromagnetic/insulating/ferromagnetic trilayer system: the Fermi energy E_F, the wave vectors of spin up ($k_\uparrow$) and spin down ($k_\downarrow$) electrons in the ferromagnets and in the insulating layer (k), the Stoner splitting in the ferromagnets Δ, and the effective mass of the electron m_{Fe}. When a two-band model is used to describe the ferromagnets, the coupling strength is

$$J = \frac{(U - E_F)}{8\pi^2 d^2} \frac{8k^3(k^2 - k_\uparrow k_\downarrow)(k_\uparrow - k_\downarrow)^2(k_\uparrow + k_\downarrow)}{(k^2 + k_\uparrow^2)^2(k^2 + k_\downarrow^2)^2} e^{-2kd}. \tag{1}$$

For the estimations of the coupling strength, we use bulk band structure parameters [12] for Fe: $k_\uparrow \simeq 1.09$ Å^{-1} and $k_\downarrow \simeq 0.43$ Å^{-1} are extracted from $k_\sigma = \sqrt{(E_F + \Delta\sigma)2m_{\mathrm{Fe}}/\hbar^2}$ (where $\sigma = \pm 1/2$), which correspond to $E_F \simeq 2.6$ eV and $\Delta \simeq 3.6$ eV.

With these values, the IEC coupling is expected to be antiferromagneticlike (AF) when $k^2 < k_\uparrow k_\downarrow = 0.469$ Å^{-2}. By using a reasonable value for the effective mass of the electron in the barrier, m_i, and an experimental determination [13] of the barrier height $u = U - E_F$, the above equation, and the relation $k = \sqrt{(U - E_F)2m_i/\hbar^2}$, a net AF coupling in the Fe/MgO/Fe system is predicted.

Within the same range of parameters, the temperature variation of the coupling strength estimated using Bruno's model,

$$J(T) = J(0\ \mathrm{K}) \frac{2\pi m k_B T d/\hbar^2 k_F}{\sinh(2\pi m k_B T d/\hbar^2 k_F)}, \tag{2}$$

predicts no significant difference of the coupling strength between $T = 0$ K and the room temperature; k_B is the Boltzmann constant, m is the mass of electron, T is the temperature, and $k_F = ik$ is the complex wave vector of the electron in the insulating layer. Thus, the quantitative analysis of the experimental variation of the coupling strength with t_{MgO} obtained at room temperature, can be achieved within the framework of the interlayer exchange theories [3,5].

The epitaxy of metal/insulator superlattice MgO(100)/Fe in ultrahigh vacuum is very well established [14–16]. By using molecular-beam epitaxy (MBE) a two-dimensional growth mode of MgO on Fe was obtained with high quality ultrathin layers without pinholes and with very flat surfaces. The growth conditions have been detailed in our previous study [17]. Briefly, after annealing the MgO substrate at 500 °C for 20 min, first a 50-nm-thick Fe layer is deposited, then annealed at 450 °C for 15 min. Then, the thin MgO insulating layer is subsequently deposited by means of an electron gun. We observe a two-dimensional layer-by-layer growth of MgO up to 10 to 15 monolayers asserted by reflection high-energy electron diffraction (RHEED) intensity oscillations and oscillations of the in-plane lattice parameter [18]. The observation of clear RHEED intensity oscillations (Fig. 1) gives access to a precise determination of t_{MgO} with a low absolute uncertainty, certainly below ± 0.05 nm, and even better relative accuracy. The second magnetic electrode is a bilayer composed by a 5-nm-thick Fe layer, epitaxially grown on the top of the MgO barrier magnetically hardened by a 50-nm-thick Co layer deposited on the top of it. The continuity of the insulating MgO layer has been previously checked down to 0.8 nm thickness, at different spatial scales by means of morphological (high resolution transmission electronic microscopy), electrical (the local impedance), magnetoresistance measurements, and down to 0.5 nm in the present work by magnetic measurements. As a similar example, MgO(100)/Fe/MgO/Fe/Co/Pd tunnel junctions have shown tunnel magnetoresistance up to 17% for a 1 nm thick MgO layer [17].

The magnetic properties have been investigated by a superconducting quantum interference device and alternating gradient field magnetometers. Magnetization versus field loops have been performed on continuous multilayer films with lateral sizes above a few millimeters, in order to avoid spurious antiferromagnetic dipolar coupling introduced by patterning of small size devices. In these films, the MgO thickness ranges from 0.4 to 2.5 nm. Because of the epitaxial growth, both soft and hard layers present fourfold symmetries [17], with the same directions for the easy axis. The contrast between their coercive fields is significant: $H_c = 40$ Oe for the soft layer and $H_c > 350$ Oe for the hard layer. This will define in the hysteresis loop a large field window where one of the magnetic layers is magnetically rigid, while the other layer can easily be turned by a small external field. Therefore, the interlayer

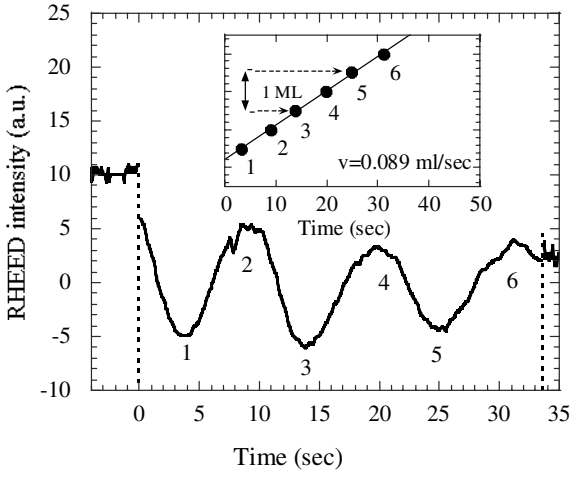

FIG. 1. RHEED intensity during the deposition of 79 nm thick MgO. The period of oscillations corresponds to the growth of 1 monolayer. In order to determine the rate of the growth we plot (inset) the positions of the maxima and minima as a function of time.

magnetic coupling can be extracted from the shift of the minor hysteresis loops, taken for the soft magnetic layer in a field window where the hard layer is magnetically ''locked'' by a previous magnetization saturation.

For a spacer thickness $t_{MgO} < 0.8$ nm, we observe clearly (Fig. 2) a net positive shift of the *M-H* minor loop. Such a shift can be explained by the IEC through the insulating layer, but it could also be attributed to an exchange biasing of the first Fe layer by a possible antiferromagnetic/ferrimagnetic oxide layer at the interface between the bottom Fe layer and the oxide insulating barrier. The exchange bias hypothesis would lead to a coupling mainly independent of the insulating spacer thickness and/or should also be present in samples without the second top hard magnetic layer. However, in our samples we observe a fast dependence of the measured AF coupling strength J with the spacer thickness, as discussed below. The rapid variation of the coupling with the thickness of the spacer is directly illustrated in the inset of Fig. 2, where we can see that by increasing the spacer thickness from 0.5 to 0.63 nm the shift reduces drastically from 58 to 7.5 Oe. Moreover, on simplified samples where we excluded on purpose the hard (top) layer: MgO(100)/Fe/MgO, we observe no shift of the M(H) loops. At least the shift is below the uncertainty of the measurement setup (1 Oe), whereas for the Fe/MgO/Fe/Co multilayer a shift up to 133 Oe, has been obtained for the $t_{MgO} = 0.5$ nm layer. Consequently, we can exclude the occurrence of the AF biasing. Therefore, the observed field shift of the *M-H* minor loops can be unambiguously attributed only to interlayer coupling effects.

The coupling energies, J, have been extracted from the *M-H* minor loops for all the samples. J is calculated as the product between the field offset of the minor *M-H* curves (see Fig. 2) and the magnetization of the soft magnetic layer. Conventionally, we associated the sign of J with the type of the coupling: antiferromagnetic ($J < 0$) and ferromagnetic (F) coupling ($J > 0$). Three regimes can be clearly distinguished: An AF coupling ($J < 0$) is measured for $t_{MgO} < 0.8$ nm, with a very fast increase of amplitude ($|J|$), when the thickness of the spacer is reduced from $t_{MgO} = 0.8$ to 0.5 nm (Fig. 3).

Below 0.5 nm, we observe unambiguously a modification of the shape of the magnetization reversal, and a decrease of the apparent coupling strength. Indeed, with such a low interlayer thickness, we expect the occurrence of pinholes, and consequently a direct ferromagnetic coupling competing with the AF exchange coupling studied here. This leads to significant deviations from the pure bilinear coupling interaction and can be simulated by a biquadratic interaction, which could also explain the shape of the magnetic hysteresis loops. For thicker insulating layer, we cannot exclude the occurrence of any pinholes. However, for thicker insulators the measured minor hysteresis loops are square. Therefore, we can reasonably assume that above 0.5 nm the contribution of direct coupling via ferromagnetic pinholes is certainly much smaller than the one of the AF exchange interaction.

On the other hand, for larger spacer thickness, namely, above 1 nm, we observe always a net ferromagnetic coupling. We may easily attribute this F coupling to the well known ''Orange Peel'' interaction [19], associated with the

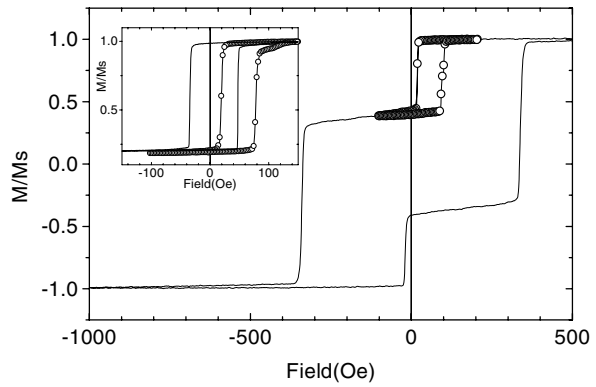

FIG. 2. Magnetization curve along the easy axis for MgO(100)/Fe/MgO(0.5 nm)/Fe/Co. The minor loop (- ∘ -) is taken after a positive saturation of the whole system, in a field window where the hard Fe/Co bilayer is magnetically rigid. In this sample, the positive shift of 58 Oe in the minor loop is the signature of a strong AF coupling. Inset: The rapid variation of the coupling strength with the thickness of the insulator is reflected by two minor loops, (—) $t_{MgO} = 0.63$ nm and (- ∘ -) $t_{MgO} = 0.5$ nm.

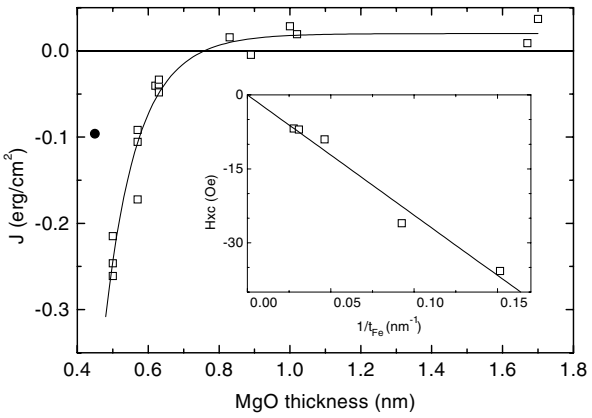

FIG. 3. Variation of the coupling strength J with the insulator thickness. The experimental data are represented by empty square features. Theoretical estimation of J, performed within the framework of the spin-polarized tunneling of Slonczewski, is illustrated by the filled line. For $t_{MgO} = 0.45$ nm (point represented by a filled circle) the net coupling is still AF, but it is reduced by the ferromagnetic pinholes contribution. Inset: Variation of the exchange field with the thickness of the soft ferromagnetic layer.

correlated roughness of the ferromagnetic/insulator interfaces. Having in view the large fluctuation length of the roughness determined by high resolution transmission electron microscopy in our epitaxially grown layers ($>$ 10 nm), the orange peel coupling is basically constant in the thickness range involved in our study. Moreover, as we already discussed in a previous paper [17], because of the high quality of the two-dimensional growth, this coupling is small, i.e., lower than 0.04 erg/cm^2.

With a surface interaction, we expect a linear variation (linear increase) of the coupling field with t_{Fe}^{-1}, where t_{Fe} is the thickness of the soft magnetic layer. Experimental results presented in the inset of Fig. 3, and obtained on three different epitaxies with the same spacer thickness $t_{\mathrm{MgO}} = 0.62$ nm, are in good agreement with this expectation. In one of the epitaxies, three different Fe thicknesses have been obtained for the same MgO layer, by using shadow masks during the growth of the soft magnetic layer. Therefore, we confirm that the observed shift is due to a surface interaction. Moreover, since the dependence of the AF coupling with t_{MgO} is abrupt as discussed below, the reproducibility, and then the relative determination, of the spacer thickness is very good.

We present also in Fig. 3, the theoretical variation of J with t_{MgO}, estimated from Eq. (1) (Full line). For the calculation we have used first the bulk Fe band structure parameters, ($k_{\uparrow} \simeq 1.09$ Å^{-1}, $k_{\downarrow} \simeq 0.43$ Å^{-1}, and $E_F \simeq 2.6$ eV) [12], and, second, reasonable parameters for the insulating barrier: a barrier height of $U - E_F = 1$ eV and an effective mass in the barrier $m_{\mathrm{eff}} = 0.4 m_0$. Indeed, through a determination of the prefactor and the exponential decay length in Eq. (1), we could expect an independent determination of $u = U - E_F$ and m_{eff}. However, it would require an even greater ''accuracy'' in evaluating the insulating layer thickness t_{MgO}. Finally, the orange peel coupling is described in terms of a constant positive ''coupling offset'' of 0.02 erg/cm^2, which corresponds to the average value observed for spacer thickness above 1.2 nm, and it also represents a reasonable assumption having in view the roughness fluctuation length in our epitaxial samples. From Fig. 3, we can conclude that the experimental variation of the coupling strength with the insulating spacer thickness is well fitted in the framework of the Slonczewski's spin-current model. Moreover, we obtain an estimation of the relationship between the barrier height and the effective mass in the barrier: namely, $(U - E_F) m_{\mathrm{eff}} = 0.44$ eV. Finally, let us note that the experimental data cannot be fitted by a simple exponential law $J \alpha e^{-2kd}$. The observation of a faster variation, namely, $J \alpha e^{-2kd}/d^2$, is a clear signature of the equilibrium spin-current IEC model.

In summary, antiferromagnetic interlayer coupling through an insulating spacer has been unambiguously evidenced. The shape of the variation of the experimental coupling strength J with the insulating spacer thickness t_{MgO}, the quantitative value of $|J|$, and finally the thickness range of t_{MgO} for which the antiferromagnetic coupling is observed represent an experimental proof of the interlayer exchange theory [3,5] by the spin-polarized quantum tunneling of electrons between the ferromagnetic layers.

The authors are grateful to G. Marchal and M. Alnot for the ingenious conceiving of the MBE system, S. Andrieu and M. Piecuch for stimulating discussions, Y. Henry for magnetic characterization facilities in IPCMS Strasbourg, and Martin Thornton for the careful reading of the text. This work was supported by the EC NANOMEM Programme (IST-1999-13741), and by the ''Conseil Régional de Lorraine.''

[1] P. Grünberg, R. Schreiber, Y. Pang, M. B. Brodsky, and H. Sowers, Phys. Rev. Lett. **57**, 2442 (1986).
[2] A. Fert and P. Bruno, in *Ultrathin Magnetic Structures*, edited by B. Heinrich and J. A. C. Bland (Springer-Verlag, Berlin, 1994), Vol. 2, Chap. 2.2, p. 82.
[3] J. C. Slonczewski, Phys. Rev. B **39**, 6995 (1989).
[4] R. P. Erickson, K. B. Hathaway, and J. R. Cullen, Phys. Rev. B **47**, 2626 (1993).
[5] P. Bruno, Phys. Rev. B **52**, 411 (1995).
[6] S. Toscano, B. Briner, H. Hopster, and M. Landolt, J. Magn. Magn. Mater. **114**, L6 (1992).
[7] E. E. Fullerton, J. E. Mattson, S. R. Lee, C. H. Sowers, Y. Y. Huang, G. Felcher, S. D. Bader, and F. T. Parker, J. Magn. Magn. Mater. **117**, L301 (1992).
[8] G. J. Strijkers, J. T. Kohlhepp, H. J. M. Swagten, and W. J. M. de Jonge, Phys. Rev. Lett. **84**, 1812 (2000).
[9] R. R. Gareev, D. E. Bürgler, M. Buchmeier, D. Olligs, R. Schreiber, and P. Grünberg, Phys. Rev. Lett. **87**, 157202 (2001).
[10] C. Heide, R. J. Elliott, and N. S. Wingreen, Phys. Rev. B **59**, 4287 (1999).
[11] N. F. Schwabe, R. J. Elliott, and N. S. Wingreen, Phys. Rev. B **54**, 12 953 (1996).
[12] V. Moruzzi, *Calculated Electronic Properties of Transition Metal Alloys* (World Scientific, Singapore, 1994).
[13] M. Klaua, D. Ullmann, J. Barthel, W. Wulfhekel, J. Kirschner, R. Urban, T. L. Monchesky, A. Enders, J. F. Cochran, and B. Heinrich, Phys. Rev. B **64**, 134411 (2001).
[14] T. Urano and T. Kanaji, J. Phys. Soc. Jpn. **57**, 3403 (1988).
[15] J. L. Vassent, M. Dynna, A. Marty, B. Gilles, and G. Patrat, J. Appl. Phys. **80**, 5727 (1996).
[16] W. Wulfhekel, M. Klaua, D. Ullmann, F. Zavaliche, J. Kirschner, R. Urban, T. Monchesky, and B. Heinrich, Appl. Phys. Lett. **78**, 509 (2001).
[17] E. Popova, J. Faure-Vincent, C. Tiusan, C. Bellouard, H. Fischer, E. Snoeck, M. Hehn, F. Montaigne, V. da Costa, M. Alnot, S. Andrieu, and A. Schuhl, Appl. Phys. Lett. **81**, 509 (2002).
[18] P. Turban, L. Hennet, and S. Andrieu, Surf. Sci. **446**, 241 (2000).
[19] L. Néel, C. R. Acad. Sci. **255**, 1676 (1962).

Interfacial Resonance State Probed by Spin-Polarized Tunneling in Epitaxial Fe/MgO/Fe Tunnel Junctions

C. Tiusan, J. Faure-Vincent, C. Bellouard, M. Hehn, E. Jouguelet, and A. Schuhl

Laboratoire de Physique des Matériaux, BP 239, F-54506 Vandoeuvre lès Nancy, France

(Received 17 February 2004; published 2 September 2004)

The direct impact of the electronic structure on spin-polarized transport has been experimentally proven in high-quality Fe/MgO/Fe epitaxial magnetic tunnel junctions, with an extremely flat bottom Fe/MgO interface. The voltage variation of the conductance points out the signature of an interfacial resonance state located in the minority band of Fe(001). When coupled to a metallic bulk state, this spin-polarized interfacial state enhances the band matching at the interface and therefore increases strongly the conductivity in the antiparallel magnetization configuration. Consequently, the tunnel magnetoresistance is found to be positive below 0.2 V and negative above. On the other hand, when the interfacial state is either destroyed by roughness-related disorder or not coupled to the bulk, the magnetoresistance is almost independent on the bias voltage.

DOI: 10.1103/PhysRevLett.93.106602 PACS numbers: 72.25.Mk, 73.40.Gk, 73.40.Rw, 85.75.–d

The tunnel magnetoresistance (TMR) effect is widely studied not only due to the large-scale applications of the magnetic tunnel junctions (MTJs) [1] but also for the understanding of the complex physics of spin dependent transport. By using epitaxial growth techniques, one can "engineer" model-quasiperfect MTJ systems, in which theory and experiment may confront each other. After a series of pioneering results on the tunnel transport in epitaxial systems [2], a couple of nontrivial physical effects, predicted by theoretical calculations, have experimentally emerged. One could cite the magnetic coupling mediated by tunneling of electrons [3] or, beyond the free electron framework, the influence of the realistic electronic structure of the electrodes on the tunnel transport [4,5]. Recently, *ab initio* calculations [6–8] performed on epitaxial MTJ systems have shown that the deviations of the wave function from a single plane-wave form and of the Fermi surface from a sphere, related to the anisotropy of the electronic properties in the reciprocal space, are crucial for the physics of tunneling. In particular, a totally counterintuitive result, directly driven by the influence of the interfacial resonant states on the tunneling, showed that electrons with nonzero quasimomentum parallel to the interface could have a larger probability to tunnel compared to those with zero parallel quasimomentum. Moreover, very large TMR ratios have been theoretically predicted in single crystalline MTJs, namely, Fe/MgO/Fe. They are determined by the different tunneling mechanisms and symmetry-related decay rates of the Bloch waves for the majority and the minority spin channels. Roughly, an emitter monocrystalline ferromagnetic (FM) electrode filters in terms of symmetry the electrons subsequently injected across the insulating (I) barrier. The tunnel transport probes: (i) the differences in spin injection (extraction) efficiency (directly related to the interfacial FM/I matching/coupling) and (ii) the differences in decay rates when tunneling across the barrier. Consequently [6,7], for large MgO thickness, in the asymptotic regime, the tunneling is found to be governed by a majority spd-like character state Δ_1. The conductance in the antiparallel (AP) configuration is very low (almost zero). The spin asymmetry is predicted to increase above 1000%. On contrary, when the thickness of the insulating layer decreases, the contribution of the double degenerate pd character state Δ_5 becomes significant, the conductance in the AP state increases, and therefore the TMR ratio decreases. Moreover, the tunnel transmission becomes strongly affected by resonant effects either at the interfaces [6–9] or in the barrier [10]. For the Fe(001)/MgO interface, a peak in the interfacial minority density of states (DOS) is found above the Fermi energy. It is related to an interfacial resonance (IR), arising from an effect of electronic confinement between the bulk and the barrier where the electronic wave is evanescent. The IR states from both sides of the barrier may couple to each other, leading to a resonant tunneling mechanism [8] which manifests itself as spikes in the conductance distribution in particular $k_{\parallel}$ points in the two-dimensional Brillouin zone. The width of these spikes is determined by the strength of the coupling in the barrier, which decreases exponentially with the barrier thickness. Consequently, the conductance from an IR state is particularly important for thin barriers. Alternatively, as shown in this Letter, the contribution to the tunneling of an interfacial state may be activated by biasing the junction at finite bias voltage.

In this Letter, we show that spin-polarized tunneling transport in high-quality MTJs can be used as a probe for the IR states in the Fe(001)/MgO system. Experimentally, the IRs are "controlled" via the topological quality of the Fe/MgO interface, perfectly monitored by the epitaxial growth of the layers. Atomically flat Fe/MgO interfaces provide IRs, located in the minority spin bands. When these resonances get "activated," the increase in the interfacial spin-polarized DOS compensates the spin filtering in the electrodes and reverses the

VOLUME 93, NUMBER 10 PHYSICAL REVIEW LETTERS week ending 3 SEPTEMBER 2004

sign of the magnetoresistance. This explains the bias-voltage variation of the experimental TMR, observed to be positive below 0.2 V and negative above. However, in systems where the interfacial state is either not coupled to the bulk or destroyed by interfacial disorder, we observe that its contribution to the tunneling is annihilated. In this case, the magnetoresistance is observed to be always positive and almost independent of voltage, as expected for the symmetry of the electrons filtered by the Fe monocrystalline electrodes and by the MgO insulating barrier.

In order to support our experimental data, we calculated the electronic structure of the Fe/MgO/Fe stack with the Full Potential-Linear Augmented Plane-Wave WIEN2K code [11], using a supercell consisting of ten Fe layers, sandwiched in between six MgO layers. To describe a "realistic" Fe/MgO interface of an experimental junction, a complete monolayer of O has been alternatively considered at 0.4 Å above the interfacial Fe, in the surface Fe hollow site [12]. The calculation is performed within a full potential framework, without any empty sphere in the interstitial. We found a gap of about 6.8 eV for the outer MgO layer (fair description of bulk MgO E_g = 7.8 eV), whereas, in the middle of the slab, bulklike properties are found for the innermost Fe layer. In agreement with previous calculations [6,13,14], we find an IR state located in the minority d_{z^2} orbital, belonging to a Δ_1 symmetry (s, p_z, d_{z^2}) band of the interfacial Fe for both Fe(001)/MgO and Fe/Fe-O/MgO systems [Fig. 1(a)]. This IR gets slightly shifted upwards in energy, when the complete O monolayer is introduced between the Fe and MgO, in the surface Fe hollow site. However, the presence of the Fe-O layer does not alter the effect of the resonant state in the tunnel transport, because this state lies in the minority d_{z^2} vertical orbitals of the surface Fe and these electrons are not affected by the bonding between Fe and O. The O has only planar bonding via the in-plane s, p_x, p_y orbitals with the surface Fe atoms. Moreover, the vertical bonding of O with the subsurface Fe via O_{p_z}-$Fe_{d_{z^2}}$ orbitals does not affect the surface resonance. In order to uncouple the interfacial state from the bulk DOS of the bottom electrode, we have used a Pd/Fe/MgO/Fe/Co structure with a rather thin Fe bottom layer. The bulk electronic structure of Pd is illustrated in Fig. 1(b). One can observe that slightly above the Fermi energy the DOS vanish abruptly. Although the epitaxy conserves the Δ_1 symmetry from the bcc Fe in the fcc Pd, beyond 0.2 eV above the Fermi energy the only remaining band in Pd is a dispersive Δ_1 symmetry, one which shows mainly s and p character. Thus, one can immediately see that the d_{z^2} IR in Fe finds no similar orbital character in Pd. This leads to a "filtering effect," directly related to the orbital character "mismatch" of the electronic bands above E_F, between Fe and Pd, and affects drastically the propagation of the Bloch

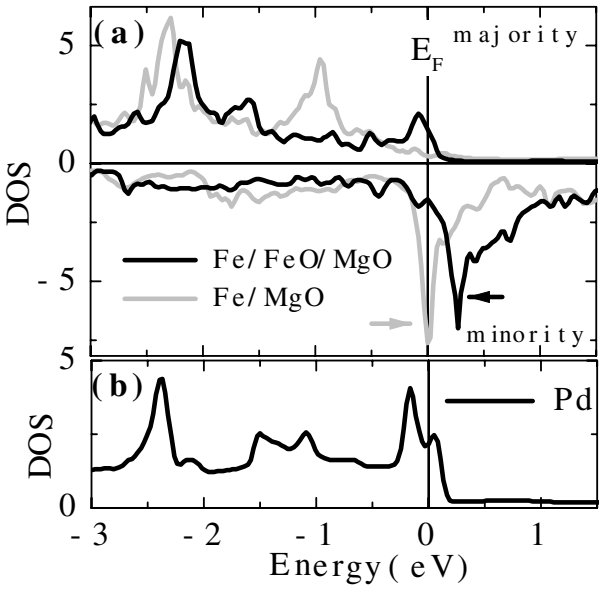

FIG. 1. (a) Calculated local spin-polarized DOS for the interfacial Fe in Fe/MgO/Fe and Fe/FeO/MgO/Fe stacks. The arrows indicate the IR in the minority DOS of Fe. (b) The total DOS of bulk Pd.

waves coming from the Fe side for electrons having a coherence/spin diffusion length larger than the thickness of the bottom Fe.

Our MTJ multilayer stacks are grown [15] by molecular beam epitaxy (MBE). Two distinct sets of samples have been elaborated, both on MgO substrates annealed at 500 °C for 20 min. For the first set, labeled (S1), a first 50 nm-thick Fe layer is deposited at room temperature (RT) using a Knudsen cell, then annealed at 450 °C for 15 min in order to smooth its surface and to induce a perfectly flat bottom Fe/MgO interface. For the second set of samples, labeled (S2), we introduce a 40 nm-thick Pd buffer, flattened by annealing at 400 °C, in between the substrate and a 2 nm-thick bottom Fe electrode. During the entire growth of this 2 nm Fe layer, a two-dimensional (2D) layer-by-layer growth is asserted by reflection high energy electron diffraction (RHEED) intensity and in-plane lattice parameter oscillations. The similitude of the bottom Fe electrode quality in both sets of samples is furthermore confirmed by RHEED (small scale) and *ex situ* atomic force microscopy analysis. Furthermore, on both set of samples, onto the bottom flat Fe electrode, a nominal 2.5 nm MgO insulating layer is subsequently deposited at room temperature using an electron gun. We observe again the 2D layer-by-layer growth of MgO up to 10 to 15 monolayers, asserted by the oscillations of RHEED intensity and in-plane lattice parameter. The continuity of the insulating MgO layer and its pseudomorphic epitaxial growth on Fe were checked down to 0.6 nm thickness, at different spatial

scales, as shown in our previous studies [3,15,16]. We point out that the pseudomorphic epitaxial growth of MgO on Fe is a key parameter for the conservation of symmetry from the Fe electrode through the MgO barrier (conservation of $k_{\parallel}$). This has a huge impact on the Bloch wave propagation in the stack. Finally, on the top of the MgO barrier, a second magnetic electrode is epitaxially grown. It consists on a bilayer composed of a 5 nm-thick Fe layer, magnetically hardened by 10 nm-thick Co layer. However, as confirmed by the RHEED analysis for both sets of samples, the growth of the top Fe electrode onto the MgO leads to a rough top MgO/Fe interface. This affects drastically the interfacial electronic structure of the top Fe, for which the IR is destroyed by the disorder. Lastly, the sample is capped with a 10 nm Au layer.

Magnetotransport properties of the MTJ have been measured at RT [17] in 20 μm micrometric-size junctions patterned by UV lithography and Ar ion etching [15]. In Fig. 2 we illustrate the tunnel magnetoresistance curves as a function of the bias voltage, measured for the two samples issued from set (S1) and set (S2). The amplitude of the TMR presented here is moderate with respect to the theoretical expectations. Indeed, the 2.5 nm MgO is below the asymptotic limit (large MgO thickness, where only *s*-like electrons of majority band tunnel). This argument is furthermore supported by a net signature of an IR state, located in the minority *d* band, on the tunnel transport characteristics. Moreover, one could alternatively consider the influence of a Fe-O layer at the interface Fe-MgO, related to the elaboration procedure [12]. Recent *ab initio* calculations [14] have shown that the interfacial Fe-O layer affects the propagation of the majority spin of Δ_1 symmetry in the MgO barrier, reducing the TMR ratio by reducing drastically the majority conductance.

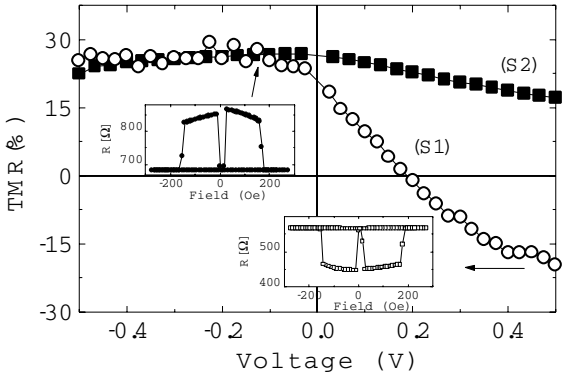

FIG. 2. TMR versus the voltage V curves measured in samples (S1) and (S2), respectively. Insets: Positive TMR versus magnetic field H [TMR(H)] curve measured at $V = -0.1$ V ($V+$ = top MTJ electrode); negative TMR(H) curve measured at $V = +0.5$ V ($V+$ = bottom MTJ electrode).

For positive biasing of the bottom electrode, the electrons, extracted from the top Fe(001) electrode by tunneling across the barrier, "scan" in energy the bottom "flat" Fe(001) electronic structure. Then, when the energy of the collected electrons "matches" the energy of the interface resonant state, a strong enhancement of the AP conductance with respect to the parallel one occurs, via the enhancement of the wave function matching at the interface. This is directly reflected by the sign reversal of the TMR (Fig. 2) and by the AP conductance which overcomes the parallel one above 0.2 eV [Fig. 3(a)]. However, when the interfacial state is not coupled to the bulk (S2), it will not provide a resonant-assisted enhancement of the AP conductance. Moreover, as illustrated by Fig. 3(b), the parallel conductance associated to the majority spin decreases with increasing the bias voltage. This counterintuitive effect simply reflects the electronic structure of Pd whose DOS vanishes abruptly above E_F [see Fig. 1(b)]. This influences directly the Bloch wave matching at the interfaces Pd/Fe/MgO, important for the propagation of electrons whose characteristic lengths (coherence/spin diffusion) overcome the thickness of the bottom Fe (tunneling electrons which see the Pd). Note that in a ferromagnetic material for the majority spin the diffusion length is larger than the one of minority. When the bias voltage is furthermore increased, the energy of hot electrons in the bottom Fe/Pd electrode increases, their characteristic lengths decrease. These electrons get rapidly thermalized to E_F, within the 2.5 nm Fe electrode. Consequently, the conductance becomes gradually insensitive to the Pd electronic structure. Let us now emphasize the influence of the top rough electrode. The disorder

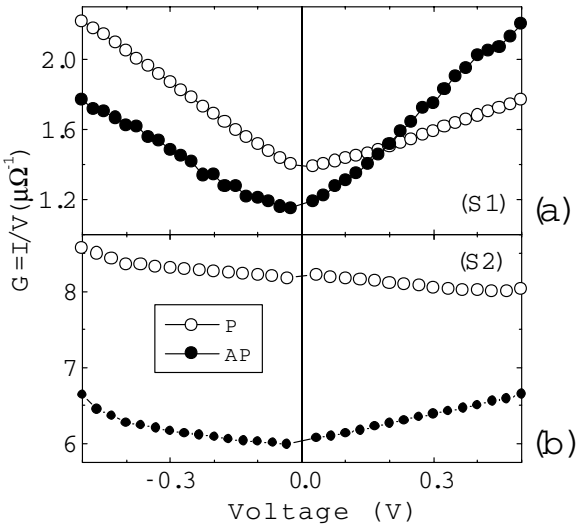

FIG. 3. Conductance versus voltage curves for samples (S1) (a) and (S2) (b) measured in parallel (○) and antiparallel (●) magnetic configurations of the MTJ electrodes, respectively.

VOLUME 93, NUMBER 10 PHYSICAL REVIEW LETTERS week ending 3 SEPTEMBER 2004

breaks the symmetry of the system and mixes in terms of symmetry the propagating Bloch states in the leads [18]. This influences the tunneling of electrons injected towards the bottom flat one. It makes possible the injection and the tunneling of states which, due to their symmetry, would not be able to tunnel effectively through the barrier in perfect junctions. However, the electrons are "filtered" in symmetry by the barrier and the bottom flat Fe electrode (equivalent of a large band emitter and a narrow band filter). Therefore, the total conductivity of the junctions reflects the electronic properties of the bottom electrode and the interfacial band structure matching at the bottom Fe/MgO interface.

For negative voltage, when the electrons tunnel towards the rough top electrode positively biased, we observe a quasiconstant magnetoresistance versus V, up to an applied voltage of 0.5 V. Because of the interfacial roughness, one can easily assume that the interfacial DOS possesses no sharp feature and that no interfacial resonant state is present. It is worthwhile to remark here the enormous potential for applications of tunnel junctions where the TMR is "almost" constant with the bias voltage. The measured variation of the TMR with the bias voltage is very small ($V_{1/2} > 1.5$ V). It indicates that the mechanisms involved in the bias voltage variation of the TMR are not dominant in our MTJ. These mechanisms are (i) incoherent tunneling due to scattering at impurities or defects located in the barrier [10]; (ii) energy dependence of spin-polarized DOS, which affects the spin polarization [4]; and (iii) quenching of TMR by hot electrons or spin excitation of magnons [19]. In our monocristalline MTJ, the first mechanism is not dominant. Here, the quality of the insulator is rigorously controlled by the 2D epitaxial growth. As shown by Ding *et al.* [9], using indirect spin-polarized scanning tunneling microscopy measurements, in case of MTJs involving perfect thick vacuum barriers (asymptotic regime), the TMR as a function of the bias voltage is found to be constant. Concerning the second mechanism, one can assume that the energy dependence of spin-polarized DOS of a rough electrode, above the Fermi level, is small (no sharp features). This will translate an almost constant TMR versus V. This effect is furthermore enhanced by the symmetry dependent filtering of electrons by the bottom flat Fe "emitter" electrode and by the MgO barrier. These two filters favor the tunneling of dispersive s-like bands, whose DOS are smooth and extended [6]. Moreover, when the junction is biased, one cannot neglect the contribution to the tunneling of the electrons from the negatively biased electrode located below the Fermi level within an energy range $[E_F - eV, E_F]$. They will tunnel into the positively biased electrode within a $[E_F, E_F + eV]$ unoccupied band. This would implicate an extremely complex analysis of the tunneling in a nonequilibrium biased MTJ stack for electrons coming beyond the Fermi level. Lastly, one can assign the slight variation of the TMR with V in our junctions to the third mechanism, implicating interfacial magnons.

In summary, by using spin dependent tunnel transport characteristics of model monocrystalline Fe/MgO/Fe-type MTJ systems, we pointed out the influence of the interfacial states on the spin-polarized tunneling. In our samples the electronic structure of the Fe/MgO interface is controlled via the topological quality of the Fe layers. We show that, in order to contribute to the total conductance, the interfacial state has to be coupled to the bulk. Last, one should remark that in high-quality epitaxial junctions the spin-polarized current voltage characteristics can be controlled via the engineering of the electronic structure of the layers, a fact extremely important for potential applications of the MTJs.

The authors acknowledge D. Stoeffler, B. Kierren, S. Andrieu, F. Montaigne, and M. Alnot. This work was supported by the "Conseil Régional de Lorraine."

[1] J. M. Daughton, J. Appl. Phys. **81**, 3758 (1997); W. J. Gallagher *et al.*, U.S. Patent No. 5 640 343 (1997).
[2] M. Bowen *et al.*, Appl. Phys. Lett. **79**, 1655 (2001).
[3] J. Faure-Vincent *et al.*, Phys. Rev. Lett. **89**, 107206 (2002).
[4] J. M. de Teresa *et al.*, Science **286**, 507 (1999).
[5] P. LeClair *et al.*, Phys. Rev. Lett. **88**, 107201 (2002).
[6] J. M. MacLaren *et al.*, Phys. Rev. B **59**, 5470 (1999); W. H. Butler *et al.*, Phys. Rev. B **63**, 054416 (2001).
[7] J. Mathon and A. Umerski, Phys. Rev. B **63**, 220403(R) (2001).
[8] O. Wunnicke *et al.*, Phys. Rev. B **65**, 064425 (2002).
[9] H. F. Ding *et al.*, Phys. Rev. Lett. **90**, 116603 (2003).
[10] R. Jansen and J. S. Moodera, Phys. Rev. B **61**, 9047 (2000).
[11] P. Blaha, K. Schwarz, G. K. H. Madsen, D. Kvasnicka, and J. Luitz, *Wien2k, An Augmented Plane Wave + Local Orbitals Program for Calculating Crystal Properties* (Kalheinz Schwartz, Technical University of Wien, Austria, 2001), ISBN 3-9501031-1-2.
[12] H. L. Meyerheim *et al.*, Phys. Rev. Lett. **87**, 76 102 (2001).
[13] C. Li and A. J. Freeman, Phys. Rev. B **43**, 780 (1991).
[14] X.-G. Zhang, W. H. Butler, and A. Bandyopadhyay, Phys. Rev. B **68**, 92 402 (2003).
[15] E. Popova *et al.*, Appl. Phys. Lett. **81**, 1035 (2002).
[16] J. Faure-Vincent *et al.*, J. Appl. Phys. **93**, 7519 (2003).
[17] From the transport analysis, we extract only a "qualitative" signature of the IR. Indeed, the temperature affects the transport mechanisms and the surface electronic properties, and therefore the analysis of the temperature dependence of the IR performed by transport measurements constitutes a complex task.
[18] E. Y. Tsymbal *et al.*, J. Phys. Condens. Matter **15**, R109 (2003).
[19] S. Zhang *et al.*, Phys. Rev. Lett. **79**, 3744 (1997); J. S. Moodera *et al.*, Phys. Rev. Lett. **80**, 2941 (1998).

PHYSICAL REVIEW B **73**, 104439 (2006)

Low-resistance magnetic tunnel junctions with an MgO-Al_2O_3 composite tunnel barrier: Asymmetric transport characteristics and free electron modeling of a self-limited oxidation bilayer

C. de Buttet, M. Hehn, F. Montaigne, C. Tiusan, G. Malinowski, and A. Schuhl
Laboratoire de Physique des Matériaux, UMR CNRS 7556, B.P. 239, 54506 Vandœuvre lès Nancy Cedex, France

E. Snoeck
CEMES-CNRS-Groupe NanoMatériaux, 29 rue Jeanne Marvig, B.P. 94347, F-31055 Toulouse Cedex, France

S. Zoll
CROLLES 2, FREESCALE-PHILIPS-STMICROELECTRONICS, 850 rue Jean Monnet, F-38926 CROLLES Cedex, France
(Received 29 September 2005; revised manuscript received 23 January 2006; published 24 March 2006)

Low-resistance magnetic tunnel junctions with an MgO-Al_2O_3 composite tunnel barrier have been grown. From the theoretical point of view, current-voltage and magnetoresistance-voltage characteristics are predicted to be asymmetric. These asymmetries are studied as a function of barrier thicknesses for given experimental MgO and Al_2O_3 barrier heights. From an experimental point of view, the bottom alumina barrier acts as a diffusion barrier allowing the complete oxidation of the thin deposited Mg layer. As a result, composite Al_2O_3/MgO tunnel barriers show a lower area resistance and a magnetoresistance signal at nonzero applied voltage that is predicted to be equivalent as single Al_2O_3 tunnel barriers with the same total thickness. Current-voltage and magnetoresistance-voltage characteristics are shown to be asymmetric at high voltages.

DOI: 10.1103/PhysRevB.73.104439 PACS number(s): 85.75.−d, 72.25.−b

I. INTRODUCTION

The discovery of a tunnel magnetoresistance (TMR) effect at room temperature in oxide barrier based magnetic tunnel junctions[1] (MTJ) paved the way to intense developments in this field area with many possible application prospects.[2] Those numerous studies devoted to different aspects of this topic permit us to get a better understanding of the fundamentals of spin polarized tunneling transport. A large effort was paid to optimize the growth of thin insulating materials[1,3–5] and to model the magnetotransport properties across those tunnel barriers.[6,7] Much of the attention was then paid on the study of single tunnel barrier structures and the quality of the grown materials allows us now to pass a further step.

The next step consists to associate two or more tunnel barriers made with different materials in a single structure. Results have been reported on two terminal double tunnel barriers[8,9] or double Schottky barriers[10] and also on three terminal double tunnel barriers[11] or tunnel barrier/Schottky barrier.[12] Here, the tunnel barriers and/or Schottky barriers are separated by a metallic or magnetic layer or multilayer. Up to now, no real and complete experimental report on composite barriers, made of a multilayered insulator, has been done. One bottle neck relays on the difficulty to grow a dielectric layer on top of another one. Indeed, the dielectric layer is commonly made by post-deposition oxidation of a metallic layer. While the growth of a first dielectric layer of a dielectric bilayer is straightforward, the growth of the second one is hindered by the difference in surface energy between the first dielectric material and the metallic atoms of the second material before oxidation. This leads often to a growth of a discontinuous layer and nucleation of clusters.[13,8] Previous studies have shown that in composite Al_2O_3/TaO barriers,[14] the magnetoresistance versus applied voltage asymmetries are linked to the insulator band structure. However, composite tunnel junctions are expected to show intrinsically highly nonsymmetric electrical characteristics[7] and it would have an important technological impact in spintronics applications.[8]

In this paper, we report on the theoretical and experimental magnetotransport properties of low-resistance magnetic tunnel junctions with an MgO-Al_2O_3 composite tunnel barrier.

From the theoretical point of view, current-voltage, $I(V)$, and magnetoresistance-voltage, TMR(V), characteristics are predicted to be asymmetric and this is directly linked to the difference in barrier heights of Al_2O_3 and MgO. The origin of asymmetries will be discussed. These asymmetries are modeled as a function of barrier thicknesses for given experimental microcrystalline MgO and amorphous Al_2O_3 barrier heights measured directly in previous studies.[4,5] The asymmetry of the TMR(V) and especially the location of the maximum of TMR at finite bias voltage could be used in applications if this potential corresponds to the working potential of the device.

From an experimental point of view, this study follows the one made on single microcrystalline MgO magnetic tunnel barriers.[5] Those junctions exhibit an area resistance of $10^5\ \Omega\ \mu m^2$ for a 1.6 nm thick MgO barrier. Nevertheless we were not able to grow fully oxidized MgO layers with thicknesses less than 1.6 nm mainly because of the hard oxidation conditions of a pure dc plasma glow discharge. Indeed, the oxidation conditions lead to instantaneous over oxidized junctions perpendicular to the Co/Mg interface while lateral oxidation of the Mg layer is not completed. This is explained

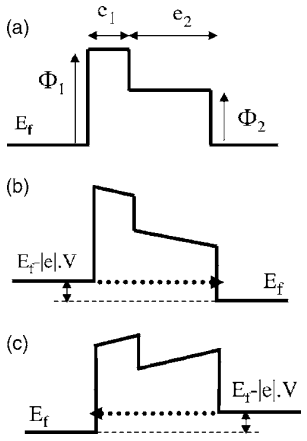

FIG. 1. Composite tunnel barrier potential profile at zero applied voltage (a), under a positive applied voltage (b), and under a negative applied voltage (c).

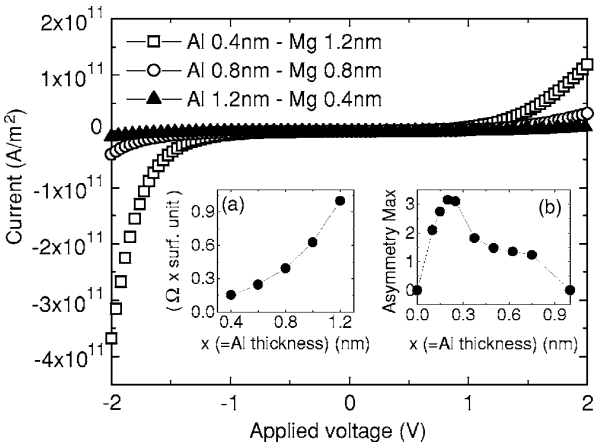

FIG. 2. Computed current density as a function of applied voltage in a composite $Al_2O_3(x\ \text{nm})/MgO(1.6\ x\ \text{nm})$ tunnel junctions for $x=1.2$ nm, 0.8 nm, and $x=0.4$ nm. Inset (a), variation of the area resistance as a function of x; inset (b), variation of the maximum current asymmetry as a function of x.

by the preferential oxidation at Mg grain bounderies. Then, adding a bottom alumina barrier will act as a diffusion barrier allowing the complete oxidation of the thin deposited Mg layer. As a result, composite Al_2O_3/MgO tunnel barriers show lower area resistance and predicted equivalent magnetoresistance signal at nonzero applied voltage as single Al_2O_3 tunnel barriers with the same thickness.

II. THE COMPOSITE BARRIER—TOWARDS ASYMMETRIC MAGNETOTRANSPORT CHARACTERISTICS

Composite barriers are made of a bilayer or of a multilayer composed with two or more insulating materials. In the case addressed in the present work, a bilayer is made of two insulators with different barrier heights. This configuration leads to the asymmetrical potential profile given in Fig. 1(a). The effective barrier heights are fixed and measured to be equal to $\phi_{Al_2O_3}=1.5$ eV and $\phi_{MgO}=0.7$ eV from our previous experimental measures.[4,5] Then, the respective thicknesses of both barriers can be varied and effects on the magnetotransport characteristics of the composite tunnel junction can be theoretically evaluated. It has been shown that either through Al_2O_3 or MgO, the electron tunneling can be modeled with the parabolic band model using such effective tunnel barrier heights.[7,5] Indeed, spin filtering by the tunnel barrier associated to the symmetry of the system and the associated high magnetoresistance ratio require epitaxial magnetic tunnel junctions[15] or highly textured.[16] As soon as a polycrystalline and/or an amorphous barrier is grown, band effects are smeared out and the parabolic band model applies with effective barrier height and thickness. These parameters are the result of an average over the tunnel junction surface of the wave vector dependent tunnel probabilities. Finally, the parabolic band model is suitable to take into account such complex barrier potentials but also the distortion of the barrier under an applied voltage. The model is described in detail in Refs. 7 and 17. Briefly speaking, it relies on elastic coherent tunneling in a laterally invariant system. The total energy and the transverse wave vector are thus conserved in the process. The transmission coefficient is computed by resolving analytically the Schrödinger equation considering linear potential and exchange splitting for the magnetic electrodes. The transmission coefficient is integrated over the possible energies for a zero temperature. For the band structure of the electrodes, parameters proposed by Davies and MacLaren[18] are used; for the barriers, a normalized effective mass of 0.4 is assumed.

In a first step, the modeling of a 1.6 nm thick composite barrier $Al_2O_3(x\ \text{nm})/MgO(1.6\ x\ \text{nm})$ is presented. This highlights the tendencies of the resistance, the current asymmetry, and the TMR ratio and shift when x is varied. First of all, the $I(V)$ characteristics exhibit an asymmetric behavior as shown in Fig. 2. This asymmetry is directly linked to the asymmetric barrier potential. When the barrier is negatively biased as in Fig. 1(b), the effective barrier height and thickness decrease with the potential increase. This leads to a strong increase in the tunnel current. When the barrier is positively biased as in Fig. 1(c), the effective barrier height and thickness are quite constant as the potential increases before a reduction at high potential. As a consequence, the $I(V)$ characteristic appears to be asymmetric. The composite barrier area resistance increases strongly with the Al_2O_3/MgO thickness ratio [inset (a), Fig. 2]. The more the aluminum layer is thick, the more the resistance is high. Obviously, increasing x increases the mean barrier height and so the barrier resistance. Then, if a low resistance tunnel barrier is desired, a weak proportion of Al_2O_3 would be preferred. The $I(V)$ asymmetric behavior is quantified by the current asymmetry ratio $\alpha(V)=I(V)/-I(-V)$.

This asymmetry first increases as the thickness of MgO increases, reaches a maximum and then decreases. In inset (b) of Fig. 2, we report the maximum of asymmetry as a function of x. This behavior has been observed even for a broad range of the whole barrier. As shown in Fig. 3, the TMR(V) characteristics are asymmetric and, interestingly,

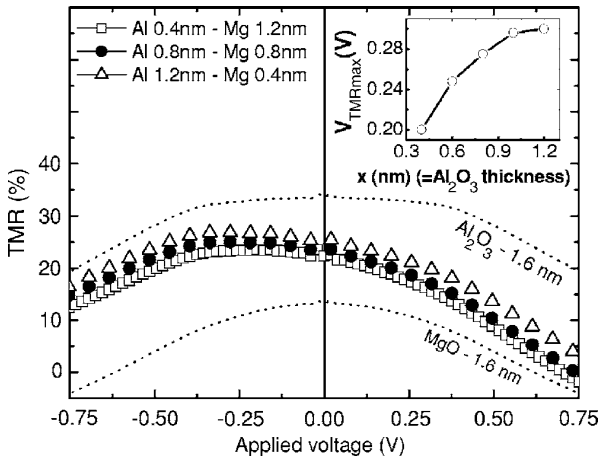

FIG. 3. Computed variation of the tunnel magnetoresistance, TMR, as a function of applied voltage in a composite $Al_2O_3(x\ \text{nm})/MgO(1.6\ x\ \text{nm})$ tunnel junctions for $x=1.2$ nm, 0.8 nm, and $x=0.4$ nm. Inset: variation of $V_{\text{TMR max}}$ as a function of x. The TMR(V) for single 1.6 nm thick Al_2O_3 and MgO barriers have been added in as dotted lines in the figure.

the maximum value of TMR is not reached at zero bias voltage but for a value, labeled $V_{\text{TMR max}}$, which depends on x. The inset of Fig. 3 shows the variation of $V_{\text{TMR max}}$ with x. Both the maximum of TMR and $V_{\text{TMR max}}$ increase with x, the thickness of the Al_2O_3 part of the 1.6 nm thick composite barrier. The drift of $V_{\text{TMR max}}$ towards high potential is beneficial if we consider that the maximum of TMR could be available if the device works under a bias voltage more or less equal to the $V_{\text{TMR max}}$. In brief, this result encourages the elaboration of hybrid junctions with large Al_2O_3 proportion.

In a second step, the modeling of a composite barrier with constant Al_2O_3/MgO thickness ratio but varying total thickness has been done. From the previous paragraph, it can be seen that if the purpose consists to grow low resistive junctions with visible current asymmetries, the composite barrier must be made with a MgO layer thicker than the Al_2O_3 one. Therefore, an Al_2O_3/MgO thickness ration of 0.33 has been chosen in the following calculations. Resistance versus total composite barrier thickness is not reported here since the result is straightforward. Indeed, obviously, the junction resistance increases exponentially with its barrier thickness. In Fig. 4(a), it appears clearly that the current asymmetry increases when the total thickness increases. It is worth noting that the maximum of $\alpha(V)$ shifts to low applied voltage when thickness increases. As far as TMR is concerned, its value globally increases when the thickness of the whole stack decreases. This result was already shown in single MTJ.[7] The inset of Fig. 4(b) shows the variation of $V_{\text{TMR max}}$ with the total composite barrier thickness. In this case, $V_{\text{TMR max}}$ decreases as the total thickness increases. The drift of $V_{\text{TMR max}}$ towards high potential is beneficial if we consider that the maximum of TMR could be used if the device works under a bias voltage more or less equal to the $V_{\text{TMR max}}$. This result encourages the elaboration of hybrid junction with low total composite barrier thickness.

In summary, the theoretical calculations on magnetotransport characteristics of composite Al_2O_3/MgO tunnel barriers

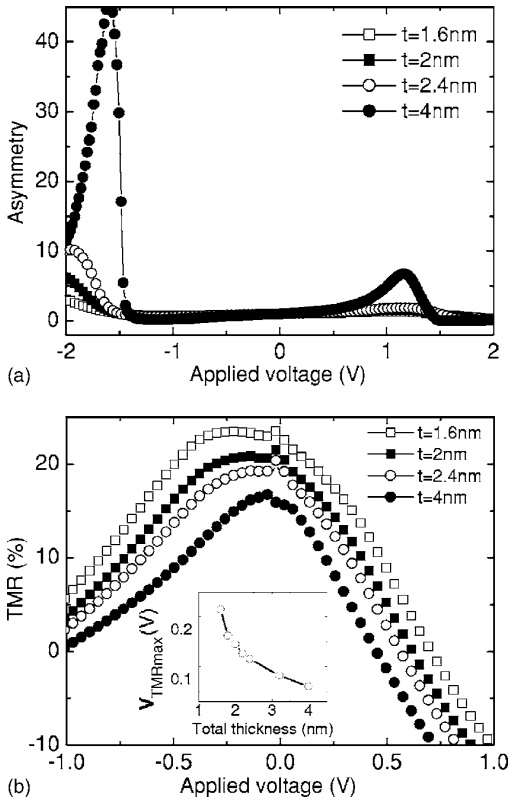

FIG. 4. (a) Calculated variation of current asymmetry with applied voltage for $Al_2O_3[(3t/4)\ \text{nm}]/MgO[(t/4)\ \text{nm}]$ tunnel junctions for $t=1.6$ nm, 2 nm, 2.4 nm, and 4 nm. (b) Calculated variation of magnetoresistance with applied voltage for $Al_2O_3[(3t/4)\ \text{nm}]/MgO[(t/4)\ \text{nm}]$ tunnel junctions for $t=1.6$ nm, 2 nm, 2.4 nm, and $t=4$ nm. Inset: variation of $V_{\text{TMR max}}$ as a function of t.

predict that: (i) with fixed Al_2O_3/MgO thickness ratio, high $\alpha(V)$ is supported by a thick barrier while high TMR and $V_{\text{TMR max}}$ are supported by a thin barrier; (ii) with fixed total barrier thickness, both TMR and $V_{\text{TMR max}}$ increase with the Al_2O_3 layer thickness. From this conclusion, it is clear that combining a high TMR ratio with low area resistance, high $V_{\text{TMR max}}$ and high $\alpha(V)$ within a given composite barrier is hard to achieve. So priorities have been defined for experimental investigations. First, in the continuity of our work on single MgO magnetic tunnel barriers,[5] a low area resistance suitable for future generations of magnetic random access memory (MRAM) is wanted. So the thinnest barriers have been grown. Then, in order to show the asymmetric character of the hybrid junctions, we promoted composite barriers with a MgO layer thickness larger than the Al_2O_3 layer thickness. This is also in agreement with an Al_2O_3 layer used as a diffusion barrier rather than to increase the TMR signal of the composite barrier.

III. FORMATION OF A COMPOSITE ALUMINE/MAGNESIUM OXIDE BARRIER

Junctions are deposited onto float-glass substrates by sputtering tantalum, platinum, magnesium targets mounted

on rf magnetron cathodes and cobalt on a dc magnetron cathode. The base pressure is less than 5×10^{-7} mbar and the substrates are maintained at room temperature. The studied samples are composed of Glass/Ta(5 nm)/Pt(20 nm)/Co(10 nm)/[Al(x nm)/Mg(y nm), oxidized t_{Ox} s]/Co*(20 nm)/Pt(5 nm). All the layers are deposited at an operating pressure fixed to 5×10^{-3} mbar except the last Co layer of the stack, denoted by Co*, deposited at 1.5×10^{-2} mbar. When Co is deposited at low Ar pressure (5×10^{-3} mbar), the magnetization reversal is sharp with nucleation and propagation of domain walls. When the Ar pressure increases up to an optimum equal to 1.5×10^{-2} mbar, the grain size and the coercive field increase up to a maximum. In this way, two electrodes with different coercive fields can be made at each side of the barrier.[4]

To obtain the Al_2O_3/MgO composite barrier, the oxidation is made just after deposition of the metallic Al/Mg bilayer using a dc glow discharge at a power of 200 W and voltage of 600 V under a pure 10^{-1} mbar O_2 plasma in the sputtering load lock. The samples are transferred to this chamber without breaking the vacuum.

To define the junction geometry for electronic transport measurements, we have used *ex situ* changed contact masks with a path width of 200 μm. Each sample was prepared to include 14 tunnel junctions. Details on the junction geometry can be found elsewhere.[4] The electrical resistivity was measured with a standard four-probe dc technique.

Three series of composite barriers have been grown with deposited metal layers of Al(0.7 nm)/Mg(1.6 nm), Al(0.7 nm)/Mg(1.1 nm), and Al(0.5 nm)/Mg(1.4 nm). The properties of tunnel junctions formed from a single Al(0.7 nm) or Mg(1.6 nm) film have already been reported.[4,5] For each structure, the oxidation time t_{Ox} has been varied to achieve an optimal oxidation of the bilayer. The average values and standard deviation of resistance and magnetoresistance for different samples and different oxidation conditions are represented in Fig. 5. These values are based on measurements of 12 to 14 junctions per sample. For Al(0.7 nm)/Mg(1.6 nm) bilayer [Fig. 5(a)] an optimum TMR of 7% at room temperature could be measured with t_{Ox}=48 s. For longer oxidation times the MR is slightly reduced (6%) and the resistance seems to saturate from $t_{Ox}>53$ s. This saturation of the resistance and the weak decrease in magnetoresistance suggests that the Al layer acts as a diffusion barrier and prevents further oxidation of the bottom Co electrode. A similar behavior is observed for Al(0.7 nm)/Mg(1.1 nm) bilayers [Fig. 5(b)]. Due to the reduced Mg thickness, the resistance saturates around 20 kΩ (instead of 110 kΩ for a 1.6 nm thick Mg layer).

For a 0.5 nm thickness of aluminum, a different phenomenology is observed [Fig. 5(c)]. The resistances and the magnetoresistances are very dispersed for a same sample and the statistical properties vary from sample to sample (see, for example, 20 and 25 s). Unlike the previous case, a reduction of magnetoresistance is observed for longer oxidation times and larger resistances. Then, for a reduced Al thickness, this layer does not play its role of diffusion barrier and small process variations lead to different results concerning TMR ratio and junction area resistance. For such a thickness, considering the roughness of the bottom electrode, the Al layer might not be continuous.

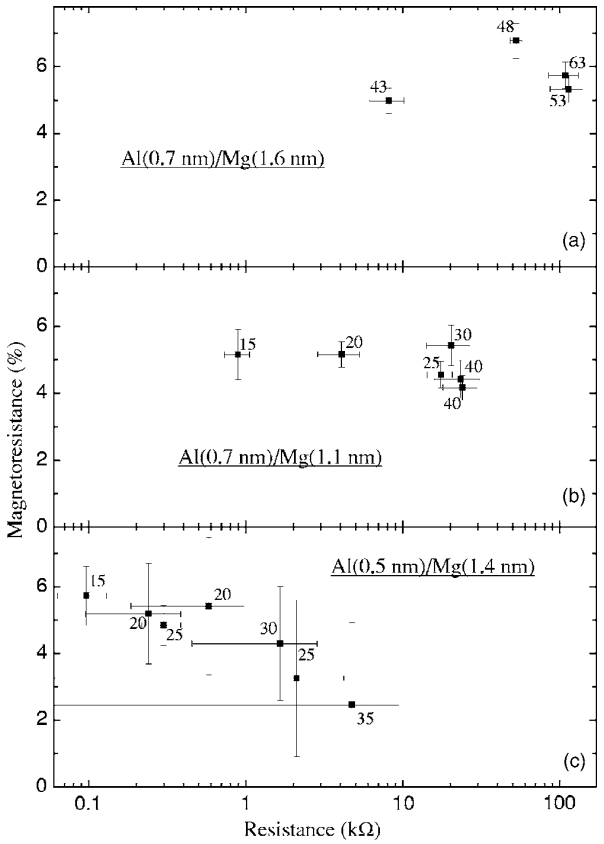

FIG. 5. Variation of the TMR as a function of junction resistance for tunnel composite barriers made with an oxidation of a Al(0.7 nm)/Mg(1.6 nm) bilayer (a), a Al(0.7 nm)/Mg(1.1 nm) bilayer (b), and a Al(0.5 nm)/Mg(1.4 nm) bilayer. In each curve, the numbers indicate the oxidation time.

The structure and the microstructure of the stacking sequence were studied by transmission electron microscopy (TEM) on cross sectional samples prepared by the usual method, i.e., first mechanically thinned then ion milled down to the electron transparency. The TEM studies were performed using a FEI 200 kV field emission gun microscope fitted with a Cs corrector whose point resolution is 0.12 nm. The low magnification TEM image inset Fig. 6 illustrates the whole stacking sequence with quite rough interfaces while the high resolution TEM (HRTEM) micrograph shows the fine structure of the Al_2O_3+MgO barrier. As expected the alumina barrier is amorphous while crystalline MgO grains are visible. The crystalline fcc structure of Co is verified and no evidence of a possible oxidation of the bottom Co layer was observed proving the efficiency of Al_2O_3 as a diffusion barrier. Figure 6 shows clearly that the Al_2O_3/MgO interface is not well defined. This mixing can originate directly from the diffusion between Al and Mg during the growth before oxidation. Furthermore, the oxidation step can cause some mixing at the interfaces through the diffusion of Al or Mg atoms.

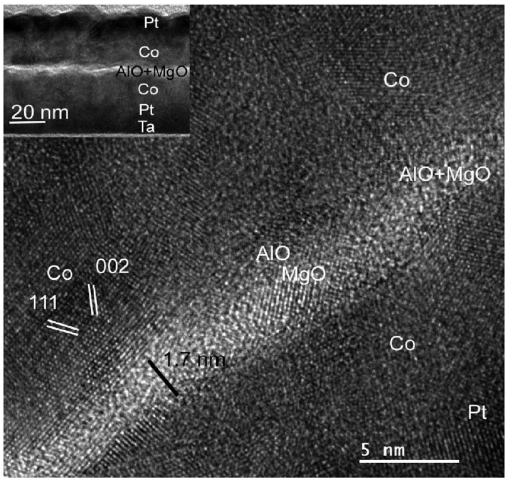

FIG. 6. HREM micrograph of the insulating composite barrier observed on a cross sectional MJT sample with a low TEM micrograph of the whole stacking in the inset.

This study has shown that it is possible to oxidize a metallic bilayer in a single oxidation step. Furthermore, a 0.7 nm thick Al layer acts as a diffusion barrier for oxygen preventing the oxidation of the bottom electrode. This effect is not observed for a single Al layer and is not related to the total thickness of the bilayer. This feature is thus specific to the nature of the bilayer.

We now detail magnetotransport properties for the optimized junctions.

IV. MAGNETOTRANSPORT IN A COMPOSITE BARRIER

The presence of TMR is an indication of the quality of the composite barrier formed by oxidation of the metallic bilayer. The surfacic resistance of a barrier formed from a Mg(1.6 nm) layer is 200 kΩ μm^2.[5] The high surface resistance of the composite barrier (>1 GΩ μm^2) thus proves that the composite barrier acts as a single tunnel barrier and that direct tunneling is the main mode of transport through the barrier. This increase of resistance by association of different barriers is quantitatively described by the parabolic band model (a difference of resistance by a factor of 10^4 exists between the composite Al_2O_3/MgO and the MgO single barrier and by a factor of 10^6 between the composite Al_2O_3/MgO and the Al_2O_3 single barrier). The prominence of direct tunneling in the transport is also confirmed by the temperature dependence of the resistance[19] (not shown). The resistance increases by a factor of 1.5 between 300 K and 77 K. According to Stratton,[20] this tunnel resistance increase at low temperature depends on the mean barrier height. With a composite tunnel barrier, the mean barrier height is located between MgO and Al_2O_3 barrier heights. Then, the resistance variation should also be between the one observed for single MgO and Al_2O_3 barriers. This is indeed the case with a resistance increase by a factor of 2 (respectively, 1.2) for a MgO (respectively, Al_2O_3) single barrier of the same total thickness.

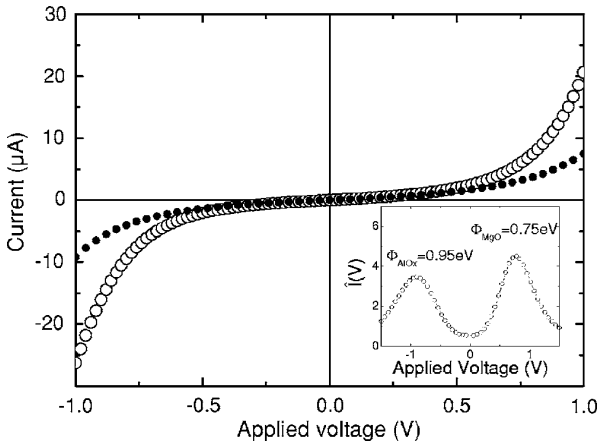

FIG. 7. Current as a function of applied voltage in a composite Al(0.7 nm)/Mg(1.6 nm) tunnel barrier with t_{Ox} equal to 48 s measured at 300 K (-○-) and 77 K (-●-). Inset: calculus of the $\hat{I}(V)$ also on the same junction.

Figure 7 shows the $I(V)$ characteristics measured at 77 and 300 K between -1 and $+1$ V for a Al(0.7 nm)/Mg(1.6 nm) bilayer. As expected, the characteristics are asymmetric. The maximum measured asymmetry is 1.9. This value is not a maximum as represented in Fig. 4 but is limited experimentally by the breakdown of the junctions (occurring at voltages around 1 V whereas from calculations maxima of asymmetry are expected at voltages beyond 1.5 V). For single barriers, effective barriers parameters are usually deduced from fits to analytical formula. Brinkman model[21] can be used to fit an asymmetric $I(V)$ characteristic with a third order polynomial. This leads in our case to a barrier height of 0.68 eV with barrier asymmetry of 1.28 eV and a barrier thickness of 2.8 nm. This expresses the asymmetry of the barrier but no information can be extracted from this fit. An original method, based on the temperature variation of the $I(V)$ characteristic, was used to determine the barrier height at each interface of the barrier. It can be shown that the temperature variation of the current, represented by $\hat{I}(V)=[I(V,T)-I(V,0)]/I(V,0)$, exhibit a maxima at a voltage related to the barrier height.[22] According to the sign of the applied bias voltage, the MgO interface or the Al_2O_3 interface can be probed. From the inset of Fig. 7, an Al_2O_3 barrier height of 1 eV is found which is a low value compared to former studies but the extracted MgO barrier height of 0.75 eV is in agreement with the previous study. This experiment confirms the different value of the barrier height at each interface and confirms once again that a composite barrier has been made.

The magnetoresistance ratio has been studied as a function of applied voltage for barriers formed by oxidation of Al(0.7 nm)/Mg(1.6 nm) and Al(0.7 nm)/Mg(1.1 nm) bilayers (Fig. 8). The TMR(V) is asymmetric, the magnetoresistance ratio is reduced to half of its maximum value at bias voltages $V_{1/2}$ of about 0.31 V at the Al_2O_3 and of about 0.21 V at the MgO interface. Those values are in agreement with those measured on single tunnel barriers (the parabolic band model predicts that the decrease rate of the magnetore-

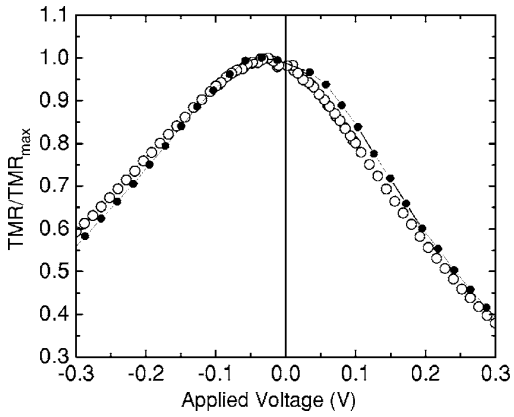

FIG. 8. Measure of the normalized TMR as a function of applied voltage at 300 K in a composite Al(0.7 nm)/Mg(1.6 nm) tunnel barrier with t_{Ox} equal to 48 s (-○-) and in a composite Al(0.7 nm)/Mg(1.1 nm) tunnel barrier with t_{Ox} equal to 20 s (-●-).

sistance for a given polarity depends essentially on the interface at which electrons are collected[17]). As expected, the maximum of magnetoresistance is slightly shifted from zero bias with a shift of 25 mV for Al(0.7 nm)/Mg(1.6 nm) bilayer and 45 mV for Al(0.7 nm)/Mg(1.1 nm) bilayer.

Asymmetries in the $I(V)$ characteristics are often observed in magnetic tunnel junctions. They have been associated to an imperfect oxidation of the barrier (nonuniform, over or under oxidized) or to nonsymmetric electrodes. To our knowledge, it is the first time that a shift of the maximum of magnetoresistance is observed for identical electrodes. Thanks to our systematic study of the oxidation, we can exclude that this asymmetry is related to an over or under oxidation of the Al or Mg layer.

The parabolic band model explains the increase of the TMR shift with the reduction of the MgO thickness. However, the values of the shift are lower than the ones predicted theoretically. This difference might be explained by the reduced value of the alumina barrier height (1 eV instead of 1.5 eV). The reduction of the difference in barrier between Al_2O_3 and MgO reduces obviously the asymmetry of the $I(V)$ and the shift of the maximum TMR. Using the barrier heights measured with the $\hat{I}(V)$ curves, the calculated $V_{\mathrm{TMR\ max}}$ falls down to 50 mV instead of 140 mV. But this value is still higher than the 25 mV measured value. From the TEM observations, it appears that the interface between Al_2O_3 and MgO is not perfectly abrupt and might be quite different from the perfect interface considered in the calculations. However, the effect of a nonabrupt interface on the parabolic band model is not that important. If it influences notably the asymmetry of $I(V)$ characteristic, especially for high biases, it has almost no influence on the shift of the maximum of TMR.

Another origin of the discrepancy between theory and experiments relies on the other possible mode of transport through the barrier as incoherent tunneling via one or several defects as localized state or inelastic tunnel assisted by phonons or magnons. The latter is mainly responsible for the decrease of magnetoresistance observed at low biases[23] in magnetic tunnel junctions. As the voltage dependence of this magnon assisted tunneling in this voltage range (below 100 mV) is essentially dominated by the structure of the magnon spectra and thus by the electrodes, this contribution to the current which reduces the magnetoresistance is symmetric. Magnon assisted tunneling can thus be responsible for the reduction of the TMR(V) shift.

V. CONCLUSIONS

In conclusion, we have successfully modeled and synthesized by sputtering composite Al_2O_3/MgO magnetic tunnel junctions. This has been done by using a common oxidation step for both Al and Mg layer. Regarding the Al layer, we have demonstrated that it can act as a good oxygen diffusion barrier, which enabled us to reduce the lower limit value of the thickness of a fully oxidized MgO layer. From our experimental point of view, we have made composite junctions with levels of resistance as low as comparable MgO magnetic tunnel junctions ($<10^7\ \Omega\ \mu m^2$ for 1.9 nm thick composite magnetic tunnel junction), and with levels of TMR equivalent to our Al_2O_3 based junctions (around 8%). Moreover, we have collected proofs of an hybrid junction tunneling and demonstrated experimentally that changes in the barrier thicknesses induces changes in terms of asymmetry behavior.

ACKNOWLEDGMENTS

The authors would like to thank D. Lacour for valuable discussions. This work is partially supported by La Région Lorraine and the Crolles 2 Alliance.

[1] J. S. Moodera, L. R. Kinder, T. M. Wong, and R. Meservey, Phys. Rev. Lett. **74**, 3273 (1995).
[2] S. A. Wolf, J. Supercond. **13**, 195 (2000).
[3] J. Nowak and J. Rauluszkiewicz, J. Magn. Magn. Mater. **109**, 79 (1992); J. S. Moodera and L. R. Kinder, J. Appl. Phys. **79**, 4724 (1996); C. L. Platt, B. Dieny, and A. E. Berkowitz, *ibid.* **81**, 5523 (1997); J. M. De Teresa, A. Barthélémy, A. Fert, J. P. Contour, R. Lyonnet, F. Montaigne, P. Seneor, and A. Vaurès, Phys. Rev. Lett. **82**, 4288 (1999); P. Rottländer, M. Hehn, O. Lenoble, and A. Schuhl, Appl. Phys. Lett. **78**, 3274 (2001).
[4] M. Hehn, O. Lenoble, D. Lacour, C. Féry, M. Piécuch, C. Tiusan, and K. Ounadjela, Phys. Rev. B **61**, 11643 (2000).
[5] M. Hehn, C. de Buttet, G. Malinowski, E. Snoeck, C. Tiusan, and F. Montaigne, Eur. Phys. J. B **40**, 19 (2004).
[6] M. Jullière, Phys. Lett. **54A**, 225 (1975); J. C. Slonczewski, Phys. Rev. B **39**, 6995 (1989); I. I. Mazin, Phys. Rev. Lett. **83**, 1427 (1999); I. I. Oleinik, E. Y. Tsymbal, and D. G. Pettifor, Phys. Rev. B **62**, 3952 (2000); J. M. MacLaren, X. G. Zhang,

W. H. Butler, and X. Wang, *ibid.* **59**, 5470 (1999).
[7] F. Montaigne, M. Hehn, and A. Schuhl, Phys. Rev. B **64**, 144402 (2001).
[8] C. Tiusan, M. Chshiev, A. Iovan, V. da Costa, D. Stoeffler, T. Dimopoulos, and K. Ounadjela, Appl. Phys. Lett. **79**, 4231 (2001).
[9] F. Montaigne, J. Nassar, A. Vaurès, F. Nguyen Van Dau, F. Petroff, A. Schuhl, and A. Fert, Appl. Phys. Lett. **73**, 2829 (1998).
[10] D. J. Monsma, R. Vlutters, and J. C. Lodder, Science **281**, 407 (1998).
[11] M. Hehn, F. Montaigne, and A. Schuhl, Phys. Rev. B **66**, 144411 (2002); D. Lacour, M. Hehn, F. Montaigne, H. Jaffrès, P. Rottlander, G. Rodary, F. Nguyen Van Dau, F. Petroff, and A. Schuhl, Europhys. Lett. **60**, 896 (2002); S. Stein, R. Schmitz, and H. Kohlstedt, Solid State Commun. **117**, 599 (2001).
[12] S. van Dijken, X. Jiang, and S. S. P. Parkin, Phys. Rev. B **66**, 094417 (2002).
[13] P. LeClair, H. J. M. Swagten, J. T. Kohlhepp, R. J. M. van de Veerdonk, and W. J. M. de Jonge, Phys. Rev. Lett. **84**, 2933 (2000); and references therein.
[14] M. Sharma, S. X. Wang, and J. H. Nickel, Phys. Rev. Lett. **82**, 616 (1999).
[15] C. Tiusan, J. Faure-Vincent, C. Bellouard, M. Hehn, E. Jouguelet, and A. Schuhl, Phys. Rev. Lett. **93**, 106602 (2004); C. Tiusan, J. Faure-Vincent, M. Sicot, M. Hehn, C. Bellouard, F. Montaigne, S. Andrieu, and A. Schuhl, Mater. Sci. Eng., B **126**, 112 (2006).
[16] S. Yuasa, T. Nagahama, A. Fukushima, Y. Suzuki, and K. Ando, Nat. Mater. **3**, 868 (2004); S. S. P. Parkin, C. Kaiser, A. Panchula, P. M. Rice, B. Hughes, M. Samant, and S.-H. Yang, Nat. Mater. **3**, 862 (2004).
[17] F. Montaigne, M. Hehn, and A. Schuhl, J. Appl. Phys. **91**, 7020 (2002).
[18] A. H. Davies and J. M. MacLaren, J. Appl. Phys. **87**, 5224 (2000).
[19] J. J. Akerman, R. Escudero, C. Leighton, S. Kim, D. A. Rabson, R. W. Dave, J. M. Slaughter, and I. K. Schuller, J. Magn. Magn. Mater. **204**, 86 (2002).
[20] R. Stratton, Phys. Chem. Solids **23**, 1177 (1962).
[21] W. F. Brinkman, R. C. Dynes, and J. M. Rowell, J. Appl. Phys. **41**, 1915 (1971).
[22] P. Rottländer, M. Hehn, and A. Schuhl, Phys. Rev. B **65**, 054422 (2002).
[23] S. Zhang, P. M. Levy, A. C. Marley, and S. S. P. Parkin, Phys. Rev. Lett. **79**, 3744 (1997).

APPLIED PHYSICS LETTERS **91**, 132504 (2007)

High bias voltage effect on spin-dependent conductivity and shot noise in carbon-doped Fe(001)/MgO(001)/Fe(001) magnetic tunnel junctions

R. Guerrero, D. Herranz, and F. G. Aliev[a)]
Departamento de Fisica de la Materia Condensado C-III, Universidad Autonoma de Madrid, 28049 Madrid, Spain

F. Greullet, C. Tiusan, M. Hehn, and F. Montaigne
Laboratoire de Physique des Matériaux, UMR CNRS 7556, Nancy Université, Bd. des Aiguillettes, B.P. 239, 54506 Vandœuvre-lès-Nancy Cedex, France

(Received 14 June 2007; accepted 11 September 2007; published online 26 September 2007)

Low temperature (10 K) high voltage bias dynamic conductivity (up to 2.7 V) and shot noise (up to 1 V) were studied in epitaxial Fe(100)/Fe–C/MgO(100)/Fe(100) magnetic tunnel junctions as a function of the magnetic state. The junctions show large tunnel magnetoresistance (185% at 300 K and 330% at 4 K). Multiple sign inversion of the magnetoresistance is observed for bias polarity when the electrons scan the electronic structure of the bottom Fe–C interface. The shot noise shows a Poissonian character. This demonstrates a pure spin-dependent direct tunneling mechanism and validates the high structural quality of the MgO barrier. © *2007 American Institute of Physics*.
[DOI: 10.1063/1.2793619]

Magnetic tunnel junctions[1,2] (MTJs) are nowadays one of the most active areas of material science and spintronics. Recent theoretical predictions[3,4] and experimental demonstrations[5–9] of coherent spin-dependent tunneling in single crystal Fe(100)/MgO(100)/Fe(100) MTJs revolutionized this area. The large tunneling magnetoresistance (TMR) at low bias voltages is mostly due to fully spin polarized Δ_1 bulk electron states in Fe(001), reflected for antiparrallel (AP) ferromagnetic electrodes configuration or well transmitted for the parallel (P) state.[3,4] However, the tunneling mechanism gets more complex when taking into account the electronic structure of the interfaces[10] and when biasing the junction. Therefore, for finite bias polarities, the antiparallel conductance may exceed the parallel one, resulting in TMR suppression[8] or its sign reversal.[10] By engineering the chemical and electronic structure of the Fe/MgO interface, the voltage variation of the TMR in amplitude and sign can be skilfully manipulated. It has been recently demonstrated that the carbon doping of the bottom Fe/MgO interface leads to a strongly asymmetric TMR versus bias, providing a root for the creation of high-output voltage device applications.[9]

Our letter presents a first study of dynamical conductance and TMR in a large bias window, up to 2.7 V, for Fe(100)/Fe–C/MgO(100)/Fe(100) MTJs. The shot noise analysis in different magnetization configurations is performed at voltages up to 1 V. The experiments are done at room temperature (300 K) and low temperature (4–10 K). The measured TMR ratio increases from 185% at 300 K to 330% at 4 K. Our tunneling spectroscopy experiments show a clear maximum in the AP conductivity for a finite bias and a multiple TMR sign inversion. Furthermore, in both P and AP configurations, the shot noise measurements demonstrate an uncorrelated direct tunneling mechanism across the MgO barrier. The shot noise analysis and the large breakdown voltage of the junctions (up to 3 V) demonstrates the high quality of our MgO barriers (i.e., absence of defects such as oxygen vacancies).

[a)]Electronic mail: farkhad.aliev@uam.es

Our epitaxial Fe(45 nm)/MgO(3 nm)/Fe(10 nm)/Co (20 nm)/Pd(10 nm)/Au(10 nm) samples were grown by molecular beam epitaxy on MgO(100) substrates under UHV condition (4×10^{-11} mbar base pressure). Prior to deposition, the substrate is annealed at 600°; then the layers are grown at room temperature. For flattening, the Fe electrodes are annealed to 450° (bottom Fe) and 380° (top Fe). Following the growth procedure of Ref. 13, two different samples can be grown: samples with clean Fe/MgO bottom interfaces and samples with carbon doping at bottom Fe/MgO interface (Fe/Fe–C/MgO). The Reflection high-energy electron diffraction (RHEED) analysis performed on each layer of the MTJ stack allows a direct control of the epitaxial growth and the high crystalline quality of the epitaxial layers. Compared to clean samples, in the samples with carbon, the bottom Fe(001) electrode presents a $c(2\times2)$ surface reconstruction (Fig. 1). The RHEED, however, showed no clear evidence of any structural difference between the two systems. This opens perspectives for further analysis which should involve techniques with local "resolution:" x-ray appearance near-edge structum extended x-ray absaptie fine structure surface x-Ray diffraction, etc. After the growth of the multilayer stack, MTJs with micrometric lateral size have been patterned using standard optical lithography/ion etching process. All the MTJs studied here contain carbon doped Fe/MgO interface. They have shown a large voltage stability of up to 3 V. The larger stability of the junctions with carbon

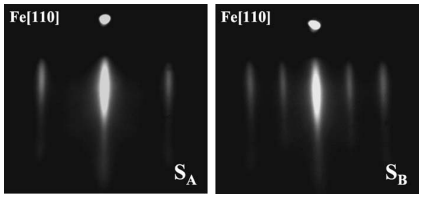

FIG. 1. RHEED patterns of the Fe bottom layer for (a) carbon-free Fe and (b) Fe/Fe–C along the [110] crystallographic direction. Additional pattern for Fe/Fe–C surface demonstrate the $c(2\times2)$ reconstruction related to carbon.

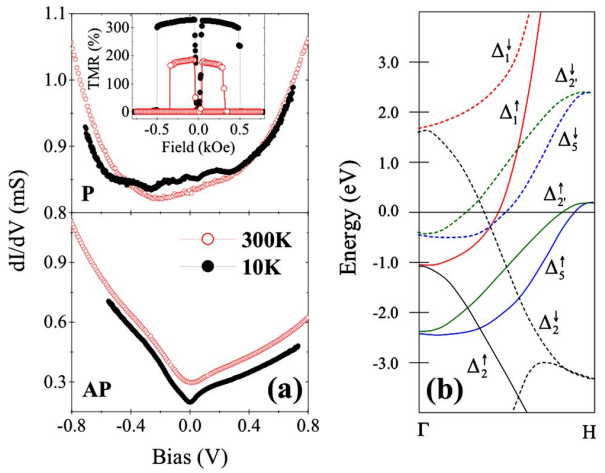

FIG. 2. (Color online) (a) Dynamic conductivities in P (top panel) and AP (bottom panel) magnetization states at 300 K (open circles) and 10 K (full circles). Top panel inset: TMR curves at 300 K (red open circles) and 4 K (black full circles). (b) Bulk band structure diagram of bcc Fe.

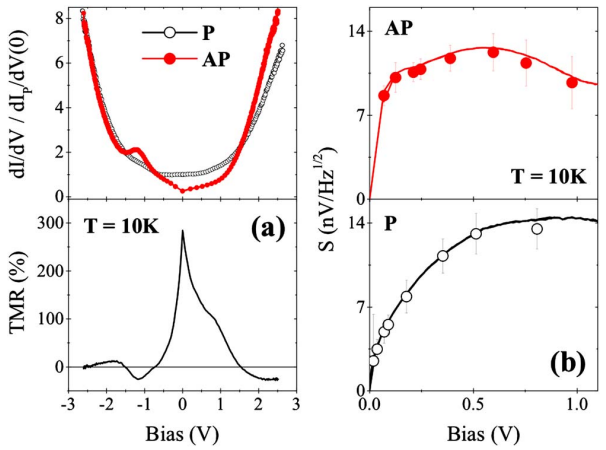

FIG. 3. (Color online) (a) Dynamic conductivities at 10 K (top panel) and related TMR (V) (bottom panel). (b) Shot noise measurements in P and AP states measured at 10 K in bias when the electrons are injected from the top toward the bottom MTJ electrode [negative voltage in Figs. 2 and 3(a)].

at the Fe/MgO interface has been observed performing experiments on more than ten junctions belonging to different sets of wafers.

Dynamic conductance $G(V)$ and shot noise bias dependence have been studied using a four-probe method with a setup allowing us to vary the temperature between 2 and 300 K, equipped with preamplifiers situated on top of the cryostat. Two different techniques were employed to measure dynamic conductance in P or AP states, providing nearly identical results. In the first, the MTJ is biased by dc voltage with superimposed low amplitude sinusoidal wave ($V_{ac}<20$ mV). The second technique, mainly employed at high bias, uses square current wave superimposed on dc current. Shot noise measurements were done using a cross-correlation technique. More details of setup were published elsewhere.[11,12]

At 300 K, the Fe/Fe–C/MgO(3 nm)/Fe/Co MTJs show RA product values (RT) ranging from 0.42 to 0.48 MΩ μm^2. The inset in the top panel of Fig. 2 shows typical TMR curves measured at 10 mV either at 300 K and at 4 K. The large TMR ratio of 185% at 300 K indicates the high quality of the MTJs. Interestingly, the low temperature TMR (~330%) notably exceeds previously reported (250%) maximum values of zero-bias TMR in epitaxial Fe(100)/MgO/Fe MTJs with "undopped" Fe/MgO interfaces.[8] The temperature variation of the TMR is understood from the dynamic conductivity experiments $G=dI/dV$ shown in Fig. 2(a), which plots $G(V)$ at 300 and 10 K within a voltage range of 0.8 V. Firstly, asymmetric $G(V)$ characteristics in positive and negative voltages demonstrate different electronic structures of the top and bottom electrodes and Fe/MgO interfaces.[9] Secondly, we claserve significantly different temperature variations of conductivity in P and AP magnetization configurations. In the AP configuration [Fig. 2(b)], we claserve almost no temperature dependent shape variation, except the enhancement of low bias anomaly at 10 K. However, we notice a strong reduction of $G_{AP}(V)$ by 50% at low temperature. On the other hand, a net temperature dependent shape variation between 300 and 10 K [Fig. 2(a), top panel] is clearly seen for $G_P(V)$. Interestingly, the zero bias G_P is mostly constant with temperature (only 2% variation). Additional local minima appear at 10 K for both positive and negative finite bias voltages. At low temperature, all studied MTJs reveal novel P-state low-bias conductance oscillations with about four minima [Fig. 2(a), top panel]. We note that low-bias conductivity minima in the P state have been already observed in carbon-free samples even at 300 K. However, we always measured only two local conductance minima.[13] These minima were explained by the Δ_5 majority electron contribution to the total conductivity at low voltage [<0.3 eV, which is the top of the majority Δ_5 band [Fig. 2(b)]. The origin of low temperature $G_P(V)$ minima observed in Fe/Fe–C/MgO/Fe MTJs opens interesting theoretical perspectives.

Figure 3(a) presents high bias conductance for voltages up to 2.7 V, measured at 10 K. The influence of joule heating (few Kelvins) on the I-V's is neglected due to the rather weak observed low temperature dependence of both G_P and G_{AP}. Interestingly, while $G_P(V)$ is rather symmetric, in negative voltage when the electrons tunnel into the bottom Fe–C/MgO electrode, the $G_{AP}(V)$ shows a strong asymmetric local maximum superimposed on roughly parabolic background. This "local" resonant increase of the G_{AP} ($G_{AP}>G_P$) in a narrow[14] energy window will lead to the lower voltage sign reversal of the TMR [Fig. 3(a), bottom panel]. Similar to scanning tunneling spectroscopy experiments,[15] and as we have previously shown,[10] the resonant enhancement of G_{AP} is attributed to the contribution to the tunneling of the Fe minority interfacial resonance (IRS). However, we only observed this phenomena in carbon-free Fe/MgO/Fe samples with thinner MgO barrier, where the Fe IRS still significantly contributes to the tunneling.[16] In the samples studied here, having carbon at the Fe–C/MgO interface, an important effect of the G_{AP} resonant activation by IRS is observed even for 3 nm thick MgO barriers. To elucidate this interesting property, theoretical investigation of two effects is in progress: (i) the effect of Fe–C–MgO bounding on the minority spin Fe(001) IRS (i.e., shift in energy and dispersion in k) and (ii) the carbon induced periodical perturbation of the potential at the bottom Fe/MgO interface (i.e., $c(2\times2)$ reconstruction, Fig. 1) induces scat-

tering events which change k vector. This has direct consequences on the total conductivity.

In positive bias, when electrons are injected toward the top electrode, the low bias TMR changes the sign above 1.5 V. This is determined by the G_{AP} strong enhancement when, in the AP configuration, the injected Δ_1 electrons from the bottom Fe electrode arrive as hot electrons in the top electrode and find an equivalent symmetry in the minority band. In negative voltage, when electrons tunnel into the bottom Fe–C/MgO electrode, similar contribution of the minority Δ_1 symmetry to the conductivity is expected. However, the TMR second sign reversal seems to appear at much higher voltages, above 2.5 V [Fig. 3(a), bottom panel]. One possible reason would be the reduction of the hot electron thermalization length in the bottom electrode. The effect of the IRS at Fe–C/MgO interface on this phenomena requires further theoretical investigation.

Figure 3(b) presents shot noise measurements carried out at $T=10$ K on Fe/Fe–C/MgO/Fe MTJs, with bias direction corresponding to the injection of electrons from the top to the bottom (carbon doped) Fe/MgO interface. For comparison, the solid curves show the "theoretical" expectation for the shot noise, for electron tunneling having Poissonian character: $S_V=2e\langle I\rangle/G^2$, with G as the dynamic conductivity [Fig. 3(a)] and I as the applied current. Within the error bars, showing dispersion of the shot noise "white" spectrum in the kilohertz range, the experimental data clearly indicate the absence of electron correlations and/or sequential tunneling phenomena. This proves that both P and AP spin-dependent conductances and the shot noise are due to direct tunneling between electron bands, as expected for the coherent tunneling.[17] The absence of resonant assisted tunneling in the shot noise demonstrates the high quality of our epitaxial MgO barriers (i.e., the absence of oxygen vacancies). This high quality is furthermore confirmed by the large breakdown voltage of the MTJs (up to 3 V).

The authors thank G. Lengaigne for technological process of MTJs. The work in Madrid has been supported by Spanish-French Integrated Action project (HF2006-0039), Spanish MEC(MAT2006-07196), and Comunidad de Madrid (S-505/MAT0194). This work, as a part of the European Science Foundation EUROCORES Programme 05-FONE-FP-010-SPINTRA, was also supported by funds from the Spanish MEC (MAT2006-28183-E) and the EC Sixth Framework Programme under Contract No. ERAS-CT-2003-980409.

[1] J. S. Moodera, L. R. Kinder, T. M. Wong, and R. Meservey, Phys. Rev. Lett. **74**, 3273 (1995).
[2] T. Miyazaki and N. Tezuka, J. Magn. Magn. Mater. **139**, L231 (1995).
[3] W. H. Butler, X. G. Zang, T. C. Schulthess, and J. M. MacLaren, Phys. Rev. B **63**, 054416 (2001).
[4] J. Mathon and A. Umerski, Phys. Rev. B **63**, 220403R (2001).
[5] M. Bowen, V. Cros, F. Petroff, A. Fert, C. Martínez Boubeta, J. L. Costa-Krämer, J. V. Anguita, A. Cebollada, F. Briones, J. M. de Teresa, L. Morellón, M. R. Ibarra, F. Güell, F. Peiró, and A. Cornet, Appl. Phys. Lett. **79**, 1655 (2001).
[6] J. Faure-Vincent, C. Tiusan, E. Jouguelet, F. Canet, M. Sajieddin, C. Bellouard, E. Popova, M. Hehn, F. Montaigne, and A. Schuhl, Appl. Phys. Lett. **82**, 4507 (2003).
[7] S. S. P. Parkin, C. Kaiser, A. Panchula, P. M. Rice, B. Hughes, M. Samant, and S. H. Yang, Nat. Mater. **3**, 862 (2004).
[8] S. Yuasa, T. Nagahama, A. Fukushima, Y. Suzuki, and K. Ando, Nat. Mater. **3**, 868 (2004).
[9] C. Tiusan, M. Sicot, M. Hehn, C. Bellouard, S. Andrieu, F. Montaigne, and A. Schuhl, Appl. Phys. Lett. **88**, 062512 (2006).
[10] C. Tiusan, J. Faure-Vincent, C. Bellouard, M. Hehn, E. Jouguelet, and A. Schuhl, Phys. Rev. Lett. **93**, 106602 (2004).
[11] R. Guerrero, F. G. Aliev, R. Villar, J. Hauch, M. Fraune, G. Güntherodt, K. Rott, H. Bückl, and G. Reiss, Appl. Phys. Lett. **87**, 042501 (2005).
[12] R. Guerrero, F. G. Aliev, Y. Tserkovnyak, T. S. Santos, and J. S. Moodera, Phys. Rev. Lett. **97**, 026602 (2006).
[13] C. Tiusan, F. Greullet, M. Hehn, F. Montaigne, S. Andrieu, and A. Schuhl, J. Phys.: Condens. Matter **19**, 165201 (2007).
[14] The spatial variation of the realistic electronic structure of the Fe–C/MgO interface (related to realistic morphology) will lead to a distribution in energy of the interfacial resonance.
[15] J. A. Stroscio, D. T. Pierce, A. Davies, R. J. Celotta, and M. Weinert, Phys. Rev. Lett. **75**, 2960 (1995).
[16] The interfacial resonance state of Fe has a d_{z^2} orbital character and belongs to the Δ_1 symmetry. However, due to the strong localization of the d_{z^2} band, this state decays rapidly with the MgO thickness. Therefore, for large MgO thickness its contribution to the total AP conductivity is expected to be small.
[17] Ya. M. Blanter and M. Büttiker, Phys. Rep. **336**, 1 (2000).

Temperature dependence of the interlayer exchange coupling in epitaxial Fe1/MgO/Fe2/Co tunnel junctions

E. Popova[a] and N. Keller
GEMaC, CNRS-UVSQ, 78035 Versailles, France

F. Gendron
INSP, Université Pierre et Marie Curie, 75015 Paris, France

C. Tiusan
LPM, CNRS-UHP, 54506 Vandoeuvre-lès-Nancy, France

A. Schuhl
SPINTEC, URA-CEA/CNRS, CEA/DRFMC, 38054 Grenoble, France

N. A. Lesnik
Institute of Magnetism of National Academy of Sciences of Ukraine, 03142 Kyiv, Ukraine

(Received 21 June 2007; accepted 23 August 2007; published online 13 September 2007)

The temperature dependence of the interlayer exchange coupling has been investigated in epitaxial tunnel junctions Fe1/MgO/Fe2/Co/V with thin MgO layers using *X*-band ferromagnetic resonance (FMR) in the range 2–300 K. Variations of FMR parameters allow concluding that the coupling strength increases with temperature. This is in agreement with predictions of the theories considering pure tunneling mechanisms and contradicts the model of a resonant assisted tunneling related to defects in the insulator. The temperature dependence of the FMR linewidth shows the line narrowing under the sample heating. This may be due to the additional mechanism associated with the coupling. © *2007 American Institute of Physics*. [DOI: 10.1063/1.2784942]

Advanced magnetic tunnel junctions (MTJs), consisting of Fe and Co electrodes separated by the MgO spacer, are developed for spintronics applications as magnetic sensors or random access memory elements.[1–3] From a physical standpoint, such systems are remarkable for the interlayer exchange coupling (IEC) which modifies significantly their magnetic properties.[4,5] The mechanisms of the magnetic coupling are still a subject of discussions though. A theory describing the conductance of MTJ systems has been developed by Slonczewski,[6] who proposed a model for the interlayer coupling through a tunneling barrier at $T=0$. According to recent studies, the tunnel transmission probability is strongly influenced by resonant effects either at the interfaces[7–10] or within the barrier.[11] All the theories predict an exponential decay of the IEC with a barrier thickness, but different temperature dependencies of the coupling. The IEC is expected to increase with the temperature in the framework of Bruno's free electron model,[12] as the tunneling barrier is lower at higher T. An increase of the coupling strength with the temperature is also expected from realistic electronic structure calculations, where the interfacial resonant state of Fe lies slightly above the Fermi level and could be activated by increasing temperature.[7–10] On the contrary, after Zhuravlev *et al.*,[11] a decrease of the IEC with the temperature is theoretically expected for resonant assisted tunneling due to defects (e.g., oxygen vacancies) within the MgO barrier. Thus, reliable data on the temperature dependence of the IEC would clarify the coupling nature and the tunneling mechanism. A quantitative estimation made in the framework of the free electron model[12] shows a weak change of the coupling in the range from 0 to 300 K.[5] Since magnetometry does not allow distinguishing such IEC variations on the background of temperature changes of other film parameters, in particular, the anisotropy, we use the *X*-band ferromagnetic resonance (FMR) to study the coupling in Fe/MgO/Co and Fe1/MgO/Fe2/Co MTJ systems. In the latter, the Co film has been used as hard magnetic layer to pin the top Fe layer in fully epitaxial MTJs.

These stacks were deposited using the molecular-beam epitaxy technique (see Ref. 4). Iron films were prepared by thermal evaporation from a standard Knudsen cell. Cobalt films, vanadium capping layers, MgO sublayers, and spacer layers were fabricated by means of an electron gun deposition. The thicknesses of ferromagnetic layers (d^{Fe} and d^{Co}) were measured using a stepmeter with accuracy of ±5–7%. The MgO thickness (d^{MgO}) values have been determined using the reflection high energy electron diffraction technique with an absolute uncertainty less than ±0.05 nm. As it has been proven using transmission electron microscopy, electrical, and magnetoresistance measurements, the spacer layers were prepared without pinholes and had flat interfaces.[4] The cobalt layer lattice was hexagonal close packed with the *c* axes lying in the film plane. There were two crystallographic domains rotated one from another by 90°. The epitaxial relationship is Co(11–20)[0001]‖Fe(100)[110] and Co(11–20)[0001]‖Fe(100)[1–10].

Reference samples were fabricated on MgO (100) substrates with MgO sublayers in such a way that they simulate each layer in a stack for FMR measurements. The growth conditions and the characterization of the films are described in more detail in our previous works.[4,5] Magnetization was obtained with a superconducting quantum interference device (SQUID) and alternating gradient field magnetometers.

FMR experiments have been performed using an *X*-band Varian spectrometer operating at the frequency $f \approx 9.25$ GHz in the field range of −100–2500 mT and temperature range of 2–300 K. The power of the microwave

[a]Electronic mail: popova@physique.uvsq.fr

field $\boldsymbol{h}$, directed in most cases parallel to the sample surface, was 1 mW.

An analysis of FMR data is performed solving a well known resonance equation[13] together with equations of equilibrium. One obtains the equilibrium angles of the film magnetization M by minimizing the free energy density F. In the case of films with coupled layers $F=d_1F_1+d_2F_2+E_{ex}$, where F_i and t_i are the free energy density and the thickness of the layer 1 or 2, respectively, and E_{ex} is the exchange coupling between the magnetic layers 1 and 2. F_i includes the Zeeman contribution, as well as the shape, magnetocrystalline, and uniaxial anisotropy energies. In the theory of FMR in films with coupled layers,[14] the exchange coupling energy is given by $E_{ex}=-J_{12}(\mathbf{M}_1\mathbf{M}_2/M_1M_2)$, where J_{12} is the coupling parameter and $\mathbf{M}_1$ and $\mathbf{M}_2$ are the magnetizations of the layers 1 and 2. The theory[14] gives a prediction on the behavior of acoustic (H_r^{acoust}) and optical (H_r^{optic}) resonance modes occurring under the IEC effect instead of separate iron (H_r^{Fe}) and cobalt (H_r^{Co}) [or iron/cobalt ($H_r^{Fe/Co}$)] resonances. The mode positions and intensities depend on a sign and strength of the coupling. In other words, a difference between acoustic and optical resonance fields $\delta=H_r^{acoust}-H_r^{optic}$ and the signal intensity ratio I^{acoust}/I^{opt} are a measure of the IEC strength. Both of them are expected to be practically insensitive to temperature variations of the magnetic parameters of MTJ layers as, according to Ref. 14, the fields and intensities should depend rather on differences of layer magnetization and anisotropy field values, than on M_i and H_{Ai} directly. However, quantitative assessments of J_{12} may be incorrect as the model[14] does not take into account neither the influence of the ferromagnetic layer thickness[15] nor the effect of the ferromagnetic material and its electronic state[16] on the IEC.

According to magnetometric data, both soft and hard layers of stacks present fourfold symmetry, with the same directions for the easy axes. Similar to iron films,[15] the parallel resonance spectra of cobalt epitaxial samples at 9.25 GHz consist of two lines, if the film is magnetized along the *hard* magnetic axis. The lines correspond to unsaturation and saturation regimes, associated with the large magnetocrystalline anisotropy field $\boldsymbol{H}_A$. Meanwhile, along the easy axes and other directions, there is no resonance signal in positive applied fields. The bilayer $Fe_5/Co_{35}/V_{10}$, which represents a second MTJs electrode, demonstrates a strong magnetic coupling between iron and cobalt layers and hence, weighted mean magnetic parameters, as has been estimated by FMR. It has been found by SQUID that Fe and Co film magnetizations $M_s^{Fe}\cong 1700$ G and $M_s^{Co}\cong 1400$ G and remain almost unchanged in the temperature range from 300 to 2 K. At 2 K, the resonance fields of iron, cobalt, and iron/cobalt electrodes increase by 10%, 60%, and 50%, respectively. Yet the temperature increase of H_r^{acoust} in MTJs is about 10% and H_r^{opt} decreases by 6% (see Fig. 2).

A unidirectional shift of the minor hysteresis loops, obtained using SQUID in both stacks Fe/MgO/Co/V and Fe1/MgO/Fe2/Co/V, indicates an antiferromagnetic (AF) coupling in agreement with FMR data shown below. The coupling parameter J_{12}, calculated using the values of exchange fields determined from the hysteresis loops, is in the range of $-0.26-0.01$ erg/cm^2 at room temperature for the spacer thickness range $0.5<d^{MgO}<1$ nm.

Figure 1 shows the temperature dependence of the parallel FMR spectra (saturation signals) for a representative sample $Fe_{32}/MgO_{0.57}/Fe_{3.5}/Co_{35}/V_{10}$. Subscripts mark the corresponding layer thicknesses in nanometers. The optical mode is observed at higher fields than the acoustic one implying an AF coupling.[14] In the inset, the intensity ratio of the modes is plotted as the function of the temperature. Such behavior of optical and acoustic modes and of their intensity ratio denotes a weakening of the coupling with the temperature decrease.

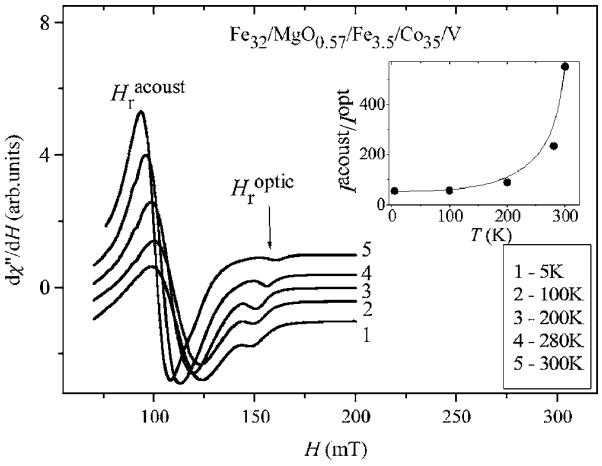

FIG. 1. FMR spectra of a representative $MgO/Fe_{32}/MgO_{0.57}/Fe_{3.5}/Co_{35}/V_{10}$ MTJ at different temperatures. The intensity ratio of acoustic and optical modes, plotted as a function of temperature, is shown in the inset. The spectra were recorded in the parallel configuration of FMR.

Temperature dependencies of the acoustic and optical parallel resonance fields in $Fe_{34}/MgO_{0.6}/Co_{35}/V_{10}$ and $Fe_{32}/MgO_{0.57}/Fe_{3.5}/Co_{35}/V_{10}$ films are shown in Fig. 2. In both stacks, the difference in resonance fields of the two modes increases with increasing temperature. For the sake of clarity, this is also shown in the inset to this figure. The change of $|\delta|$ amounts to $\sim$36% and clearly designates the increase of the AF coupling strength at higher T or vice versa, weakening of the IEC under sample cooling. The sensitivity of the FMR technique to the changes in coupling strength is demonstrated in the inset of Fig. 2 by plotting δ vs d^{MgO} (upper-right scale). The line through the symbols (spheres) represents an exponential fit. Note that in this case, the layer magnetizations and anisotropy fields did not change experimentally.

It is well known that in ferromagnetic films, a dominating inhomogeneous part of the FMR linewidth (ΔH) is mainly sensitive to the anisotropy dispersion and the magnetostriction, both being temperature dependent quantities. The dispersion should be larger at interfaces due to imperfections and strains which tend to relax with increasing temperature. A number of interface regions is greater in stacks than in reference samples; thus, the former are expected to have broader lines. However, in spite of this expectation, it has been found that ΔH in the stacks is essentially smaller than the linewidths in MgO/Co/V and MgO/Fe/Co/V samples mimicking electrodes of MTJs. With layers similar to reference films in magnetic and crystalline structure, the stacks may basically have an additional origin of line narrowing, associated with the interlayer coupling. Could IEC narrowing be a phenomenon similar to a well-known exchange narrowing effect? This issue remains open until an advanced theoretical study is conducted. As regards experiments, a strong correlation between ΔH and IEC has been found.

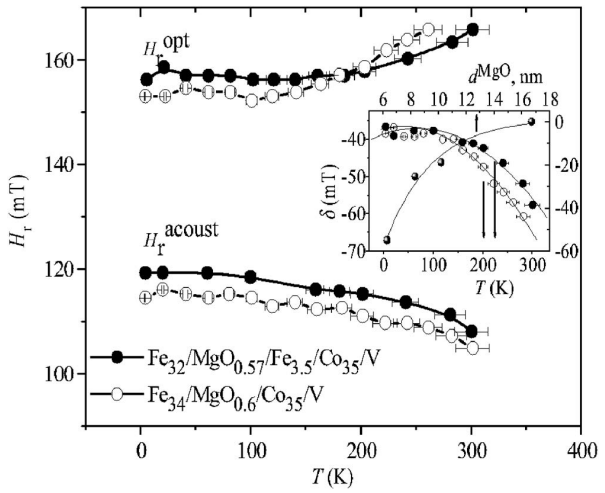

FIG. 2. Temperature dependencies of the acoustic and optical parallel resonance fields are plotted for the $MgO/Fe_{34}/MgO_{0.6}/Co_{35}/V_{10}$ and $MgO/Fe_{32}/MgO_{0.57}/Fe_{3.5}/Co_{35}/V_{10}$ MTJs. The inset depicts the temperature dependencies of $\delta=H_r^{acoust}-H_r^{opt}$ in both samples (lower and left scale) and the MgO room temperature thickness dependence of δ in the $MgO/Fe_{35}/MgO_x/Fe_{3.5}/Co_{35}/V_{10}$ MTJ (upper and right scale).

Temperature dependence of the normalized linewidth ($\Delta H/\Delta H_{T=5\ K}$) in both reference samples and MTJs is depicted in Fig. 3(a) with the dc field applied in plane. On one hand, in MTJs ΔH narrowing under sample heating gets stronger, especially close to the room temperature. As shown by temperature dependencies of resonance fields and signal intensities (Figs. 1 and 2), the IEC is the strongest at 300 K. On the other hand, the FMR linewidth narrowing with IEC increase was also found in MTJs at room temperature. This is obvious in Fig. 3(b) where ΔH is plotted either as a function of the difference between the resonance fields of acoustic and optical modes (curve δ) or depending on the exchange field obtained using SQUID (curve H_{ex}). In both cases, the films were magnetized in the plane. The growth of $|\delta|$ and $|H_{ex}|$ implies IEC increasing.

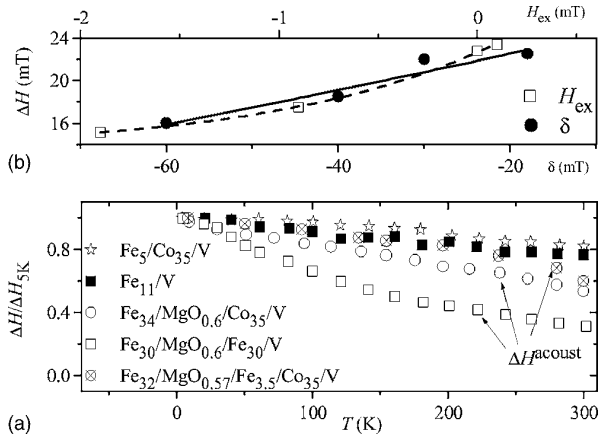

FIG. 3. (a) Temperature dependencies of the normalized linewidth $\Delta H/\Delta H_{at\ T=5\ K}$ in MTJs and in reference films. (b) Dependencies of the FMR linewidth on the distance between acoustic and optical modes (curve δ) and on the exchange field (curve H_{ex}) in the MTJs $Fe_{35}/MgO_x/Fe_{3.5}/Co_{35}/V_{10}$ at $T=300$ K. Lines are exponential fits. The dc field is applied in the film plane.

In summary, temperature dependencies of *X*-band FMR fields, signal intensities, and linewidths in epitaxial MTJ-systems Fe/MgO/Co/V and Fe1/MgO/Fe2/Co/V, as well as in reference films, have been studied. FMR data indicate the AF interlayer coupling occurring at very thin MgO barriers (<1 nm). The sign of the coupling correlates with a shift of a minor hysteresis loop. The temperature behavior of FMR fields and signal intensities in the range of 2–300 K allow concluding that the coupling strength increases with heating. This is in agreement with a pure tunneling mechanism and its more sophisticated version taking into account the interfacial realistic electronic structure.[7–10] To this point, noteworthy are the results obtained on our Fe/MgO/Fe films, where shot noise analysis demonstrates a pure tunneling mechanism and absence of defects within the MgO barrier.[17] All adduced experimental results invalidate theoretical approaches promoting the resonant assisted tunneling mechanism related to defects (oxygen vacancies) within the barrier as an origin of the IEC.

Finally, in the parallel FMR configuration under sample heating from 2 to 300 K, the narrowest lines were observed close to the room temperature, where the IEC has been found to be the strongest. At 300 K, ΔH also decreased with increasing IEC while the spacer thickness was reduced. These facts point out an additional narrowing mechanism associated with the exchange coupling. We obtained similar results studying Fe1/MgO/Fe2/V films;[15] however, in MTJs including the Co layer, they are more pronounced.

[1] Y. Ando, T. Miyakoshi, M. Oogane, T. Miyazaki, H. Kubota, K. Ando, and S. Yuasa, Appl. Phys. Lett. **87**, 142502 (2005).
[2] S. Yuasa, T. Katayama, T. Nagahama, A. Fukushima, H. Kubota, Y. Suzuki, and K. Ando, Appl. Phys. Lett. **87**, 222508 (2005).
[3] S. Yuasa, A. Fukushima, H. Kubota, Y. Suzuki, and K. Ando, Appl. Phys. Lett. **89**, 042505 (2006).
[4] E. Popova, J. Faure-Vincent, C. Tiusan, C. Bellouard, H. Fischer, M. Hehn, F. Montaigne, M. Alnot, S. Andrieu, A. Schuhl, E. Snoeck, and V. da Costa, Appl. Phys. Lett. **81**, 1035 (2002).
[5] J. Faure-Vincent, C. Tiusan, C. Bellouard, E. Popova, M. Hehn, F. Montaigne, and A. Schuhl, Phys. Rev. Lett. **89**, 107206 (2002).
[6] J. C. Slonczewski, Phys. Rev. B **39**, 6995 (1989).
[7] J. M. MacLaren, X.-G. Zhang, W. H. Butler, and X. Wang, Phys. Rev. B **59**, 5470 (1999).
[8] J. Mathon and A. Umerski, Phys. Rev. B **63**, 220403(R) (2001).
[9] O. Wunnicke, N. Papanikolaou, R. Zeller, P. H. Dederichs, V. Drchal, and J. Kudrnovsky, Phys. Rev. B **65**, 064425 (2002).
[10] H. F. Ding, W. Wulfhekel, J. Henk, P. Bruno, and J. Kirschner, Phys. Rev. Lett. **90**, 116603 (2003).
[11] M. Ye. Zhuravlev, E. Y. Tsymbal, and A. V. Vedyayev, Phys. Rev. Lett. **94**, 026806 (2005).
[12] P. Bruno, Phys. Rev. B **49**, 13231 (1994).
[13] H. Suhl, Phys. Rev. **97**, 555 (1955).
[14] B. Heinrich and J. F. Cochran, Adv. Phys. **42**, 523 (1993); J. Lindner and K. Baberschke, J. Phys.: Condens. Matter **15**, S465 (2003).
[15] E. Popova, C. Tiusan, A. Schuhl, F. Gendron, and N. A. Lesnik, Phys. Rev. B **74**, 224415 (2006).
[16] H. Yanagihara, Y. Toyoda, and E. Kita, J. Appl. Phys. **101**, 09D101 (2007).
[17] R. Guerrero, D. Herranz, F. G. Aliev, F. Greullet, C. Tiusan, M. Hehn, and F. Montaigne, Appl. Phys. Lett. (submitted).

Bibliography

[1] J. S. Moodera, L. R. Kinder, T. M. Wong, and R. Meservey, Phys. Rev. Lett. **74**, 3273 (1995); T. Miyazaki and N. Tezuka, J. Magn. Magn. Mat. **139**, L231 (1995).

[2] J. C. Slonczewski, Phys. Rev. **B 39**, 6995 (1989).

[3] P.M. Tedrow, R. Meservey, Phys. Rep. **238**, 174 (1994).

[4] M. Julierre, Phys. Lett. **26**, 192 (1975).

[5] X-G. Zhang, W. H. Butler, J. Phys: Condens. Matter **15**, R1603, (2003).

[6] W. F. Brinkman, R. C. Dynes, and J. M. Rowell, J. Appl. Phys. **41**, 1915, (1971).

[7] V. Bellini, Ph.D Thesis: Rheinisch-Westfalischen Technischen Hochschule Aachen p. 121 (2000); P.H. Dederichs et al, Journal of Magn. Magn. Mat., 240 108-113 (2002).

[8] J. P. Velev, K. D. Belashchenko, D. A. Stewart, M. van Schilfgaarde, S. S. Jaswal, and E. Y. Tsymbal Phys. Rev. Lett. **95**, 216601, (2005).

[9] M. Bowen, A. Barthelemy, V. Bellini, M. Bibes, P. Seneor, E. Jacquet, J.-P. Contour, and P. H. Dederichs Phys. Rev. B 73, 140408 (2006).

[10] W. H. Butler, X.-G. Zhang, Xindong Wang, Jan van Ek, and J. M. MacLaren, J Appl. Phys. **81**, 5518 (1997); W. H. Butler, X.-G. Zhang, T. C. Schulthess, J. M. MacLaren, Phys. Rev. B **63**, 054416 (2001).

[11] J.M. MacLaren, X.-G. Zhang, W.H. Butler, X. Wang, Phys. Rev. B **59** 5470, (1999);

[12] J. Mathon and A. Umerski, Phys. Rev. B **63**, 220403(R) (2001).

[13] O. Wunnicke, N. Papanikolaou, R. Zeller, and P. H. Dederichs, V. Drchal and J. Kudrnovsky, Phys. Rev. B **65**, 064425, (2002).

[14] H.F. Ding, W. Wulfhekel, J. Henk, P. Bruno, J. Kirschner, Phys. Rev. Lett. **90**, 116603, (2003).

[15] K. D. Belashchenko, J. Velev, E. Y. Tsymbal, Phys. Rev. B **72**, R140404 (2005).

[16] J. Faure-Vincent, C. Tiusan, C. Bellouard, E. Popova, M. Hehn, F. Montaigne, A. Schuhl, Phys. Rev. Lett. **89**, 107206 (2002).

[17] S. A. Wolf, J. of Superconductivity **13**, 195 (2000); J.M. Daughton, J. Appl. Phys. **81**, 3758 (1997); W.J. Gallagher,J.H. Kaufman, S.S.P. Parkin, R.E. Scheuerlin, U. S. Patent N. 5 640 343 (1997).

[18] P. Grunberg, R. Schreiber, Y. Pang, M.B. Brodsky, H. Sower, Phys. Rev. Lett.**57**, 2442, (1986).

[19] P. Bruno, Phys. Rev. B 52, 411, (1995).

[20] K. Ounadjela, L. Zhou, R. Stamps, P. Wigen, M. Hehn and J. Gregg, J. Appl. Phys. **79** (1996).

[21] Z. Zhang, L. Zhou, P. Wigen, K. Ounadjela, Phys. Rev. B**50**, 6094, (1994).

[22] S.S.P. Parkin, N. More, K.P. Roche, Phys. Rev. Lett. **64**, 2304, (1990).

[23] D.M. Edwards, J. Mathon, R. Muniz, S. Phan, J. Phys. Condens. Matter **3**, 4941, (1991).

[24] N. Persat, H.A.M. van den Berg, A. Dinia, J. Magn & Magn. Mater. **165**, 446, (1997).

[25] S.S.P. Parkin, Phys. Rev. Lett. **67**, 3598, (1991).

[26] S. Zoll, A. Dinia, D. Stoeffler, M. Gester, H.A.M. Van den Berg, K. Ounadjela, Europhys. Lett. **39**, (3), 323, (1997).

[27] S. Zoll, A. Dinia, H. A. M. van den Berg, J. P. Jay, C. Mny, G. Pan, A. Michel, V. P. Bohnes, P. Panissod, Phys. Rev. B**57**, 4842, (1998).

[28] R. M. J. van de Verdoonk, J. Nowak, R. Meservey, J. S. Moodera, and W. J. M. de Jonge, Appl. Phys. Lett. **71**, 2839 (1997).

[29] J. H. Greiner, J. Appl. Phys.**42**, 5151 (1971).

[30] C. Tiusan, M. Hehn, K. Ounadjela, Y. Henry, J. Hommet, C. Meny, H.A.M. van den Berg, L. Baer, R. Kinder, J. Appl. Phys. **8**, (1999).

[31] J. S. Moodera, E. F. Gallagher, K. Robinson and J. Nowak, Appl. Phys. Lett. **70**, 3050 (1997).

[32] L. Baer, Private communications

[33] K. Ounadjela, L. Zhou, P. Wigen, R. Stamps and J. Gregg , Europhys. Lett. **39**, 213 (1997).

[34] H. A. M. van den Berg, W. Clemens, G. Gieres, G. Rupp, M. Vieth, J. Wecker and S. Zoll, J. Magn. Magn. Mat. **165**, 524 (1997).

[35] P. Panissod, from NATO ASI Series, eds. Wigen & Baryakhtar, Kluwer Academic, 1998, "Frontiers in Magnetism of Reduced Dimension Systems".

[36] H. W. Fuller, M. E. Hale, J. Appl. Phys, **31**, 238, (1960).

[37] K. D. Laver, Thin Solid Films, 2, (1968), 149-172, Elsevier, Laussane-Printed in the Neterlands.

[38] K. J. Harte, J. Appl. Phys. **39**, 1503, (1997).

[39] H. Herzer, IEEE. Trans. on Magn. **25**, 5 , 3327, (1989).

[40] R.J. Spain, I. B. Puchalska, J. Appl. Phys. **35**, 824, (1968).

[41] D. V. Berkov, N. L. Gorn, Phys. Rev. B**57**, 14332, (1998).

[42] H. N. Lin, Y. H. Chiou, B. M. Chen, H. P. D. Shieh, C. R. Chang, J. Appl. Phys. **83**, 4997, (1998).

[43] J. J. Saenz, N. Garcia, J. C. Zlonczewski, Appl. Phys. Lett. **53**, 1449, (1998).

[44] D. Rugar, H. M. Mamin, P. Guethner, S.E. Lambert, J. E. Starn, I. McFadyen, T. Yogi, J. Appl. Phys. **68**, 1169, (1990).

[45] L. J. Heydermann, J. N. Chapmann, S.S.P. Parkin, J. Magn. Magn. Mater. **96**, 125, (1991).

[46] M. F. Gillies, J. N. Chapman, J. C. S. Kools, J. Appl. Phys. **78**, 5554, (1995).

[47] A Hubert, W Rave, S. L. Tomlinson, Phys. Rep., **258**,173,(1995).

[48] R. I. Potter, J. Appl. Phys, **41**, 1648, (1970).

[49] H. S. Cho, C.Hou, M. Sun, H. Fujikawa, J. Appl. Phys. **85**, 5160, (1999).

[50] R. L. Stamps, A. S. Carrico, P. E. Wigen, Phys. Rev.B **55**, 6473, (1997).

[51] R. L. Stamps, Phys. Rev.B **49**, 339, (1994).

[52] C. Tiusan, T. Dimopoulos, K. Ounadjela, M. Hehn, Phys. Rev. **B 64** (10), 104423,(2001).

[53] C. Tiusan, T. Dimopoulos, K. Ounadjela, M. Hehn, H. van den Berg, V. da Costa, Y. Henry J. Appl. Phys. **87** (9), 4676,(2000).

[54] C. Tiusan, M. Hehn, T. Dimopoulos, K. Ounadjela, J. Appl. Physics **89** (11), 6668,(2001).

[55] T. Dimopoulos, C. Tiusan, V. Da Costa, K. Ounadjela, H. van den Berg Applied Physics Letters 77, (22), 3624, (2000).

[56] L. Néel, C.R. Acad. Sci. 255, 1676 (1962).

[57] S. Demokritov, E. Tsymbal, P. Grnberg, W. Zinn, I. K. Schuller , Phys. Rev. B 49, 720 (1994).

[58] A.Anguelouch, B. Shrang, G. Xiao, Y. Lu, P.Trouilloud, W.J. Gallagher, S.S.P.Parkin, Appl .Phys. Lett. 76, 622 (2000).

[59] L. Thomas, M.G. Samant, S.S.P. Parkin, Phys. Rev. Lett. 84, 1816 (2000).

[60] C. Tiusan, T. Dimopoulos, K. Ounadjela, M. Hehn, H.A.M. van den Berg, Y. Henry, V. Da Costa, Phys. Rev. B 61, 580 (2000).

[61] V. da Costa, C. Tiusan, T. Dimopoulos, K. Ounadjela, Phys. Rev. Lett. 85, 876 (2000).

[62] W.J. Gallagher, J.H. Kaufman, S.S.P Parkin, R.E. Scheuerlin, *Magnetic Memory Array using Magnetic Tunnel Junction Devices in Memory Cells*, United States Patent N. 5 640 343 (1997)

[63] C.L. Platt, B. Dieny, A.E. Berkowitz, J. Appl. Phys., **81**, 5523 (1997).

[64] M. Chshiev, D. Stoeffler, A. Vedyayev, K. Ounadjela, cond-mat/0105264, submitted to Europhys. Lett.;*Proceedings of MML'01*, to be published in JMMM.

[65] Leo Esaki, Rev. Mod. Phys., **46**, 237 (1974).

[66] L.F.Schelp, A.Fert, F. Fettar, P. Holody, S.F.Lee, J.L.Maurice, F.Petroff, A.Vaures, Phys. Rev. B **56**, R5747 (1997).

[67] A. Iovan, V. Da Costa, Y. Henri, D. Stoeffler, Mat. Sci. Eng. B **126**, 258, (2006).

[68] A. Iovan, V. Korenivski, and D. B. Haviland J. Appl. Phys. **99**, 08E502 (2006).

[69] T. Dimopoulos, V. Da Costa, C. Tiusan, K. Ounadjela, H. van den Berg Appl. Phys. Lett. **79** (19), 3110, (2001).

[70] D. J. Keavney, E. E. Fullerton, and S. D. Bader, J Appl. Phys. **81**, 795 (1996).

[71] M. Klaua, D. Ullmann, J. Barthel, W. Wulfhekel, J. Kirschner, R. Urban, T. L. Monchesky, A. Enders, J. F. Cochran, B. Heinrich, Phys. Rev. B **64**, 134411 (2001).

[72] M. Bowen, V. Cros, F. Petroff, A. Fert, C. Martinez Boubeta, J. L. Costa-Kramer, J. V. Anguita, A. Cebollada, F. Briones, J. M. de Teresa, L. Morellon, M. R. Ibarra, F. Guell, F. Peiro, and A. Cornet, Appl. Phys. Lett. **79**, 1655 (2001).

[73] J. Faure-Vincent, C. Tiusan, E. Jouguelet, F. Canet, M. Sajieddine, C. Bellouard, E. Popova, M. Hehn, F. Montaigne, A. Schuhl, Appl. Phys. Lett. **82**, 4507 (2003).

[74] C. Tiusan, M. Sicot, J. Faure-Vincent, M Hehn, C Bellouard, F. Montaigne, S. Andrieu and A. Schuhl, J. Phys.: Condens. Matter **18** , 941-956 (2006).

[75] C. de Buttet, M. Hehn, F. Montaigne, C. Tiusan, G. Malinowski, A. Schuhl, E. Snoeck, and S. Zoll, Phys. Rev. B **73**, 104439 (2006).

[76] C. Tiusan, J. Faure-Vincent, C. Bellouard, M. Hehn, E. Jouguelet, A. Schuhl, Phys. Rev. Lett. **93**, 106602, (2004).

[77] C. Tiusan, M. Sicot, M. Hehn, C. Belouard, S. Andrieu, F. Montaigne, A. Schuhl, Appl. Phys. Lett. **88**,62512, (2006).

[78] S. Yuasa, T. Nagahama, A. Fukushima, Y. Suzuki and K. Ando, Nature Materials **3**, 868 (2004);

[79] S. Yuasa, A. Fukushima, H. Kubota, Y. Suzuki, K. Ando, Appl. Phys. Lett. 89 042505, (2006).

[80] C. Tusche, H. L. Meyerheim, N. Jedrecy, G. Renaud, A. Ernst, J. Henk, P. Bruno, J. Kirschner, Phys. Rev. Lett. **95**, 176101 (2005).

[81] T. Dimopoulos, G. Gieres, J. Wecker, N. Wiese, Y. Luo, K. Samwer, J. Appl. Phys., **98** (7), 073705, (2005).

[82] S. S. P. Parkin, C. Kaiser, A. Panchula, P. M. Rice, B. Hughes, M. Samant, S.-H. Yang, Nature Materials **3**, 862 (2004).

[83] S. Yuasa, A. Fukushima, T. Nagahama, K. Ando, Y. Suzuki, Jpn. J. Appl. Phys. **43**, No. 4B (2004); D. D. Djayaprawira, K. Tsunekawa, M. Nagai, H. Maehara, S. Yamagata, N. Watanabe, S. Yuasa, Y. Suzuki and K. Ando, Appl. Phys. Lett. **86**, 092502 (2005).

[84] W. Shen, D. Mazumdar,X. Zou, X. Liu, X.B.D. Schrag, G. Xiao, Appl. Phys. Lett. **88** (18), 182508, (2006).

[85] J. Hayakawa S. Ikeda, F. Matsukura, H. Takahashi, H. Ohno, Japan. Journ. Appl. Phys. **44**(19), L587, (2005); Y. Lee, J. Hayakawa, S. Ikeda, F. Matsukura, H. Takahashi, H. Ohno, Oral presentation to 10th Joint MMM/Intermag Conference, Baltimore (2007).

[86] K. Tsunekawa, D.D. Djayaprawira, M. Nagai, H. Maehara, S. Yamagata, N. Watanabe, S. Yuasa, Y. Suzuki, K. Ando, Appl. Phys. Lett. **87**, 72503 (2005).

[87] M. Mizuguchi, Y. Suzuki, T. Nagahama and S. Yuasa,Appl. Phys. Lett. **91**, 012507 (2007)

[88] H. Kubota, A. Fukushima, Y. Ootani, S. Yuasa, K. Ando, H. Maehara, K. Tsunekawa,D. Djayaprawira, N. Watanabe, Y. Suzuki, IEEE Transactions on, **41**, 2633-2635, (2005).

[89] S. Ikeda, J. Hayakawa, Y. M. Lee, T. Tanikawa, F. Matsukura, and H. Ohno, J. Appl. Phys. 99, 08A907 (2006).

[90] Z. Diao, D. Apalkov, M. Pakala, Y. Ding, A. Panchula, Y. Huai, Appl. Phys. Lett. **87**, 232502, (2005).

[91] A. A. Tulapurkar, Y. Suzuki, A. Fukushima, H. Kubota, H. Maehara, K. Tsunekawa, D. D. Djayaprawira, N. Watanabe, S. Yuasa, Nature **438**, 339, (2005).

[92] T. Nozaki, N. Tezuka, K. Inomata, Phys. Rev. Lett. **96**, 27208 (2006).

[93] J.A. Stroscio, D.T. Pierce, A. Davies, and R.J. Celotta, M. Weinert, Phys. Rev. Lett. **75** (16), 2960-2963 (1995).

[94] Katayama, S. Yuasa, J. Velev, M. Ye. Zhuravlev, S. S. Jaswal and E. Y. Tsymbal, Appl. Phys. Lett **89**, 112503 (2006).

[95] M. Y. Zhuravlev, E. Y. Tsymbal, and A. V. Vedyayev, Phys. Rev. Lett. **94**, 026806 (2005).

[96] V. Blum, A. Schmidt, W. Meier, L. Hammer, K. Heinz, J. Phys.: Condens. Matter **15**, 3517, (2003).

[97] H.A.M. van den Berg, W. Clemens, G. Gieres, G. Rupp, M. Vieth, J. Wecker, and S. Zoll, J. Magn. Magn. Mater. **165**, 524, (1997).

[98] C. Tiusan, T. Dimopoulos, K. Ounadjela, M. Hehn, H.A.M. van den Berg, Y. Henry, and V. Da Costa, Phys. Rev. B **61**, 580, (2000).

[99] C. Tiusan, M. Hehn, K. Ounadjela, Eur. Phys. J. B bf 26, 431, (2002).

[100] E. Popova, J. Faure-Vincent, C. Tiusan, C. Bellouard, H. Fischer, M. Hehn, F. Montaigne, M. Alnot, S. Andrieu, A. Schuhl, E. Snoeck, V. da Costa, Appl. Phys. Lett. **81**, 1035 (2002).

[101] J. S. Moodera, J. Nowak, R. J. M. vandeVeerdonk, Phys. Rev. Lett. **80**, 2941, (1998).

[102] X.-G. Zhang, W. Butler, J. Phys.: Condens Matter **15**, R1603, (2003).

[103] D. Stoeffler, Private communication.

[104] [P. Blaha, K. Schwarz, G.K.H.Madsen, D. Kvasnicka, J.Luitz, WIEN2k, *An Augmented Plane Wave + Local Orbitals Program for Calculating Crystal Properties* (K. Schwartz, Techn. Univ. Wien, Austria), 2001. ISBN 3-9501031-1-2].

[105] X.-G. Zhang, W. H. Butler, and A. Bandyopadhyay, Phys. Rev. B **68**, 092402 (2003).

[106] C. Zhang, X.-G. Zhang, P.S. Krstic, H.-P. Cheng, W. H. Butler, J. M. MacLaren, Phys. Rev. B **69**, 134406, (2004).

[107] R. Jansen, J.S. Moodera, Phys. Rev. B **61**, 9047, (2000).

[108] J.M. de Teresa, A. Barthelemy, A. Fert, J.P. Contour, F. Montaigne, P. Seneor, Science **286**, 507, (1999).

[109] S. Zhang, P.M. Levy, A.C. Marley, S.S.P. Parkin, Phys. Rev. Lett. **79**, 3744, (1997); J.S. Moodera, J. Nowak, R.J.M. van de Veerdonk, Phys. Rev. Lett. **80**, 2941, (1998).

[110] M. Pajda, J. Kudrnovsky, I. Turek, V. Drchal, P. Bruno, Phys. Rev B **64**, 174402, (2001).

[111] K.Parlinski, J.Lazewski and Y.Kawazoe, J.Phys.Chem. Solids, **61**, 87 (2000).

[112] F. Bardou, Europhys. Lett. **39**, 239 (1997); V. Da Costa, M. Romeo and F. Bardou J. Magn. Magn. Mat., **258-259**, 90 (2003).

[113] M. Przybylski, J. Grabowski W. Wulfhekel, M. Rams, K. Tomala, J. Kirschner, J. of Appl. Phys. **95**, 597 (2004).

[114] C. Zhang, X.-G. Zhang, P.S. Krstic, H. P. Cheng., W.H. Butler, J.M. MacLaren, Phys. Rev B **69**, 134406 (2004).

[115] G. Malinowski, M. Hehn, S. Robert, O. Lenoble, A. Schuhl, P. Panissod, Phys. Rev. B **68**, 184404 (2003).

[116] J. Slonczewski, J. Magn. Magn. Mat. 159, p. L1 (1996).

[117] L. Berger, Phys. Rev. **B 54**, p. 9353 (1996); L Berger, Phys. Rev. B 59, p. 11465 (1999).

[118] M. Tsoi, R. E. Fontana, and S. S. P. Parkin, Appl. Phys. Lett. 83, 2617, (2003).

[119] E. Y. Tsymbal, et al., J. Phys.: Condens. Matter **15**, R109 (2003).

[120] F. Kanjouri N. Ryzhanova, N. Strelkov, A. Vedyayev , B. Dieny, Journ. Appl. Phys.**98**, 083901 (2005).

[121] B.R. Bulka et al, Phys. Rev. **B 62**, 1186 (2000).

[122] Ya.M. Blanter, M. Buttiker, Physics Reports **336**, 1 (2000).

[123] S. F. Kaka, M. R. Pufall, W. H. Rippard, T. J. Silva, and S. E. Russek, Nature **437**, 389 (2005).

[124] T. J. Silva, C. S. Lee, T. M. Crawford, and C. T. Rogers, J. Appl. Phys. 85, 7849 (1999).

[125] G. Counil, Joo-Von Kim, T. Devolder, C. Chappert, K. Shigeto and Y. Otani, J. Appl. Phys. 95, 5646 (2004).

[126] Chshiev et al, arXiv: cond-mat/0509561; J. Appl. Phys **99**, (2006).

[127] M.D. Stiles and A. Zangwill, PRB **66**, 014407,(2002).

[128] R. P. Erickson, K. B. Hathaway, J. R. Cullen, Phys. Rev. **47**, 2626, (1993).

[129] T.-W. Chang, C.-G. Jiang, Chinese Journal of Physics, Vol. 36, 817, (1998); C. J. Bradley, A. P. Cracknell, The Mathematical Theory of Symmetry in Solids (Clarendon Press, Oxford, 1972).

[130] Alexandre M. Bataille, PhD thesis, Université Paris-XI, Orsay (2005) (in french).

[131] A. Yanase and K. Siratori, J. Phys. Soc. Jpn. 52, 312 (1984).

[132] R.A. de Groot and K.H.J. Buschow, J. Magn. Magn. Mater. 54, 1377 (1986).

[133] Z. Zhang and S. Satpathy, Phys. Rev. B 44, 13319 (1991).

[134] D.J. Huang, C.F. Chang, J. Chen, L.H. Tjeng, A.D. Rata, W.P. Wu, S.C. Chung, H.J. Lin, T. Hibma and C.T. Chen, Jour. Magn. Magn. Mater. 239, 261 (2002).

[135] S.A. Morton, G.D. Waddill, S. Kim, I.K. Schuller, S.A. Chambers and J.G. Tobin, Surf. Sci. 513, L451 (2002).

[136] A.M. Bataille, R. Mattana, P. Seneor, A. Tagliaferri, S. Gota, K. Bouzehouane, C. Deranlot, M.J. Guittet, J.B. Moussy, C. de Nadaï, N.B. Brookes, F. Petroff and M. Gautier-Soyer, Jour. Magn. Magn. Mater. 316, e963 (2007).

[137] J.M. De Teresa, A. Barthélémy, A. Fert, J.P. Contour, R. Lyonnet, F. Montaigne, P. Seneor and A. Vaurès, Phys. Rev. Lett. 82, 4288 (1999).